Theoretical and Computational Studies of Isotropic Homogeneous Turbulence

Thesis by
Mei-Jiau Huang

In Partial Fulfillment of the Requirements
for the Degree of
Doctor of Philosophy

California Institute of Technology
Pasadena, California

1994

(Defended April 28, 1994)

To Lin Ming-Chyuan

Acknowledgements

I would like to express my deepest gratitude to my advisor, Professor Anthony Leonard, for his support and understanding during my years as a graduate student. I would like to thank him in particular for the freedom he allowed me in the course of investigation, for his always being so thoughtful of my poor self-expressing ability in English, and for the ways he inspired me to approach a scientific life as well as a real life. It is a pleasure and honor being his student.

I would also like to thank all the members of the Caltech community and in particular the people of GALCIT as well as ME whose insightful comments and suggestions were very helpful. For lending their time, interest and insight, I wish to sincerely thank the members of my Examining Committee: Prof. Brennen, Prof. Dale Pullin, Prof. P.G. Saffman and Prof. Zukoski. I would like to thank sincerely Prof. Dale Pullin for those inspirational discussions and Prof. Paul Dimotakis for his interest in this thesis and for providing treasurable literature information.

I would like to thank my advisor's secretary Connie and Jean as well as all the secretaries and staff in GALCIT and ME, who have been very helpful in so many ways.

This work was supported by the U.S. Air Force Office of Scientific Research under grant #AFOSR-91-0241 and was performed in part using the Intel Touchstone Supercomputing Consortium whose help is gratefully acknowledged.

Finally, it's my deepest pride to thank my mother and grandfather for their endless love and encouragement of my education. I would like to thank my elder brother as well for his leading me to the world of mechanical engineering and his support of our family.

Abstract

Numerical simulations are presented for viscous incompressible homogeneous turbulent flows with periodic boundary conditions. Our numerical method is based on the spectral Fourier method. Rogallo's code is modified and extended to trace fluid particles and simulate the evolution of material line elements.

The first part of the thesis is about modifying and applying the code to simulate a passive vector field convected and stretched by the so-called ABC flows in the presence of viscosity. The correlation of the geometry of the physical structures of the passive vector with the external straining is investigated. It is observed that most amplifications either occur in the neighborhoods of local unstable manifolds of the stagnation points of the ABC flows, if they exist, especially those with only one positive eigenvalue, or they are confined within the chaotic regions of the ABC flows if there is no stagnation point. Tube-like structures in all simulations are observed.

The second part of the thesis is an investigation of the power-law energy decay of turbulence. Two decay exponents, 1.24 and 1.54, are measured from simulations. A new similarity form for the double and triple velocity autocorrelation functions using the Taylor microscale as the scaling, consistent with the Kármán-Howarth equation and a power-law energy decay, is proposed and compared with numerical results. The proposed similarity form seems applicable at small to intermediate Reynolds number. For flows with very large Reynolds number, an expansion form of energy spectrum is proposed instead. Two lengthscales are used to express the energy spectrum in the energy-containing range and in the dissipation range of wave numbers. The uniform expansion is obtained by matching spectra in the inertial subrange to the famous Kolmogorov's $k^{-5/3}$ spectrum.

The third part of the thesis is a presentation of the Lagrangian data collected by tracking fluid particles in decaying turbulent flows. The mean growth rates of the magnitudes of material line elements, that of the vorticity due to nonlinear forces, and

the mean principal rates of strain tensors are found to be proportional to the square root of the mean enstrophy. The proportional coefficients remain constant during the decay. The mean angles between material line elements and the principal directions of the strain tensors corresponding to the most stretching and the intermediate principal rates are about the same which is probably caused by the averaging process and by the possible switch of principal directions. The evolution of these angles under the action of one Burger's vortex is examined and the results support the conjecture. Following fluid particles which suffer substantial stretching in their history, we, through use of flow visualization tools, observe the evolution of nearby vorticity structures. It is observed that vortex sheets are created first by the nonlinear stretching which gradually become tubes at later times by diffusion.

List of Symbols

English Symbols

A, B, C	parameters in the ABC flows
a	uniform rate of strain
A_{ij}	the antisymmetric part of velocity gradient tensor
B, m, b	parameters in the model energy spectrum, Eq.(4.111)
$\mathbf{B}$	magnetic field
D^*	dimensionless energy dissipation spectrum
$E(k)$	three dimensional energy spectrum
$E_1(k)$	energy spectrum of large eddies
$E_2(k)$	energy spectrum of small eddies
$E_\alpha(k)$	one dimensional energy spectrum, α=1,2,3
E_{ij}	energy spectral tensor
$\mathbf{e}_i$	eigenvectors of a stagnation point, i=1,2,3
$\mathbf{e}_{\alpha,\beta,\gamma}$	unit eigenvectors of the strain tensor
$e_{r\theta}$	azimuthal shear
$F_j(k)$	expansion function of energy spectrum for large eddies; external force in j^{th} direction
$\widehat{F}_j(k)$	generalized expansion function of energy spectrum for large eddies

f	two-point-one-time velocity autocorrelation function
f_1, f_2	self-similar functions defined by Eq.(4.18a)
f_E	one-point-two-time Eulerian velocity autocorrelation function
f_L	Lagrangian velocity autocorrelation function
$\tilde{f}_L$	self-similar Lagrangian velocity autocorrelation function defined by Eq.(5.31)
f_j^{NL}	the j^{th} component of the nonlinear terms
f_j^{NL+P}	the j^{th} component of the nonlinear terms combined with the pressure term
$\widehat{f}_j^{NL}$	the j^{th} component of the Fourier coefficient of the nonlinear terms
$\widehat{f}_i^{NL+P}$	the j^{th} component of the Fourier coefficient of the nonlinear terms combined with the pressure term
G	defined by Eq.(4.14)
$G_j(k)$	expansion function of energy spectrum for small eddies
$\widehat{G}_j(k)$	generalized expansion function of energy spectrum for small eddies
$\mathbf{H(x)}$	eigenfunction
$\widehat{H}_j(k)$	generalized expansion function of energy transfer spectrum for large eddies
$\mathcal{H}$	helicity
$h(z)$	defined by Eq.(4.28c)
I_α	indicator of isotropy defined by Eq.(4.51)
i	$\sqrt{-1}$
K	turbulent kinematic energy
$K_j(k)$	expansion function of energy transfer spectrum for small eddies

$\widehat{K_j}(k)$	generalized expansion function of energy transfer spectrum for small eddies
k_j	wave vector in j^{th} direction
k	wave number; triple velocity autocorrelation function
k_{max}	maximum available wave number
k_p	peak wave number in the initial energy spectrum
k_1, k_2	self-similar functions defined by Eq.(4.18b) and Eq.(4.59)
k^*	the product of wave number and Kolmogorov dissipation lengthscale
k_η	Kolmogorov wave number
L	the size of simulated domain
$\mathcal{L}$	a linear operator defined by Eq.(3.8); lengthscale in Eq.(4.68); an operator defined by Eq.(4.104)
$\mathcal{L}_f$	longitudinal integral length scale defined by Eq.(5.25)
$\mathcal{L}_E$	Eulerian integral length scale
$\mathcal{L}_L$	Lagrangian integral length scale
$\underline{\ell}$	material line element vector
$\ell_{r,\theta,z}$	components of a material line element in the cylindrical coordinates
$\widehat{\ell}_{r,\theta,z}$	dimensionless components of a material line element in the cylindrical coordinates
ℓ	magnitude of a material line element vector
M	number of fluid particles released
$M(a, b, z)$	regular confluent hypergeometric function
N	numerical resolution

n	decay exponent of turbulent energy
p	eigenvalue; turbulent pressure
q	turbulent velocity
R	transformation matrix which diagonalizes strain tensor
$\hat{R}$	dimensionless radius of a Burger vortex
Re_λ	Taylor Reynolds number
$Re_{\lambda max}$	Taylor Reynolds number at which skewness is maxmum
$Re_{\lambda\omega}$	enstrophy Reynolds number ($\equiv (\overline{\omega^2})^{3/2}/\epsilon_\omega$)
r	spatial separation
S	skewness of longitudinal velocity derivative
S_{max}	maximum skewness
S_{ij}	strain tensor (the symmetric part of velocity gradient tensor)
s, s'	dimensionless time variable
T_s	inverse of the exponent of the exponential tail of the self-similar Lagrangian velocity autocorrelation function
$T(k)$	energy transfer spectrum
t	time variable
t_o	reference time origin
$\mathcal{T}_E$	Eulerian integral time scale
$\mathcal{T}_L$	Lagrangian integral time scale
$\mathcal{T}_o$	eddy turnover time defined by Eq.(4.46) and Eq.(5.13)

$U(a,b,z)$	singular confluent hypergeometric function
u_j	turbulent velocity component in j^{th} direction;
	velocity component in j^{th} direction of the ABC flows
$u_{r,\theta,z}$	velocity components in the cylindrical coordinates
$\widehat{u}_{r,\theta,z}$	dimensionless velocity components in the cylindrical coordinates
$\widehat{u}_j$	velocity Fourier coefficient in j^{th} direction
u,v,w	turbulent velocity component in x-, y-, and z- directions
X^2	particle square displacement
$\mathbf{x}_p$	particle position
x_j	spatial coordinate in j^{th} direction
x,y,z	x-, y- , z- coordinates
$\bar{x},\bar{y},\bar{z}$	stagnation point
x_o,y_o,z_o	particle initial position

Greek Symbols

α	the most positive principal rate of strain tensor; exponent in the
	power-law dependence of skewness on Taylor Reynolds number;
	ratio of dissipation scales defined by Eq.(5.26)
β	the intermediate principal rate of strain tensor;
	ratio of dissipation scales defined by Eq.(5.27)
Γ	Gamma function

Γ_o circulation

$\hat{\Gamma}$ dimensionless circulation

γ the most negative principal rate of strain tensor

Δ' defined by Eq.(5.56)

δ Dirac's delta function

ϵ energy dissipation rate

ϵ_ω enstrophy dissipation rate

η Kolmogorov dissipation lengthscale

$\Im$ a linear operator defined by Eq.(3.13)

χ defined by Eq.(4.73)

λ Taylor microscale

λ_i principal rates at a stagnation point, i=1,2,3

λ_ω defined by Eq.(3.26)

μ molecular diffusivity

μ_j order function in Eq.(4.69)

ν kinetic viscosity

ν_j order function in Eq.(4.70)

Ω mean squart root enstrophy

$\Omega(k)$ enstrophy spectrum

Ω^* dimensionless enstrophy dissipation spectrum

$\overline{\Omega}$	1/2 mean enstrophy
ω	vorticity magnitude; frequency
ω_j	vorticity component in j^{th} direction
ω_η	Kolmogorov frequency
$\phi_{\alpha,\beta,\gamma}$	angles between a vorticity vector (or a material line element) and the principal directions of strain tensor defined by Eq.(5.51) (or Eq.(5.50))
$\phi_L(\omega)$	Lagrangian frequency spectrum
ρ	fluid density; resolvent of a linear operator
σ	spectrum of a linear operator; 5/n (n = decay exponent of turbulent energy); growth rate of vorticity by nonlinear forces ($\equiv \omega_i S_{ij} \omega_j / \omega^2$)
σ_i	variance, i=1,2,3
σ_S	variance of straining magnitude
τ, τ'	time measured since particles were released
τ_o	reference time origin
τ_η	Kolmogorov dissipation time scale defined by Eq.(4.47)
τ_E	Eulerian dissipation time scale defined by Eq.(5.21)
τ_L	Lagrangian dissipation time scale defined by Eq.(5.22)
τ_s	characteristic turbulence time scale

$\theta_{\alpha,\beta,\gamma}$ mean angles of a vorticity vector (or a material line element) with respect to the principal directions of strain tensor defined by Eq.(5.49)

ξ the product of wave number, Taylor microscale, and Taylor Reynolds number; initial position of fluid particle

ζ spatial separation nondimensionalized by Taylor microscale; the product of wave number and Kolmogorov dissipation lengthscale; the growth rate of the magnitude of a material line element vector

Contents

List of Figures

List of Tables

Chapter 1

Introduction

What is turbulence? Those who study turbulence usually ask this question. According to Batchelor [7], a turbulent flow is a flow in which the velocity takes different values under seemingly identical macroscopic conditions, although the average motions may be determined uniquely by these macroscopic conditions. And even if the average motion in turbulence is determined completely by macroscopic conditions, its substantial variations in space that often exist in actual turbulent flows leads to poorly understood interactions. What are the mechanisms that causes a flow so intricate and unpredictable? One must try to answer this question for turbulent flows occur in many applications, e.g., aeronautics, hydraulics, and chemical engineering, and in nature.

Homogeneous isotropic turbulence is an idealized turbulent flow in which average properties are independent of position in the fluid and are invariant under the reflection and rotation of the coordinates. In this respect it is the simplest turbulent flow one can investigate to understand the physical properties of turbulence. There is no way of realizing such a flow exactly, but in the laboratory there are various ways of producing such a flow with only a slight departure from the idealized flow. One example is uniform flow passing through a regular array of holes or bars held at right angles to the flow. The fast development and progress of modern computers

now makes it also possible to perform experiments on a computer. There is some sacrifice due to the limited capacity and speed of computers (e.g., only small Reynolds numbers possible), but in a numerical simulation it is relatively easy, for example, to collect full flow-field data at any number of times during the simulation. This can provide much needed qualitative and quantitative information for further study by both theorists and experimentists. The motivation of this thesis comes from this consideration.

In this thesis we are particlarly interested in investigating the small-scale structures of turbulence in physical space. Two reasons are considered. The first is an attempt to explain the observed intermittency phenomenon by a random distribution of small-scale structures in turbulence and enable the study of its effects on the statistic properties of turbulence. A review on this issue is given below. The history begins with the shadowgraphs of flows taken in the laboratory which suggest many characteristics of a turbulent motion. First, for a flow to be turbulent, its Reynolds number must be large enough, but once it becomes a turbulent flow, the magnitude of Reynolds number becomes of less importance. The primary consequence of higher Reynolds number is the production of finer scales of the smallest eddies in flow. Secondly, the large-scale characteristics of flows certainly must be determined by the macroscopic conditions such as the geometry of the boundary, but the small-scale properties may be universal. Moreover, for sufficient large Reynolds numbers it is thought that the small-scale eddies are approximately isotropic and homogeneous. These observations lead to the concept of energy cascade of turbulence. Large eddies are considered unstable and break into smaller eddies under the action of nonlinear forces. The higher the Reynolds number, the stronger the inertial forces are. This leads to finer scale eddies. Energy is transferred in this way from large eddies to small eddies and is eventually dissipated by the action of viscosity. The information of the large scales is gradually lost during the process of cascade, thus introducing universal small-scale eddies.

It is the energy cascade concept and the isotropy and homogeneity of small eddies that led Kolmogorov to his local similarity hypothesis of 1941 [37][38][39] which states that, provided the Reynolds number is large enough, there may exist a range of scales (universal equilibrium range) in which the associated motions are independent of the nature of large-scale motions and thus are determined statistically only by the rate of energy transfer ϵ and the viscosity ν. For an even larger Reynolds number, there may exist a subrange of scales (inertial subrange) between the large-scale motions and the small-scale motions, in which not only information of large-scale motions is lost but also little viscous effects are present and thus inertial forces become the only dominant forces within this subrange of scales. Assuming that ϵ is uniformly distributed in space, dimensional analysis shows that, within this subrange of scales, the energy spectrum is given by

$$E(k) \sim \epsilon^{2/3} k^{-5/3}. \tag{1.1}$$

This famous $k^{-5/3}$ spectrum has subsequently been observed in many experiments (for example, Chapman in 1979 [15] and Saddoughi and Veeravalli in 1993 [56]). It is found that this spectrum exists sometimes even if the assumptions in the hypothesis are not satisfied, implying an excluded generality.

Kolmogorov's scaling was not questioned until intermittency or spotiness of the dissipation rate ϵ was observed. The resulting structures or the regions of intense dissipation rates have a profound effect on the statistic properties of turbulence such as the probability distribution of the velocity derivatives. To understand how intermittency affects statistic properties, many different modifications of Kolmogorov's scaling (1941) have been proposed using various models: fractal (e.g., β-model by Frisch, Sulem, and Nelkin, 1978 [25]; Mandelbrot, 1976 [43]) or multifractal (e.g., p-model by Meneveau and Sreenivasan, 1987 [45]; random-β model by Benzi et al., 1984 [14]), statistical (e.g., Lognormal- (LN-) model by Kolmogorov, 1962 [40] and Oboukhov, 1962 [48]) or physical (e.g., vortex sheets used by Corrsin, 1962 [17]; vortex tubes used by Tennekes, 1968 [68]; Lundgren-Townsend vortex used by Pullin and

Saffman, 1993 [52]), and dynamic models (e.g., Two-Fluid model by She et al., 1991 [62]). With the help of flow visualization tools, the geometry and size of the small-scale structures have shown their importance in determining the statistic properties of turbulence. We don't intend to review all of the models mentioned above. Readers who are interested in the models are referred to the literature cited. The main goal of the present research is to capture small-scale structures from direct numerical simulations and to increase our understanding of the mechanism of the nonlinear (inertial) interactions through observing the formation or origin of these structures.

Another reason that an understanding of the small-scale structures is important is in subgrid modelling for large-eddy simulations. In real applications of engineering interest, the Reynolds numbers are usually very large ($\sim 10^5$ or higher) compared with those reachable in direct numerical simulations at the present time ($\sim 10^3$). A truncation of resolved scales is therefore required for economic and practical simulations. A large-eddy simulation is a simulation which models the effects of small-scale eddies on large eddies and solves the averaged equations for the large-scale motions, say for incompressible fluid and constant viscosity, solves

$$\rho\left(\frac{\partial \overline{u}_i}{\partial t}+\frac{\partial}{\partial x_j}\overline{u}_i\overline{u}_j\right)=-\frac{\partial \overline{P}}{\partial x_i}+\mu\frac{\partial^2}{\partial x_j\partial x_j}\overline{u}_i+\overline{F}_i-\frac{\partial}{\partial x_j}\tau_{ij}$$

$$\begin{aligned}\tau_{ij}&=\overline{u_iu_j}-\overline{u}_i\overline{u}_j\\&=\overline{\overline{u}_i\overline{u}_j}+\overline{\overline{u}_iu'_j}+\overline{u'_i\overline{u}_j}+\overline{u'_iu'_j}-\overline{u}_i\overline{u}_j\end{aligned}\qquad(1.2)$$

with proper boundary conditions, where $\mathbf{u}=\overline{\mathbf{u}}+\mathbf{u}'$ ($\mathbf{u}$ is turbulent velocity), $\overline{\mathbf{u}}$ is the large-scale velocity, and $\overline{\mathbf{F}}$ are external forces. The subgrid stress τ_{ij} needs modelling. It is obvious that a good model must be a model which captures the correct nonlinear interaction mechanism among motions of different scales. Ideally direct numerical simulations (DNS), simulations which solve all scales of motion without using any models, could provide new qualitative concepts for developing new and improving subgrid models. In addition DNS could provide quantitative measures of

the performance of existing subgrid models.

Other statistic properties of turbulence of great interest are considered in this thesis as well, such as similarities, correlations, and so on. Our aim is to obtain an improved understanding of turbulence and to accumulate numerically or analytically as much new knowledge as possible for further study of turbulence in the future and, in some cases, to be confirmed experimentally in the future.

This thesis is arranged as follows. In chapter 2 we first describe the numerical method used in the simulations. The relation between the vorticity structures and the straining is simplified and investigated in chapter 3 by studying a "passive" vorticity field under the action of a known and independent velocity field. Effects of straining and chaotic properties of the flow on the origin of vorticity structures are of interest. The actual Navier-Stokes equations for decaying turbulence with zero mean are simulated and the results are presented in chapter 4. Power-law decay of turbulent energy is observed and similarity laws for the energy spectrum and the double and triple velocity autocorrelation functions are studied. In chapter 5, we discuss numerical experiments including tracking fluid particles and material line element vectors. Lagrangian and Eulerian statistics are considered. Effects of the small-scale structures on the statistics are investigated. The origin of small-scale structures is examined by following fluid particles and observing the evolution of nearby vorticity structures. Finally, conclusions and future work are given in chapter 6.

Chapter 2

Navier-Stokes Solver

We consider a periodic divergence-free vector field $\mathbf{u}(\mathbf{x}, t)$ which satisfies the incompressible Navier-Stokes equations. Direct numerical simulations are performed by a Fourier spectral method. In this work we use a slightly modified version of a code by Robert Rogallo [55], originally developed for the Illiac computer at NASA Ames, but later optimized for the CRAY, Intel iPC, and the Intel Delta. Much of the code is written in VECTORAL language, which is a high-level vector language for scientific programing developed at NASA Ames. Unlike a FORTRAN program which vectorization depends on the particular compiler being used, a VECTORAL program defines a set of vector operations which will use vector hardware to the fullest extent possible after it is compiled. Meanwhile, FORTRAN and C subroutines are callable from VECTORAL and like in C, subroutines in VECTORAL may be recursive. In this chapter we describe features of this code.

We write the governing equations in general form as follows

$$\begin{aligned} \frac{\partial u_i}{\partial t} + u_j \frac{\partial u_i}{\partial x_j} &= -\nabla P + \nu \nabla^2 u_i, \\ \nabla \cdot \mathbf{u} &= 0, \end{aligned} \tag{2.1}$$

where ν is molecular viscosity, P is the pressure and the density $\rho = 1$. The velocity field $\mathbf{u}$ (and therefore the pressure) is assumed periodic with period (L_1, L_2, L_3) in a 3D

physical domain. A direct numerical simulation resolves motion of all scales without using a model and therefore several basic requirements have to be met. First, since the flow is periodic, the size of the largest eddies in turbulence cannot be too large compared with the size of the simulated box. Secondly, because the sample of wave numbers is proportional to the square of wave numbers, statistical resolution at low wave numbers is thus poor. The resolution can be improved by shifting energy to smaller scales, but then a smaller mesh is required to capture the viscous dissipation scales if the Reynolds number of turbulence remains the same.

2.1 Fourier Spectral Method

Let $\hat{\mathbf{u}}$ and $\hat{P}$ be the Fourier coefficients of $\mathbf{u}$ and P. Note we denote fields in the wave space by adding a "^" on the top of the symbols throughout the thesis. The velocity $\mathbf{u}(\mathbf{x}, t)$ therefore can be expanded as

$$\mathbf{u}(\mathbf{x}, t) = \sum_{\mathbf{k}} \hat{\mathbf{u}}(\mathbf{k}, t) \exp(i\mathbf{k} \cdot \mathbf{x}), \tag{2.2}$$

where $i = \sqrt{-1}$. If N_j is the resolution in the j^{th} direction, then $k_j = \frac{2\pi m}{L_j}$, $m = -\frac{N_j}{2} + 1, \cdots, \frac{N_j}{2} - 1$. In the wave space, equation (2.1) becomes

$$\frac{\partial \hat{u}_i}{\partial t} + \hat{f}_i^{NL} = -k_i \hat{P} - \nu k^2 \hat{u}_i \tag{2.3}$$

$$k_i \hat{u}_i = 0, \tag{2.4}$$

where $k^2 = \mathbf{k} \cdot \mathbf{k}$ and

$$\hat{f}_i^{NL} = \sum_{\mathbf{p}+\mathbf{q}=\mathbf{k}} i q_j \hat{u}_i(\mathbf{p}) \hat{u}_j(\mathbf{q}). \tag{2.5}$$

Multiplying (2.3) by k_i and applying the incompressibility condition (2.4) to the result, one obtains

$$\hat{P} = k_j \hat{f}_j^{NL} / k^2. \tag{2.6}$$

Therefore, with

$$\widehat{f}_i^{NL+P} \equiv (\delta_{ij} - \frac{k_i k_j}{k^2}) \cdot \widehat{f}_j^{NL}, \tag{2.7}$$

the governing equations are rewritten as

$$\frac{\partial \widehat{u}_i}{\partial t} + \widehat{f}_i^{NL+P} + \nu k^2 \widehat{u}_i = 0 \tag{2.8}$$

or

$$\frac{\partial}{\partial t}\Big(\exp(\nu k^2 t)\ \widehat{u}_i \Big) = -\exp(\nu k^2 t) \cdot \widehat{f}_i^{NL+P}. \tag{2.9}$$

By applying a suitable time-marching scheme to (2.9), we are able to obtain the evolution in time of the $\widehat{u}_i$.

2.2 Dealiasing

A direct computation of the convolution summation required for the nonlinear term (2.5) would yield a very time-consuming and inefficient code. An alternative approach is the so-called pseudo-spectral method which is described as follows. Suppose we want to calculate the Fourier coefficients of the product of variables $u(\mathbf{x})$ and $v(\mathbf{x})$ given their Fourier coefficients $\widehat{u}(\mathbf{k})$ and $\widehat{v}(\mathbf{k})$. Taking advantage of the Fast Fourier Transform (FFT), we first compute $u(\mathbf{x})$ and $v(\mathbf{x})$ and then make the product $u(\mathbf{x})v(\mathbf{x})$ in the physical space. The Fourier coefficients of the product are then obtained by applying FFT once again over the discrete mesh in $\mathbf{x}$.

However, in the pseudospectral method an error called "aliasing error" usually arises for the Fourier transformation used is discrete and finite. For simplicity, we explain this error in a one-dimensional problem with period 2π. Provided we have

$$\begin{aligned} u(x) &= \sum_k \widehat{u}(k) \exp(ik \cdot x) \\ v(x) &= \sum_k \widehat{v}(k) \exp(ik \cdot x), \end{aligned} \tag{2.10}$$

the product is computed by

$$u(x)v(x) = \sum_p \sum_q \hat{u}(p)\hat{v}(q)\exp(i(p+q)\cdot x) \tag{2.11}$$

and consequently

$$\widehat{uv}(k) = \frac{1}{N}\sum_x \sum_p \sum_q \hat{u}(p)\hat{v}(q)\exp(i(p+q-k)\cdot x), \tag{2.12}$$

where $x = 2\pi j/N$, $j = 0, 1, 2, \cdots, N-1$. Noting that

$$\sum_x \exp(i\ (p+q-k)\cdot x) = N\delta(p+q-k = 0\ mod\ N), \tag{2.13}$$

we actually obtain in the pseudo-spectral method

$$\widehat{uv}(k) = \sum_{p+q=k} \hat{u}(p)\hat{v}(q) + \sum_{p+q=k\pm N} \hat{u}(p)\hat{v}(q) \tag{2.14}$$

for $-\frac{N}{2}+1 \le p, q \le \frac{N}{2}-1$. The second term on the right-hand side arises from the fact that the wave numbers of a product can exceed the maximum available wave number in the discrete expansion so that instead of contributing to the correct wave number $k \pm N$, these terms contribute to the wave number k. Such an error is called an "aliasing error."

There are many investigations of the effects of the aliasing error and a number of ways of eliminating this error (see [30] [49] [50]). For example, the aliasing errors in the 1D problem (2.14) can be easily eliminated by nullifying Fourier coefficients with wave numbers outside the range $(-\frac{N}{3}, \frac{N}{3})$. In the present research, we use a variation of Orszag's phase-shift technique [49] as summarized below. To obtain alias-free Fourier coefficients of uv, we consider the products $uv = u(x)v(x)$ and $u'v' = u(x')v(x')$, where $x' = x + \Delta x/2$. The Fourier coefficients $\widehat{uv}(k)$ and $\widehat{u'v'}(k)$ are then computed as

$$\widehat{uv}(k) = \frac{1}{N}\sum_x u(x)v(x)\exp(-ik\cdot x) \tag{2.15}$$

and

$$\widehat{u'v'}(k) = \frac{1}{N}\sum_{x'} u(x')v(x')\exp(-ik\cdot x'). \tag{2.16}$$

The former is also given by (2.14) and a similar analysis leads to

$$\widehat{u'v'} = \sum_{p+q=k} \hat{u}(p)\hat{v}(q) - \sum_{p+q=k\pm N} \hat{u}(p)\hat{v}(q). \tag{2.17}$$

Therefore, the alias-free Fourier coefficient of the product uv can now be obtained by taking the average of $\widehat{uv}$ and $\widehat{u'v'}$.

The situation in 3D problems is a little more complicated. Supposing the period in j^{th} direction is $2m_j\pi$, i.e., a multiple of 2π, it can be shown that

$$\widehat{uv} = \sum_{\mathbf{p+q=k}} \hat{u}(\mathbf{p})\hat{v}(\mathbf{q}) + \sum_{\mathbf{p+q=k+N_o}} \hat{u}(\mathbf{p})\hat{v}(\mathbf{q}) \tag{2.18}$$

and

$$\begin{aligned}\widehat{u'v'} &= \sum_{\mathbf{p+q=k}} \hat{u}(\mathbf{p})\hat{v}(\mathbf{q}) \;+ \sum_{\mathbf{p+q=k+N_o}} e^{-i\mathbf{N_o}\cdot\frac{1}{2}\Delta\mathbf{x}}\, \hat{u}(\mathbf{p})\hat{v}(\mathbf{q}) \\ &= \sum_{\mathbf{p+q=k}} \hat{u}(\mathbf{p})\hat{v}(\mathbf{q}) \;+\; (-1)^{\sum_{j=1}^{3}\sigma_j} \sum_{\mathbf{p+q=k+N_o}} \hat{u}(\mathbf{p})\hat{v}(\mathbf{q}),\end{aligned} \tag{2.19}$$

where $u' = u(\mathbf{x}') = u(\mathbf{x}+\frac{1}{2}\Delta\mathbf{x})$ and $\mathbf{N_o}$ is a nonzero vector defined as $N_{oj} = \sigma_j N_j/m_j$, $\sigma_j \in \{-1, 0, 1\}$ but not all zero. The second term in (2.19) should include all possible $\mathbf{N_o}$ (a total of 26 terms). The average of (2.18) and (2.19) is

$$\frac{1}{2}\left(\widehat{uv} + \widehat{u'v'}\right) = \sum_{\mathbf{p+q=k}} \hat{u}(\mathbf{p})\hat{v}(\mathbf{q}) + \sum_{\substack{\mathbf{p+q=k+N_o} \\ \sum_{j=1}^{3}\sigma_j \ even}} \hat{u}(\mathbf{p})\hat{v}(\mathbf{q}). \tag{2.20}$$

The remaining aliasing error (the second summation) can be further eliminated by nullifying Fourier coefficients outside the following truncated wave domain $\mathcal{D}$:

$$\begin{aligned} |k_j| &\le \frac{N_j}{2m_j} \\ \left|\frac{m_i k_i}{N_i} \pm \frac{m_j k_j}{N_j}\right| &\le \frac{4}{3}, \quad \text{for i, j = 1, 2, 3 and i} \neq \text{j.} \end{aligned} \tag{2.21}$$

For an "isotropic" resolution, a "spherical" wave domain,

$$\left(\frac{m_1 k_1}{N_1}\right)^2 + \left(\frac{m_2 k_2}{N_2}\right)^2 + \left(\frac{m_3 k_3}{N_3}\right)^2 \leq \frac{2}{9}, \tag{2.22}$$

which is the maximum "spherical" wave domain that can be inscribed in domain $\mathcal{D}$, is recommended and used in the present research.

2.3 Time Marching

We now describe our time differencing scheme used to evolve (2.9) in time.

2.3.1 Second Order Runge-Kutta Method

We recall given an ordinary differential equation,

$$\frac{dy}{dt} = h(y,t) \tag{2.23}$$

the 2nd order Runge Kutta method differences the equation as follows

$$k_1 = dt \cdot h(y_n, t_n), \tag{2.24}$$

$$k_2 = dt \cdot h(y_n + \alpha k_1, t_n + \beta dt), \tag{2.25}$$

$$y^{n+1} = y^n + \gamma_1 k_1 + \gamma_2 k_2, \tag{2.26}$$

where γ_1, γ_2, α, and β are free parameters. In Rogallo's code, $\gamma_1 = \gamma_2 = \frac{1}{2}$ and $\alpha = \beta = 1$. When applied to (2.9), the first substep gives

$$\boxed{\widehat{u}_i^{n+\frac{1}{2}} = \exp(-\nu k^2 dt) \cdot (\widehat{u}_i^n - \widehat{f}_i^{NL+P}(\widehat{\mathbf{u}}^n) \cdot dt)} \tag{2.27}$$

as a result of

$$k_1 = dt \cdot \left(-\exp(\nu k^2 t_n) \widehat{f}_i^{NL+P}(\widehat{\mathbf{u}}^n)\right), \tag{2.28}$$

$$\begin{aligned} \exp(\nu k^2 t_{n+1}) \widehat{u}_i^{n+\frac{1}{2}} &= y^n + \alpha k_1 \\ &= \exp(\nu k^2 t_n) \widehat{u}_i^n - dt \cdot \exp(\nu k^2 t_n) \widehat{f}_i^{NL+P}(\widehat{\mathbf{u}}^n). \end{aligned}$$

In the second substep one computes

$$k_2 = dt \cdot \left(-\exp(\nu k^2 t_{n+1}) \widehat{f}_i^{NL+P}(\hat{\mathbf{u}}^{n+\frac{1}{2}}) \right), \tag{2.29}$$

$$\exp(\nu k^2 t_{n+1}) \widehat{u}_i^{n+1} = \exp(\nu k^2 t_n) \widehat{u}_i^n - \frac{dt}{2} \exp(\nu k^2 t_n) \widehat{f}_i^{NL+P}(\hat{\mathbf{u}}^n) - \frac{dt}{2} \exp(\nu k^2 t_{n+1}) \widehat{f}_i^{NL+P}(\hat{\mathbf{u}}^{n+\frac{1}{2}})$$

resulting in

$$\boxed{\widehat{u}_i^{n+1} = \exp(-\nu k^2 dt) \left(\widehat{u}_i^n - \tfrac{dt}{2} \widehat{f}_i^{NL+P}(\hat{\mathbf{u}}^n) \right) - \tfrac{dt}{2} \widehat{f}_i^{NL+P}(\hat{\mathbf{u}}^{n+\frac{1}{2}}).} \tag{2.30}$$

Note once the Fourier coefficients of the nonlinear terms $\mathbf{f}^{NL}$ are obtained by the pseudo-spectral method, those of $\mathbf{f}^{NL+P}$ are obtained as follows:

$$\boxed{\begin{array}{c} \widehat{f}_i^{NL+P} = \widehat{f}_i^{NL} + k_i \cdot \xi, \\ \text{where } \xi \equiv -\sum_{j=1}^{3} \dfrac{k_j \widehat{f}_j^{NL}}{k^2}. \end{array}} \tag{2.31}$$

2.3.2 Phase Shifts

To eliminate completely the aliasing errors based on the grid-shift technique, we would need to compute both $\mathbf{u}(\mathbf{x}, t)$ and $\mathbf{u}(\mathbf{x} + \Delta\mathbf{x}/2)$ at each substep. Additional FFTs would then be required at each time step. In order to reduce the computational time, we execute the phase-shift technique in a slightly different way as described below. At the first substep we calculate $\mathbf{f}^{NL}(\mathbf{x}')$ with $\mathbf{x}' = \mathbf{x} + \Delta\mathbf{x}/2$ and its Fourier coefficients $\widehat{\mathbf{f}'}^{NL}(k)$ (note we use " $'$ " to represent fields related to the grid $\mathbf{x}'$); while at the second substep we compute on the grid $\mathbf{x}$. In other words, we compute for each time step in the present code

$$\boxed{\widehat{u_i'}^{n+\frac{1}{2}} \equiv \exp(-\nu k^2 dt) \cdot (\widehat{u}_i^n - \widehat{f}_i'^{NL+P}(\hat{\mathbf{u}}^n) \cdot dt)} \tag{2.32}$$

at the first substep and

$$\boxed{\widehat{u_i}^{n+1} \equiv \exp(-\nu k^2 dt)\left(\hat{u}_i^n - \frac{dt}{2}\widehat{f_i'}^{NL+P}(\hat{\mathbf{u}}^n)\right) - \frac{dt}{2}\widehat{f_i}^{NL+P}(\widehat{\mathbf{u}'}^{n+\frac{1}{2}})} \tag{2.33}$$

at the second substep. It is obvious then that this scheme is not completely aliasing-free. However, we take one step further to help eliminate remaining aliasing errors by introducing random numbers $\mathbf{r}_1$ and $\mathbf{r}_2$ at each time step [55]. That is, instead of forming nonlinear terms at grids $\mathbf{x}$ and $\mathbf{x}'$, we form them at grids $\mathbf{x}' + \mathbf{r}_1$ and $\mathbf{x} + \mathbf{r}_2$, where $\mathbf{r}_1$ and $\mathbf{r}_2$ are uniformly distributed within $(0,\ \Delta\mathbf{x})$. The aliasing error terms in (2.32) can be evaluated as follows

$$-dt\ (-1)^{\sum_{j=1}^{3}\sigma_j}\ e^{i\mathbf{N_o}\cdot\mathbf{r}_1} e^{-\nu k^2 dt}\ \hat{f}_i^{\circ}(\mathbf{k}+\mathbf{N_o};\hat{\mathbf{u}}^n) \tag{2.34}$$

and those in (2.33) are given by

$$-\frac{dt}{2}\ (-1)^{\sum_j \sigma_j}\ e^{i\mathbf{N_o}\cdot\mathbf{r}_1} e^{-\nu k^2 dt}\ \hat{f}_i^{\circ}(\mathbf{k}+\mathbf{N_o};\hat{\mathbf{u}}^n)$$

$$-\frac{dt}{2}\ e^{i\mathbf{N_o}\cdot\mathbf{r}_2}\ \hat{f}_i^{\circ}(\mathbf{k}+\mathbf{N_o};\widehat{\mathbf{u}'}^{n+\frac{1}{2}})$$

$$-\frac{dt}{2}\ \left(\hat{f}_i^{\circ}(\mathbf{k};\widehat{\mathbf{u}'}^{n+\frac{1}{2}}) - \hat{f}_i^{\circ}(\mathbf{k};\widehat{\mathbf{u}^{\circ}}^{n+\frac{1}{2}})\right), \tag{2.35}$$

where $\hat{f}_i^{\circ}(\mathbf{k};\hat{\mathbf{u}}^n)$ is the alias-free coefficient of the nonlinear terms based on $\hat{\mathbf{u}}^n$ and $\widehat{\mathbf{u}^{\circ}}^{n+\frac{1}{2}}$ is the alias-free coefficient of velocity at the first substep. These errors can be controlled to be very small as long as motion of small scales is well resolved so that $\hat{f}_i^{\circ}(\mathbf{k}+\mathbf{N_o};\hat{\mathbf{u}}^n)$ is extremely small. The idea of introducing random numbers $\mathbf{r}_1$ and $\mathbf{r}_2$ is as seen to multiply the aliasing errors by a random value taken from a uniform distribution around the unit circle ($e^{i\mathbf{N_o}\cdot\mathbf{r}_1}$ and $e^{i\mathbf{N_o}\cdot\mathbf{r}_2}$).

The accuracy of the original Rogallo's code was tested by Eswaran and Pope [23]. They found the scheme is stable and the accuracy is satisfactory as long as

$$\Delta t\left(\frac{|u|}{\Delta x} + \frac{|v|}{\Delta y} + \frac{|w|}{\Delta z}\right)_{max} < 1. \tag{2.36}$$

2.4 Initialization

Simulations are initialized by imposing a specified energy spectrum

$$E(k) \equiv \frac{1}{2} \int \hat{u}_i \hat{u}_i^*(\mathbf{k}) dA(\mathbf{k}) \tag{2.37}$$

and the incompressibility condition.

Let ($\mathbf{e}_1$,$\mathbf{e}_2$,$\mathbf{e}_3$) be the normal Cartesian coordinates in the wave space. To satisfy the incompressibility condition, we consider another coordinate system in wave space, ($\mathbf{e}'_1$,$\mathbf{e}'_2$,$\mathbf{e}'_3$), such that $\mathbf{e}'_3$ is parallel to the wave vector $\mathbf{k}$. Therefore, $\mathbf{k} = k\mathbf{e}'_3 = k_1\mathbf{e}_1 + k_2\mathbf{e}_2 + k_3\mathbf{e}_3$ and

$$\hat{\mathbf{u}} = \hat{u}_i \mathbf{e}_i = \hat{u}'_i \mathbf{e}'_i = \alpha(k)\ \mathbf{e}'_1 + \beta(k)\ \mathbf{e}'_2 + 0\mathbf{e}'_3, \tag{2.38}$$

where $\alpha(k)$ and $\beta(k)$ are functions of wave number k related to the specified initial energy spectrum $E(k)$. Substituting (2.38) into (2.37), one finds

$$E(k) = \frac{1}{2} \int (\alpha\alpha^* + \beta\beta^*)\ dA(\mathbf{k}). \tag{2.39}$$

By introducing three free parameters θ_1,θ_2 and ϕ, one can write

$$\begin{aligned} \alpha(k) &= \left(\frac{E(k)}{2\pi k^2}\right)^{1/2} e^{i\theta_1} \cos\phi \\ \beta(k) &= \left(\frac{E(k)}{2\pi k^2}\right)^{1/2} e^{i\theta_2} \sin\phi, \end{aligned} \tag{2.40}$$

if $k \neq 0$ and $\alpha = \beta = 0$ if $k = 0$. If θ_1 , θ_2 and ϕ are random numbers uniformly distributed on the interval $(0, 2\pi)$, there is no mean helicity $\mathcal{H} = -\overline{\mathbf{u} \cdot (\nabla \times \mathbf{u})}$ in the initial flow. On the other hand, if

$$|\sin(\theta_1 - \theta_2)| = |\sin 2\phi| \equiv 1 \tag{2.41}$$

or

$$\theta_1 - \theta_2 \equiv -\frac{\pi}{2} \text{ and } \phi = \frac{\pi}{4}, \tag{2.42}$$

then the initial flow has the maximun helicity since the helicity, $\mathcal{H}$, is defined as

$$\begin{aligned}\mathcal{H} &= -\overline{\mathbf{u}\cdot(\nabla\times\mathbf{u})} \\ &= 2Im\sum_{\mathbf{k}}(k_1\hat{u}_2\hat{u}_3^* + k_2\hat{u}_3\hat{u}_1^* + k_3\hat{u}_1\hat{u}_2^*) \qquad (2.43)\\ &= 2Im\sum_{\mathbf{k}'}(k_1'\hat{u}_2'\hat{u}_3'^* + k_2'\hat{u}_3'\hat{u}_1'^* + k_3'\hat{u}_1'\hat{u}_2'^*) \\ &= 2Im\sum_{\mathbf{k}'}k_3'\ \alpha\beta^*(k) \\ &= \sum_{\mathbf{k}'}k_3'\frac{E(k)}{2\pi k^2}\sin(\theta_1-\theta_2)\sin 2\phi. \qquad (2.44)\end{aligned}$$

In the latter case, we have

$$\begin{aligned}\alpha(k) &= \left(\frac{E(k)}{2\pi k^2}\right)^{1/2}\cdot e^{i\theta_1}\cdot\frac{1}{\sqrt{2}}, \\ \beta(k) &= \left(\frac{E(k)}{2\pi k^2}\right)^{1/2}\cdot e^{i(\theta_1+\frac{\pi}{2})}\cdot\frac{1}{\sqrt{2}} = i\cdot\alpha\ , \qquad (2.45)\end{aligned}$$

and

$$\mathcal{H} = \mathcal{H}_{max} = -\sum_{\mathbf{k}}\frac{E(k)}{2\pi k} = -\sum_{\mathbf{k}}2k\alpha\alpha^*(k)\ <\ 0. \qquad (2.46)$$

At the last step of constructing an initial flow field, we need to recover $\hat{\mathbf{u}}$ from $\hat{\mathbf{u}}'$. This can be easily done by making the choice $\mathbf{e}_1'\cdot\mathbf{e}_3 = 0$. With the help of Fig. 2.1, we find that the transformation matrix between the coordinates $(\mathbf{e}_1,\mathbf{e}_2,\mathbf{e}_3)$ and the coordinates $(\mathbf{e}_1',\mathbf{e}_2',\mathbf{e}_3')$ is given by

$$T = \begin{pmatrix} k_2/k_{12} & k_1k_3/kk_{12} & k_1/k \\ -k_1/k_{12} & k_2k_3/kk_{12} & k_2/k \\ 0 & k_{12}/k & k_3/k \end{pmatrix} \qquad (2.47)$$

if $k_{12}\neq 0$ and $T = I$ (the identity matrix) if $k_{12} = 0$, where $k_{12}\equiv\sqrt{k_1^2+k_2^2}$. Therefore, $\mathbf{u} = T\mathbf{u}'$, or

$$\hat{\mathbf{u}} = \begin{cases} \left(\dfrac{\alpha kk_2+\beta k_1k_3}{k(k_1^2+k_2^2)^{1/2}}\right)\mathbf{e}_1 + \left(\dfrac{\beta k_2k_3-\alpha kk_1}{k(k_1^2+k_2^2)^{1/2}}\right)\mathbf{e}_2 + \left(\dfrac{\beta(k_1^2+k_2^2)^{1/2}}{k}\right)\mathbf{e}_3 & \text{if } k_1\&k_2\neq 0; \\ \alpha\mathbf{e}_1+\beta\mathbf{e}_2+0\ \mathbf{e}_3 & \text{otherwise.} \end{cases} \qquad (2.48)$$

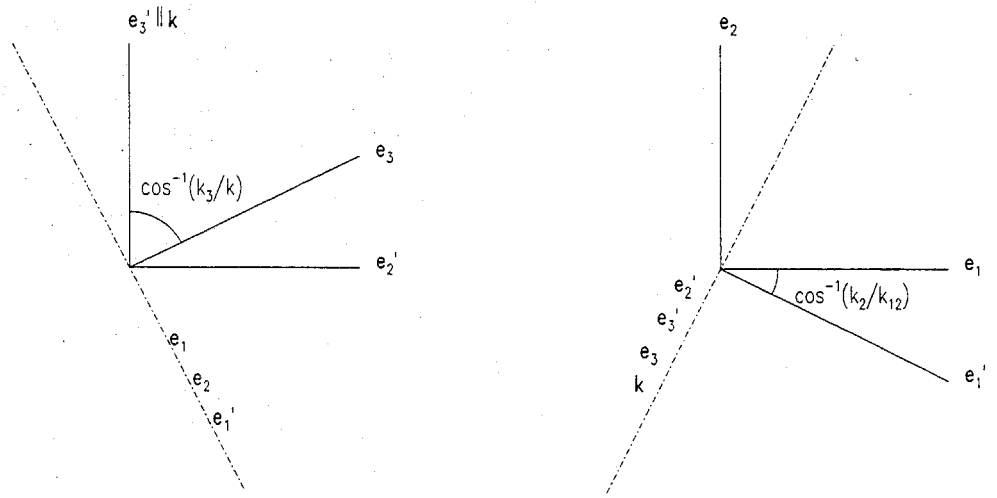

Figure 2.1: The transformation between laboratory coordinates $(\mathbf{e}_1, \mathbf{e}_2, \mathbf{e}_3)$ and $(\mathbf{e}'_1, \mathbf{e}'_2, \mathbf{e}'_3)$ where $\mathbf{e}'_3 \parallel \mathbf{k}$ and $\mathbf{e}'_1 \cdot \mathbf{e}_3 = 0$.

The initial velocity field is thus constructed as follows. We first specify the initial energy spectrum $E(k)$. A set of three random numbers $(\theta_1, \theta_2, \phi)$, different for each wave vectors, is obtained by the random-number generator if zero mean helicity is specified; otherwise, only θ_1 needs to be determined if maximum helicity is desired in the initial velocity field. The velocity Fourier coefficients satisfying the incompressibility condition and a prescribed energy spectrum are then obtained by (2.48).

2.5 Vectorization and Parallelization

There are a total of $3 \times N_1 \times N_2 \times N_3$ ordinary differential equations in (2.9). With the Intel Delta parallel computer at Caltech, we are able to solve these equations simultaneously with at most 512 nodes based on a "plane" scheme. Basically, the 3D data are distributed over and stored at, say, N_3 nodes. Each node then is responsible for time marching its one "plane" 3D data $(3 \times N_1 \times N_2)$. Communication among nodes is required for these nodes do not share their memories and the evaluations

of the nonlinear terms f_i^{NL+P} for a single wave vector $\mathbf{k}$ requires information from all $3 \times N_1 \times N_2 \times N_3$ Fourier coefficients. Except for communication time, i.e., time consumed in sending messages among nodes, the computation is roughly speeded up by a factor of the number of nodes used.

The transpose of the 3D data array is required also in order to finish the 3D Fourier transformation. For example, with a $3 \times N_1 \times N_2$ data plane stored in a node, each of the N_3 nodes can execute the Fourier transformation in the first and the second directions. However, transformations in the third direction require all k_3-Fourier coefficients for every pair of (k_1, k_2) and therefore can not be executed until the data array is transposed such that a $3 \times N_1 \times N_3$ data plane is stored in each of N_2 nodes.

An alternative is a "pencil" scheme which performs an $\mathcal{O}(N^3)$ simulation on $\mathcal{O}(N^2)$ processors such that each processor can span only one dimension at a time and that requires twice as many transposes as a "plane" scheme does. The number of messages per processor required in a "pencil" scheme is generally smaller than that in a "plane" scheme, but the length of the message is longer. Because the communication time is determined by the number of messages per processor as well as the length of the messages, which scheme, the "plane" one or the "pencil" one, has a higher efficiency is still under investigation (for example at NASA Ames); but a "pencil" scheme is seemingly more beneficial on a larger machine.

The code is vectorized on each node. A flow chart of the Navier-Stokes solver can be found in Fig. 2.2.

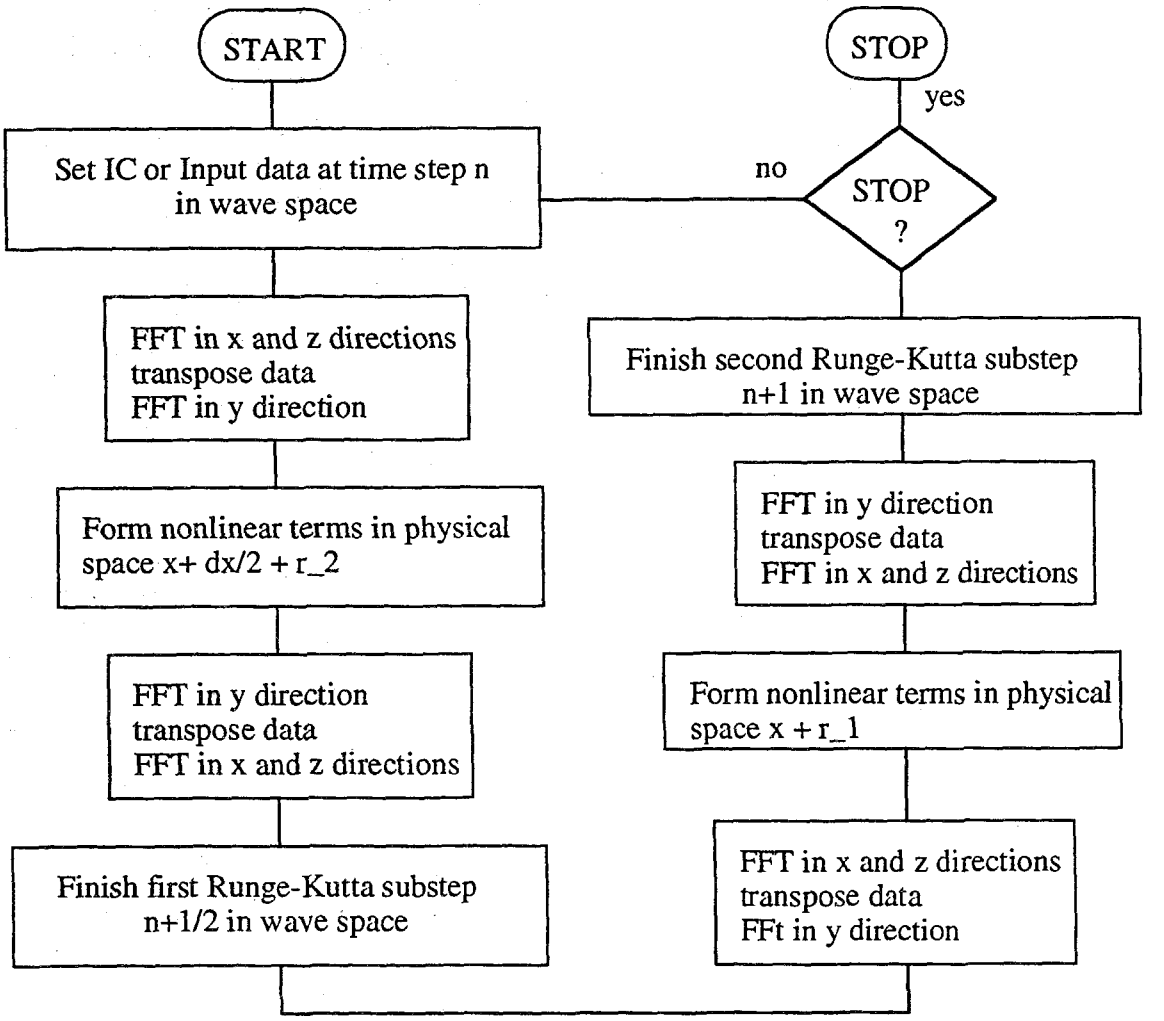

Figure 2.2: Flow Chart of Rogallo's Navier-Stokes solver using the spectral method and a 2nd order Runge-Kutta time marching scheme. A grid-shift technique is also implemented to nearly eliminate aliasing errors.

Chapter 3

Dynamo Action of ABC-Flow

Non-zero vorticity is usually named as one of the primary ingredients of a turbulent flow, for the chaotic characteristics and the unpredictability of a turbulent flow come often from a seemingly random distribution of its vorticity field. For a Navier-Stokes' fluid, the equations of evolution for the vorticity vector, $\omega = \nabla \times \mathbf{u}$, are given by

$$\frac{\partial \omega}{\partial t} + (\mathbf{u} \cdot \nabla)\omega = (\omega \cdot \nabla)\mathbf{u} + \nu \nabla^2 \omega, \tag{3.1}$$

where $\mathbf{u}$ is the velocity and ν is the kinematic viscosity. In physical space, the vorticity field sometimes reveals particular structures, i.e., the regions over which the vorticity field has rapid variations, such as horseshoes, tubes, sheets and so on. The existence of these vorticity structures implies a non-uniform distribution of turbulent quantities, for example the energy dissipation rate ϵ, and non-Gaussian turbulent statistics. An understanding of what these vorticity structures really look like and how they are created in a turbulent flow may be very useful in turbulent theories, for instance in the subgrid modelling of small eddies.

In studying the phenomenon of intermittency in a turbulent flow, investigators sometimes search for prominent physical structures of the vorticity. For instance, Corrsin [17] assumed that a turbulent flow has randomly distributed vorticity sheets having characteristic thickness on the order of the Kolmogorov dissipation microscale $\eta = (\nu^3/\epsilon)^{1/4}$; while Tennekes [68] thought the intermittency phenomenon is caused

by randomly distributed vorticity tubes with diameters on the order of η and stretched by eddies of size λ, where λ is Taylor microscale. It is thought that these vorticity structures occupy only a small fraction of volume in a flow and, although having large magnitudes of vorticity themselves, are created by a "background" straining field, a straining field created by the large-scale motions. A solution of (3.1) by assuming ω and $\mathbf{u}$ are independent in the sense that ω represents the vorticity of the structures and $\mathbf{u}$, the velocity of the large-scale motions, that is, by assuming ω is just a passive vector in the $\mathbf{u}$-motion, would then yield a possible vorticity structure appearing in an actual turbulent flow. Probably the most impressive work along these lines is by Townsend in 1951 [70]. By choosing a shearing motion $\mathbf{u}(\mathbf{x},t) = (\alpha x, -\alpha y, 0)$ $(\alpha > 0)$, Townsend identified a stationary solution of (3.1) which is sheet-like of finite thickness $\sim \sqrt{\nu/\alpha}$. A tube-like solution is obtained instead if one selects $\mathbf{u}(\mathbf{x},t) = (2\beta x, -\beta y, -\beta z)$ $(\beta > 0)$. The diameters of these tubes are found to be $\mathcal{O}(\sqrt{\nu/\beta})$. One can further improve the models by taking the induced motion of ω into account when solving (3.1). Lundgren's tube-like structures surrounded by spiral sheets [42] are an example.

In this chapter, we are particularly interested in obtaining a picture of how a velocity field $\mathbf{u}$ acts on the ω-field and creates the ω-structures. Thus we assume $\mathbf{u}(\mathbf{x},t)$ is known at all time and ω is a passive vector. Equation (3.1) then becomes linear. We hope that knowledge obtained from this study can help us understand and explain the origin of vorticity structures in an actual turbulent flow when we simulate the full Navier-Stokes equations and accumulate Lagrangian statistics (see Chapter 5). This chaper is arranged in the following way. In Sec. 3.1, an analogous problem in magnetohydrodynamics is discussed. Terminology used in magnetohydrodynamics such as "dynamo" is introduced. In Sec. 3.2 we study the property of the compact linear operator $\mathcal{L}$, where $\mathcal{L}\omega \equiv \nabla \times (\mathbf{u} \times \omega) + \nu\nabla^2\omega$. Next we introduce the ABC (Arnold-Beltrami-Childress) flows in Sec. 3.3 as we will use this class of flows as the model velocity field $\mathbf{u}(\mathbf{x},t)$ in (3.1). The numerical methods and the initial conditions used for simulations are described in Sec. 3.4. The simulations were all performed

with 128^3 Fourier components. Discussions of numerical results are given in Sec. 3.5, and finally conclusions are given in Sec. 3.6.

3.1 What is a Dynamo?

The interaction between the motion $\mathbf{u}$ of an electrically conducting fluid and a magnetic field $\mathbf{B}$ is governed by the magnetohydrodynamic (MHD) equations:

$$\frac{\partial \mathbf{u}}{\partial t} + \mathbf{u} \cdot \nabla \mathbf{u} = \mathbf{B} \cdot \nabla \mathbf{B} - \nabla P + \nu \nabla^2 \mathbf{u} + \mathbf{f}, \tag{3.2}$$

$$\frac{\partial \mathbf{B}}{\partial t} + \mathbf{u} \cdot \nabla \mathbf{B} = \mathbf{B} \cdot \nabla \mathbf{u} + \nu_B \nabla^2 \mathbf{B}, \tag{3.3}$$

and

$$\nabla \cdot \mathbf{u} = \nabla \cdot \mathbf{B} = 0, \tag{3.4}$$

where ν and ν_B are the kinematic viscosity and magnetic diffusivity and $\mathbf{f}$ is the driving force. The magnetic field lines are stretched, folded and/or twisted by the velocity field and act back on the velocity field as Lorentz forces. In some cases the stretching of the magnetic field lines by the fluid motion may be sufficiently strong to overcome the Joule dissipation and therefore prevent the magnetic field from decaying. Such a flow, capable of maintaining a magnetic field, is said to be a "dynamo."

Considering the cases in which the magnetic field is so weak that the Lorentz forces are negligible and therefore do not affect the fluid motion, the equation of evolution of the magnetic field (3.3) then becomes linear and analogous to (3.1). In the following text, all the discusions are applied to the magnetic field which, however, according to the analogy, can be applied equally effectively to the vorticity field. We are not concerned with how the velocity field $\mathbf{u}$ is maintained by the forcing. We focus our attention on the following problem: Given a precribed fluid motion $\mathbf{u}$, will

the passive magnetic field $\mathbf{B}$ or the passive vorticity field ω grow exponentially with time? Or, equivalently, what fluid motions ($\mathbf{u}$) can be a dynamo?

Working with the spatially periodic motions of an infinite fluid, Roberts [54] proved that if the determinant of a certain symmetric tensor determined by $\mathbf{u}$ is not zero, then there exists some $\mathbf{j}$ and magnetic (vorticity) field solutions in the form of

$$\mathbf{B}(\mathbf{x}, t) = \mathbf{H}(\mathbf{x}) \exp(pt + i\mathbf{j} \cdot \mathbf{x}) \tag{3.5}$$

such that $Re(p(\mathbf{j})) > 0$ to the first order in $|\mathbf{j}|$ for all positive values of diffusivity ν_B except possibly a bounded set of discrete values, where $\mathbf{H}$ has the same periodicity as $\mathbf{u}$ and $|\mathbf{j}|$ is assumed as a small parameter. However, we note the solutions of this particular form can not appear in the present research for in our simulations the velocity field and the vorticity field are both spatially periodic of the same period (2π). That is $|j| = 0$ always.

The possible existence of a dynamo at large magnetic Reynolds numbers, $Re_m \equiv 1/\nu_B$, is of particular interest. A dynamo is said to be a "fast dynamo" if the exponential growth rate of the magnetic field approaches a positive nonzero value as the diffusivity approaches to zero; otherwise, it is said to be a "slow dynamo" ([74]). Moffatt and Proctor [46] studied the zero-diffusivity system and argued that a fast dynamo is impossible at least under the assumption of a smooth eigenfunction if the diffusivity is exactly zero because of the invariance of helicity of the magnetic field. However, considering the analog of

$$\frac{\partial \mathbf{B}}{\partial t} = \nabla \times (\mathbf{u} \times \mathbf{B}) \tag{3.6}$$

to the equations of evolution of an infinitesimal material line element, which characterizes the separations of fluid particles in a turbulent flow, the amplification of magnetic energy is expected if a flow $\mathbf{u}$ produces Lagrangian chaos, i.e., positive Lyapunov exponents or the exponential growth rate of the separation of particles

infinitesimally close over a long time on a set of positive measure. Another approach to the diffusionless system instead of eigenfunction approach is thus required. For example, Bayly [13] had approached the diffusionless system by catching an eigenfunction which when multiplied by any smooth function is measurable, and Finn and Ott [24] measured dynamo action by integrating the flux of $\mathbf{B}$ across a fixed surface in space.

We now come back to hydrodynamic problems. Knowledge accumulated from magnetohydrodynamic studies, due to the analogy, can be very helpful to us in explaining and understanding phenomena observed in our simulations. Conversely, we hope the study here is also useful to those interested in magnetohydrodynamic problems.

3.2 Theoretical Results

Before we perform numerical simulations, it is worth exploring (3.1) analytically. When the flow is time-independent such as the ABC flows, the dynamo problem, (3.1) or (3.3), can be viewed as an eigenvalue problem. If we write $\omega(\mathbf{x}, t) = \mathbf{H}(\mathbf{x})e^{pt}$, where p is complex, equation (3.1) becomes

$$p\mathbf{H} = \nabla \times (\mathbf{u} \times \mathbf{H}) + \nu\nabla^2\mathbf{H}. \tag{3.7}$$

Thus we are led to consider the eigenvalues and eigenfunctions of the linear operator of

$$\mathcal{L}\mathbf{H} \equiv \nabla \times (\mathbf{u} \times \mathbf{H}) + \nu\nabla^2\mathbf{H}. \tag{3.8}$$

The properties of $\mathcal{L}$ are determined by the flow $\mathbf{u}(\mathbf{x})$ and the diffusivity ν. At large time, solutions to (3.1) will be dominated by the eigenfunction(s) corresponding to the eigenvalue(s) which has (have) the maximum real part. A steady state (time-independent) solution of (3.1) is an eigenfunction of (3.7) corresponding to the zero eigenvalue.

If we write $\mathbf{H}(\mathbf{x}) = \overline{\mathbf{H}} + \mathbf{H}'(\mathbf{x})$, where $\overline{\mathbf{H}}$ is the spatial average and $\mathbf{H}'(\mathbf{x})$ is the fluctuation, assume $\overline{\mathbf{u}} = 0$, and spatially average (3.7), we obtain

$$p\overline{\mathbf{H}} = 0 \tag{3.9}$$

and consequently

$$p\mathbf{H}' = \nabla \times (\mathbf{u} \times \overline{\mathbf{H}}) + \nabla \times (\mathbf{u} \times \mathbf{H}') + \nu\nabla^2\mathbf{H}'. \tag{3.10}$$

Therefore, if $\overline{\mathbf{H}} \neq 0$, $p = 0$ and $\mathcal{L}\mathbf{H}' = -\nabla \times (\mathbf{u} \times \overline{\mathbf{H}})$. Equation (3.7) is thus reduced to $\mathcal{L}\mathbf{H} = 0$ and the zero solution becomes the only solution of (3.1) if $\mathcal{L}$ is invertible (no dynamo action).

For the rest of this section, we look for steady solutions of (3.1) with a fixed spatially periodic $\mathbf{u}(\mathbf{x})$ and $\overline{\mathbf{H}} = 0$. That is, we consider the eigenproblem

$$\mathcal{L}\mathbf{H} = p\mathbf{H} \tag{3.11}$$

with $\overline{\mathbf{H}} = 0$ and look for the values of viscosity ν which give a nontrivial kernel of $\mathcal{L}$. According to Roberts' analysis [54], the linear operator $\mathcal{L}$ in this case is a compact linear operator (see [22]). Let

$$\mathcal{L}\mathbf{H} = \nabla^2 (\nu I - \Im)\, \mathbf{H}, \tag{3.12}$$

where

$$\Im\mathbf{H} \equiv \left(\nabla^2\right)^{-1} \{-\nabla \times (\mathbf{u} \times \mathbf{H})\} \tag{3.13}$$

is a compact linear operator as well, and let $\rho(\Im)$ denote the resolvent of $\Im$ and $\sigma(\Im)$ be the spectrum. Therefore, if $\nu \in \rho(\Im)$, $(\nu I - \Im)^{-1}$ exists as a bounded operator, so does $\mathcal{L}^{-1}$. That means the operator $\mathcal{L}$ does not have a zero eigenvalue and therefore (3.1) has no non-zero steady solution. On the other hand, if $\nu \in \sigma(\Im)$, eigenfunction(s) corresponding to the zero eigenvalue of $\mathcal{L}$ exists and a steady state of (3.1) is possible. Because the spectrum of a compact linear operator is bounded and discrete with

no non-zero point of accumulation, we can make the following assertation. For ν sufficiently large, greater than the bound of $\sigma(\Im)$, equation (3.1) has no non-zero steady solution. If $\mathcal{L}$ has eigenvalues with positive real part, there exist solutions of equation (3.1) which grow exponentially with time (a dynamo action). The situation becomes complicated and interesting as $\nu \to 0$ because zero is the only possible point of accumulation of $\sigma(\Im)$.

3.3 ABC Flow

The ABC-flow is defined as $\mathbf{u} = (u, v, w)$, where

$$\begin{aligned} u &= A\sin z + C\cos y, \\ v &= B\sin x + A\cos z, \\ w &= C\sin y + B\cos x. \end{aligned} \tag{3.14}$$

It was named by Dombre et al. [21] after Arnold [1], who first recognized it as a three dimensional steady solution of the incompressible Euler equations

$$\frac{\partial \mathbf{u}}{\partial t} + (\nabla \times \mathbf{u}) \times \mathbf{u} = -\nabla(p + \frac{1}{2}\mathbf{u}^2) \tag{3.15}$$

$$\nabla \cdot \mathbf{u} = 0, \tag{3.16}$$

Beltrami, for the flow possesses the Beltrami properties ($\nabla \times \mathbf{u} = \xi \mathbf{u}$ and $\mathbf{u} \cdot \nabla \xi = 0$), and Childress, who introduced the specal case $A = B = C = 1$ independently [16]. This class of flows is of interest for it is simple (spatially periodic and steady) from an Eulerian viewpoint but varied and intricate from a Lagrangian viewpoint.

The flow is integrable (the flow has invariants) when one of the three parameters A, B, and C is zero. For example, if $C = 0$, the invariant is $B\sin x + A\cos z =$ constant; that is, particles' motions are restricted to the surfaces of $B\sin x + A\cos z = B\sin x_o + A\cos z_o$ and the y-motion is simply linear, namely, $y(t) = y_o + (B\sin x_o + A\cos z_o)t$,

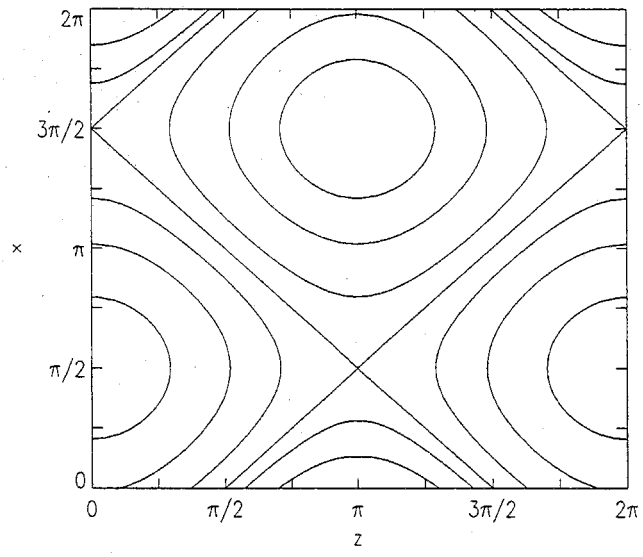

Figure 3.1: The projected orbits of an integrable ABC flow with A=B=1 and C=0 on the x-z plane.

where (x_o, y_o, z_o) is the initial position of a particle. Orbits projected on the x-z plane of this special case are shown in Fig. 3.1.

The flow has stagnation points when a triangle can be formed out of sides with lengths A^2, B^2 and C^2. Let $(\overline{x}, \overline{y}, \overline{z})$ denote the stagnation points. They are determined by

$$\begin{aligned} -C\sin\overline{y} = B\cos\overline{x} &= \pm\left(\frac{1}{2}(B^2+C^2-A^2)\right)^{1/2} \\ -A\sin\overline{z} = C\cos\overline{y} &= \pm\left(\frac{1}{2}(C^2+A^2-B^2)\right)^{1/2} \\ -B\sin\overline{x} = A\cos\overline{z} &= \pm\left(\frac{1}{2}(A^2+B^2-C^2)\right)^{1/2}. \end{aligned} \tag{3.17}$$

The characteristic polynomial associated with the linearized motion about the stagnation points is given by

$$\lambda^3 - \frac{1}{2}(A^2+B^2+C^2)\lambda - 2ABC\cos\overline{x}\cos\overline{y}\cos\overline{z} = 0, \tag{3.18}$$

where the λ are the principal values of the velocity gradient tensor at the stagnation

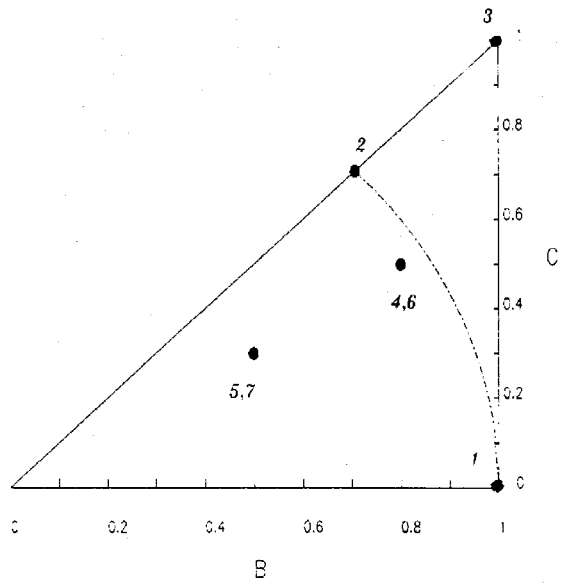

Figure 3.2: The space of parameters A,B, and C normalized by $A = 1 \geq B \geq C \geq 0$. The bifurcation values of parameters ($B^2 + C^2 = 1$) are indicated by the dash dotted line. Solid circles represent the values of parameters chosen for the present simulations.

points. The eigenvectors e's, which represent the local stable, unstable, or center manifold of the stagnation points, are given by solving

$$\begin{pmatrix} -\lambda & -C\sin y & A\cos z \\ B\cos x & -\lambda & -A\sin z \\ -B\sin x & C\cos y & -\lambda \end{pmatrix} \mathbf{e} = 0. \tag{3.19}$$

Since an ABC flow possesses the Beltrami properties (with $\xi = 1$), the vorticity at the stagnation points is also zero and therefore the eigenvalues λs and eigenvectors determined by (3.18) and (3.19) are also the principal rates and principal directions, respectively, of the strain tensor at these points.

To be consistent with the terminology used by previous investigators [19] [21], we identify an α-type stagnation point as a stagnation point having two stable and one unstable local manifolds and a β-type stagnation point as one with one stable and two unstable local manifolds. When the normalization $A \equiv 1 \geq B \geq C \geq 0$ is used, with no loss of generality (see the analysis of Dombre et al. [21]), the saddle-node

bifurcation occurs at $B^2 + C^2 = 1$. That is, when $B^2 + C^2 <, =$, and > 1, there exist zero, four, and eight stagnation points (excluding the integrable cases). These bifurcation values are shown in Fig. 3.2 (dash dotted line). Several sets of parameters (A,B,C), including an integrable case, cases with discrete stagnation points, and cases without stagnation points, are selected for the present simulations, and they are shown by the solid symbols in Fig. 3.2.

3.4 Numerical Scheme and Simulations

3.4.1 Mathematical Formulation

The spatial periodicity of an ABC flow makes it possible to implement a code solving (3.1) by taking advantage of the Navier-Stokes' solver described in Chapter 2. We consider a "passive" vorticity field, which is initially randomly distributed and has the same period as that of the ABC flow, i.e., 2π in each direction, under the action of the ABC flow. Because both ω and $\mathbf{u}$ are divergence-free ($\nabla \cdot \mathbf{u} = \nabla \cdot \omega = 0$), we may rewrite (3.1) as follows

$$\frac{\partial \omega_i}{\partial t} + \frac{\partial}{\partial x_j}(u_j \omega_i - u_i \omega_j) = \nu \nabla^2 \omega_i \tag{3.20}$$

for i=1,2, and 3. The corresponding equations in wave space are given by

$$\frac{d\hat{\omega}_i}{dt} + i \sum_{\mathrm{p}} k_j \Big(\hat{u}_j(\mathrm{p}) \hat{\omega}_i(\mathrm{k}-\mathrm{p}) - \hat{u}_i(\mathrm{p}) \hat{\omega}_j(\mathrm{k}-\mathrm{p}) \Big) + \nu k^2 \hat{\omega}_i = 0. \tag{3.21}$$

Because $\hat{\mathrm{u}}(\mathrm{k}) = 0$ unless $\mathrm{k} = \sigma$, where $\sigma = (\pm 1, 0, 0)$ and its permutations, the interactions among ω-Fourier components are local in the sense that a Fourier component of a wave vector k only interacts with Fourier components of wave vectors $\mathrm{k} + \sigma$. Let $\Phi_{ij} \equiv u_j \omega_i - u_i \omega_j$. Because Φ_{ij} is an antisymmetric matrix, only three independent components of Φ_{ij} need to be evaluated and stored. The following equations are then marched in time by the second order Runge-Kutta method:

$$\frac{d}{dt}\Big(\hat{\omega}_i(\mathrm{k})\exp(\nu k^2 t)\Big) = -ik_j\hat{\Phi}_{ij}(\mathrm{k})\exp(\nu k^2 t). \tag{3.22}$$

The estimate of the numerical stability of (3.21) is simplified by frozening the velocity components of the ABC flow. The result shows the scheme is stable if the time increment dt satisfies

$$dt \cdot Max(k_1\|u_1\| + k_2\|u_2\| + k_3\|u_3\|) \leq C \tag{3.23}$$

where C is the Courant number.

3.4.2 Simulation Conditions

We restrict our attention to ω-fields which satisfy $\nabla \cdot \omega = 0$. According to the method described in the section 5 of chapter 2, we need three sets of random numbers and need to specify an initial "enstrophy" spectrum. In this chapter, we shall use $\Omega(k)$ to denote the enstrophy spectrum or ω- spectrum and $D(k) = 2\nu k^2\Omega(k)$ the enstrophy dissipation spectrum. The mean enstrophy $\overline{\Omega}$ is then the integral of $\Omega(k)$ over the wave numbers. The turbulent vorticity magntitude $\overline{\omega}$ is defined as

$$\frac{3}{2}\,\overline{\omega}^2 = \overline{\Omega} = \int_0^{k_{max}} \Omega(k)dk; \tag{3.24}$$

and the mean enstrophy dissipation (ϵ_ω) is defined as

$$\epsilon_\omega = \int_0^{k_{max}} D(k)dk. \tag{3.25}$$

The smallest scale λ_ω generated by (3.1) with finite ν is $\mathcal{O}(\nabla^2\omega/\omega)^{-1/2} \propto \nu^{1/2}$ for $\nabla \mathrm{u} \sim \mathcal{O}(1)$ (see [46] and [24]), which may be characterized as

$$\lambda_\omega = \left(5\int_0^{k_{max}} \Omega(k)dk \Big/ \int_0^{k_{max}} k^2\Omega(k)dk\right)^{1/2}. \tag{3.26}$$

We would like to define a vorticity Reynolds number as $Re_\omega = (2\overline{\Omega})^{3/2}/\epsilon_\omega$.

In the present simulations, two initial energy spectra are employed. One is

$$\Omega(k) = \begin{cases} \frac{3q_\omega^2 k^2}{2(k_h - k_c)}, & \text{if } k_c \leq k \leq k_h; \\ 0, & \text{otherwise.} \end{cases} \tag{3.27}$$

For this case the initial lengthscale and the enstrophy Reynolds number are

$$\lambda_\omega = \sqrt{\frac{25}{3}} \cdot \left(\frac{k_h^3 - k_c^3}{k_h^5 - k_c^5} \right)^{1/2} \tag{3.28}$$

and

$$Re_\omega = \frac{5q_\omega}{3\nu} \cdot \frac{(k_h^2 + k_h k_c + k_c^2)^{3/2}}{(k_h^4 + k_h^3 k_c + k_h^2 k_c^2 + k_h k_c^3 + k_c^4)}. \tag{3.29}$$

The other initial spectrum is given by

$$\Omega(k) = 16\sqrt{\frac{2}{\pi}} q_\omega^2 k_p \left(\frac{k}{k_p} \right)^6 exp(-2 \left(\frac{k}{k_p} \right)^2). \tag{3.30}$$

The initial lengthscale and Reynolds number are computed as

$$\lambda_\omega = \sqrt{\frac{20}{7k_p^2}} \tag{3.31}$$

and

$$Re_\omega = \frac{2\sqrt{15} q_\omega}{7\nu k_p}. \tag{3.32}$$

The code was tested by choosing the initial ω-field to be exactly the vorticity field generated by the ABC flow.

Presented in Table 3.1 are the initial conditions for the simulations. Stagnation points of the ABC flow, if they exist, and their local manifolds are summarized in Table 3.2 - 3.4. Poincaré maps of these ABC flows are shown in Fig. 3.3a - 3.6a, revealing some of the regular and/or chaotic zones of the flow. Points on the the Poincarè map are shown whenever a trajectory pierces the plane. Regions of positive and negative normal velocity are separated by solid lines (at which the normal velocity of particles is zero). We expect the stable and unstable manifolds of stagnation points, if they exist, to dominate the geometry of vorticity structures, while significant stretching of vorticity is expected in chaotic regions for they usually possess positive Lyapunov exponents. We shall come back to this later.

Table 3.1: Initial conditions. $q_\omega = 1$ for all cases and s.p. means "stagnation points."

	A	B	C	# of s.p.	ν	$\overline{\Omega}_o$	k_p	k_h	k_c	λ_ω	Re_ω
run1	1	1	0	∞	0.0132	14	-	2	4	0.686	138.3
run2	1	$1/\sqrt{2}$	$1/\sqrt{2}$	4	0.006	16.9	3	-	-	0.563	61.5
run3	1	1	1	8	0.0036	16.9	3	-	-	0.563	102.5
run4	1	0.8	0.5	0	0.005	16.9	3	-	-	0.563	73.8
run5	1	0.5	0.3	0	0.0036	16.9	3	-	-	0.563	102.5
run6	1	0.8	0.5	0	0.0036	16.9	3	-	-	0.563	102.5
run7	1	0.5	0.3	0	0.0036	16.9	3	-	-	0.563	102.5

Table 3.2: Stagnation points in run1, where $0 \leq \overline{y} \leq 2\pi$, and their local manifolds (**e**). Eigenvalues of the associated linearized systems are denoted as λ_i, i=1, 2, and 3.

$\overline{x}$	$\overline{y}$	$\overline{z}$	λ_1	λ_2	λ_3	$\mathbf{e}_1$	$\mathbf{e}_2$	$\mathbf{e}_3$
$(\pi/2,$	$\overline{y},$	$\pi)$	1	0	-1	(1,0,-1)	(0,1,0)	(1,0,1)
$(3\pi/2,$	$\overline{y},$	$0)$	1	0	-1	(1,0,1)	(0,1,0)	(1,0,-1)

Table 3.3: Stagnation points in run2 and their local manifolds (e). Eigenvalues of the associated linearized systems are denoted as λ_i, i=1, 2, and 3.

$\overline{x}$	$\overline{y}$	$\overline{z}$	λ_1	λ_2	λ_3	$\mathbf{e}_1$	$\mathbf{e}_2$	$\mathbf{e}_3$
$(\pi/2,$	$0,$	$5\pi/4)$	1	0	-1	$(1,-1,-\sqrt{2})$	(1,1,0)	$(1,-1,\sqrt{2})$
$(\pi/2,$	$\pi,$	$3\pi/4)$	1	0	-1	$(1,1,-\sqrt{2})$	(1,-1,0)	$(1,1,\sqrt{2})$
$(3\pi/2,$	$0,$	$7\pi/4)$	1	0	-1	$(1,1,\sqrt{2})$	(1,-1,0)	$(1,1,-\sqrt{2})$
$(3\pi/2,$	$\pi,$	$\pi/4)$	1	0	-1	$(1,-1,\sqrt{2})$	(1,1,0)	$(1,-1,-\sqrt{2})$

Table 3.4: Stagnation points in run3 and their local manifolds (e). The eigenvalues of the α-type stagnation points are $\lambda_1 = \sqrt{2}$ and $\lambda_2 = \lambda_3 = -1/\sqrt{2}$; those of the β-type are $\lambda_1 = \lambda_2 = 1/\sqrt{2}$ and $\lambda_3 = -\sqrt{2}$.

$\overline{x}$	$\overline{y}$	$\overline{z}$	type	$\mathbf{e}_1$	$\mathbf{e}_2$	$\mathbf{e}_3$
$(\pi/4,$	$5\pi/4,$	$3\pi/4)$	α	$(1,1,-1)$	(1,0,1)	$(0,1,1)$
$(3\pi/4,$	$\pi/4,$	$5\pi/4)$	α	$(1,-1,-1)$	(1,1,0)	$(1,0,1)$
$(5\pi/4,$	$3\pi/4,$	$\pi/4)$	α	$(1,-1,1)$	(1,1,0)	$(0,1,1)$
$(7\pi/4,$	$7\pi/4,$	$7\pi/4)$	α	$(1,1,1)$	(1,-1,0)	$(1,0,-1)$
$(\pi/4,$	$7\pi/4,$	$5\pi/4)$	β	$(1,1,0)$	(0,1,1)	$(1,-1,1)$
$(3\pi/4,$	$3\pi/4,$	$3\pi/4)$	β	$(1,-1,0)$	(1,0,-1)	$(1,1,1)$
$(5\pi/4,$	$\pi/4,$	$7\pi/4)$	β	$(1,0,1)$	(0,1,1)	$(1,1,-1)$
$(7\pi/4,$	$5\pi/4,$	$\pi/4)$	β	$(1,1,0)$	(1,0,1)	$(1,-1,-1)$

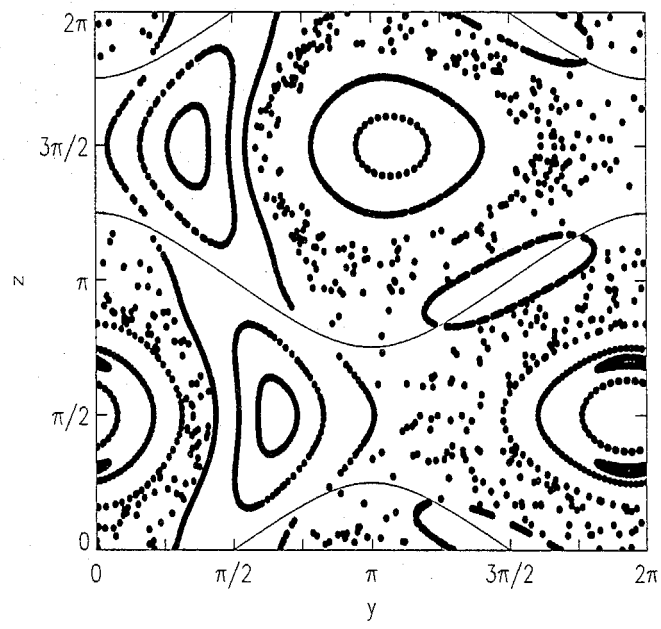

Figure 3.3a: Poincarè Map of the ABC flow (A=1 and $B = C = 1/\sqrt{2}$) for run2 on the section x=0. Solid lines represent points where $\dot{x} = 0$.

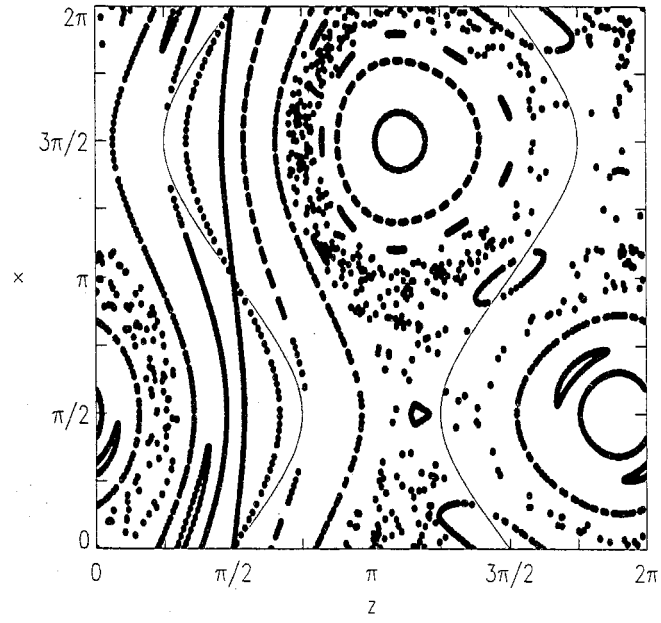

Figure 3.3b: Poincarè Map of the ABC flow (A=1 and $B = C = 1/\sqrt{2}$) for run2 on the section y=0. Solid lines represent points where $\dot{y} = 0$.

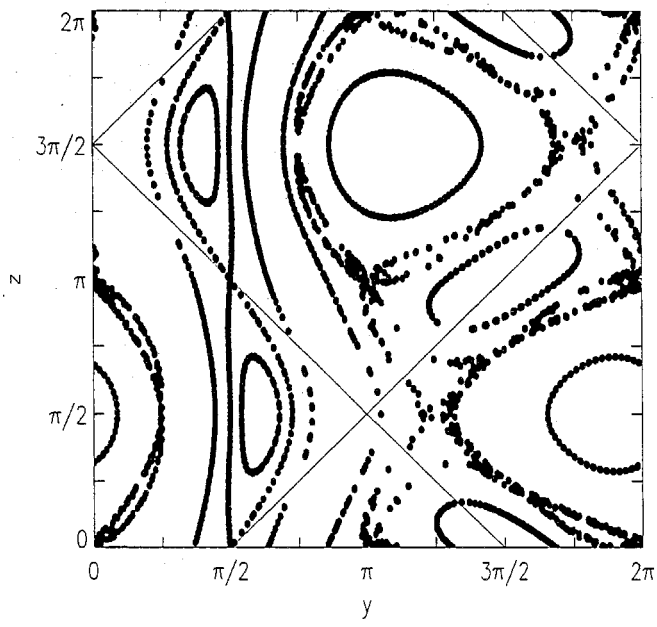

Figure 3.4a: Poincarè Map of the ABC flow (A=B=C=1) for run3 on the section x=0. Solid lines represent points where $\dot{x} = 0$.

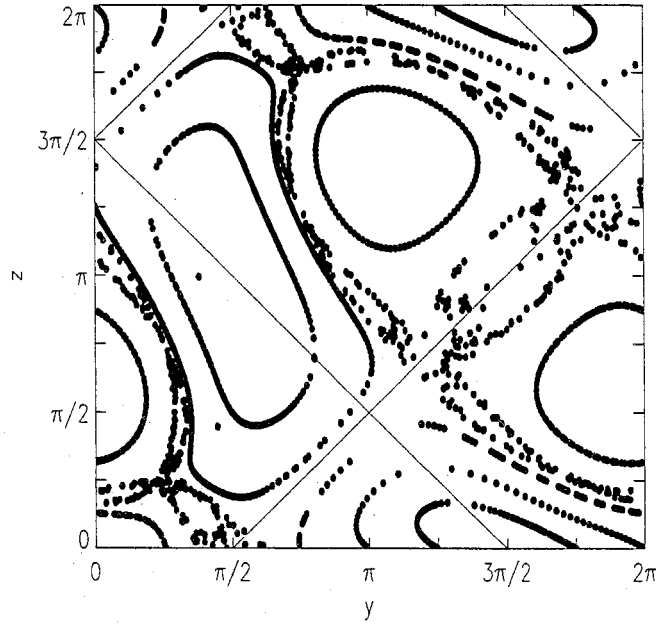

Figure 3.4b: Poincarè Map of the ABC flow (A=B=C=1) for run3 on the section x=$\pi/4$. Solid lines represent points where $\dot{x} = 0$.

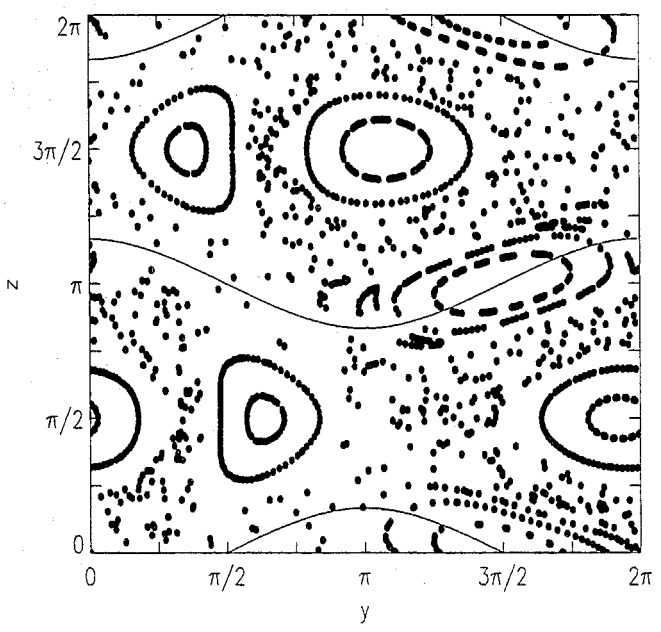

Figure 3.5a: Poincarè Map of the ABC flow (A=1, B=0.8, and C=0.5) for run4 and run6 on the section x=0. Solid lines represent points where $\dot{x} = 0$.

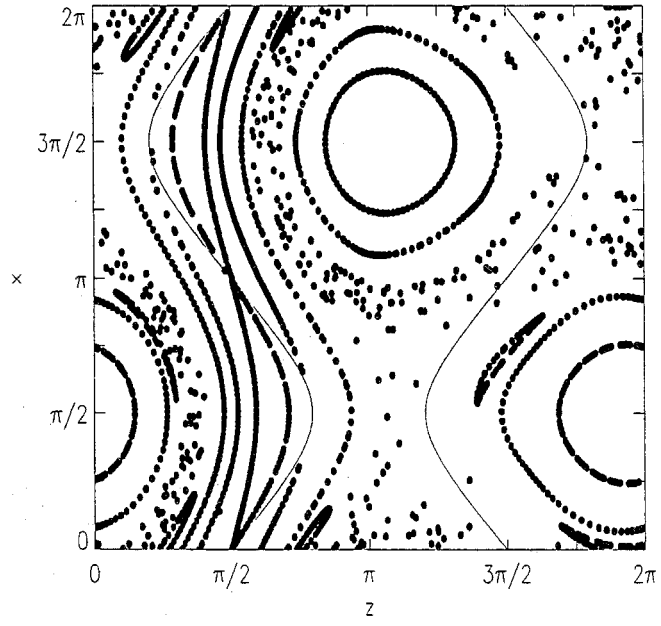

Figure 3.5b: Poincarè Map of the ABC flow (A=1, B=0.8, and C=0.5) for run4 and run6 on the section y=0. Solid lines represent points where $\dot{y} = 0$.

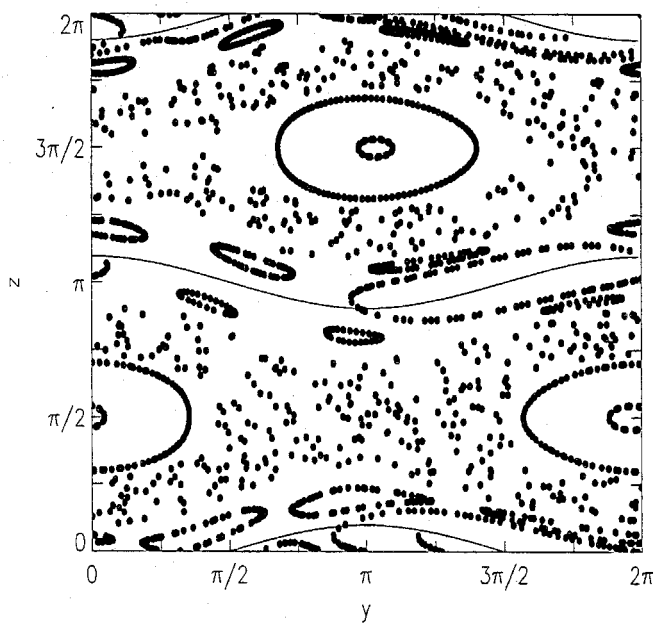

Figure 3.6a: Poincarè Map of the ABC flow (A=1, B=0.5, and C=0.3) for run5 and run7 on the section x=0. Solid lines represent points where $\dot{x} = 0$.

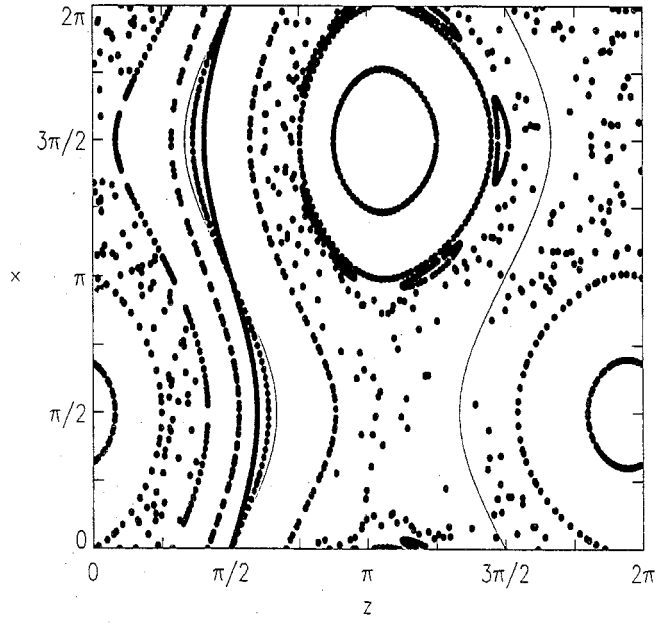

Figure 3.6b: Poincarè Map of the ABC flow (A=1, B=0.5, and C=0.3) for run5 and run7 on the section y=0. Solid lines represent points where $\dot{y} = 0$.

3.5 Discussions

3.5.1 3D Structures

The evolution of the enstrophy $\overline{\Omega}(t)$ and the enstrophy Reynolds numbers Re_ω are shown in Fig. 3.7 and 3.8. The decay of enstrophy by molecular viscosity is clearly overcome by dynamo action in all cases. Except for run2, the enstrophy grows exponentially at large time implying that the compact linear operator $\mathcal{L}$ has eigenvalues with positive real parts for those values of viscosity investigated. The enstrophy of run2 ($\nu = 0.006$) stays approximately stationary. However, we may not be observing a non-zero steady solution of the eigenproblem, because the evolution time required for the eigenfunction(s) corresponding to the eigenvalue(s) with the maximum positive real part(s) to dominate is determined by the initial conditions. For example, consider run5 and run7 which have the same initial energy spectrum for the same ABC flow and viscosity, but use different sets of random numbers to generate the initial Fourier components. The long-time behaviors are dominated by the same eigenfunction(s) but run7 clearly develops faster than run5.

Although the enstrophy grow exponentially in time, the smallest scale λ_ω involved is determined only by ν. It should approach to the constant lengthscale which characterizes the dominant eigenfunction(s) at large time. The evolution of λ_ω is shown in Fig. 3.9. The prediction $\lambda_\omega \propto \nu^{1/2}$ is obtained if one examines the ratio of λ_ω of run4 and run6 which have the same ABC flow but different viscosities. The enstrophy spectra $\Omega(k)$ at late times are also given in Fig. 3.10. The "tails" of the spectra are well resolved, implying a satisfactory numerical resolution is obtained.

We now consider the 3D vorticity structures in the physical space. We recall that the ABC flow in run1 is integrable and has a continuum of stagnation points which are connected by heteroclinic orbits. Each heteroclinic orbit is a stable manifold of one stagnation point and an unstable manifold of another. To help interpret the

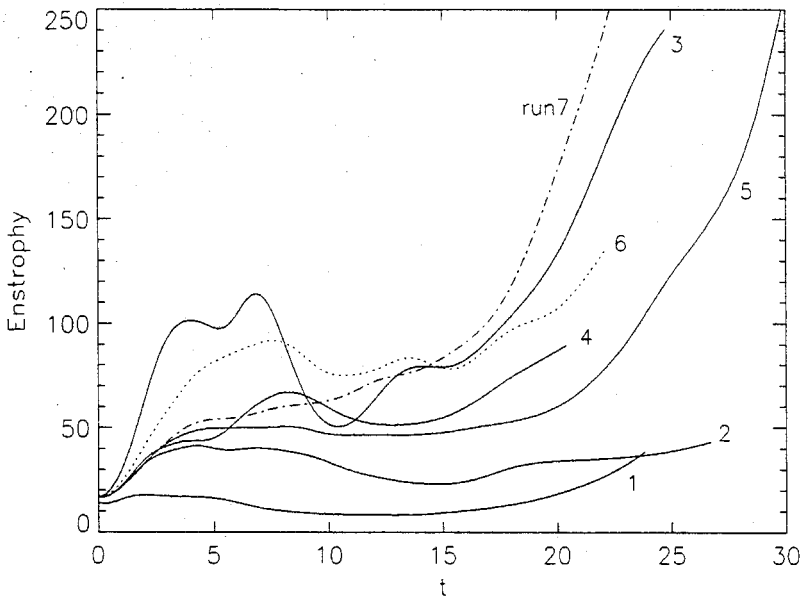

Figure 3.7: Evolutions of mean enstrophy $\overline{\Omega}(t)$.

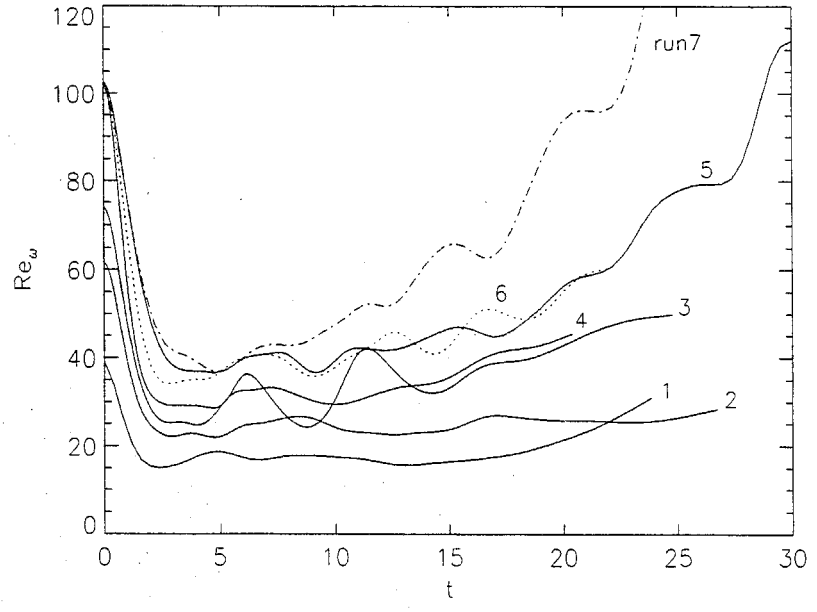

Figure 3.8: Evolutions of $Re_\omega \equiv (2\overline{\Omega})^{3/2}/\epsilon_\omega$.

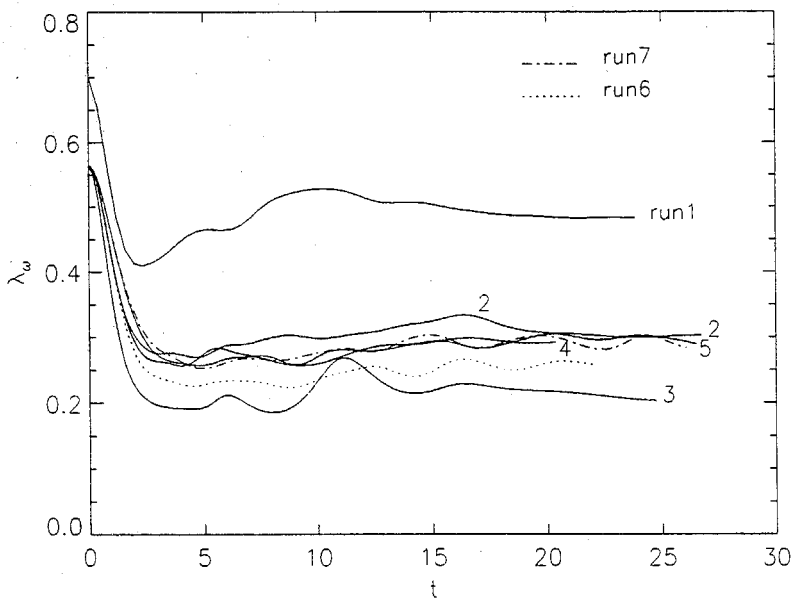

Figure 3.9: Evolutions of λ_ω.

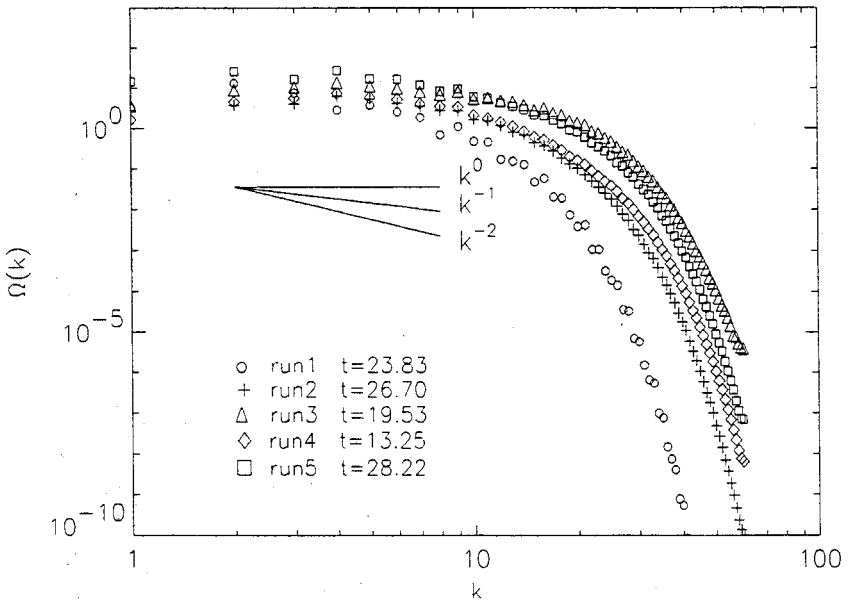

Figure 3.10: Enstrophy spectra at large times.

results, we superpose the projected orbits of the integrable ABC flow on the section $y = 0$. In addition, the reader should keep in mind the flow direction, i.e., $\dot{x} = \sin z$. The regions with vorticity magnitudes higher than 30% of the maximum value are shown in Fig. 3.11a for run1. It is observed the high amplitude vorticity is confined to a small neighborhood of the heteroclinic orbits and are shaped like "tubes," even although the manifolds form the plane $x \pm z = -\pi/2 + 2n\pi$, n an integer. In addition to the memory effect of the initial conditions, the effect of viscosity may produce the tube-like structures. Noticed also that the vorticity magnitude is small along the directions of the stable manifolds near the stagnation points. (Refer also to Fig. 3.16a in which vorticity contours on the section $y = 0$ are plotted.) Evidently, when the vortex lines approach the stagnation points along the stable manifold, not only are they largely stretched in the direction of unstable manifold, but also they compressed in the direction of the stable manifold. Thus gradients of vorticity and the viscous dissipation can be significant in those regions. Moreover, cancellations are also expected for folded, compressed vortex lines in the presence of viscosity.

Vortex lines starting from a neighborhood of the stagnation points $(3\pi/2, \overline{y}, 0)$ and $(\pi/2, \overline{y}, \pi)$, $0 \leq \overline{y} \leq 2\pi$ are shown in Fig. 3.11b. These vortex lines stay close to the heteroclinic orbits and are nearly straight where vorticity magnitude is high but found spiral where the magnitude is smaller. Reasons cited above to explain the low magnitudes along the stable manifold near a stagnation point may be applied here as well. When vortex lines spread out along the direction of unstable manifold, they are eventually "cut" off by viscous dissipation or by cancellations and thus form spirals. Vortex lines in the core region shown in Fig. 3.11c are mainly y-directed which is not surprising because of the linear y- motion of the integrable ABC flow.

When the values of parameters (A,B,C) are changed to generic nonintegrable case, the heteroclinic orbits are broken and chaotic particle motions are possible. With four stagnation points (run2), the ABC flow creates tube-like physical structures of vorticity once again as shown in Fig. 3.12a in which only contours with vorticity

$\|\omega\| > 30\%\|\omega\|_{max}$ are plotted (with the locations of stagnation points indicated by solid circles). Some of the tubes actually have flattened cross sections, however. When the threshold is increased to $50\%\|\omega\|_{max}$ (see Fig. 3.12b), the tubes are seen to have nearly circular cross sections. Moreover, it is found that they surround only two of the four stagnation points, $(3\pi/2, \pi, \pi/4)$ and $(\pi/2, 0, 5\pi/4)$. From Fig. 3.12c we see that these tubes are directed along the local unstable manifolds of these two stagnation points. Vortex lines near the other two stagnation points, which have much smaller magnitudes, are found to be approximately orthogonal to the local center manifold and not particularly biased in either of the other two manifolds (Fig. 3.12d). This suggests that, in the low enstrophy regions, the stretching effect $(\omega_j \frac{\partial u_i}{\partial x_j})$ is small and the convection effect $(u_j \frac{\partial \omega_i}{\partial x_j})$ probably dominates the alignments of vorticity vectors. The reason why amplifications are observed only around two of the four stagnation points is not clear, but we believe the two where amplification is observed will become α-type stagnation points under the saddle-node bifurcation, while the other two will be β-type. This conjecture is supported by the results of run3 discussed below.

In run3, there are eight stagnation points — four of them are α-type and four are β-type. We show the vorticity structures with $\|\omega\| > 30\%\|\omega\|_{max}$ in Fig. 3.13. The α-type stagnation points are indicated by solid circles, which are "buried" in the tube-like structures and therefore are not clearly seen in Fig. 3.13. The β-type stagnation points are indicated by open squares. It is obvious that the most amplified vorticity lies close to the α-type stagnation points and is concentrated near the local unstable manifold. Physical vortex structures in this case are thus completely dominated by the α-type stagnation points. Same phenomena had been observed by Galloway and Frisch [26] who studied the possibility of ABC flows as a dynamo over a wide range of magnetic Reynolds numbers.

In run4 and run5, there are no stagnation points. Amplifications of vorticity are thus expected in the chaotic regions of the flow originating from broken KAM tori. Fig. 3.14, 3.15a, and 3.15b show the physical structures of vorticity with $\|\omega\| >$

$30\%\|\omega\|_{max}$ or $50\%\|\omega\|_{max}$ for run4 and run5. Basically, the structures are flat and long, especially for the 30% threshold. In Fig. 3.15a, the "thickness" of the tubes is of the order λ_ω while the "width" is a few λ_ωs and the length of the tubes is of the order of the simulated box size (a few tens of λ_ω). Note spiral arms like those in Lundgren's model [42] are never observed.

One thing worth mentioning is there may exist a correlation between the geometry of chaotic zones of ABC flows and that of the vorticity structures. It wouldn't be so surprising if a tube-like chaotic zone in the 3D space creates a tube-like vorticity structure. However, it is too hard to present the chaotic zones in a 3D space. To study the differences of stretching effects in regular and chaotic regions, we take advantage of Poincaré maps and the results are given in the next section.

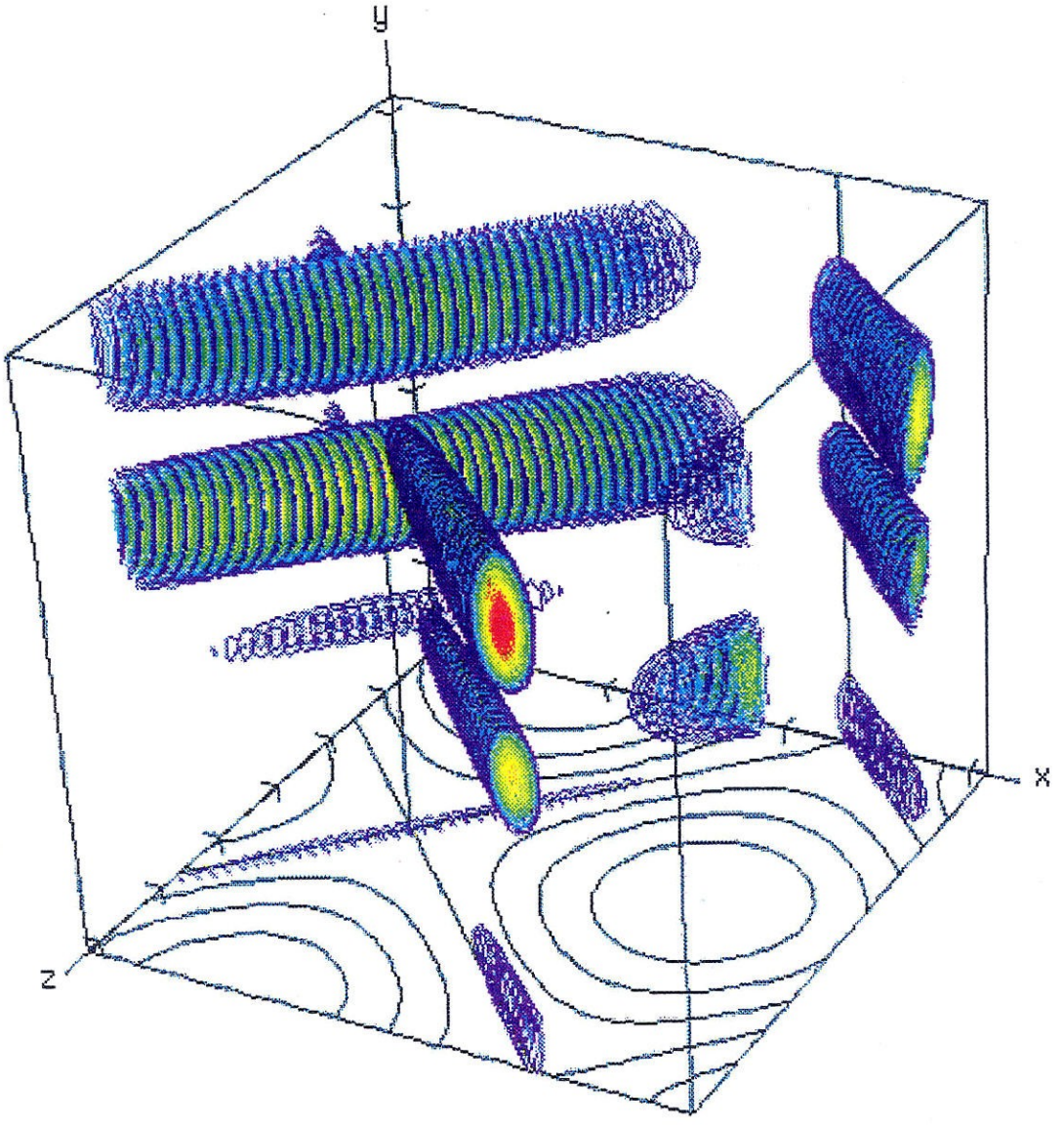

Figure 3.11a: The intense vorticity regions with $\|\omega\| > 30\%\|\omega\|_{max}$ for run1. Superposed are the projected orbits of the integrable ABC flow ($C = 0$) on the $y = 0$ section which flow direction is determined by $\dot{x} = \sin z$ or $\dot{z} = \cos x$.

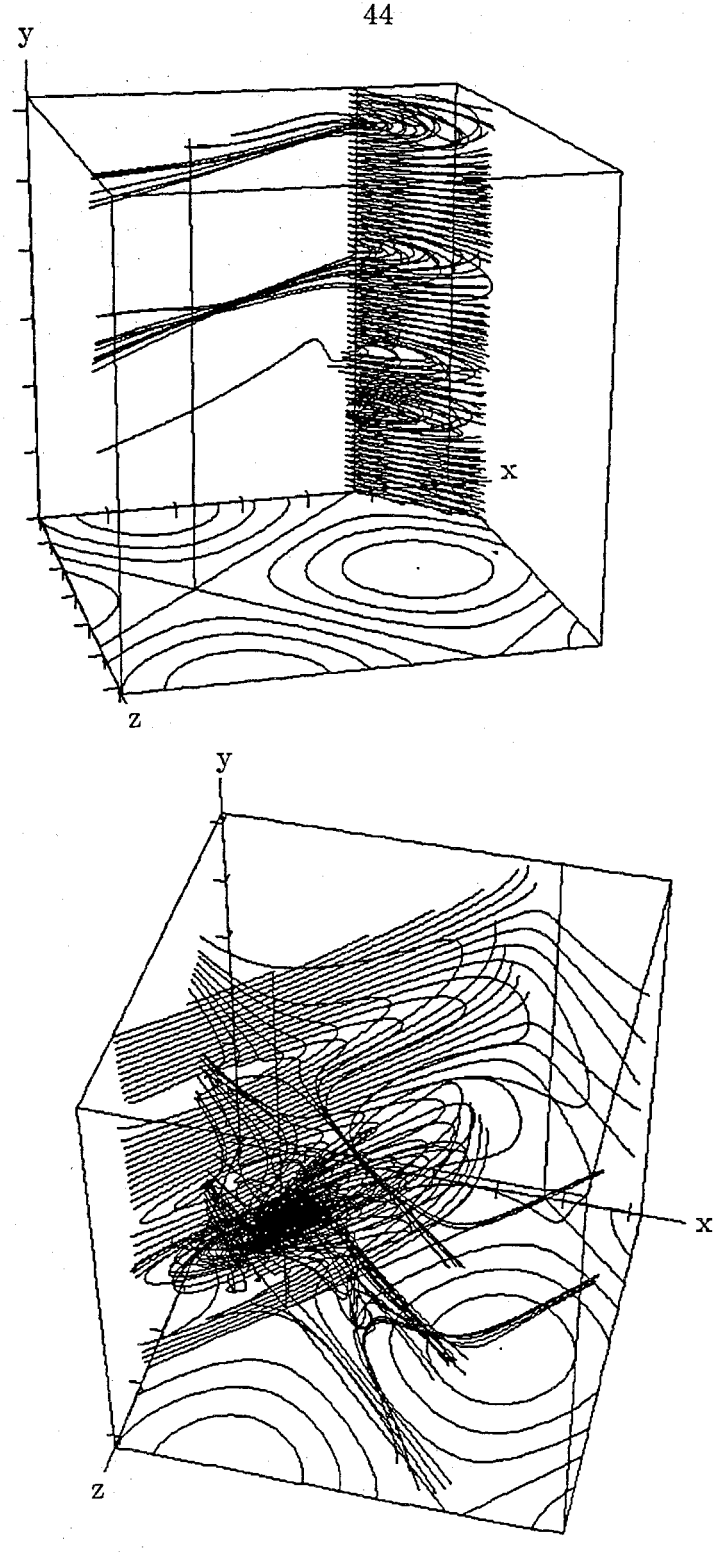

Figure 3.11b: Vortex lines starting from a neighborhood of the stagnation points for run1: (U) $(3\pi/2, \overline{y}, 0)$ (B) $(\pi/2, \overline{y}, \pi)$.

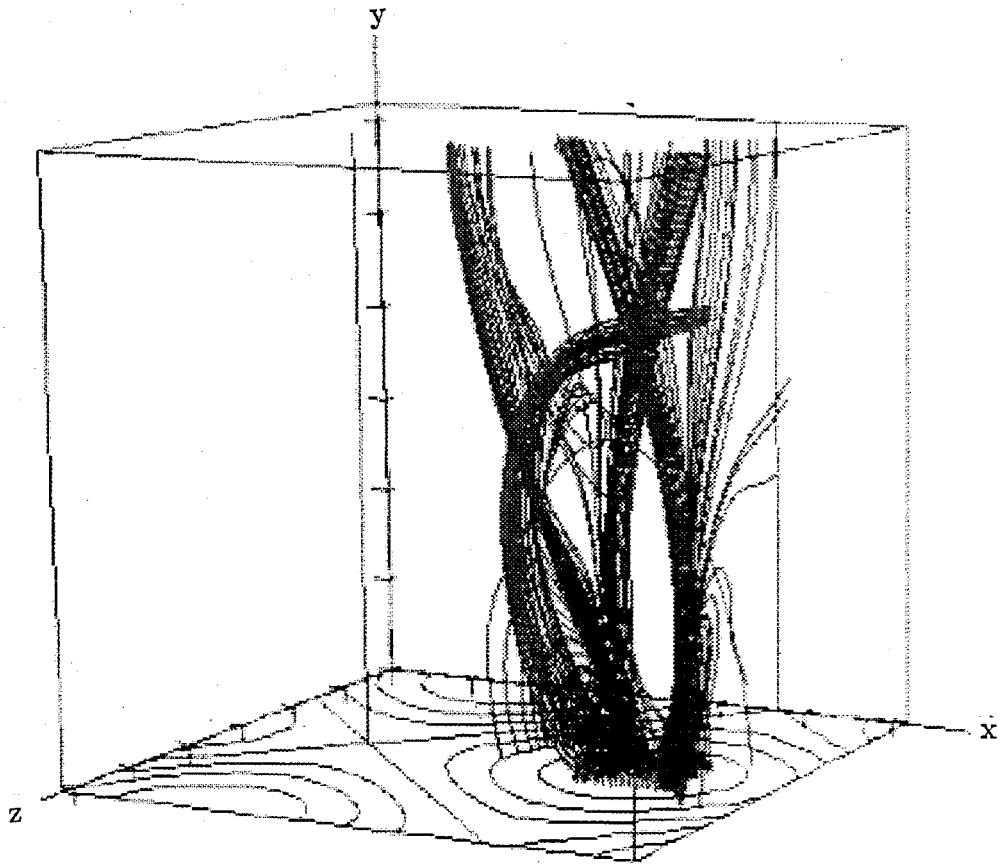

Figure 3.11c: Vortex lines in the core region of the integrable ABC flow for run1 (A=B=1, C=0).

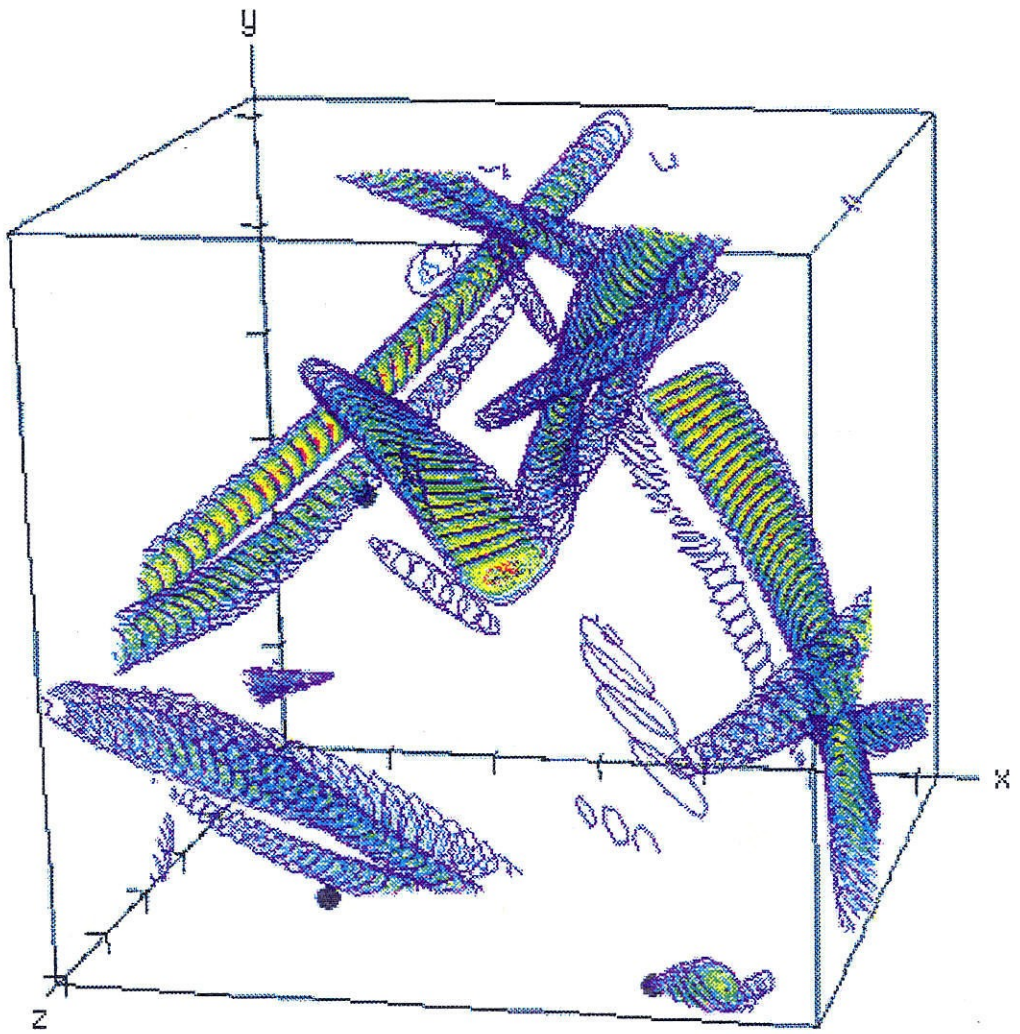

Figure 3.12a: Intense vorticity structures with $\|\omega\| > 30\%\|\omega\|_{max}$ for run2. Stagnation points are indicated by the solid circles.

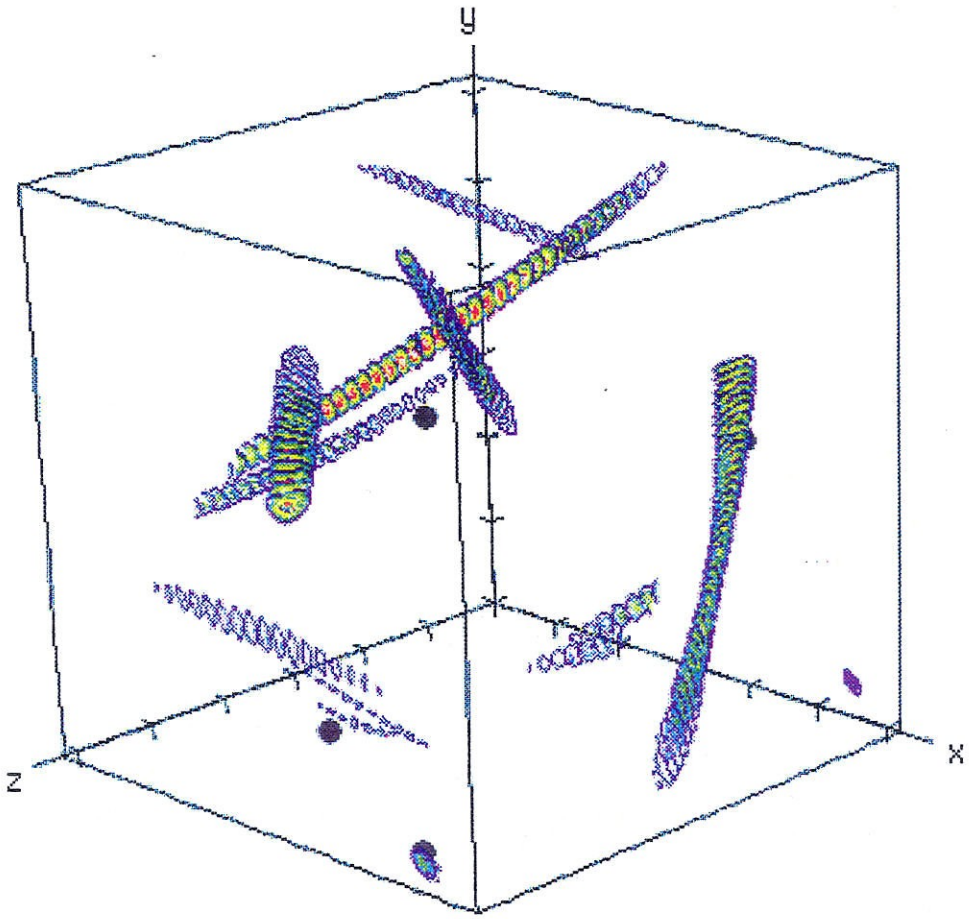

Figure 3.12b: Vorticity structures with $\|\omega\| > 50\%\|\omega\|_{max}$ for run2. Stagnation points are indicated by the solid circles.

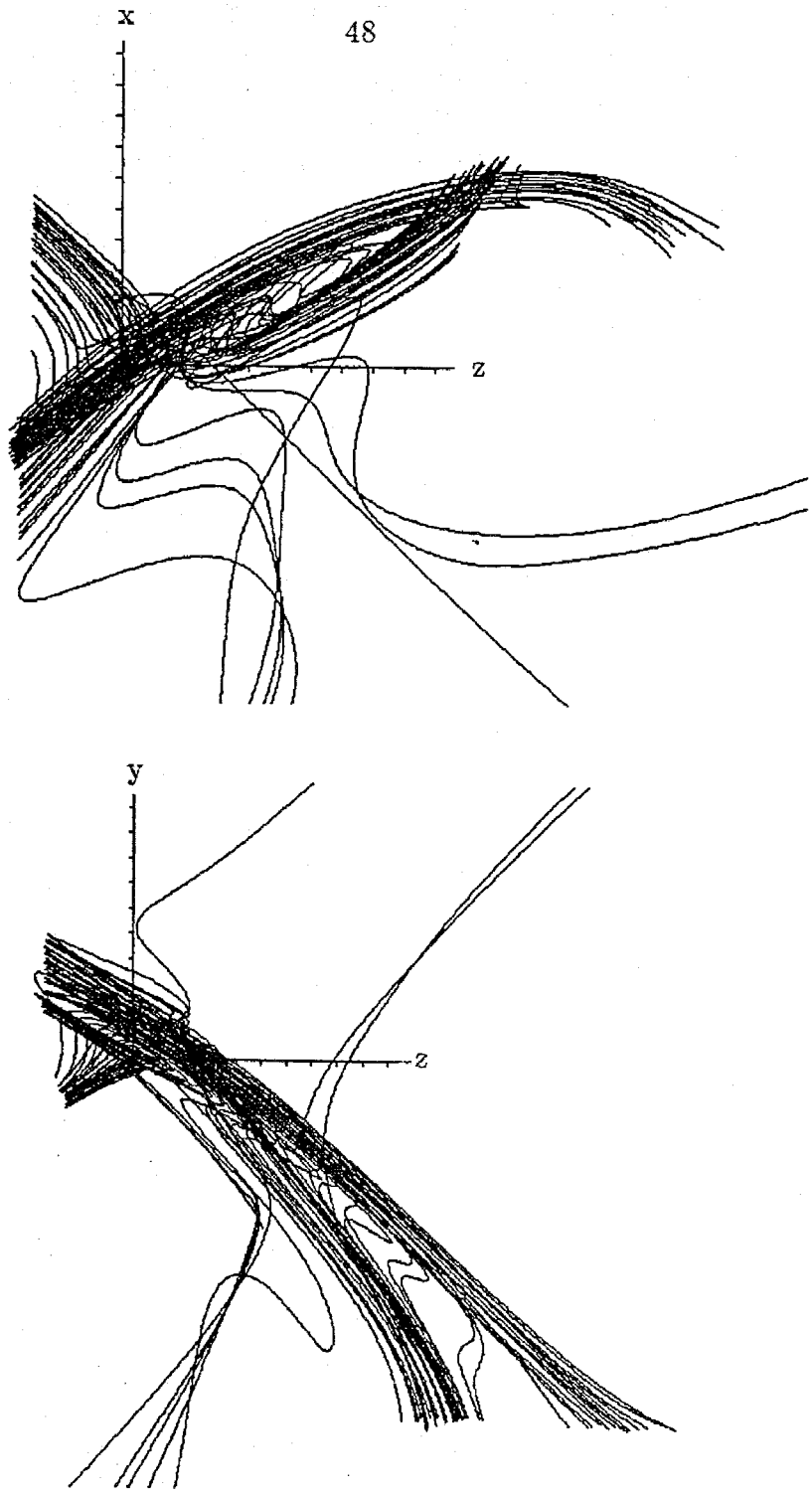

Figure 3.12c: Vortex lines near the stagnation point $(3\pi/2, \pi, \pi/4)$ of run2. The associated local unstable manifold is $(1, -1, \sqrt{2})$.

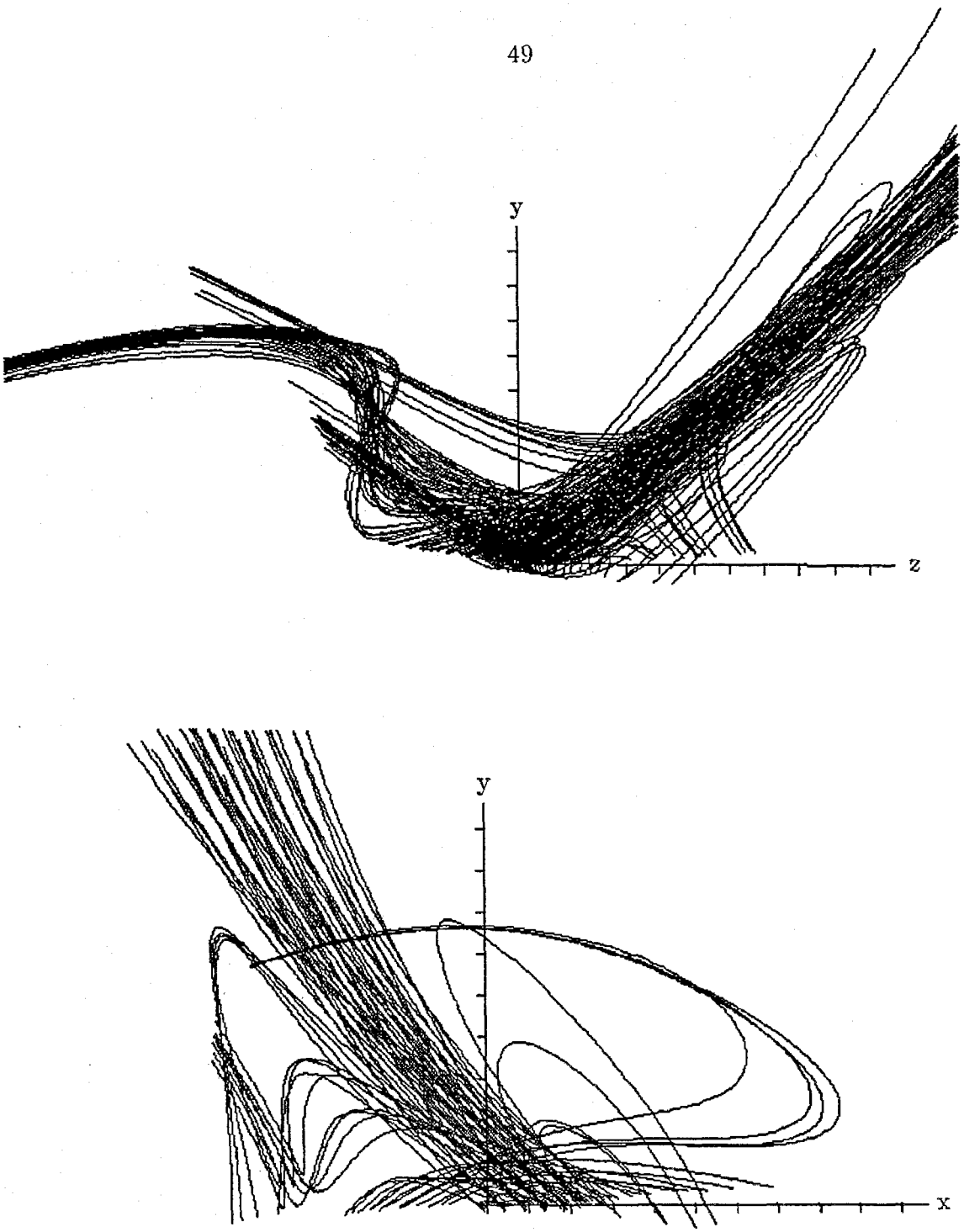

Figure 3.12d: Vortex lines near the stagnation point $(\pi/2, 0, 5\pi/4)$ of run2. The associated local unstable manifold is $(1, -1, -\sqrt{2})$ and the local center manifold is $(1, 1, 0)$.

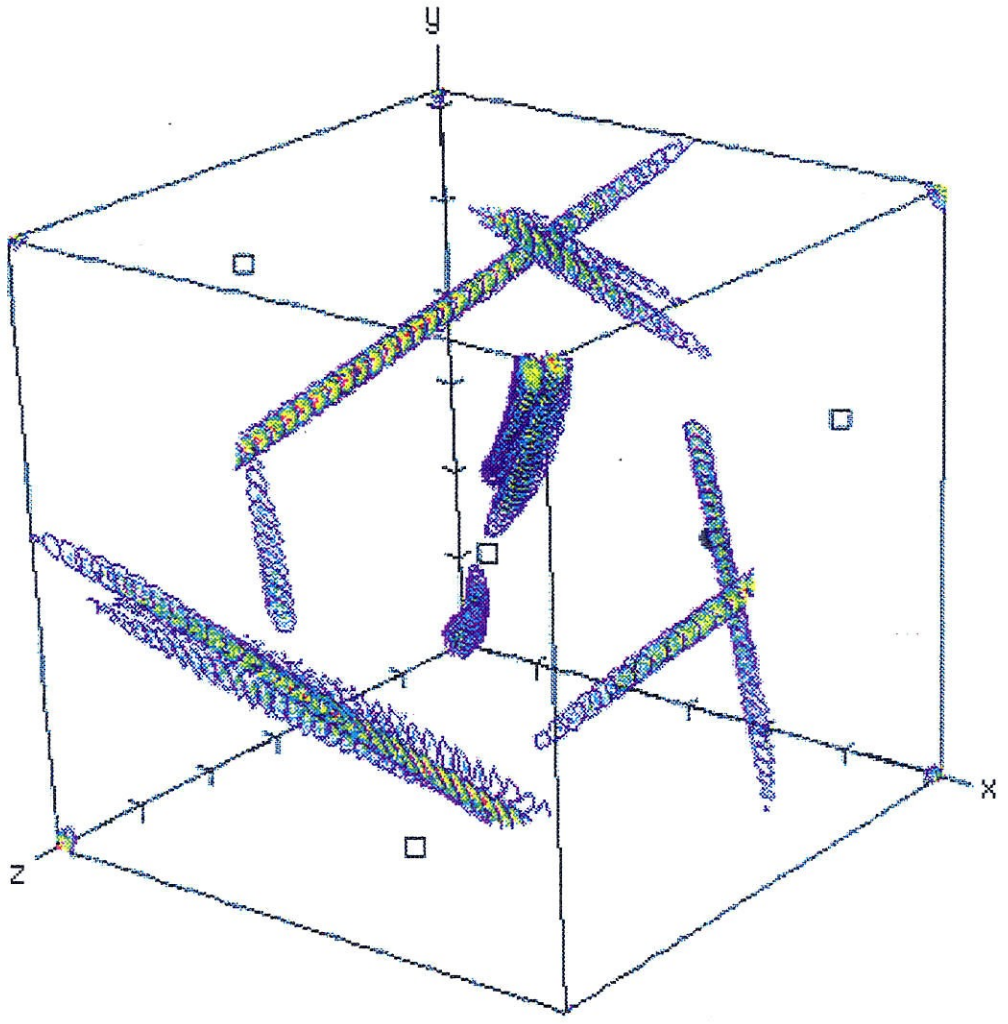

Figure 3.13: Intense vorticity structures with $\|\omega\| > 30\%\|\omega\|_{max}$ for run3. The α-type stagnation points are indicated by the solid circles and the β-type are indicated by the open squares.

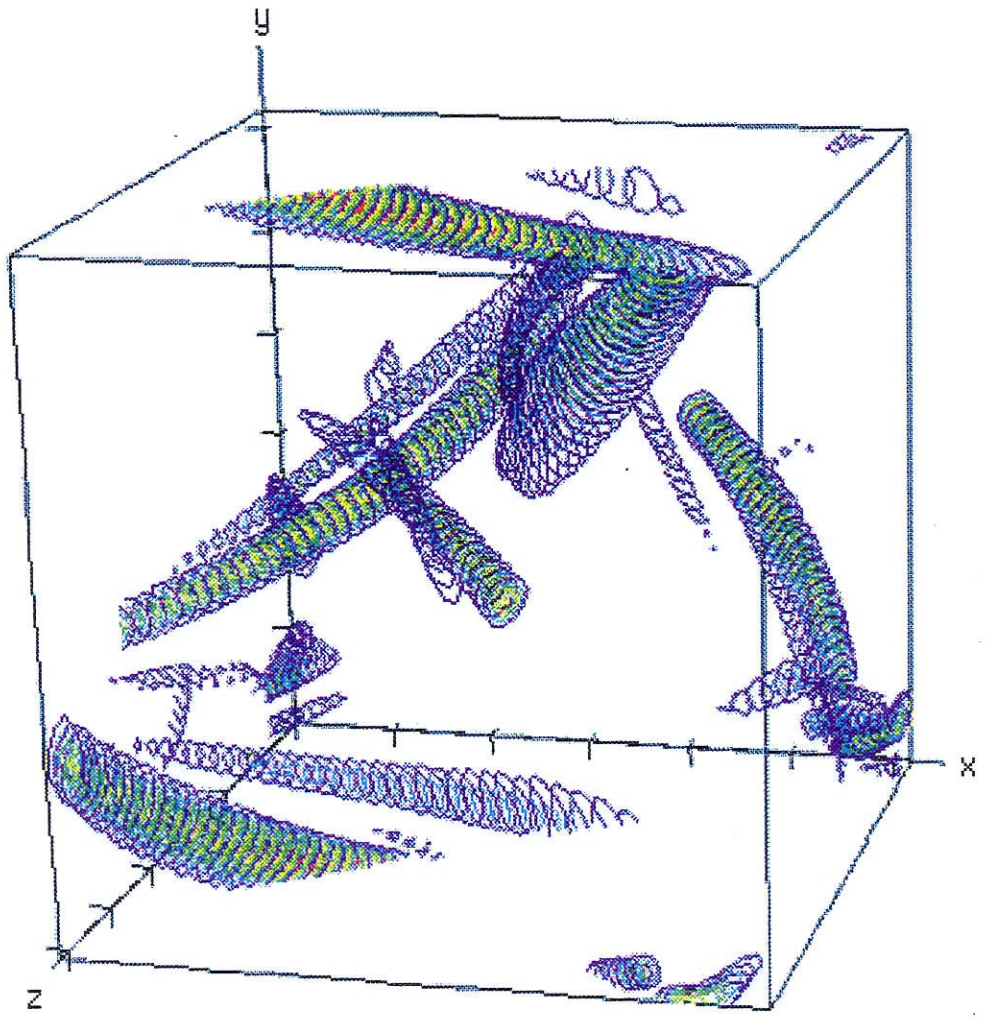

Figure 3.14: Intense vorticity structures with $\|\omega\| > 30\%\|\omega\|_{max}$ for run4 which has no stagnation points.

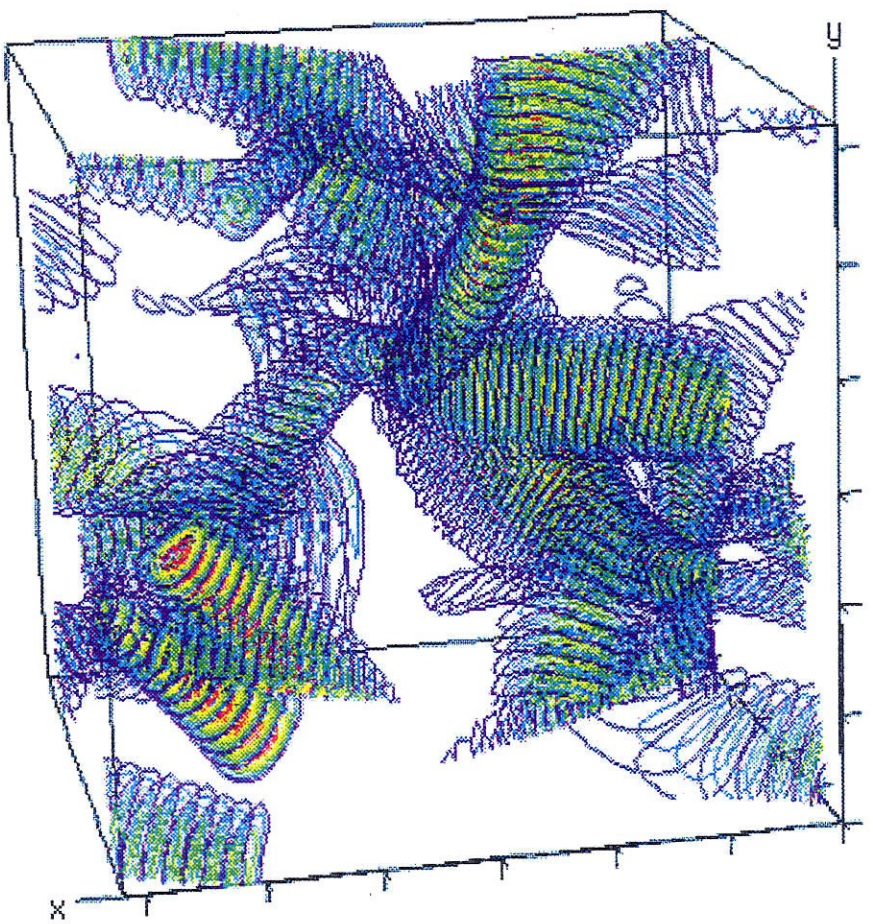

Figure 3.15a: Intense vorticity structures with $\|\omega\| > 30\%\|\omega\|_{max}$ for run5 which has no stagnation points.

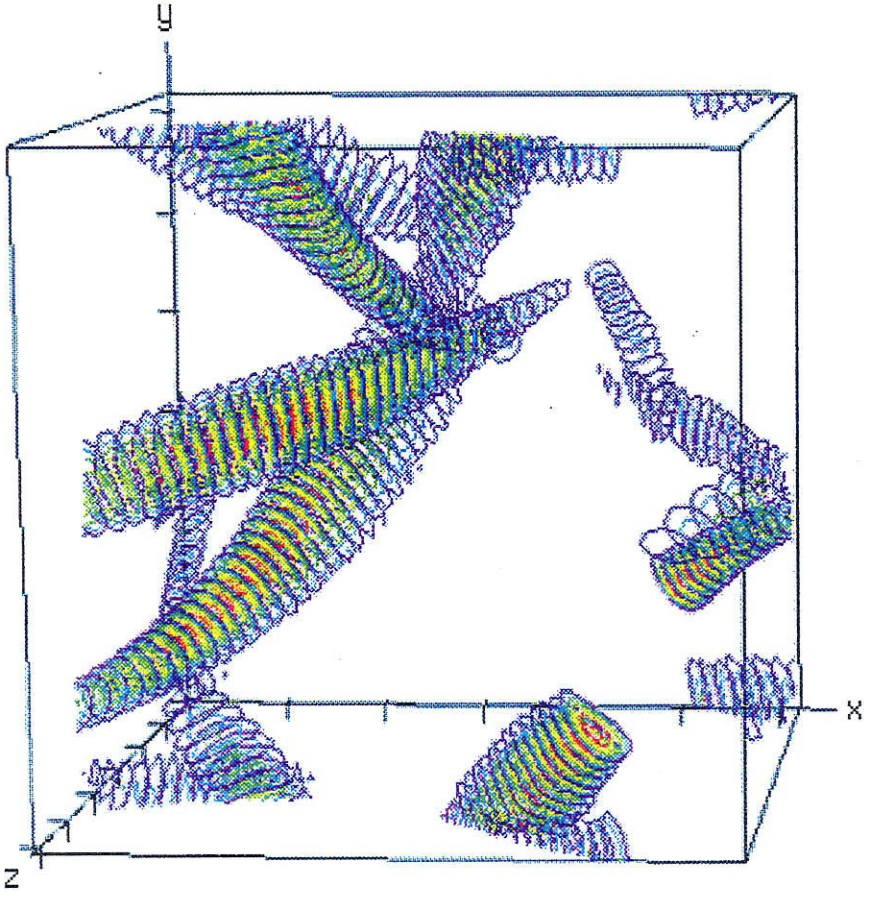

Figure 3.15b: Intense vorticity structures with $\|\omega\| > 50\%\|\omega\|_{max}$ for run5 which has no stagnation points.

3.5.2 Poincaré Sections

In this section, we study contour plots of the vorticity magnitude. The first case is that of the integrable ABC flow and is shown in Fig. 3.16ab. Note contours of large magnitudes are plotted in solid lines while those of small magnitudes are in dotted lines for distinguishment. We are now not surprised to observe substantial amplifications of vorticity in the neighborhoods of unstable and stable manifolds (except along the latter near the stagnation points). Shown in Fig. 3.17a and 3.17b are the projected vorticity vectors on the y=0 and z=0 sections. We notice in some regions vorticity vectors are directed in an opposite direction to the velocity vectors of the flow.

In order to study the correlation between the amplifications of vorticity and the chaotic zones of the ABC flow, we superpose the vorticity contour plots to the Poincare sections of the ABC flow (figures 3.3ab to 3.6ab) and the results are shown in figures 3.18ab to 3.21ab. A common figure in these maps is that amplifications are concentrated in the chaotic zones and only in some of the chaotic zones when stagnation points exist. For example, not much amplification is observed in the chaotic region in the upper right corner of Fig. 3.18a and the upper left corner of Fig. 3.18b. A stagnation point with one positive eigenvalue seems a dominant factor of dynamo actions. For example there are two stagnation points, $(\pi/2, 0, 5\pi/4)$ and $(3\pi/2, 0, 7\pi/4)$, on the section of Fig. 3.18b and large amplifications are observed along their local unstable manifolds, $(x, z) = (1, -\sqrt{2})$ and $(1, \sqrt{2})$. Similarly, contours of larger magnitudes are observed more in the neighborhood of the α-type stagnation point $(\pi/4, 5\pi/4, 3\pi/4)$ in Fig. 3.19b than in the neighborhood of the β-type, $(\pi/4, 7\pi/4, 5\pi/4)$. The other regions in Fig. 3.19b with dense contours must be caused by tubes surrounded by the other α-type stagnation points which do not lie on the section $x = \pi/4$.

We also notice that the amplifications of vorticity in run4 and run5 are more uniformly distributed in the chaotic zones than in run2. The difference must be caused

by the fact that only run2 has stagnation points. Also, more and more KAM tori are broken from run2 to run4 to run5 (compare Fig. 3.3a, Fig. 3.5a, and Fig. 3.6a). We may identify flows more and more "chaotic" from run2 to run4 to run5. The existence of a stagnation point and the survival KAM tori cause nonuniform stretching.

In the cases which flows have stagnation points, we have observed a strong correlation between the alignment of a vorticity vector and the local manifolds, especially the unstable one. For those cases which flows do not have stagnation points, we can instead study the alignment of a vorticity vector relative to the principal directions of the local strain tensor. Cases without stagnation points are actually of more interest for they are more chaotic (more KAM tori broken) and might provide more hints in the prediction of an actual turbulent flow which is believed chaotic everywhere in some sense.

3.5.3 Probabiliy Distribution

The strain tensor of ABC flows is defined as $\frac{1}{2}\left(\frac{\partial u_i}{\partial x_j}+\frac{\partial u_j}{\partial x_i}\right)$. Its correlation with the alignment of a vorticity vector is obtained through the study of a probability distribution of the absolute value of the cosine of the angle between the vorticity vector and the principal directions of the strain tensor. We shall call the directions corresponding to the most positive, the intermediate, and the most negative principal rates as the first, the second, and the third directions from now on.

Initially, the vorticity is randomly directed and thus the probability is uniformly distributed in the range of [0,1] for all three angles. As time increases, the flow motion and maybe the viscosity adjust the vorticity vector in some way and any change in the probability distribution reflects the results. Since at large time, the solutions are dominated by the eigenfunction(s) of the compact linear operator $\mathcal{L}$ with the most positive real part of eigenvalue(s), probability distributions collected here can be taken as the correlations between that (those) eigenfunction(s) with the ABC flows.

The probability distribution in the present study is constructed in the following way. We first calculate the absolute value of the cosine of the angles at 128^3 grid points in the physical space. The domain [0,1] is divided into 128 bins. The i^{th} bin collects data points having the absolute value within the range of $(\frac{i}{128}, \frac{i+1}{128}]$ for i=0,1,2,$\cdots$,127. The number of data points in each bin is then counted. The probability of finding the absolute value of $\frac{(i+0.5)}{128}$ is then approximated as the ratio of the number of data points in i^{th} bin to the total grid points 128^3. Results are presented in Fig. 3.22 to Fig. 3.27. Note in all the figures, the probability distribution for the angle between the vorticity vector and the first direction is shown by the solid lines. The dash dotted lines are for the second direction and dotted lines for the third one. Conditional probability distributions are also constructed by using only those data points having $\|\omega\| > 30\%\|\omega\|_{max}$. These probability distributions thus represent those of the observed vorticity structures in the previous section (Fig. 3.14, etc). The mean values ($\overline{|\cos\theta_i|}$) and the variances ($\sigma_i$), nonconditional and conditional, for all cases are listed in Table 3.5 and Table 3.6.

The probability distributions of run2 and run3 which both have finite stagnation points look very similar as shown in Fig. 3.23 and 3.24. The vorticity vectors tend to align with either the first direction or the third one in the low enstrophy regions, while in the high enstrophy regions they are nearly parallel to the first direction. Tails in the third directions seemingly exist at both ends. This is a little surprising for it implys some vortex lines align with the third direction also even in the high vorticity regions. The probability distribution for the first direction of run1 (see Fig. 3.22) has a peak at about 0.75 in addition to a tail at the right end which must be contributed by the high vorticity structures. A peak in the probability distribution of the third direction is also observed approximately at 0.6. Both values are greater than 0.5, the mean value of a random distribution. Obviously, the above three cases all imply the vorticity vector is not simply directed in the first direction although stretching in that direction is the strongest.

Table 3.5: Nonconditional means ($\overline{|\cos\theta_i|}$) and variances ($\sigma_i$) of the absolute values of the cosine of the angles between vorticity vectors and the principal directions of the strain tensors of the ABC flows.

	t	$\overline{\lvert\cos\theta_1\rvert}$	$\overline{\lvert\cos\theta_2\rvert}$	$\overline{\lvert\cos\theta_3\rvert}$	σ_1	σ_2	σ_3
run1	23.8	0.60	0.41	0.48	0.27	0.31	0.27
run2	26.7	0.58	0.39	0.49	0.32	0.26	0.32
run3	19.5	0.59	0.34	0.52	0.31	0.25	0.32
run4	13.2	0.58	0.42	0.48	0.30	0.27	0.29
run5	28.2	0.50	0.62	0.39	0.28	0.28	0.24
run6	22.1	0.58	0.39	0.51	0.30	0.27	0.30
run7	26.0	0.50	0.61	0.40	0.29	0.27	0.24

Table 3.6: Conditional means ($\overline{|\cos\theta_i|}$) and variances ($\sigma_i$) of the absolute values of the cosine of the angles between vorticity vectors and the principal directions of the strain tensors of the ABC flows on $\|\omega\| > 30\%\|\omega\|_{max}$.

	t	$\overline{\lvert\cos\theta_1\rvert}$	$\overline{\lvert\cos\theta_2\rvert}$	$\overline{\lvert\cos\theta_3\rvert}$	σ_1	σ_2	σ_3
run1	23.8	0.60	0.43	0.10	0.44	0.45	0.21
run2	26.7	0.79	0.24	0.21	0.34	0.23	0.32
run3	19.5	0.82	0.07	0.21	0.36	0.12	0.36
run4	13.2	0.79	0.32	0.21	0.29	0.26	0.28
run5	28.2	0.68	0.53	0.23	0.30	0.29	0.16
run6	22.1	0.75	0.30	0.24	0.32	0.28	0.32
run7	26.0	0.69	0.56	0.22	0.27	0.25	0.15

We also notice the results of run1 unlike those of run2 and run3 show it is also very likely to have a vorticity vector aligned with the second direction (implied by the tail of the dash dotted curve at the right end in Fig. 3.22). Considering run1 is a special case which flow is integrable, we believe the probability is increased by the associated linear y-motion.

Results of Run4 and run5 are very different (Fig. 3.25 and 3.26). First of all, the probability for a vorticity vector to be aligned with the third direction is largely decreased, especially in run5. In run4, a vorticity vector shows no preference in the third direction and the probability distribution for the second direction is similar to those of run1, run2, and run3; nonetheless in run5, a vorticity vector becomes more likely to be orthogonal to the third direction and a peak near the right end in the probability distribution for the second direction appears. The nonconditional probability distributions of run5 actually are very similar to those observed in direct numerical simulations of homogeneous isotropic turbulence, for example Ashurst in 1987 [3]. However, numerical simulations of turbulence also show an even larger probability of finding a vorticity vector aligned with the second direction when conditioned on high vorticity regions, which is not consistent with the results shown in Fig. 3.26b.

We notice the peak in the probability distribution for the third direction has shifted gradually to the left-hand side from run3 (8 stagnation points) to run2 (4 stagnation points) to run4 and run5 (no stagnation points). It seems true that a passive vorticity vector become more orthogonal to the third direction when the flow is more chaotic. We also notice on the alignment of vorticity vectors, the magnitude of viscosity has little effect. This is observed by comparing the results of run4 and run6 which have the same ABC flows but different viscosities.

3.6 Conclusions

In all the simulations, viscous dissipations are overcome by the dynamo actions. Or the compact linear operator $\mathcal{L}$ contructed by the ABC flows with those values of viscosity investigated has eigenvalues with postive real parts. The dominant eigenfunctions create tubes with a length on the order of the simulated box size and at least one dimension of the tubes is on the order of $\lambda_\omega \sim (\nabla^2\omega/\omega)^{-1/2}$.

The tube-like vorticity structures and their correlations with the local manifolds of stagnation points, if they exist, suggest regions with local strain tensors having one positive and two negative principal rates accumulate most of the amplifications. Otherwise, amplifications are confined within the chaotic zones of the ABC flows. An existence of a stagnation point seems dominant in a dynamo action over an existence of chaotic zones of the flow.

Conditional probability on the high vorticity regions shows the passive vorticity vector is most likely directed in the principal direction corresponding to the most positive principal rate of the strain tensor. It is found that the vorticity vector is also likely to be aligned with the principal direction corresponding to the most negative principal rate, especially in low enstrophy regions. This probability, however, is decreased when the flow becomes chaotic.

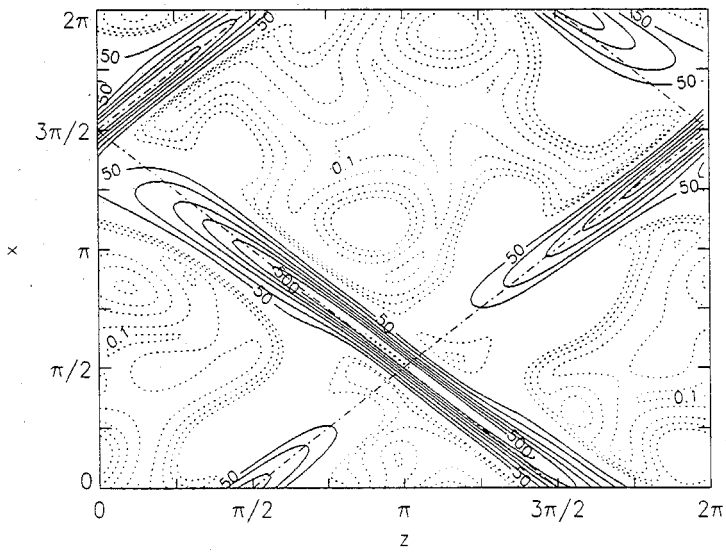

Figure 3.16a: The contour plot of the vorticity magnitude $\|\omega\|^2$ on the section y=0 for run1. Contours of large magnitudes are plotted by solid lines and those of small magnitudes by dotted lines.

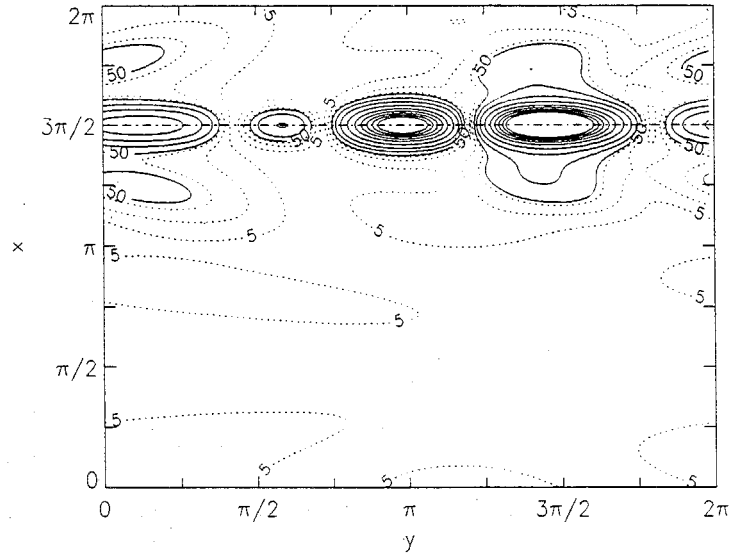

Figure 3.16b: The contour plot of the vorticity magnitude $\|\omega\|^2$ on the section z=0 for run1. Contours of large magnitudes are plotted by solid lines and those of small magnitudes by dotted lines. The dash dotted line is the continuum of stagnation points.

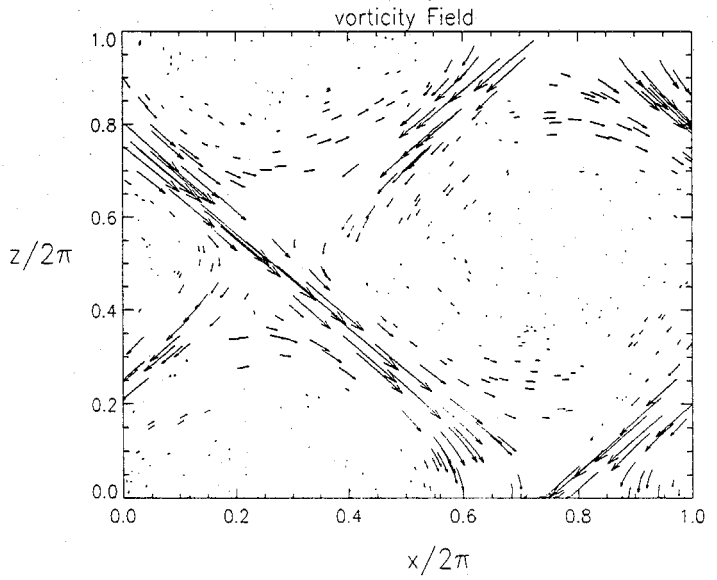

Figure 3.17a: Vorticity vectors projected on the section y=0 for run1. Compared with the projected orbit of the ABC flow shown in Fig. 3.1, the passive flow does not quite follow the stream direction.

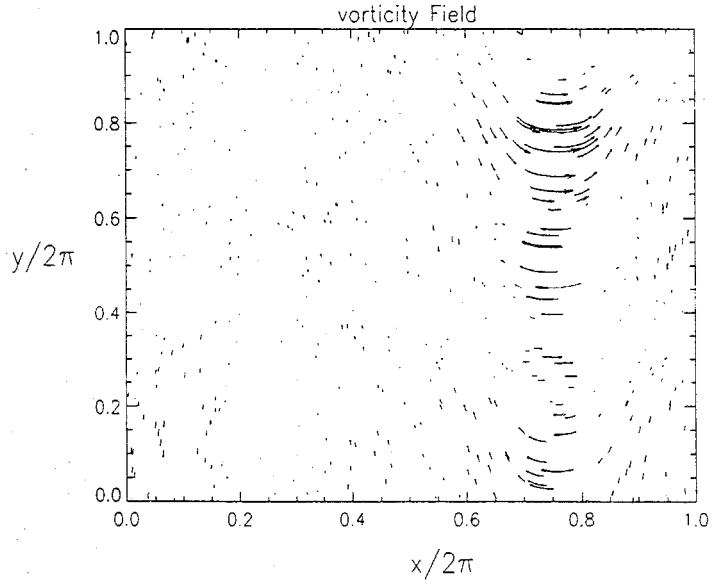

Figure 3.17b: Vorticity vectors projected on the section z=0 for run1.

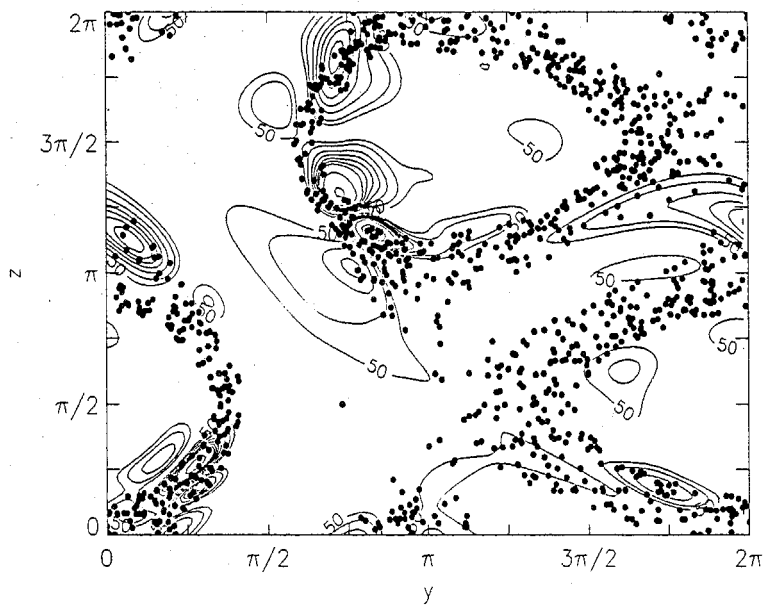

Figure 3.18a: The contour plot of the vorticity magnitude $\|\omega\|^2$ on the section x=0 superposed with the chaotic seas on the Poincaré section of the ABC flow (A=1, B=C=$1/\sqrt{2}$) for run2.

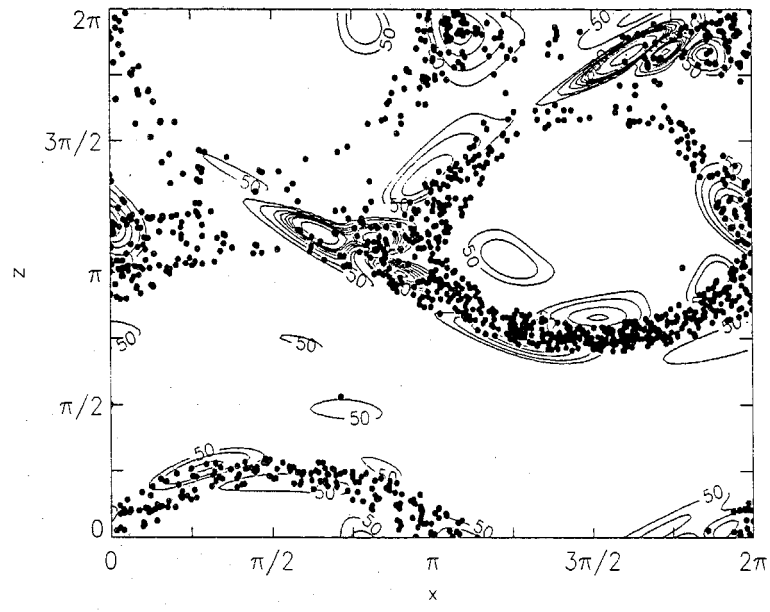

Figure 3.18b: The contour plot of the vorticity magnitude $\|\omega\|^2$ on the section y=0 superposed with the chaotic seas on the Poincaré section of the ABC flow (A=1, B=C=$1/\sqrt{2}$) for run2. Two stagnation points, $(\pi/2, 0, 5\pi/4)$ and $(3\pi/2, 0, 7\pi/4)$, are there on the section.

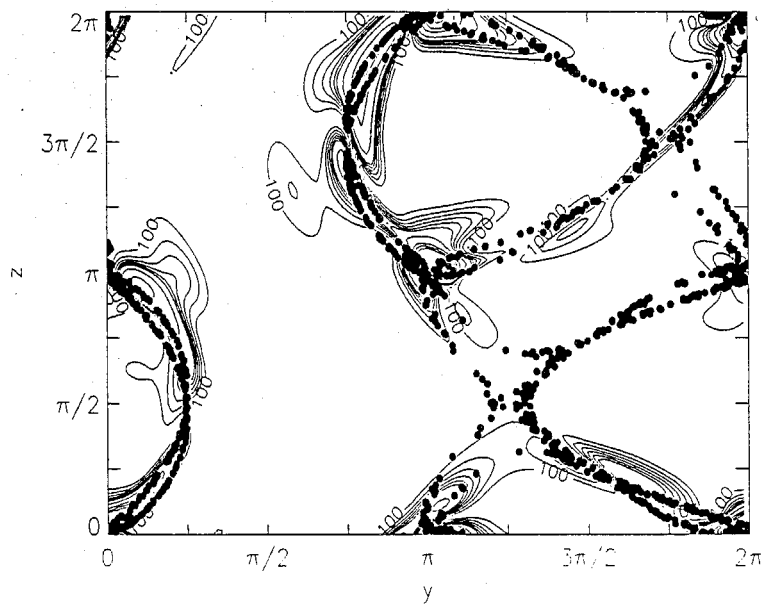

Figure 3.19a: The contour plot of the vorticity magnitude $\|\omega\|^2$ on the section x=0 superposed with the chaotic seas on the Poincaré section of the ABC flow (A=B=C=1) for run3.

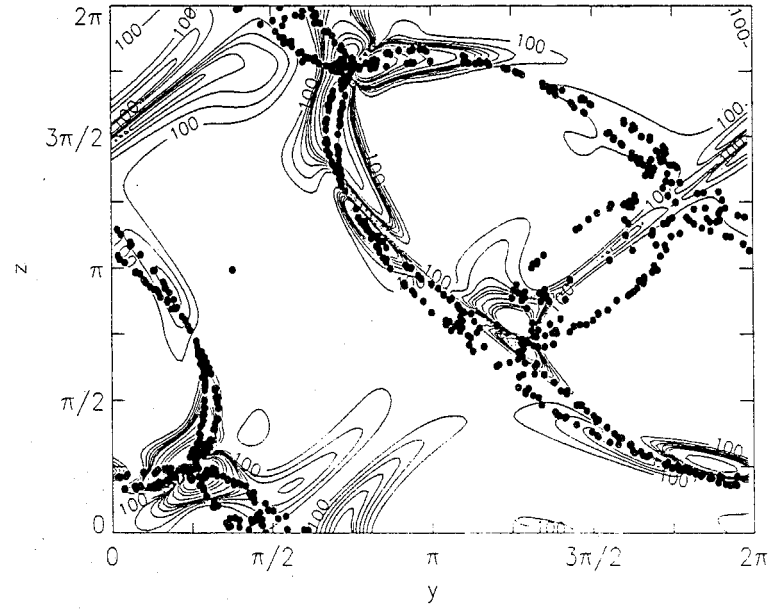

Figure 3.19b: The contour plot of the vorticity magnitude $\|\omega\|^2$ on the section $x = \pi/4$ superposed with the chaotic seas on the Poincaré section of the ABC flow (A=B=C=1) for run3. One α-type stagnation point, $(\pi/4, 5\pi/4, 3\pi/4)$, and one β-type, $(\pi/4, 7\pi/4, 5\pi/4)$, are there on the section.

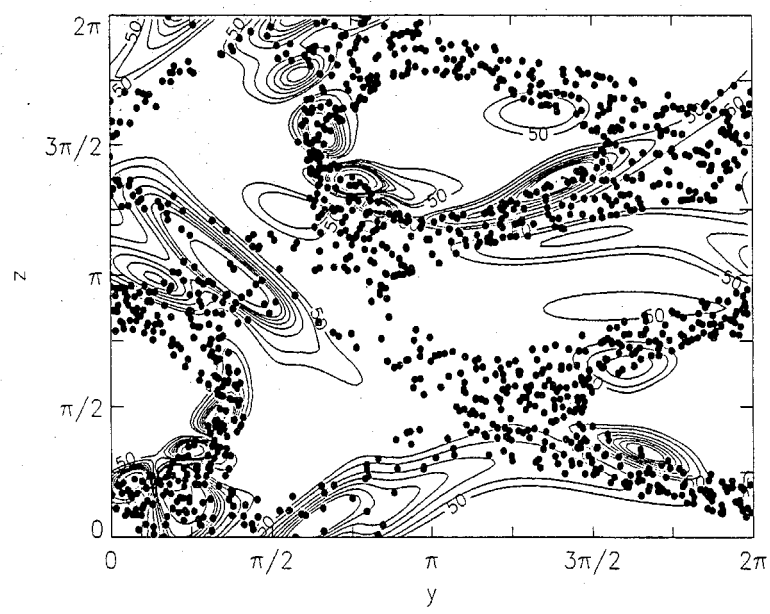

Figure 3.20a: The contour plot of the vorticity magnitude $\|\omega\|^2$ the section x=0 superposed with the chaotic seas on the Poincaré section of the ABC flow (A=1, B=0.8, and C=0.5) for run4.

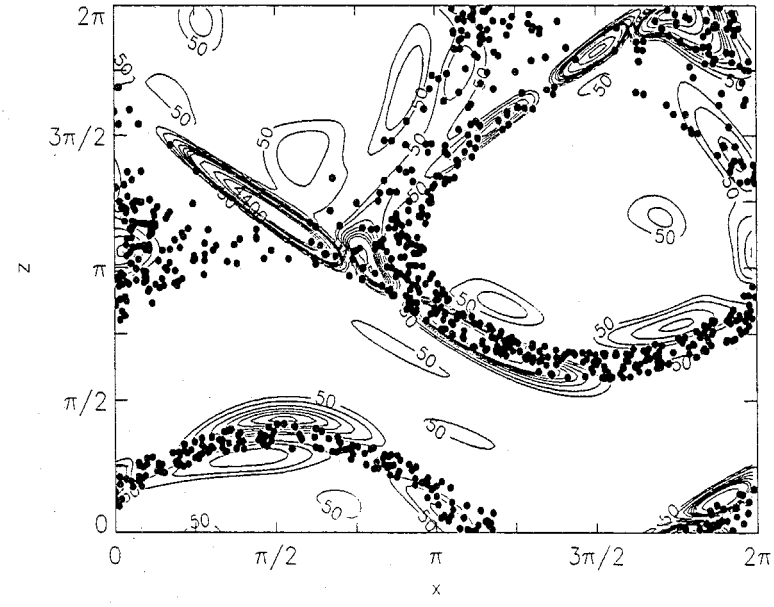

Figure 3.20b: The contour plot of the vorticity magnitude $\|\omega\|^2$ the section y=0 superposed with the chaotic seas on the Poincaré section of the ABC flow (A=1, B=0.8, and C=0.5) for run4.

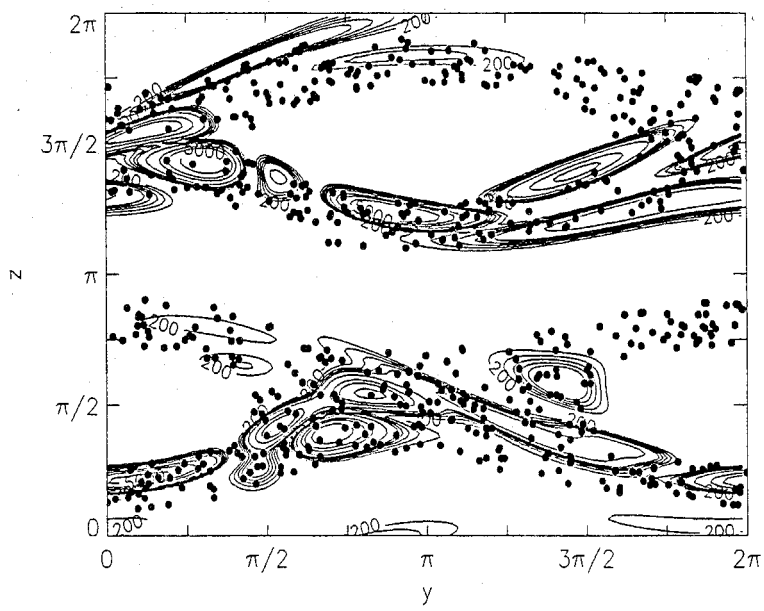

Figure 3.21a: The contour plot of the vorticity magnitude $\|\omega\|^2$ the section x=0 superposed with the chaotic seas on the Poincaré section of the ABC flow (A=1, B=0.5, and C=0.3) for run5.

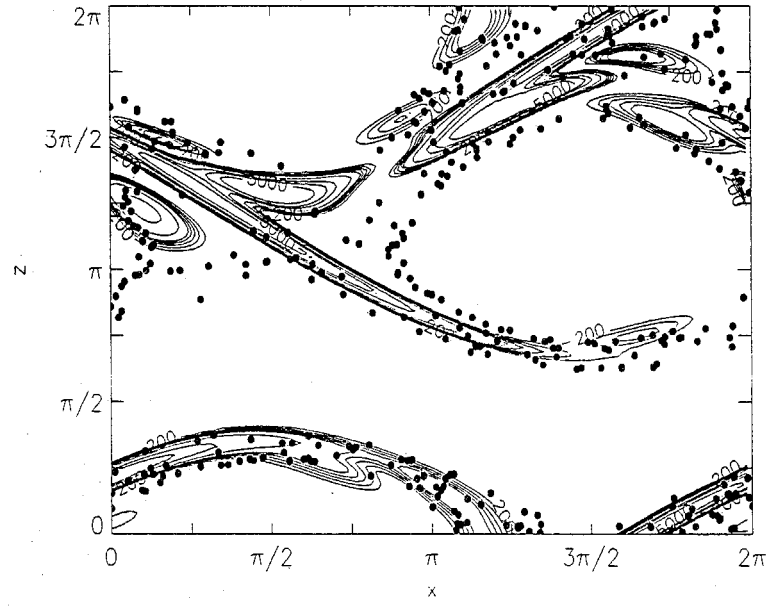

Figure 3.21b: The contour plot of the vorticity magnitude $\|\omega\|^2$ the section y=0 superposed with the chaotic seas on the Poincaré section of the ABC flow (A=1, B=0.5, and C=0.3) for run5.

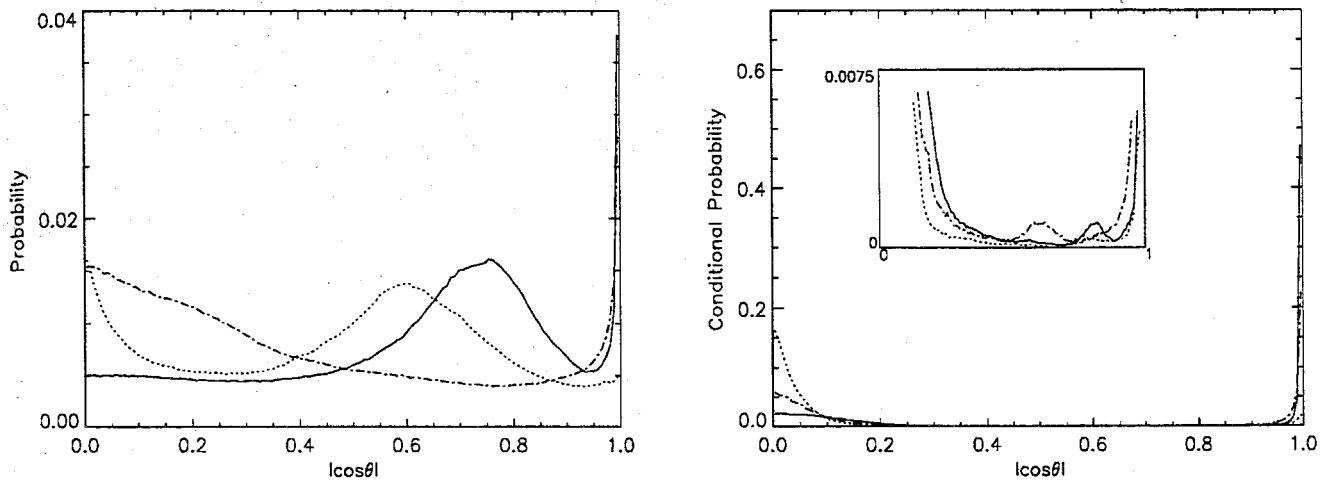

(a) (b)

Figure 3.22: (a) Nonconditional probability distributions (b) Probability distributions conditioned on $\|\omega\| > 30\%\|\omega\|_{max}$ for run1. (1) —— $\mathbf{e}_1$ (2) $-\cdot-\cdot-$ $\mathbf{e}_2$ (3) $\cdots\cdots$ $\mathbf{e}_3$

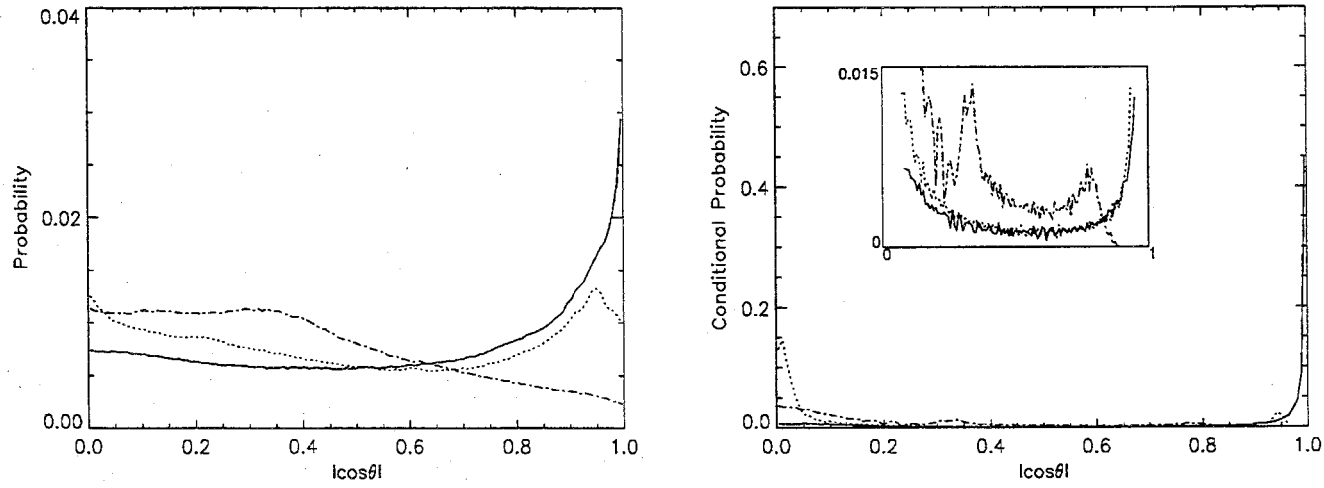

(a) (b)

Figure 3.23: (a) Nonconditional probability distributions (b) Probability distributions conditioned on $\|\omega\| > 30\%\|\omega\|_{max}$ for run2. (1) —— $\mathbf{e}_1$ (2) $-\cdot-\cdot-$ $\mathbf{e}_2$ (3) $\cdots\cdots$ $\mathbf{e}_3$

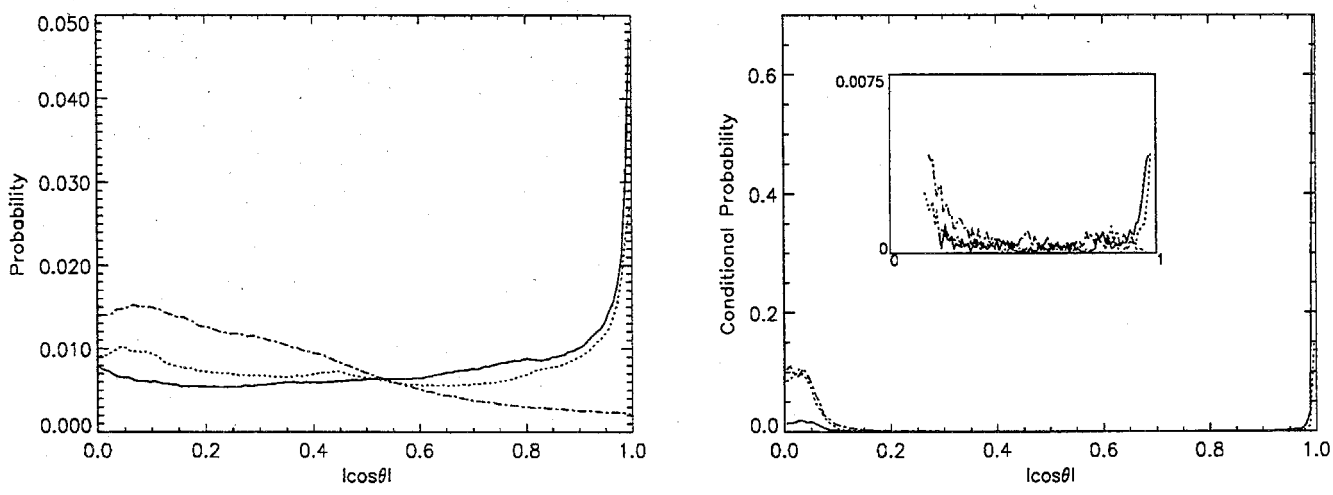

(a) (b)

Figure 3.24: (a) Nonconditional probability distributions (b) Probability distributions conditioned on $\|\omega\| > 30\%\|\omega\|_{max}$ for run3. (1) —— $\mathbf{e}_1$ (2) $-\cdot-\cdot-$ $\mathbf{e}_2$ (3) $\cdots\cdots$ $\mathbf{e}_3$

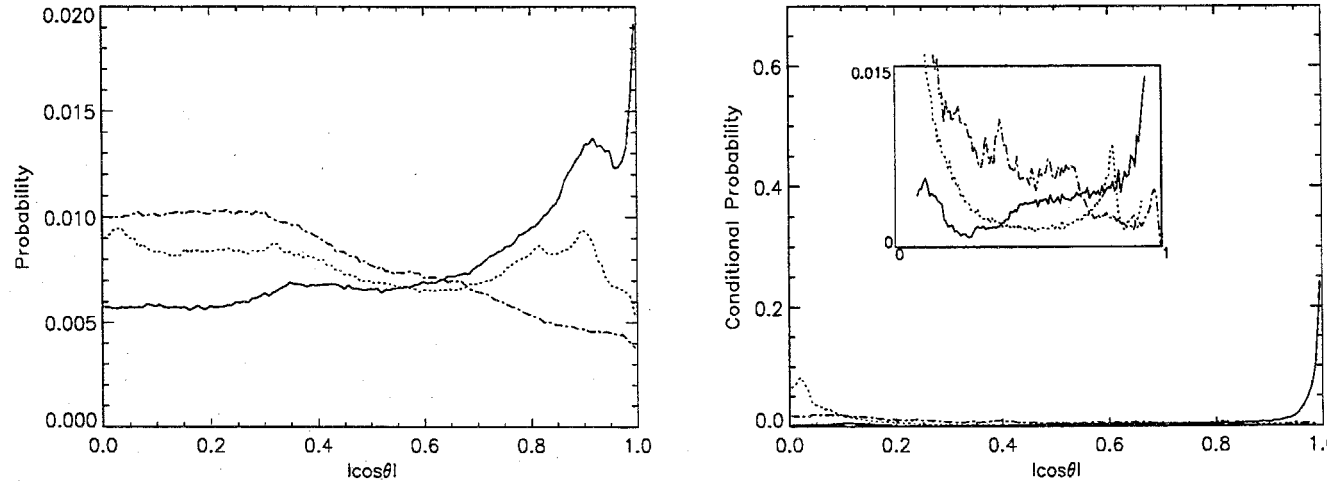

(a) (b)

Figure 3.25: (a) Nonconditional probability distributions (b) Probability distributions conditioned on $\|\omega\| > 30\%\|\omega\|_{max}$ for run4. (1) —— $\mathbf{e}_1$ (2) $-\cdot-\cdot-$ $\mathbf{e}_2$ (3) $\cdots\cdots$ $\mathbf{e}_3$

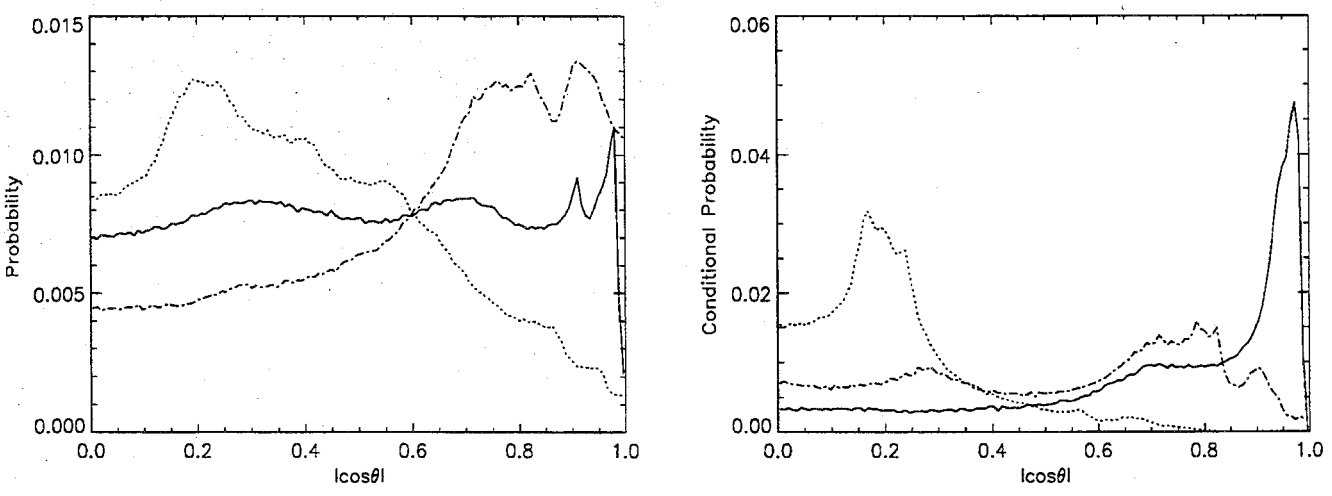

(a) (b)

Figure 3.26: (a) Nonconditional probability distributions (b) Probability distributions conditioned on $\|\omega\| > 30\%\|\omega\|_{max}$ for run5. (1) —— $\mathbf{e}_1$ (2) $-\cdot-\cdot-$ $\mathbf{e}_2$ (3) $\cdots\cdots$ $\mathbf{e}_3$

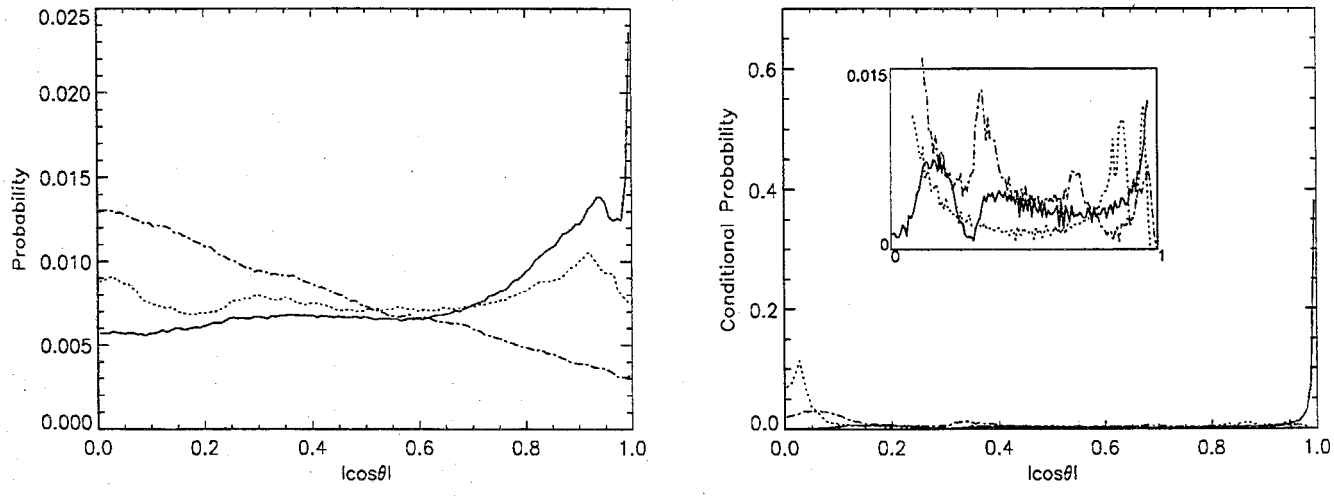

(a) (b)

Figure 3.27: (a) Nonconditional probability distributions (b) Probability distributions conditioned on $\|\omega\| > 30\%\|\omega\|_{max}$ for run6. (1) —— $\mathbf{e}_1$ (2) $-\cdot-\cdot-$ $\mathbf{e}_2$ (3) $\cdots\cdots$ $\mathbf{e}_3$

Chapter 4

Power-Law Energy Decay of Isotropic Homogeneous Turbulence

4.1 Introduction

Grid-generated turbulence was first extensively studied by Batchelor and Townsend [9] [10] [11]. The turbulence, which was nearly isotropic and homogeneous, was observed to have a power-law decay in energy. Batchelor and Townsend distinguished three stages of the decay: an initial period, during which turbulence is being developed, a transition period, and a final period, during which viscous forces are believed to dominate inertial forces throughout the full wave number range. The associated decay exponent was found to be about one for the initial period of decay and 2.5 for the final period. More recent measurements made by Sato and Yamamoto [60] also followed a power-law decay with exponent 2.5 in the final period, but found exponents between 1 and 1.3 for the initial period of decay. Recently Smith et al. [65] measured the decay of enstrophy for towed grid-generated turbulence with grid Reynolds number of order 10^5 without using Taylor's "frozen field" hypothesis. They observed a power-law decay of the rms vorticity with an exponent of 1.5 ± 0.2, corresponding to

a decay exponent of 2 for the turbulent energy.

Results of numerical simulations of turbulence at small Reynolds numbers were studied by Mansour and Wray [44]. Power-law decays were observed and decay exponents between 1.1 and 2.5 were found depending on the Reynolds number and on the behavior of the energy spectrum at low wavenumbers.

On the theoretical side, a number of analyses, based on various assumptions, have been developed to treat decaying homogeneous turbulence. As an example one may start with the hypothesis of complete and/or partial self-similarity of the double and triple velocity correlation functions and use the Kármán-Howarth equation [71] to deduce further results. A detailed study of self-similar solutions of the Kármán-Howarth equation and their stable equilibria can be found in Speziale and Bernard [66] (also see Batchelor [6]). They conclude that completely self-similar solutions always lead to a decay exponent of one, unless the Reynolds number is zero, a state that can be reached only as time goes to infinity.

Partially self-similar solutions, i.e., correlation functions that are self-similar only for some ranges of r, can lead to decay exponents other than one. Some of the criteria required by complete self-similarity must be relaxed and replaced by other assumptions. For example, by relaxing the criterion that the scaling length has to be Taylor's microscale, a decay exponent of 10/7 can be obtained provided Loitsianskii's integral is invariant in time [41] while, on the other hand, an exponent of 6/5 is found if Saffman's invariant is assumed [59].

To predict the power-law decay during the final period, one ignores the inertial force in the energy equation (almost by definition of "final period"). The turbulent energy can then be determined by

$$K \sim \int_0^\infty E(\mathrm{k}, t_o) \exp\left(-2\nu \mathrm{k}^2 (t - t_o)\right) dk, \tag{4.1}$$

where $E(\mathrm{k}, t)$ is the three dimensional energy spectrum, k is the magnitude of the wave vector k and t_o is some reference time. Because of the exponential factor in the integrand, contributions from small wave numbers dominate and a power-law

behavior of $E(\mathrm{k}, t_o)$ near $\mathrm{k} = 0$ results in a power-law decay of turbulent energy. A decay exponent of 2.5 therefore follows from an analytic behavior of $E_{ij}(\mathbf{k}, t_o)$, the energy spectral tensor, near the origin (see [33]), namely,

$$E(\mathrm{k}) \sim C\mathrm{k}^4 + o(\mathrm{k}^4). \tag{4.2}$$

However, Batchelor and Proudman [8] studied the asymptotic form for large separations of the double and triple velocity correlations based on their hypothesis and obtained a non-analytic behavior of the energy spectral tensor near the origin. Saffman subsequently [59] modified the hypothesis and made it less restrictive. He showed, in general, that the double correlation function is $\mathcal{O}(r^{-3})$ for large separation. This corresponds to a non-analytic behavior of energy spectra near the origin with the result

$$E(\mathrm{k}) \sim C\mathrm{k}^2 + o(\mathrm{k}^2). \tag{4.3}$$

The decay exponent then becomes 1.5 for the final period of decay.

The decay problem makes the motivation of the research presented in this chapter. The similarity hypotheses are studied in more details in Sec. 4.2. A new self-similar solution of the Kármán-Howarth equation is proposed based the assumption of of a power-law energy decay. Results of direct numerical simulations are presented and the self-similarity is examined in Sec.4.3. An alternative of the similarity which may be a transitional state during the initial period of decay is discussed in Sec.4.4. Both similarities involve with only one lengthscale, the Taylor microscale. In Sec.4.5 we consider a possible expression of the energy spectrum using multiscales. Multiscales are needed because it is believed that there are more than one characteristic lengthscales involved in a turbulent flow which Reynolds number is large. Part of the idea is further used to predict the skewness of longitudinal velocity derivative and the analysis is given in Sec.4.6. Conclusions of this chapter are given in Sec.4.7.

4.2 Similarity Hypotheses

4.2.1 Theoretical Review

We investigate the energy decay of incompressible turbulent flow which is governed by the Navier-Stokes equations

$$\frac{\partial \mathbf{u}}{\partial t} + \mathbf{u} \cdot \nabla \mathbf{u} = -\nabla p + \nu \nabla^2 \mathbf{u} \tag{4.4a}$$

$$\nabla \cdot \mathbf{u} = 0, \tag{4.4b}$$

where **u** is the turbulent velocity, p is the pressure and ν is the kinetic viscosity. In this paper, we restrict our attention to isotropic homogeneous turbulence. Because of homogeneity, isotropy and the incompressibility, the two-point second-order moment tensors of velocity can be expressed in term of a single scalar function $f(r,t)$, the longitudial velocity correlation coefficient, defined as

$$f(r,t) \equiv \overline{u(\mathbf{x},t)u(\mathbf{x}+\mathbf{r},t)}/q(t)^2, \tag{4.5}$$

where r is the separation of the two points, t is the time, u is the velocity component in the **r**-direction and $\frac{3}{2}q^2$ is the turbulent energy. Similarly $k(r,t)$, the triple velocity correlation coefficient, is defined as

$$k(r,t) \equiv \overline{u(\mathbf{x},t)^2 u(\mathbf{x}+\mathbf{r},t)}/q(t)^3. \tag{4.6}$$

The dynamical equation connecting these two scalar functions derived by Kármán and Howarth [71] from the Navier-Stokes equations is given by

$$\frac{\partial (q^2 f)}{\partial t} = q^3 \left(\frac{\partial k}{\partial r} + \frac{4}{r} k \right) + 2\nu q^2 \left(\frac{\partial^2 f}{\partial r^2} + \frac{4}{r} \frac{\partial f}{\partial r} \right) . \tag{4.7}$$

Kármán and Howarth [71] showed that completely self-similar solutions of the above equation, if they exist, must be of the form

$$f(r,t) = f(r/\lambda(t)) \quad and \quad k(r,t) = k(r/\lambda(t)) \tag{4.8a}$$

and two constraints,

$$q \cdot \lambda = constant \tag{4.8b}$$

and

$$\lambda \frac{d\lambda}{dt} = constant, \tag{4.8c}$$

must be satisfied. Here λ is the Taylor microscale (see [33] [66] [71]) as defined by

$$\lambda^2 \equiv \frac{5 \int_0^\infty E(\mathrm{k}) d\mathrm{k}}{\int_0^\infty \mathrm{k}^2 E(\mathrm{k}) d\mathrm{k}} . \tag{4.9}$$

A power-law decay of the turbulent energy is consequently obtained with the decay exponent equal to one, that is

$$K \equiv \frac{3}{2} q^2 \sim t^{-1}. \tag{4.10}$$

A more general hypothesis of similarity may be formulated such that the decay exponent $\neq$ 1. George [27], instead of assigning a self-similarity of the correlation coefficients, assumed a self-similar energy spectrum, $E(\mathrm{k}, t)$ and energy transfer spectrum, $T(\mathrm{k}, t)$, as follows,

$$E(\mathrm{k}, t) = E_s(t) \tilde{E}(\mathrm{k}\mathcal{L}) \tag{4.11a}$$

$$T(\mathrm{k}, t) = T_s(t) \tilde{T}(\mathrm{k}\mathcal{L}). \tag{4.11b}$$

Substituting into the spectral energy equation for isotropic turbulence

$$\frac{\partial E(\mathrm{k}, t)}{\partial t} = T(\mathrm{k}, t) - 2\nu \mathrm{k}^2 E(\mathrm{k}, t) \tag{4.12}$$

and enforcing consistency, he found

$$\mathcal{L} = \lambda, \tag{4.13a}$$

$$E(\mathrm{k},t)/q^2\lambda = \tilde{E}(\mathrm{k}\lambda), \tag{4.13b}$$

$$T(\mathrm{k},t)/q^3 = Re_\lambda^{-1}\,\tilde{T}(\mathrm{k}\lambda), \tag{4.13c}$$

and an arbitrary decay exponent n. Corresponding results were obtained earlier by Barenblatt and Gavrilov [5] using an equivalent similarity hypothesis for the double and the triple correlation coefficients.

Self-similarity assumptions such as (4.8) or (4.13) imply that for all p, $\lambda^p \frac{\partial^p f}{\partial r^p}\Big|_{r=0}$ is constant. In particular for p=4, we define

$$G \equiv \lambda^4 \frac{\partial^4 f}{\partial r^4}\Big|_{r=0} \tag{4.14}$$

a quantity that appears in the dissipation rate equation. We write the evolution equations for energy, dissipation rate and Re_λ as follows

$$\dot{K} \equiv -\epsilon = -\frac{10\nu K}{\lambda^2}, \tag{4.15a}$$

$$\dot{\epsilon} = \frac{\epsilon^2}{K}\left(\frac{7}{30}SRe_\lambda - \frac{7}{15}G\right) \tag{4.15b}$$

$$\frac{1}{Re_\lambda}\frac{dRe_\lambda}{dt} = -\frac{5\nu}{\lambda^2} + \frac{1}{\lambda}\frac{d\lambda}{dt}, \tag{4.15c}$$

where $S \equiv -\lambda^3 \frac{\partial^3 k}{\partial r^3}\Big|_{r=0}$ is the skewness of longitudinal velocity derivatives. If a power-law decay exists, i.e., there exists an n and a time reference t_o such that

$$K \sim (t+t_o)^{-n} \quad \text{and so} \quad \epsilon \sim (t+t_o)^{-n-1}. \tag{4.16}$$

Equation (4.15b) then implies that the quantity in the bracket has to be a constant. In other words, we must have

$$G = \frac{1}{2}SRe_\lambda + \frac{15}{7}\frac{(n+1)}{n}. \tag{4.17}$$

Therefore, similarity solutions of the form given by (4.8) (constant Re_λ, S and n=1) or of the form given by (4.13) with a Re^{-1}– dependence of skewness S (George's

similarity) imply a constant G during the decay. Although the early-time data from some of the runs are suggestive of a variable S and constant G, our asymptotic results show strongly a linear dependence of G with Re_λ and constant S (see Figs. 4.8 and 4.9).

4.2.2 Proposed Similarity

We propose a more general similarity form for the functions $f(r,t)$ and $k(r,t)$. Based on (4.17), we anticipate a complete similarity given by

$$f(r,t) = f_1(r/\lambda) + Re_\lambda^\beta \; f_2(r/\lambda) \tag{4.18a}$$

and

$$k(r,t) = Re_\lambda^\alpha \; k_2(r/\lambda). \tag{4.18b}$$

Since $f(r,t)$ and $k(r,t)$ are related to $E(\mathrm{k},t)$ and $T(\mathrm{k},t)$ by

$$E(\mathrm{k},t) = \frac{q^2}{\pi} \int_0^\infty \mathrm{k}r(\sin \mathrm{k}r - \mathrm{k}r \cos \mathrm{k}r) f(r,t) \; dr \tag{4.19a}$$

and

$$T(\mathrm{k},t) = \frac{q^3}{\pi} \int_0^\infty \mathrm{k}^2 r \left(\frac{3 \sin \mathrm{k}r}{\mathrm{k}r} - 3 \cos \mathrm{k}r - \mathrm{k}r \sin \mathrm{k}r \right) k(r,t) \; dr, \tag{4.19b}$$

the above hypothesis is equivalent to assuming self-similarity of the energy and energy transfer spectra of the form

$$E(\mathrm{k},t)/q^2\lambda = E_1(\mathrm{k}\lambda) + Re_\lambda^\beta \; E_2(\mathrm{k}\lambda) \tag{4.20a}$$

$$T(\mathrm{k},t)/q^3 = Re_\lambda^\alpha \; T_2(\mathrm{k}\lambda), \tag{4.20b}$$

where E_1, E_2 and T_2 are the self-similar functions related to f_1, f_2 and k_2, respectively.

Substituting (4.18a) and (4.18b) into (4.17) and (4.7) and using relations (4.15a) and (4.15c), we obtain

$$\begin{aligned} G &= \frac{d^4 f_1}{d\zeta^4}\Big|_{\zeta=0} + Re_\lambda^\beta \cdot \frac{d^4 f_2}{d\zeta^4}\Big|_{\zeta=0} \\ &= \frac{15}{7}\frac{(n+1)}{n} - \frac{1}{2}\frac{d^3 k_2}{d\zeta^3}\Big|_{\zeta=0} \cdot Re_\lambda^{\alpha+1} \end{aligned} \tag{4.21}$$

and

$$\begin{aligned} &\{\, 10 f_1 + \frac{5}{n}\zeta\frac{df_1}{d\zeta} + \frac{2}{\zeta^4}\frac{d}{d\zeta}\left(\zeta^4\frac{df_1}{d\zeta}\right)\} \\ &+ Re_\lambda^{\alpha+1} \cdot \frac{1}{\zeta^4}\frac{d}{d\zeta}\left(\zeta^4 k_2\right) \\ &+ Re_\lambda^\beta \cdot \{(10 + 5\beta - \frac{5}{n}\beta) f_2 + \frac{5}{n}\zeta\frac{df_2}{d\zeta} + \frac{2}{\zeta^4}\frac{d}{d\zeta}\left(\zeta^4\frac{df_2}{d\zeta}\right)\} = 0, \end{aligned} \tag{4.22}$$

where $\zeta \equiv r/\lambda$ and $\frac{5}{n} = \frac{\lambda}{\nu}\frac{d\lambda}{dt}$. From (4.21), we require

$$\beta = \alpha + 1, \tag{4.23a}$$

$$\frac{d^4 f_1}{d\zeta^4}\Big|_{\zeta=0} = \frac{15}{7} \cdot \frac{(n+1)}{n} \tag{4.23b}$$

and

$$\frac{d^4 f_2}{d\zeta^4}\Big|_{\zeta=0} = -\frac{1}{2}\frac{d^3 k_2}{d\zeta^3}\Big|_{\zeta=0}. \tag{4.23c}$$

If $\beta = 0$ and so $\alpha = -1$, we recover George's self-similarity [27]. On the other hand, if $\beta \neq 0$, f_1, f_2 and k_2, therefore, must satisfy

$$10 f_1 + \frac{5}{n}\zeta\frac{df_1}{d\zeta} + \frac{2}{\zeta^4}\frac{d}{d\zeta}\left(\zeta^4\frac{df_1}{d\zeta}\right) = 0 \tag{4.24a}$$

and

$$(10 + 5\beta - \frac{5}{n}\beta) f_2 + \frac{5}{n}\zeta\frac{df_2}{d\zeta} + \frac{2}{\zeta^4}\frac{d}{d\zeta}\left(\zeta^4\frac{df_2}{d\zeta}\right) + \frac{1}{\zeta^4}\frac{d}{d\zeta}\left(\zeta^4 k_2\right) = 0. \tag{4.24b}$$

Equation (4.24a) is the same equation as that governing a completely self-similar $f(r/\lambda)$ when the triple correlation coefficient $k(r,t)$ in the Kármán-Howarth relation is ignored (see [4]). It's known that (4.24a) has solutions for all $n \in (0,\infty)$ and function f_1 can be expressed in terms of the regular confluent hypergeometric function M(a,b,z) as

$$f_1(\zeta) = M(n, \frac{5}{2}, -\frac{5}{4n}\zeta^2) \tag{4.25}$$

under the conditions

$$f_1(0) = 1 \quad , \quad f_1(\infty) = 0. \tag{4.26}$$

Moreover,

$$\frac{5}{n} = 5 - \frac{3}{\int_0^\infty \zeta f_1(\zeta) d\zeta} \tag{4.27}$$

provided $f_1 \to 0$ as $\zeta \to \infty$ at least faster than ζ^{-2}.

Although (4.24b) is not closed, we can write f_2 in terms of an integral involving the unknown funtion k_2 as follows:

$$\begin{aligned} f_2(\zeta) \;\; = \;\; - \;\; & M(a,b,z) \int_0^z \frac{U(a,b,z')h(z')}{M(a,b,z')U'(a,b,z') - M'(a,b,z')U(a,b,z')} dz' \\ + \;\; & U(a,b,z) \int_0^z \frac{M(a,b,z')h(z')}{M(a,b,z')U'(a,b,z') - M'(a,b,z')U(a,b,z')} dz' \;, \end{aligned} \tag{4.28a}$$

with

$$z \equiv -\frac{5}{4n}\zeta^2 \;, \qquad a \equiv n + \frac{\beta(n-1)}{2} \;, \qquad b \equiv 5/2 \;, \tag{4.28b}$$

and

$$h(z) \equiv -\frac{2n^2}{25} \cdot \left(\frac{5k_2(\zeta)}{\zeta^3} + \frac{1}{\zeta}\frac{d}{d\zeta}\left(\frac{k_2(\zeta)}{\zeta}\right) \right) \tag{4.28c}$$

under the conditions

$$f_2(0) = 0 \quad , \quad f_2(\infty) = 0, \tag{4.29}$$

where $U(a, b, z)$ is the singular confluent hypergeometric function and $k_2(\zeta)$ is taken to be an odd function of ζ. Expanding (4.24b) about $\zeta = 0$ with (4.29), we find that

$$f_2(\zeta) \sim -\frac{1}{48}\frac{d^3k_2}{d\zeta^3}\Big|_{\zeta=0} \cdot \zeta^4 + \mathcal{O}(|\zeta|^6). \tag{4.30}$$

Condition (4.23c) is therefore satisfied implicitly. Condition (4.23b) follows by differentiating (4.24a) twice and evaluating the results at $\zeta = 0$. We now have a consistent theory with two free parameters n and β (or α), and one function that must be determined.

In some cases it is possible to fix n by using the asymptotic behaviors of $f_1(\zeta)$ and $f_2(\zeta)$ as $\zeta \to \infty$ predicted by earlier investigators ([8] [59]). In particular, consider Saffman's result [59] that $f(r, t)$ in general has a power-law asymptotic behavior, given by

$$f(r, t) \sim r^{-3} \quad as \quad r \to \infty. \tag{4.31}$$

The asympototic behaviors of functions $f_1(\zeta)$ and $f_2(\zeta)$ can be obtained from (4.25) and (4.28a). As $\zeta \to \infty$, it can be shown that

$$f_1(\zeta) \sim \zeta^{-2n}, \tag{4.32a}$$

and

$$f_2(\zeta) \sim \zeta^{-(2n+\beta(n-1))}. \tag{4.32b}$$

provided those integrals involved with $k_2(\zeta)$ in the solutions of f_2 converge rapidly enough. Solutions of f_1 corresponding to several values of n within interest are shown in Fig. 4.1 They are found everywhere positive implying from (4.27) $n \geq 1$. With $n \geq 1$ and $\beta \geq 0$ ($\alpha \geq -1$), we obtain

$$f(r, t) \sim f_1(\zeta) \sim \zeta^{-2n} \quad as \quad \zeta \to \infty, \tag{4.33}$$

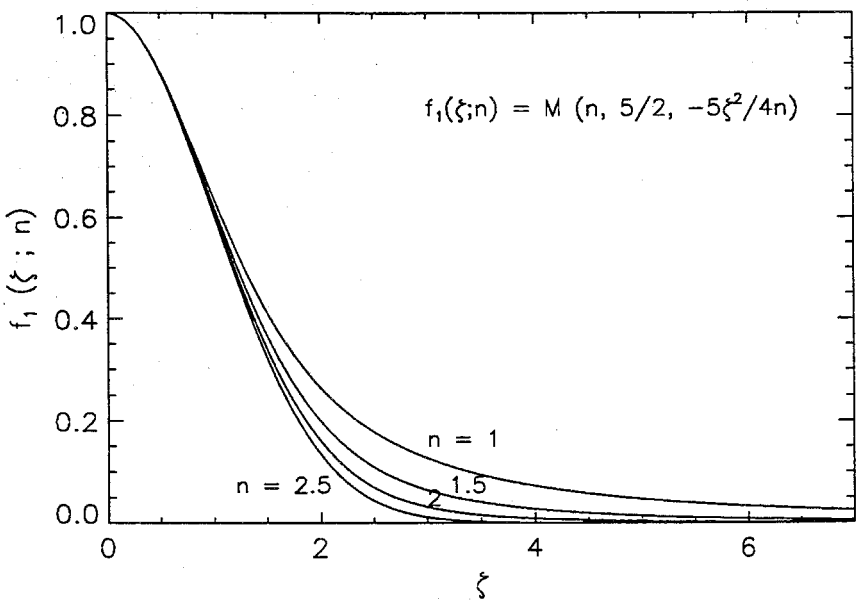

Figure 4.1: Confluent hypergeometric function $f_1(\zeta) = M(n, 5/2, -\frac{5}{4n}\zeta^2)$ with n = 1, 1.5, 2, and 2.5. $f_1(0) = 1$ and $f_1(\zeta) \to \zeta^{-2n}$ as $\zeta \to \infty$.

giving n = 1.5 if we envoke (4.31).

In summary, a complete similarity hypothsis of the velocity correlation coefficients given by

$$f(r,t) = M\left(n, \frac{5}{2}, -\frac{5}{4n}(\frac{r}{\lambda})^2\right) + Re_\lambda^\beta\ f_2(\frac{r}{\lambda}) \tag{4.34a}$$

and

$$k(r,t) = Re_\lambda^{\beta-1}\ k_2(\frac{r}{\lambda}) \tag{4.34b}$$

is proposed with f_2 and k_2 related by (4.28).

4.3 Numerical Simulations

4.3.1 Algorithmic Implementation

We perform direct numerical simulations of the decay problem by using Fourier-Spectral method presented in chapter 2. To save the memory on the disk, we write the governing equations in the following form:

$$u_t + (u^2 - v^2)_x + (uv)_y + (uw)_z = -(P + v^2)_x + \nu\nabla^2 u \tag{4.35}$$

$$v_t + (uv)_x + (vw)_z = -(P + v^2)_x + \nu\nabla^2 v \tag{4.36}$$

$$w_t + (uw)_x + (vw)_y + (w^2 - v^2)_z = -(P + v^2)_x + \nu\nabla^2 w, \tag{4.37}$$

where $\mathbf{u} = (u, v, w)$ and the subscript means the partial derivative in the specified direction. Thus we only need store $u^2 - v^2$, uv, uw, vw, and $w^2 - v^2$ in memory. Given an initial condition, solutions at later time are now available through the use of the solver discussed in chapter 2.

Due to the nonlinearity, we estimate the stability of the linearized equations; that is, we "freeze" the velocity components in the nonlinear terms, i.e.,

$$f_i \equiv |u_j| \frac{\partial u_i}{\partial x_j} \tag{4.38}$$

or

$$\widehat{f_i} \equiv |u_j| i k_j \widehat{u}_i, \tag{4.39}$$

and study the scheme stability. Empirical results are then relied on to obtain a stable scheme for the nonlinear equations. The linearized spectral Navier-Stokes equations are

$$\frac{\partial \widehat{u}_i}{\partial t} + (\delta_{ij} - \frac{k_i k_j}{k^2}) i k_r |u_r| \widehat{u}_j + \nu k^2 \widehat{u}_i = 0. \tag{4.40}$$

To study stability, we set $\widehat{u}_i(\mathrm{k},t) = \widehat{u}_i^o(\mathrm{k})e^{\lambda t}$ and substitute the result into (4.40) to obtain

$$(\lambda + \nu k^2)\widehat{u}_i^o + (\delta_{ij} - \frac{k_i k_j}{k^2})ik_r|u_r|\widehat{u}_j^o = 0. \tag{4.41}$$

The eigenvalues, λ, are readily found as

$$\begin{aligned} \lambda_1 &= -\nu k^2 \\ \lambda_{2,3} &= -\nu k^2 - i(k_1|u_1| + k_2|u_2| + k_3|u_3|). \end{aligned} \tag{4.42}$$

Therefore, we may choose the time increment to be

$$dt \equiv \frac{CFL}{(k_{1max}|u_1| + k_{2max}|u_2| + k_{3max}|u_3|)}, \tag{4.43}$$

where CFL is the Courant number (Courant-Friedrichs-Lewy). Since $k_{imax} = \frac{N_i}{2}\ \frac{2\pi}{L_i}$, where N_i is the resolution and L_i is the domain dimension in i^{th} direction, (4.43) becomes

$$dt \equiv \frac{CFL}{\pi}\left(\frac{N_1}{L_1}|u_1| + \frac{N_2}{L_2}|u_2| + \frac{N_3}{L_3}|u_3|\right)^{-1}. \tag{4.44}$$

In the solver, the value of CFL is fixed and a maximum value of the quantity in the bracket is evaluated at every time step. Experience suggests a value of $CFL \leq 1$ is necessary for the stability of Rogallo's solver.

4.3.2 Initial Conditions

Again all simulations start from a random velocity field in a periodic domain of size L on a side, with a specified initial energy spectrum. Initial energy spectra were chosen from

$$E(\mathrm{k}, t=0) = 16\sqrt{\frac{2}{\pi}}\frac{q^2}{k_p}\left(\frac{\mathrm{k}}{k_p}\right)^4 \exp\left(-2\,(\frac{\mathrm{k}}{k_p})^2\right), \tag{4.45a}$$

or

$$E(\mathrm{k}, t=0) = \begin{cases} Cq^2 \exp(-a)(\mathrm{k}/k_p)^2 & \text{for } 0 \le \mathrm{k} \le k_p \ ; \\ Cq^2(\mathrm{k}/k_p)^{-5/3} \exp\left(-a\ \mathrm{k}/k_p\right) & \text{for } \mathrm{k} \ge k_p \ , \end{cases} \tag{4.45b}$$

or

$$E(\mathrm{k}, t=0) = \frac{3}{2}\frac{q^2}{k_p}\left(\frac{2\mathrm{k}}{k_p}\right)^2 \exp\left(-\frac{2\mathrm{k}}{k_p}\right) \tag{4.45c}$$

where all spectra have a peak at $\mathrm{k} = k_p$. Parameters used in each simulation and certain dynamical quantities at the initial time and at the time the power-law decay appears to begin are listed in Table 4.1. Included are the product of the maximum available wave number $k_{max} = \frac{\sqrt{2}N}{3} \cdot \frac{2\pi}{L}$ (N is the resolution, i.e., the number of grid points in each direction) and Kolmogorov's dissipation lengthscale η, Re_λ, the eddy turnover time, and the eddy dissipation time. The eddy-turnover time, $\mathcal{T}_o$, and the dissipation time scale, τ_η, are defined as

$$\mathcal{T}_o \equiv \frac{3\pi}{4q}\int_0^\infty \mathrm{k}^{-1}E(\mathrm{k}, t)\ d\mathrm{k} \Big/ \int_0^\infty E(\mathrm{k}, t)\ d\mathrm{k} \tag{4.46}$$

and

$$\tau_\eta \equiv \eta^2/\nu \tag{4.47}$$

respectively.

Note that to produce reasonably high Re_λ when the turbulence reaches the state of power-law decay, the initial values of $k_{max}\eta$ are chosen relatively small giving rather poor resolution during the initial stage of development. However, we do not use the data from this stage.

4.3.3 Power-Law Decay

The evolutions of turbulent energy K and those of Re_λ are shown in Fig. 4.2ab and Fig. 4.3ab. The existence of a power-law decay is clear. The solid lines are the fitted curves of the form

$$K = K_o(t + t_o)^{-n} \tag{4.48}$$

Table 4.1: Initial Conditions and conditions at the beginning of power-law decay.

	run1	run2	run3	run4	run5	run6
L	2π	4π	2π	2π	4π	2π
E(k,0)	(4.45a)	(4.45a)	(4.45b)	(4.45b)	(4.45c)	(4.45c)
k_p	10	10	4	8	6	6
ν	0.0015	0.0015	0.002	0.0004	0.0013	0.003
N	128	256	128	256	256	128

time = 0

Re_λ	133.3	133.3	203.1	347.9	165.5	71.6
$k_{max}\eta$	0.53	0.53	0.40	0.39	0.51	0.78
λ/L	3%	1.6%	3%	2%	2%	3%
$\mathcal{T}_o$	0.59	0.59	0.22	0.22	0.40	0.40

time = power-law decay begins

$k_{max}\eta$	1.09	1.09	1.07	0.99	1.03	0.98
Re_λ	21.52	21.65	42.29	49.59	42.62	29.34
λ/L	2.6%	1.3%	3.6%	1.8%	1.7%	2.7%
$\mathcal{T}_o$	1.91	1.84	2.09	2.80	2.89	1.02
τ_η	0.22	0.22	0.16	0.17	0.22	0.09

Table 4.2: The decay exponents, n, and the time reference t_o in (4.48) which provide a best fitted curve to the numerical data.

	run1	run2	run3	run4	run5	run6
n	1.56	1.51	1.54	1.23	1.27	1.22
t_o	0.40	0.064	0.03	-1.28	0.45	0.21
K_o	0.31	0.26	1.71	0.24	0.65	0.38

with choices of K_o, t_o, and n which give the least square errors to those data between times during which $k_{max}\eta \geq 1$ and $\lambda/L \leq 0.1$. In Fig. 4.3ab the solid lines represent Re_λ in terms of the power-law parameters determined from Fig. 4.2ab so that

$$Re_\lambda(t) = \sqrt{\frac{20K_o}{3\nu n}}\ (t+t_o)^{(1-n)/2}\,. \tag{4.49}$$

The decay exponents, n, and the time reference, t_o, are presented in Table 4.2. Except for run3 these decay exponents are consistent with the findings of Mansour and Wray [44]. From Fig.6b of their paper, we might have predicted an exponent closer to 1 for run3 (relatively high Re_λ and k^2 low wavenumber spectrum). For power-law decay we expect $\lambda^2 = \frac{10\nu(t+t_o)}{n}$. The asymptotic time-independence of $\lambda/\sqrt{t+t_o}$ is shown in Fig. 4.4ab. In these figures the numerical data in some cases deviate from the fitted curves at large times. We believe that this occurs because the large eddies eventually become too large relative to the box size. Note run1 (Fig. 4.2a) shows this effect whereas run2 with twice the box dimension but the same initial spectrum as run1 does not show this effect.

Before we can compare the numerical results with isotropic turbulence theories, we need to check the extent of isotropy of the turbulence. Consider the one dimensional energy spectrum defined as

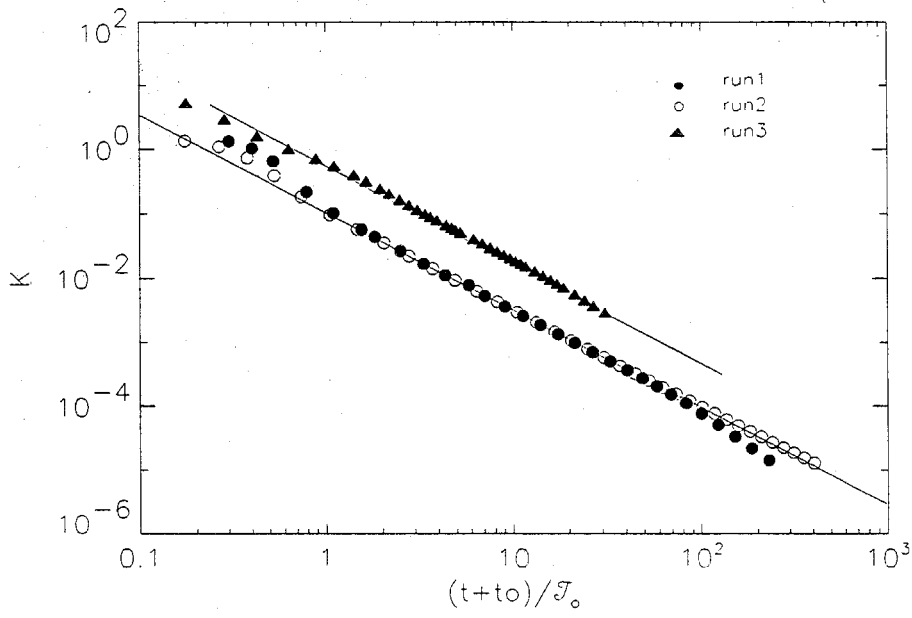

Figure 4.2a: The decay of turbulent energy $K = 3q^2/2$. The time is nondimensionalized by the eddy turnover time $\mathcal{T}_o$ at $k_{max}\eta \approx 1$.

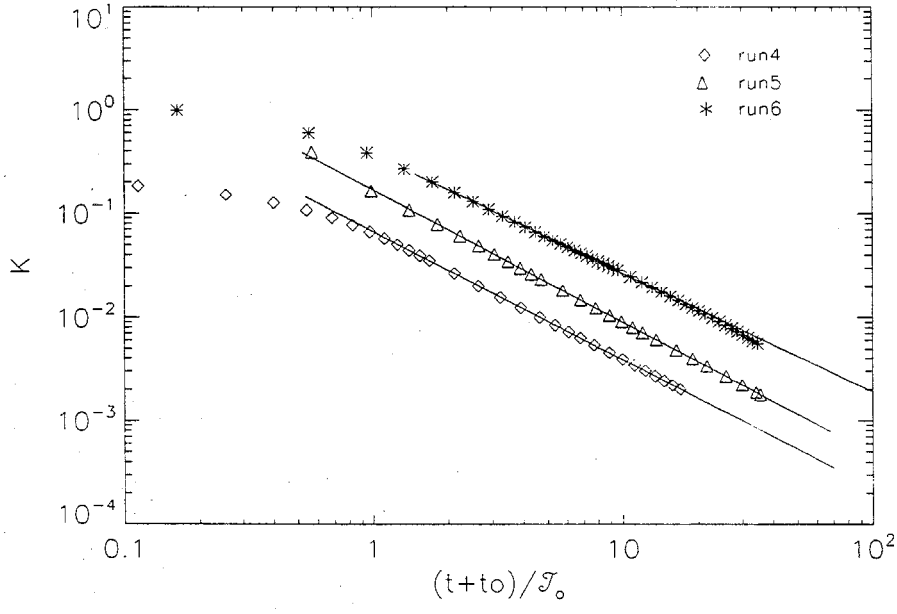

Figure 4.2b: The decay of turbulent energy $K = 3q^2/2$. The time is nondimensionalized by the eddy turnover time $\mathcal{T}_o$ at $k_{max}\eta \approx 1$.

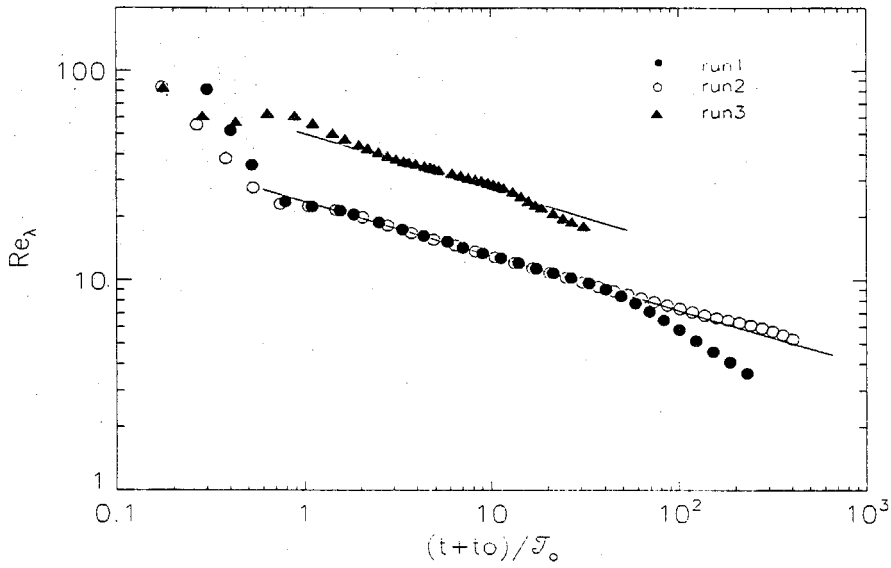

Figure 4.3a: The decay of $Re_\lambda = q\lambda/\nu$. Solid lines are the fitted curves $Re_\lambda = \sqrt{\frac{20K_o}{3\nu n}}\,(t+t_o)^{(1-n)/2}$ with n, t_o, and K_o given in Table 4.2.

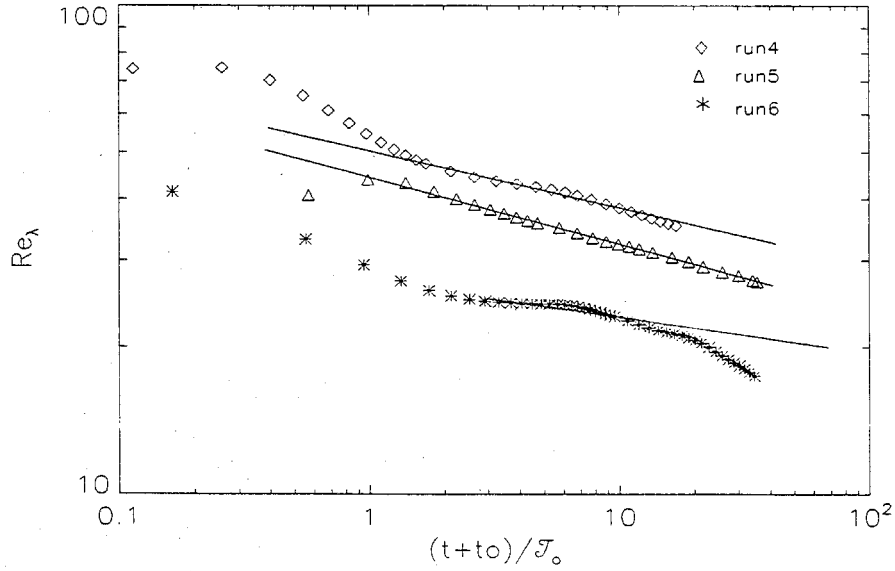

Figure 4.3b: The decay of $Re_\lambda = q\lambda/\nu$. Solid lines are the fitted curves $Re_\lambda = \sqrt{\frac{20K_o}{3\nu n}}\,(t+t_o)^{(1-n)/2}$ with n, t_o, and K_o given in Table 4.2.

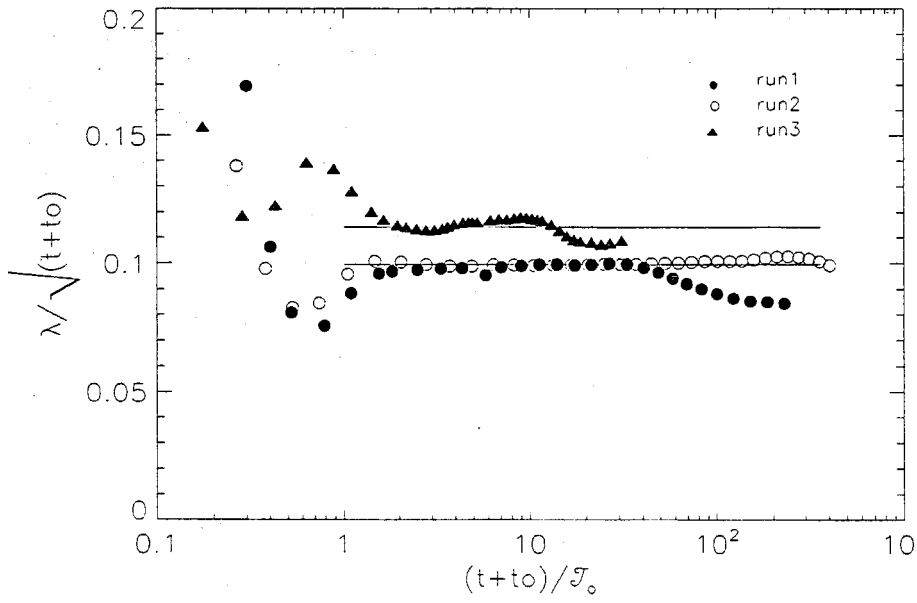

Figure 4.4a: The evolution of $\lambda/(t+t_o)^{1/2}$. Horizontal lines are $\sqrt{10\nu/n}$ with n given in Table 4.2.

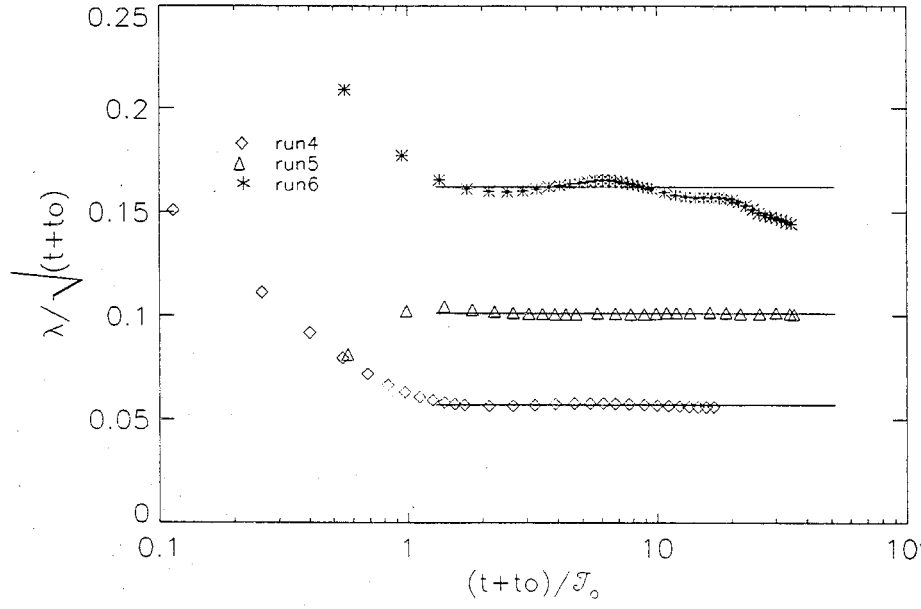

Figure 4.4b: The evolution of $\lambda/(t+t_o)^{1/2}$. Horizental lines are $\sqrt{10\nu/n}$ with n given in Table 4.2.

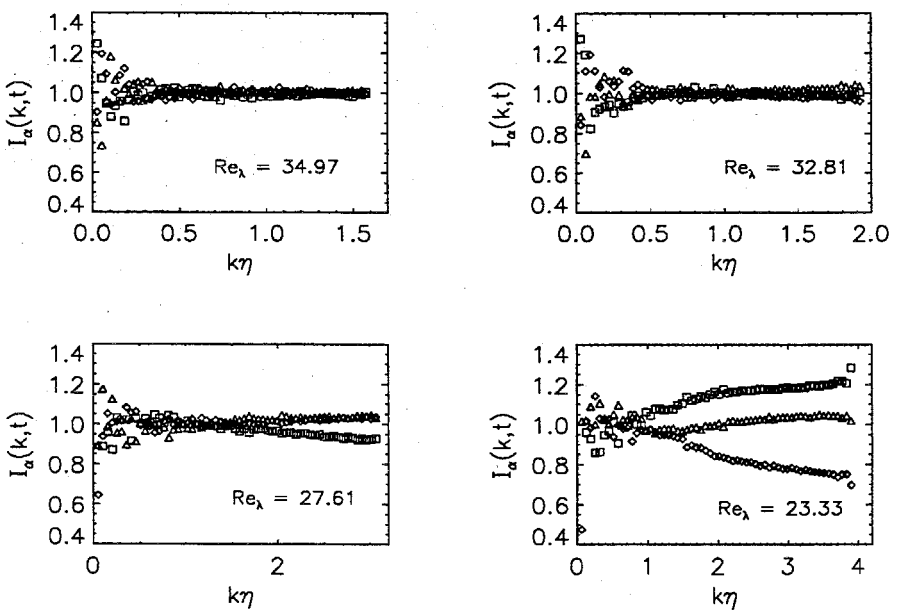

Figure 4.5a: The extent of isotropy of turbulence indicated by $I_\alpha(k,t)$ for run3 which $L = 2\pi$.

$$E_\alpha(\mathrm{k},t) \equiv \frac{1}{2}\sum_{|\mathbf{k}|=\mathbf{k}} \hat{u}_\alpha \hat{u}^*_\alpha(\mathbf{k},t), \tag{4.50}$$

where $\alpha = 1, 2, 3$. The extent of isotropy is measured by $I_\alpha(\mathrm{k},t)$ defined as

$$I_\alpha(\mathrm{k},t) \equiv 3E_\alpha(\mathrm{k},t)/E(\mathrm{k},t). \tag{4.51}$$

For isotropic turbulent flow, we expect $I_\alpha(\mathrm{k},t)$ to be close to one. The distributions of $I_\alpha(\mathrm{k},t)$ over the wave number k at several Re_λ are shown in Fig. 4.5ab. The large-scale eddies are never isotropic while the small-scale eddies lose isotropy as Reynolds number decreases. Eddies of intermediate sizes possess the isotropy longer. This anisotropy should be kept in mind for the discussions below.

4.3.4 Velocity Correlation Coeficients

In Fig. 4.6 and Fig. 4.7 we show the double and triple velocity correlation coefficients, $f(r,t)$ and $k(r,t)$ for run2. The correlations are obtained by computing the

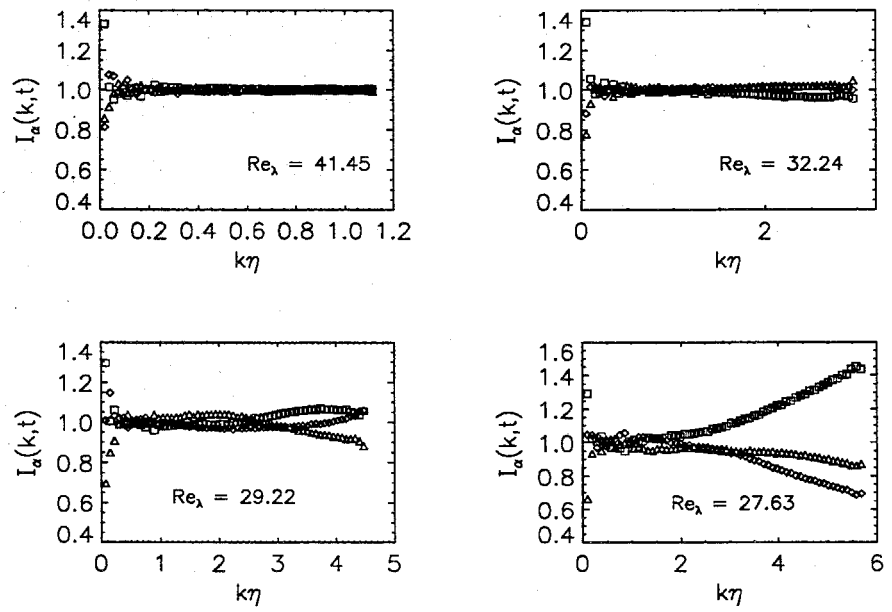

Figure 4.5b: The extent of isotropy of turbulence indicated by $I_\alpha(k,t)$ for run5 which $L = 4\pi$.

velocity structure function

$$\Delta u_\alpha(r) \equiv u_\alpha(\mathbf{x} + r\mathbf{e}_\alpha) - u_\alpha(\mathbf{x}), \tag{4.52}$$

where $\mathbf{e}_\alpha$, $\alpha = 1, 2, 3$, are the unit vectors in the Cartersian coordinates, and using the isotropic relations (in spite of the anisotropy observed above)

$$f(r,t) = 1 - \overline{\Delta u(r)^2}/2q^2 \tag{4.53}$$

and

$$k(r,t) = \overline{\Delta u(r)^3}/6q^3 \ . \tag{4.54}$$

Averaging is taken over the full volume and over the three directions.

The double correlations can also be obtained by measuring the one dimensional energy spectra and taking the Fourier transform. We found the results agree with

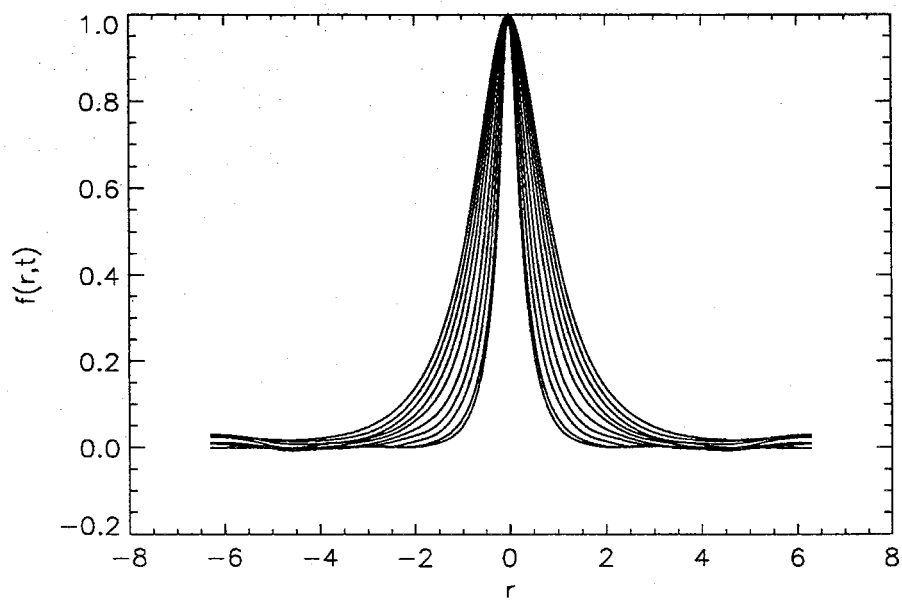

Figure 4.6: Double velocity correlation coefficient $f(r,t)$ against r for run2. Correlations increase as simulated time increases.

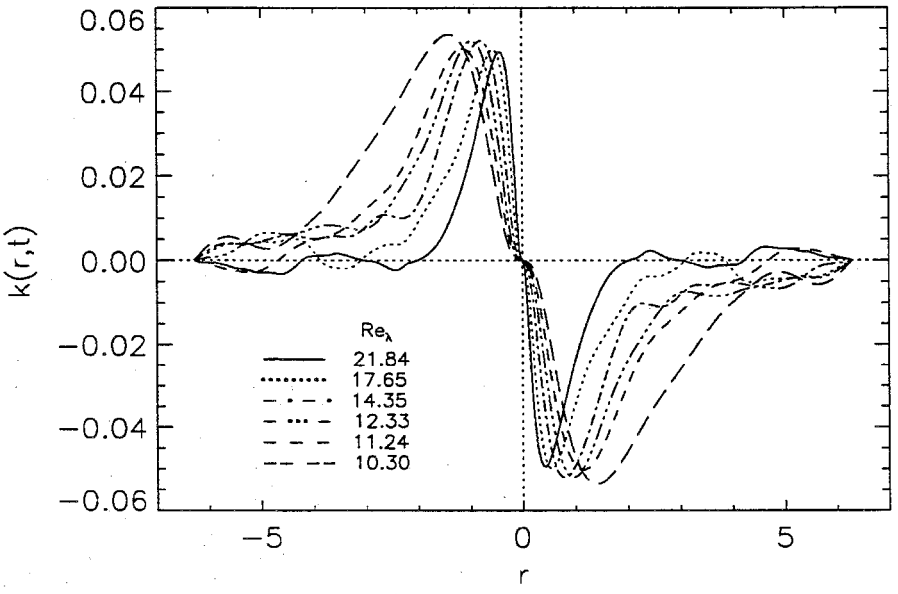

Figure 4.7: Triple velocity correlation coefficient $k(r,t)$ against r for run2.

the relation (4.53) very well. The zeros of $k(r,t)$ at $r = 0,\ \pm\frac{L}{2}$ come directly from (4.54) and the periodicity of the flow field.

The relatively high values of function $f(r,t)$ shown in Fig. 4.6 for $r \approx L/2$ ($= 2\pi$) at later times indicate the box-size contamination once again. The persistence of the peak values of function $k(r,t)$ implies the presence of the inertial forces for all time and so the so-called final period of decay is not observed in the range of Re_λ investigated in agreement with Mansour and Wray [44].

In the present study, the quantities G and S are computed as

$$G = \frac{2}{35}\frac{\lambda^4}{q^2}\int_0^\infty \mathrm{k}^4 E(\mathrm{k},t)d\mathrm{k} \tag{4.55}$$

and

$$S = -\frac{6\sqrt{15}}{7}\ \frac{\int_0^\infty \mathrm{k}^2 T(\mathrm{k},t)d\mathrm{k}}{\left(2\int_0^\infty \mathrm{k}^2 E(\mathrm{k},t)d\mathrm{k}\right)^{3/2}}. \tag{4.56}$$

From the relation (4.17) with computed Re_λ, G and S, we can also compute the decay exponent as follows:

$$n^{-1} = \frac{7}{15}\left(G - \frac{1}{2}SRe_\lambda\right) - 1. \tag{4.57}$$

These three quantities are all plotted as a function of Re_λ in the range investigated (see Figs. 4.8, 4.9, and 4.10). Again, only those data between times during which $k_{max}\eta \geq 1$ and $\lambda/L \leq 0.1$ are plotted. In this way we obtain a reasonable representation of the dissipation range and minimize the contamination due to periodicity. Except for some transitional early-time behavior, a nearly linear dependence on Re_λ of G and a nearly constant S are observed for each run during the decay, implying $\beta \approx 1$. Note also included in Fig. 4.8 is the data taken from Fig.16 of Yeung and Pope [72] for stationary turbulence.

Because the data from run1, run2, and run3 yield nearly the same decay exponents (see Table 4.2), we group them as a whole with an average n=1.54. Similarly, we group

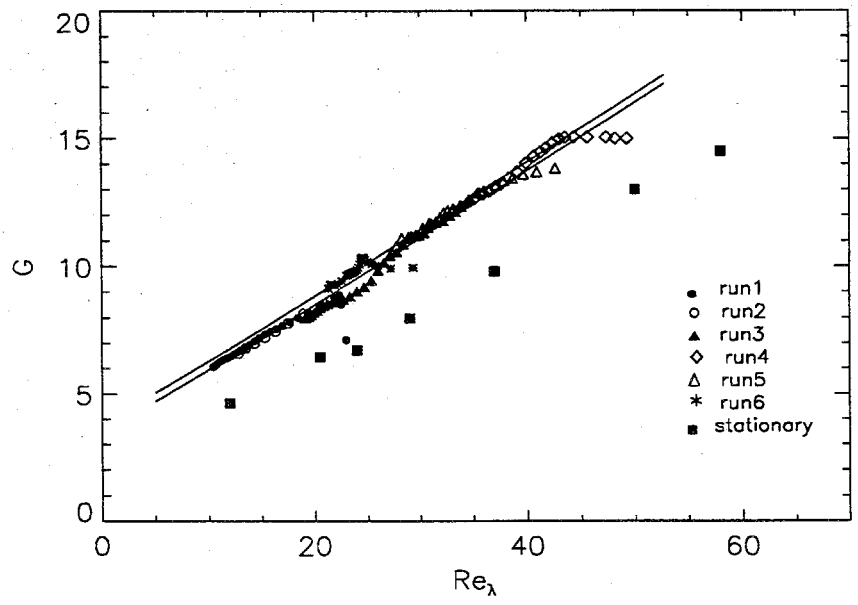

Figure 4.8: G plotted as a function of Re_λ during $k_{max}\eta \geq 1$ and $\lambda/L \leq 0.1$. Symbol ■ represents those data measured by Yeung and Pope [72] for stationary turbulence. The lower solid line is eqn. (4.17) with n=1.54 while the upper one with n=1.24.

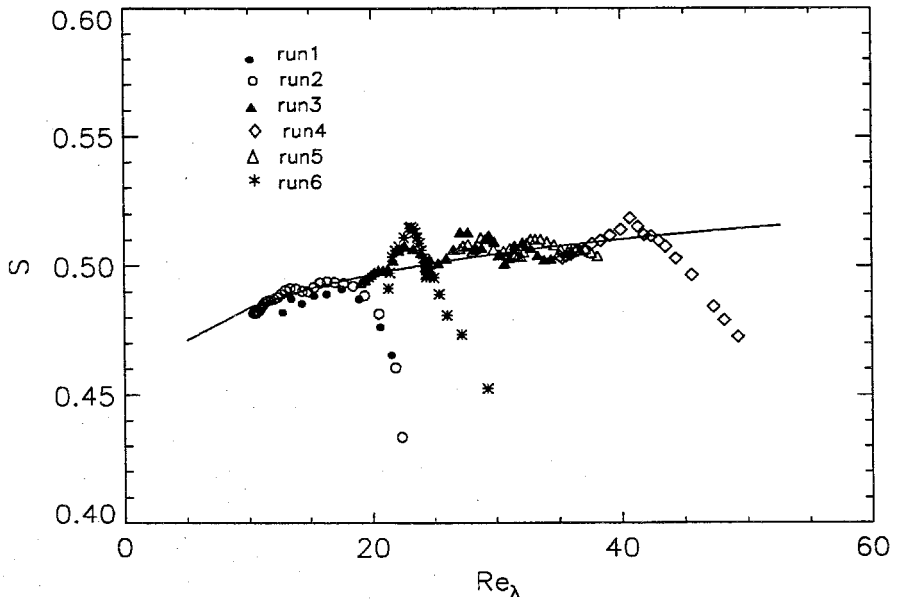

Figure 4.9: S plotted as a function of Re_λ during $k_{max}\eta \geq 1$ and $\lambda/L \leq 0.1$. The solid line is the fitted curve of the form $S = CRe_\lambda^{\beta-1}$ with $C = 0.44$ and $\beta = 1.04$.

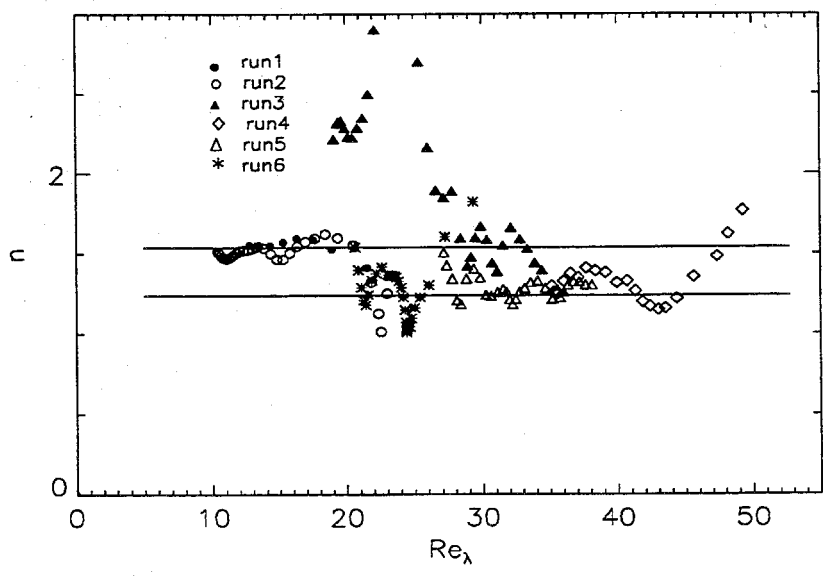

Figure 4.10: The decay exponent n calculated by using eqn.(4.57) plotted as a function of Re_λ during $k_{max}\eta \geq 1$ and $\lambda/L \leq 0.1$. Horizontal lines represent decay-exponents of 1.24 and 1.54.

run4, run5, and run6 with an average n=1.24. These two average decay exponents are shown in Fig. 4.10 as horizontal lines. Except for the results of run3, which show a significant amount of scatter, the decay exponents from Table 4.2 are in good agreement with those computed from (4.57) giving assurance that we are observing isotropic, power-law decay.

The data for S in Fig. 4.9 could be described by $S \approx$ constant ≈ 0.50 or

$$S \sim Re_\lambda^{\beta-1} \tag{4.58}$$

with $\beta = 1.04$ as shown. With the latter fit and using the two decay exponents discussed above, we plot two curves for G given by (4.17) in Fig. 4.8. Again we see consistency with the results for G computed directly by (4.55). Use of $S = 0.50$ rather makes only a slight change in the curves shown in Fig. 4.8.

Finally, we attempt to test the similarity of the form proposed, that is, to test the existence of the self-similar functions $f_2(r/\lambda)$ and $k_2(r/\lambda)$. Note to determine $f_2(r/\lambda)$

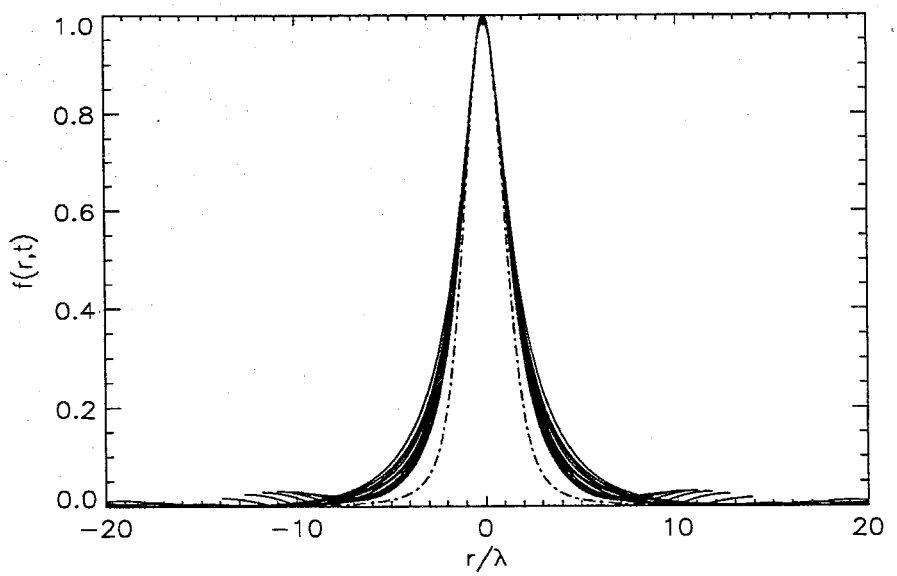

Figure 4.11a: Double velocity correlation coefficients $f(r/\lambda, t)$ against r/λ for run2 (solid lines) and the regular confluent hypergeometric function $M(n, 5/2, -5\zeta^2/4n)$ with n=1.54, where $\zeta = r/\lambda$ (dash dotted line).

and $k_2(r/\lambda)$ we need to know β and n. From the above discussion, $\beta = 1.04$ should apply to all runs and Reynold numbers investigated, but two distinct decay exponents are observed, one for each group of runs. Runs in the same group are then expected to possess the same self-similar functions f_2 and k_2. To minimize the contamination due to periodicity, we use only the 256^3 runs within each group, run2 with n=1.54 and run4 and run5 with n=1.24.

In Fig. 4.11abc we show double velocity correlation coefficients f as a function of r/λ for the three runs. Fig. 4.12ab shows the result of subtracting $f_1(r/\lambda)$ from $f(r/\lambda, t)$. Next we divide the above results by Re_λ^β to obtain our estimate for $f_2(r/\lambda)$ for the two cases. This is shown in Fig. 4.13ab. Although some spread in the curves persists, it is clearly reduced from the spread shown in Fig. 4.12ab. The difference between the f_2 functions of the two cases is clearly much larger than its spread in each.

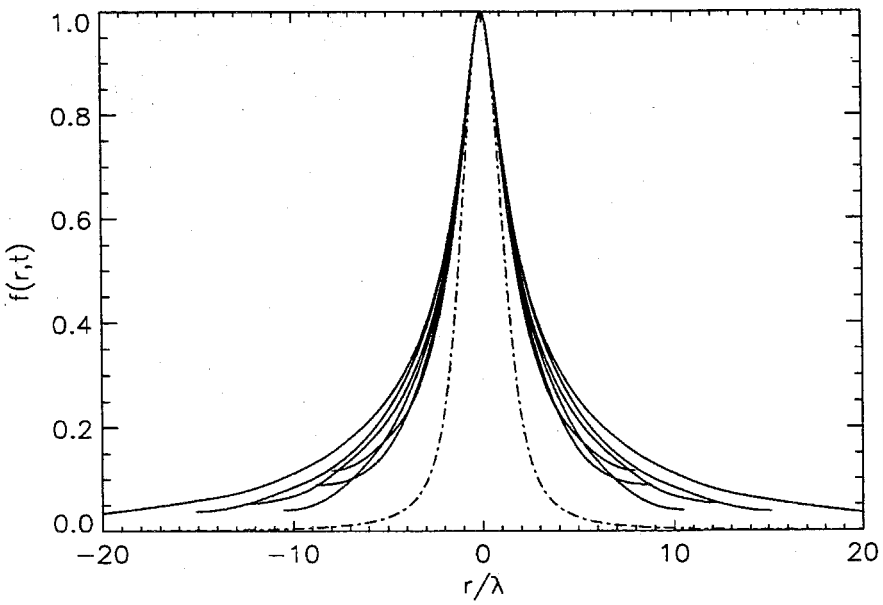

Figure 4.11b: Double velocity correlation coefficients $f(r/\lambda, t)$ for run4 against r/λ (solid lines) and the regular confluent hypergeometric function $M(n, 5/2, -5\zeta^2/4n)$ with n=1.24, where $\zeta = r/\lambda$.

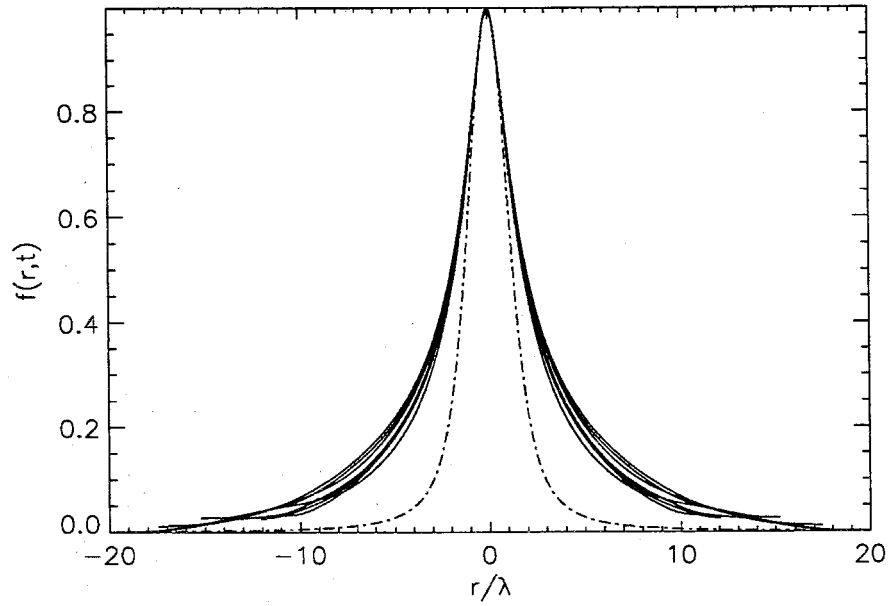

Figure 4.11c: Double velocity correlation coefficients $f(r/\lambda, t)$ against r/λ for run5 (solid lines) and the regular confluent hypergeometric function $M(n, 5/2, -5\zeta^2/4n)$ with n=1.24, where $\zeta = r/\lambda$.

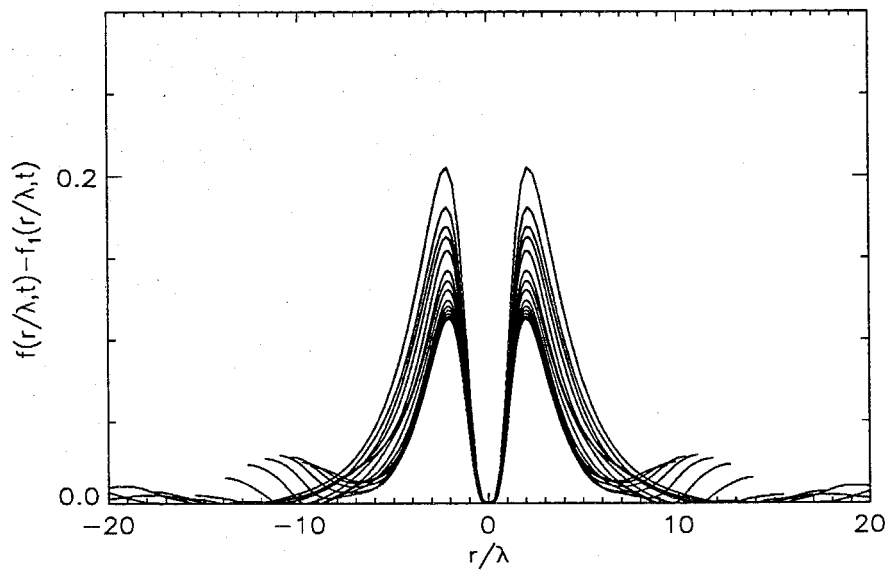

Figure 4.12a: The difference between the double correlation coefficients and the solution of f_1 in the similarity form of $f = f_1 + Re_\lambda{}^\beta f_2$, namely $f(r/\lambda, t) - f_1(r/\lambda)$, for run2.

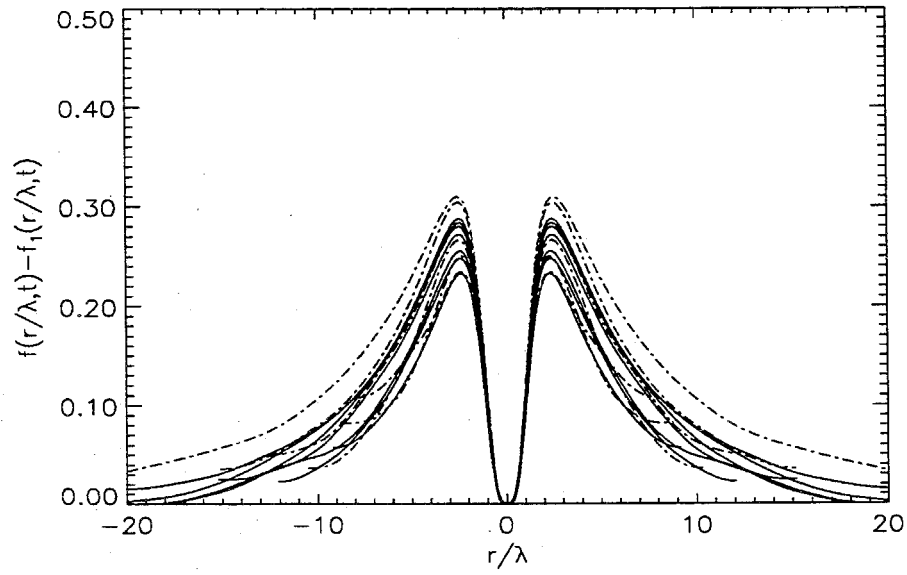

Figure 4.12b: The difference between the double correlation coefficients and the solution of f_1 in the similarity form of $f = f_1 + Re_\lambda{}^\beta f_2$, namely $f(r/\lambda, t) - f_1(r/\lambda)$, for run4 (dash dotted lines) and run5 (solid lines).

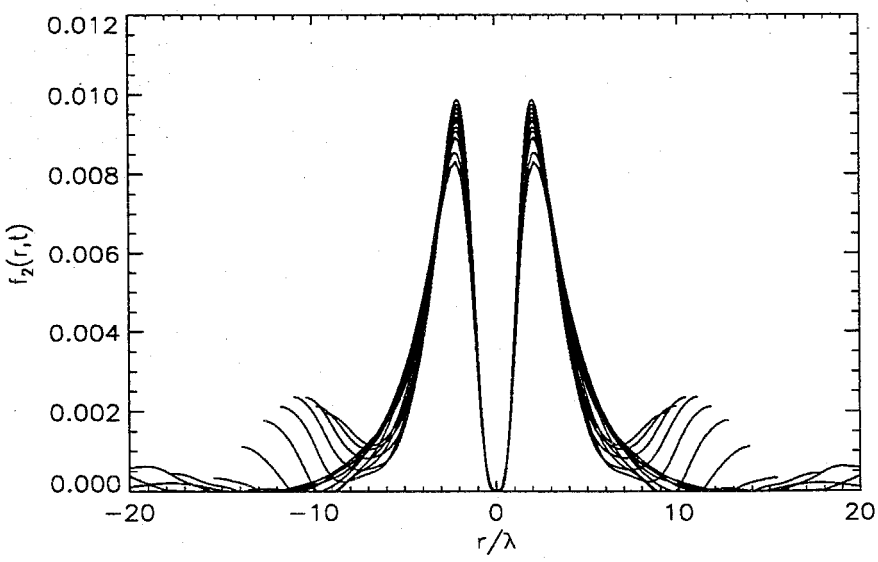

Figure 4.13a: $f_2(r/\lambda)$ for run2 by first subtracting the solution of f_1 with $n = 1.54$ from the measured double correlation coefficients f and then divided by $Re_\lambda{}^\beta$ with $\beta = 1.04$.

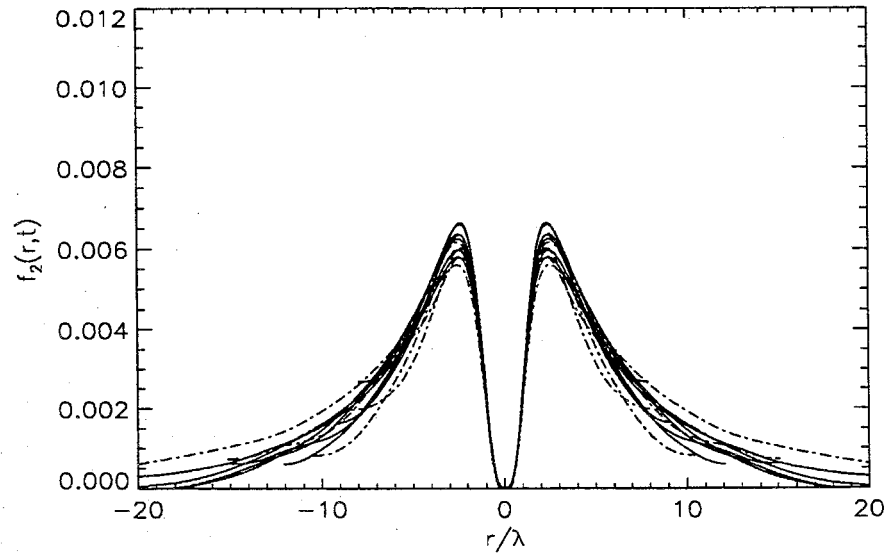

Figure 4.13b: $f_2(r/\lambda)$ for run4 (dash dotted lines) and run5 (solid lines) by first subtracting the solution of f_1 with $n = 1.54$ from the measured double correlation coefficients f and then divided by $Re_\lambda{}^\beta$ with $\beta = 1.04$.

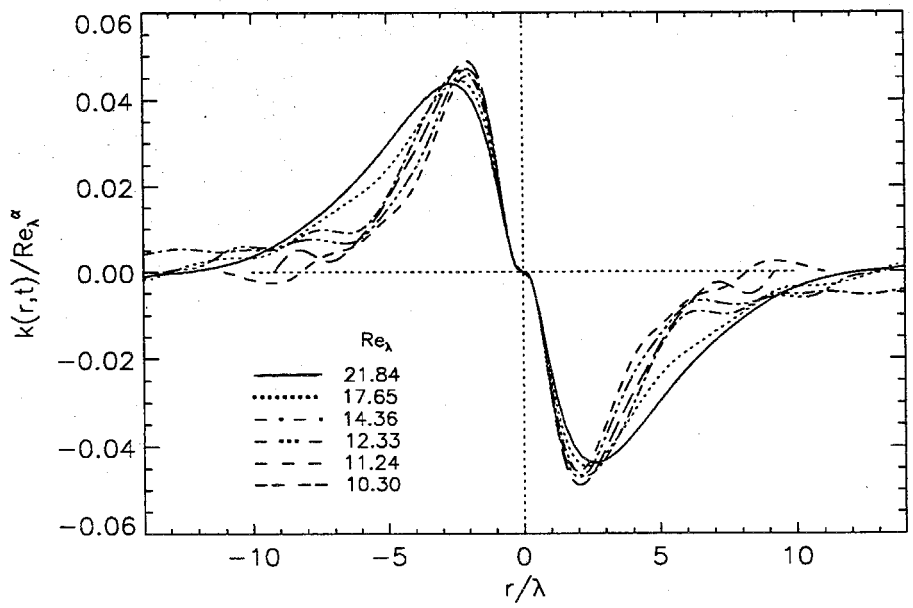

Figure 4.14a: The similarity of the scaled triple velocity correlation coefficients $k(r/\lambda, t)/Re_\lambda^{\beta-1}$ for run2 with $\beta = 1.04$.

Similarly, we show $k(r,t)$ in its proposed self-similar form in Fig. 4.14ab. Here the collape of the data is reasonably good, but seemingly not as good as it was with the double correlation functions where two functions $f_1(r/\lambda)$ and $f_2(r/\lambda)$ are used. An alternate similarity hypothesis, using two functions for $k(r,t)$, is presented in Sec. 4.4, but, at the present time, we prefer (4.18b) for its simplicity, the fact that only one undetermined function (f_2 or k_2) is at our disposal once n and β are fixed and the fact that the alternate hypothesis clearly does not apply at low Re_λ.

4.4 Modified Similarity Hypothesis

A modification to the similarity hypothesis proposed in Sec. 4.2.2 is discussed here. Instead of (4.18b), one may consider

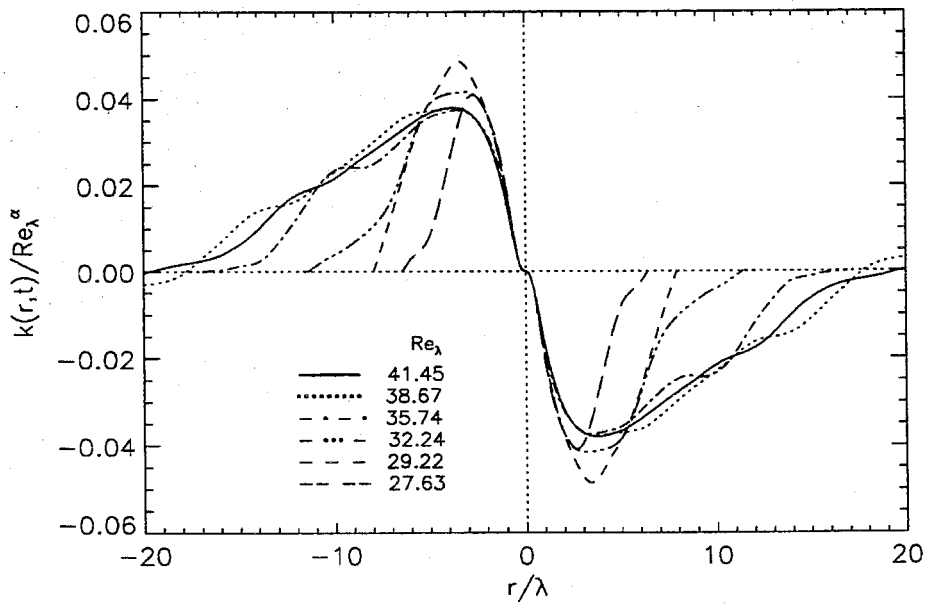

Figure 4.14b: The similarity of the scaled triple velocity correlation coefficients $k(r/\lambda,t)/Re_\lambda^{\beta-1}$ for run5 with $\beta = 1.04$.

$$k(r,t) = Re_\lambda^{-1}\ k_1(r/\lambda) + Re_\lambda^{\alpha}\ k_2(r/\lambda) \tag{4.59}$$

which together with (4.18a) also consists with relation (4.17). The expression for G (4.17) and skewness S now become

$$G = \left.\frac{d^4 f_1}{d\zeta^4}\right|_{\zeta=0} + Re_\lambda^{\beta}\left.\frac{d^4 f_2}{d\zeta^4}\right|_{\zeta=0}$$

$$= \left(\frac{15}{7}\left(\frac{n+1}{n}\right) - \frac{1}{2}\left.\frac{d^3 k_1}{d\zeta^3}\right|_{\zeta=0}\right) - \frac{1}{2}Re_\lambda^{\alpha+1}\left.\frac{d^3 k_2}{d\zeta^3}\right|_{\zeta=0} \tag{4.60}$$

and

$$S = -\left.\frac{d^3 k_2}{d\zeta^3}\right|_{\zeta=0}\cdot Re_\lambda^{\alpha} - \left.\frac{d^3 k_1}{d\zeta^3}\right|_{\zeta=0}\cdot Re_\lambda^{-1}. \tag{4.61}$$

Therefore, it is required that $\beta = \alpha + 1$ as before and

$$\left.\frac{d^4 f_1}{d\zeta^4}\right|_{\zeta=0} = \frac{15}{7}\left(\frac{n+1}{n}\right) - \frac{1}{2}\left.\frac{d^3 k_1}{d\zeta^3}\right|_{\zeta=0} \tag{4.62}$$

with

$$\left.\frac{d^4 f_2}{d\zeta^4}\right|_{\zeta=0} = -\frac{1}{2}\left.\frac{d^3 k_2}{d\zeta^3}\right|_{\zeta=0}. \tag{4.63}$$

Two equations with four unknown functions are obtained if one substitutes (4.18a) and (4.59) into Kármán-Howarth equation. They are

$$10 f_1 + \frac{5}{n}\zeta\frac{df_1}{d\zeta} + \frac{2}{\zeta^4}\frac{d}{d\zeta}\left(\zeta^4\frac{df_1}{d\zeta}\right) + \frac{1}{\zeta^4}\frac{d}{d\zeta}\left(\zeta^4 k_1\right) = 0 \tag{4.64}$$

and

$$(10 + 5\beta - \frac{5}{n}\beta) f_2 + \frac{5}{n}\zeta\frac{df_2}{d\zeta} + \frac{2}{\zeta^4}\frac{d}{d\zeta}\left(\zeta^4\frac{df_2}{d\zeta}\right) + \frac{1}{\zeta^4}\frac{d}{d\zeta}\left(\zeta^4 k_2\right) = 0. \tag{4.65}$$

This similarity form actually is favored by George (in private disscussions) for it predicts a maximum values of skewness during the decay. George suggested in his paper [27] that it is likely that the skewness S increases and reaches a maximum value during the initial period of decay and then remains approximately constant before the inertial forces die out. This self-similar solution can thus be treated as a transitional state before the flow enters the self-similar state discussed in the previous sections. The maximum value of skewness predicted from (4.61)

$$S_{max} = d\left(1 + \frac{1}{\alpha}\right)\left(\frac{d}{c\alpha}\right)^{-1/(1+\alpha)} \tag{4.66}$$

occurs at $Re_\lambda = Re_{\lambda max} = (d/c\alpha)^{1/(1+\alpha)}$, where $c \equiv -\left.\frac{d^3 k_2}{d\zeta^3}\right|_{\zeta=0}$ and $d \equiv -\left.\frac{d^3 k_1}{d\zeta^3}\right|_{\zeta=0}$. Note the maximum exists only if $-1 < \alpha < 0$, $d < 0$, and $c > 0$. Scaled by these maximum values, (4.61) becomes

$$\frac{S}{S_{max}} = \frac{1}{1+\alpha}\left(\left(\frac{Re_\lambda}{Re_{\lambda max}}\right)^{\alpha} + \alpha\left(\frac{Re_\lambda}{Re_{\lambda max}}\right)^{-1}\right), \tag{4.67}$$

suggesting that experimental data should collapse in this similarity form if (4.61) is valid and if α is universal. In most, but not all, of our computational data did we observe the existence of a maximum S. For those cases (all but run5), we show S/S_{max} against $Re_\lambda/Re_{\lambda max}$ in Fig. 4.15. The data do not collapse particularly well. In addition, this modified version of similarity with the $Re_\lambda{}^{-1}$-dependence in $k(r,t)$ is not applicable at small Reynolds numbers as predicts a negative skewness.

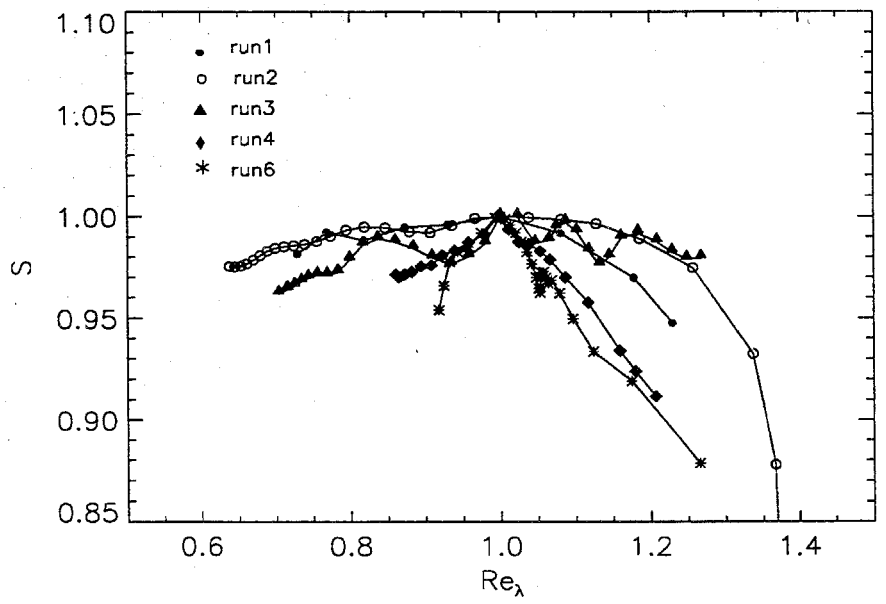

Figure 4.15: S/S_{max} against $Re_\lambda/Re_{\lambda max}$.

4.5 Multiscaling of Energy Spectra

We mentioned before that a similarity form using only one lengthscale is not applicable at large Reynolds numbers. One way to recognize a proper similarity then is use multiscales in the proposed similarity form. One must decide what lengthscales exist in a turbulent flow with large Reynolds numbers and which are dominant and thus should appear in the similarity form. One way to investigate scales involved in a turbulent flow is to express the energy spectrum function in such a way that reveals the relevant lengthscales. We first choose a lengthscale to characterize the large eddies containing most of the kinetic energy and another lengthscale to characterize the small eddies responsible for viscous dissipations. The energy spectrum is then expanded in terms of these two lengthscales. The Re_λ-dependence of the energy spectrum and the dependence on other turbulent lengthscales, if they exist, should be implicit in the expansion. We further force a match at the intermediate scales and attempt to

determine dynamical equation(s) to identify the order functions in the expansions.

A substantial amount of experimental data [6] exists which suggests that the decay of turbulent energy at large Reynolds numbers is dominated by large eddies and that there exists a lengthscale (usually an integral lengthscale) $\mathcal{L}$ such that

$$\frac{dq^2}{dt} \sim \frac{q^3}{\mathcal{L}}, \tag{4.68}$$

which in turn, from the definition of Taylor microscale $\lambda \sim \sqrt{\nu q^2/(dq^2/dt)}$, implies $\mathcal{L} \sim \lambda Re_\lambda$. We choose this lengthscale as the lengthscale which characterizes large eddies. On the other hand, the Kolmogorov dissipation lengthscale ($\eta = (\nu^3/\epsilon)^{1/4}$) is the likely choice for the characteristic lengthscale of small eddies. Our consideration now is to expand the energy spectrum by using the lengthscale $\mathcal{L}$ at small wave numbers (large eddies) and the lengthscale η at large wave numbers (small eddies). Matching is then done in the inertial subrange as proposed by Kolmogorov in 1941.

We recall that the 1941 Kolmogorov hypotheses (see [37] [38] [39]) argue the existence of a universal equilibrium range of wave numbers in turbulence having large Re_λ (more precisely $Re_{\mathcal{L}}^{3/4} \sim {Re_\lambda}^{3/2} \gg 1$, is required when the hypothesis is combined with the empirical relation (4.68)) and that of an inertial subrange for even larger Re_λ (namely $Re_{\mathcal{L}}^{3/8} \sim {Re_\lambda}^{3/4} \gg 1$ with (4.68)). The former introduces Kolmogorov dissipation lengthscale η into problem while the latter, in addition, introduces some other lengthscale which characterizes the eddies of intermediate size, perhapes the Taylor microscale. In summary at large Re_λ, turbulence has large eddies of size $\mathcal{L}$ from which energy is transferred to smaller eddies by inertial forces. Small eddies of size η are responsible for energy dissipations. For high enough Re_λ there may be eddies of intermediate size which receive energy from large eddies and transfer it with little dissipation to the smallest eddies, and which are themselves independent of the large-scale characteristics of flows. This concept should be kept in mind in the following analysis.

4.5.1 Re_λ^{-1} as a Small Parameter

We consider a series expansion of the energy spectrum using Re_λ^{-1} as a small parameter. For the low wave numbers (energy-containing eddies), we anticipate

$$E(k) \sim E_1(k) \;=\; q^2(\lambda Re_\lambda) \sum_{j=0} \mu_j(Re_\lambda)\, F_j(k\lambda Re_\lambda) \tag{4.69}$$

while at large wave numbers (dissipation eddies), we assume

$$E(k) \sim E_2(k) \;=\; (\epsilon\nu^5)^{1/4} \sum_{j=0} \nu_j(Re_\lambda)\, G_j(k\eta), \tag{4.70}$$

where $\frac{3}{2}q^2$ is the mean turbulent energy and $\mu_j(Re_\lambda)$ and $\nu_j(Re_\lambda)$ are functions of Re_λ ordered by

$$\mu_0 > \mu_1 > \mu_2 > \cdots \quad \text{and} \quad \nu_0 > \nu_1 > \nu_2 > \cdots \tag{4.71}$$

as $Re_\lambda \gg 1$. It is assumed that both spectra possess Kolmogorov's $k^{-5/3}$-spectrum in their asymptotic behaviors. For simplicity, in the rest of this section, we will denote variables $(k\lambda Re_\lambda)$ and $(k\eta)$ by ξ and ζ, that is

$$\begin{aligned} \xi &= k\lambda Re_\lambda = \left(k\lambda {Re_\lambda}^{1/4}\right) \cdot {Re_\lambda}^{3/4} \\ \zeta &= k\eta \sim \left(k\lambda {Re_\lambda}^{1/4}\right) \cdot {Re_\lambda}^{-3/4}. \end{aligned} \tag{4.72}$$

It is obvious from (4.72) an intermediate variable χ can be chosen as

$$\chi \equiv k\lambda {Re_\lambda}^{1/4} \tag{4.73}$$

such that $E_1(k)$ and $E_2(k)$ approach Kolmogorov's $k^{-5/3}$-spectrum as $\xi \to \infty$ and $\zeta \to 0$ respectively when $Re_\lambda \to \infty$ with χ fixed. Note this approach is equivelent to Kolmogorov hypothesis in a sense that ${Re_\lambda}^{3/4}$ must be much greater than one to completely separate eddies of size $\mathcal{L}$ from those of size η and to create an inertial subrange in between (see [7]). Meanwhile, $\chi \sim \mathcal{O}(1)$ suggests that the lengthscale characterizing those intermediate eddies should be $\lambda {Re_\lambda}^{1/4}$. If we define the upper and lower limits of the inertial subrange as the geometric means of adjacent chacteristic

lengthscales, $\lambda {Re_\lambda}^{5/8}$ and $\lambda {Re_\lambda}^{-1/8}$, the width of the inertial range is then $\mathcal{O}({Re_\lambda}^{3/4})$, slightly wider than the prediction of $\mathcal{O}({Re_\lambda}^{1/2})$ by Dimotakis for a jet turbulence [20].

We next assume that all functions F_j and G_j are at most $\mathcal{O}(k^{-5/3})$ when $\xi \to \infty$ or $\zeta \to 0$. We write

$$F_j(\xi) \sim f_j\, \xi^{-5/3} \qquad \text{as } \xi \to \infty, \tag{4.74}$$

$$G_j(\zeta) \sim g_j\, \zeta^{-5/3} \qquad \text{as } \zeta \to 0, \tag{4.75}$$

where f_j (or g_j) is nonzero if $F_j = \mathcal{O}(\xi^{-5/3})$ (or $G_j = \mathcal{O}(\zeta^{-5/3})$) and zero otherwise. Then if $\xi \to \infty$ and $\zeta \to 0$, we force the leading order term of the spectra to be Kolmogorov's spectrum, (4.69) and (4.70) become

$$\begin{aligned} E_1(k) &\sim q^2 \lambda Re_\lambda \sum_{j=0} f_j \mu_j(Re_\lambda)\, (k\lambda Re_\lambda)^{-5/3} \\ &\sim 15^{-2/3}\, (\epsilon\nu^5)^{1/4} \sum_{j=0} f_j \mu_j(Re_\lambda)(k\eta)^{-5/3} \\ &\sim C_K(\epsilon\nu^5)^{1/4}(k\eta)^{-5/3} \end{aligned} \tag{4.76}$$

and

$$\begin{aligned} E_2(k) &\sim (\epsilon\nu^5)^{1/4} \sum_{j=0} g_j \nu_j(Re_\lambda)(k\eta)^{-5/3} \\ &\sim C_K(\epsilon\nu^5)^{1/4}(k\eta)^{-5/3} \end{aligned} \tag{4.77}$$

where C_K is Kolmogorov constant. Therefore, we require

$$\begin{aligned} \mu_0(Re_\lambda) = \nu_0(Re_\lambda) &= 1 \\ 15^{-2/3}\, f_0 = g_0 &= C_K \end{aligned} \tag{4.78}$$

and

$$\mu_j(Re_\lambda) = \nu_j(Re_\lambda), \quad 15^{-2/3}\, f_j = g_j, \quad \text{for j } \geq 1. \tag{4.79}$$

Because the commom parts of expansions can be written as a function of ξ as well as ζ, there are two equivalent ways to write the expansion of the energy spectrum. One is

$$E(k) \sim q^2 \lambda Re_\lambda \sum_{j=0} \mu_j(Re_\lambda)\ F_j(k\lambda Re_\lambda) + (\epsilon\nu^5)^{1/4} \sum_{j=0} \mu_j(Re_\lambda)\ \left(G_j(k\eta) - g_j(k\eta)^{-5/3}\right) \tag{4.80}$$

and the other is

$$E(k) \sim q^2 \lambda Re_\lambda \sum_{j=0} \mu_j(Re_\lambda)\ \left(F_j(k\lambda Re_\lambda) - 15^{2/3}\ g_j(k\lambda Re_\lambda)^{-5/3}\right) + (\epsilon\nu^5)^{1/4} \sum_{j=0} \mu_j(Re_\lambda)\ G_j(k\eta). \tag{4.81}$$

Both expressions will be used in the following analysis.

Before we consider dynamical equations for the expansion functions F_j and G_j, we determine the constraints implied by the definitions of the kinetic energy $3q^2/2$ and the energy dissipation rate ϵ. Using (4.80) to define the kinetic energy, we find

$$\begin{aligned} \frac{3}{2}q^2 &= \int_0^\infty E(k)dk \\ &= q^2 \sum_{j=0} \mu_j(Re_\lambda) \int_0^\infty F_j(\xi)d\xi \\ &\quad + \sqrt{15}\ q^2 Re_\lambda{}^{-1} \sum_{j=0} \mu_j(Re_\lambda) \int_0^\infty \left(G_j(\zeta) - g_j\zeta^{-5/3}\right) d\zeta. \end{aligned} \tag{4.82}$$

Because $\mu_0(Re_\lambda) = 1$, we thus require

$$\int_0^\infty F_0(\xi)d\xi = \frac{3}{2}, \tag{4.83a}$$

and

$$\sum_{j=0} \left(\mu_{j+1}(Re_\lambda) \int_0^\infty F_{j+1}(\xi)d\xi + \sqrt{15}\ Re_\lambda{}^{-1}\mu_j(Re_\lambda) \int_0^\infty \left(G_j(\zeta) - g_j\zeta^{-5/3}\right) d\zeta\right) = 0. \tag{4.83b}$$

On the other hand, using(4.81) to compute ϵ, we find

$$\begin{aligned} \frac{\epsilon}{2\nu} &= \int_0^\infty k^2 E(k)dk \\ &= \frac{\epsilon}{\nu} \sum_{j=0} \mu_j(Re_\lambda) \int_0^\infty \zeta^2 G_j(\zeta)d\zeta \\ &\quad + \frac{\epsilon}{15\nu} Re_\lambda{}^{-2} \sum_{j=0} \mu_j(Re_\lambda) \int_0^\infty \xi^2 \left(F_j(\xi) - 15^{2/3}\ g_j\xi^{-5/3}\right) d\xi. \end{aligned} \tag{4.84}$$

Therefore, we also require

$$\int_0^\infty \zeta^2 G_0(\zeta) d\zeta = \frac{1}{2}, \tag{4.85a}$$

and

$$\sum_{j=0} \left(\mu_{j+1}(Re_\lambda) \int_0^\infty \zeta^2 G_{j+1}(\zeta) d\zeta + \frac{1}{15} Re_\lambda{}^{-2} \mu_j(Re_\lambda) \int_0^\infty \xi^2 \left(F_j(\xi) - 15^{2/3}\, \xi^{-5/3} \right) d\xi \right) = 0. \tag{4.85b}$$

For convenience, we introduce $\left(\widehat{F}_j(\xi),\ \widehat{G}_j(\zeta)\right)$ to denote either

$$\left(F_j(\xi)\ ,\ G_j(\zeta) - g_j \zeta^{-5/3}\right)$$

or

$$\left(F_j(\xi) - 15^{2/3} g_j \xi^{-5/3}\ ,\ G_j(\zeta)\right),$$

whichever is suitable in discussion. The uniform expansion of the energy spectrum thus becomes

$$E(k) \sim q^2 \lambda Re_\lambda \sum_{j=0} \mu_j(Re_\lambda)\ \widehat{F}_j(k\lambda Re_\lambda) + (\epsilon\nu^5)^{1/4} \sum_{j=0} \mu_j(Re_\lambda)\ \widehat{G}_j(k\eta). \tag{4.86}$$

Note we will denote the first term on the right-hand side as $E_1(k)$ and the second term as $E_2(k)$.

4.5.2 Spectral Kármán-Howarth Equation

To correspond to the energy spectrum expression (4.86), we propose an energy transfer spectrum of the form

$$\begin{aligned} T(k) = q^3 \sum_{j=0} \mu_j(Re_\lambda)\ \widehat{H}_j(k\lambda Re_\lambda) \\ + (\epsilon\nu)^{3/4} \sum_{j=0} \mu_j(Re_\lambda)\ \widehat{K}_j(k\eta). \end{aligned} \tag{4.87}$$

Relations between the functions $\widehat{F}_j$ and $\widehat{H}_j$ and between the functions $\widehat{G}_j$ and $\widehat{K}_j$ are then determined by the spectral Kármán-Howarth equation

$$\frac{\partial E(k)}{\partial t} = T(k) - 2\nu k^2 E(k). \tag{4.88}$$

We will find the following relations useful:

$$\frac{\partial \xi}{\partial t} = \frac{\nu}{\lambda^2}(2\sigma - 5)\ \xi, \tag{4.89}$$

$$\frac{\partial \zeta}{\partial t} = \left(\frac{\sigma+5}{2}\right)\frac{q}{\lambda}\ \zeta Re_\lambda{}^{-1}, \tag{4.90}$$

$$\frac{d\lambda Re_\lambda}{dt} = q(2\sigma - 5), \tag{4.91}$$

$$\frac{dq^2\lambda Re_\lambda}{dt} = q^3(2\sigma - 15), \tag{4.92}$$

$$\frac{dRe_\lambda}{dt} = \frac{q}{\lambda}(\sigma - 5), \tag{4.93}$$

$$\frac{d(\epsilon\nu^5)^{1/4}}{dt} = 15^{\frac{1}{4}}\left(-\frac{\sigma+5}{2}\right) q^3 Re_\lambda{}^{-5/2}, \tag{4.94}$$

where $\sigma \equiv \frac{\lambda}{\nu}\frac{d\lambda}{dt}$. We will also need

$$(\epsilon\nu^5)^{1/4} = 15^{\frac{1}{4}} q^2 \lambda Re_\lambda{}^{-3/2} \tag{4.95}$$

and

$$(\epsilon\nu)^{3/4} = 15^{\frac{3}{4}} q^3 Re_\lambda{}^{-3/2}. \tag{4.96}$$

The terms appearing in (4.88) can then be written as follows:

$$\begin{aligned}\frac{\partial E_1}{\partial t} &= q^3\ Re_\lambda \sum_{j=0} (\sigma - 5)\ \mu_j' \widehat{F}_j(\xi) \\ &\quad + q^3 \sum_{j=0} \left((2\sigma - 15)\ \mu_j \widehat{F}_j(\xi)\ +\ (2\sigma - 5)\ \mu_j \xi \widehat{F}_j'(\xi)\right),\end{aligned} \tag{4.97}$$

$$\begin{aligned}\frac{\partial E_2}{\partial t} &= 15^{\frac{1}{4}}\ q^3\ Re_\lambda{}^{-3/2} \sum_{j=0} (\sigma - 5)\ \mu_j' \widehat{G}_j(\zeta) \\ &\quad + 15^{\frac{1}{4}}\ q^3\ Re_\lambda{}^{-5/2} \sum_{j=0} \left(\frac{\sigma+5}{2}\right)\ \mu_j \left(\zeta \widehat{G}_j'(\zeta) - \widehat{G}_j(\zeta)\right),\end{aligned} \tag{4.98}$$

$$T(k) = q^3 \sum_{j=0} \mu_j \widehat{H}_j(\xi)\ +\ 15^{\frac{3}{4}}\ q^3\ Re_\lambda{}^{-3/2} \sum_{j=0} \mu_j\ \widehat{K}_j(\zeta), \tag{4.99}$$

$$2\nu k^2 E_1 = q^3\ Re_\lambda{}^{-2} \sum_{j=0} 2\ \mu_j \xi^2 \widehat{F}_j(\xi), \tag{4.100}$$

$$2\nu k^2 E_2 = 15^{\frac{3}{4}}\ q^3\ Re_\lambda{}^{-3/2} \sum_{j=0} 2\mu_j \zeta^2 \widehat{G}_j(\zeta). \tag{4.101}$$

We know that $1 = \mu_0 > \mu_1 > \mu_2 > \cdots$ so that the leading order terms are therefore $\mathcal{O}(1)$. In comparing the higher order terms, the appearance of factors $Re_\lambda{}^{j/2}$, $j = 1, 2, \cdots$ suggests a general choice for $\{\mu_j\}$ as

$$\mu_j(Re_\lambda) = Re_\lambda{}^{-j/2}, \quad j = 0, 1, 2, \cdots. \tag{4.102}$$

With this choice of $\{\mu_j\}$ and matching terms up to and including $\mathcal{O}(Re_\lambda{}^{-5/2})$, we find

$$\begin{aligned}
&(a) \quad \widehat{H}_0(\xi) = \mathcal{L}(\widehat{F}_0(\xi)) \\
&(b) \quad \widehat{H}_1(\xi) = \mathcal{L}(\widehat{F}_1(\xi)) - \frac{1}{2}(\sigma - 5)\widehat{F}_1(\xi) \\
&(c) \quad \widehat{H}_2(\xi) = \mathcal{L}(\widehat{F}_2(\xi)) - (\sigma - 5)\widehat{F}_2(\xi) \\
&(d) \quad \widehat{H}_3(\xi) = \mathcal{L}(\widehat{F}_3(\xi)) - \frac{3}{2}(\sigma - 5)\widehat{F}_3(\xi) \\
&(e) \quad \widehat{H}_4(\xi) = \mathcal{L}(\widehat{F}_4(\xi)) - 2(\sigma - 5)\widehat{F}_4(\xi) + 2\xi^2\widehat{F}_0(\xi) \\
&(f) \quad \widehat{H}_5(\xi) = \mathcal{L}(\widehat{F}_5(\xi)) - \frac{5}{2}(\sigma - 5)\widehat{F}_5(\xi) + 2\xi^2\widehat{F}_1(\xi) \\
&(g) \quad \widehat{K}_0(\zeta) = 2\zeta^2\widehat{G}_0(\zeta) \\
&(h) \quad \widehat{K}_1(\zeta) = 2\zeta^2\widehat{G}_1(\zeta) \\
&(i) \quad \widehat{K}_2(\zeta) = 2\zeta^2\widehat{G}_2(\zeta) + \left(\frac{\sigma + 5}{2\sqrt{15}}\right)\left(\zeta\widehat{G}_0'(\zeta) - \widehat{G}_0(\zeta)\right)
\end{aligned} \tag{4.103}$$

where

$$\mathcal{L}(\widehat{F}_j(\xi)) \equiv (2\sigma - 15)\widehat{F}_j(\xi) + (2\sigma - 5)\xi\widehat{F}_j'(\xi). \tag{4.104}$$

Table 4.3 also gives the dependencies for the order of the magnitudes from $\mathcal{O}(Re_\lambda{}^0)$ to $\mathcal{O}(Re_\lambda{}^{-5/2})$. We see that up to $\mathcal{O}(Re_\lambda{}^{-3/2})$ the decay of the energy-containing eddies is purely through the draining of energy from large eddies to smaller eddies by inertial forces and not until order $\mathcal{O}(Re_\lambda{}^{-3/2})$ do the small eddies dissipate energy. This is again consistent with Kolmogorov's hypothesis that $Re_\lambda{}^{3/2} \gg 1$ is required to separate large eddies from small eddies.

In conclusion an energy spectrum of the form

Table 4.3: Terms appearing in the spectral energy equation in order of $Re_\lambda{}^0$, $Re_\lambda{}^{-1/2}$, $Re_\lambda{}^{-1}$, $Re_\lambda{}^{-3/2}$, $Re_\lambda{}^{-2}$ and $Re_\lambda{}^{-5/2}$.

$\frac{\partial E(k)}{\partial t}$						$T(k)$						$2\nu k^2 E(k)$					
$\widehat{F}_0$	$\widehat{F}_1$	$\widehat{F}_2$	$\widehat{F}_3$	$\widehat{F}_4$	$\widehat{F}_5$	$\widehat{H}_0$	$\widehat{H}_1$	$\widehat{H}_2$	$\widehat{H}_3$	$\widehat{H}_4$	$\widehat{H}_5$	0	0	0	0	$\widehat{F}_0$	$\widehat{F}_1$
0	0	0	0	0	$\widehat{G}_0$	0	0	0	$\widehat{K}_0$	$\widehat{K}_1$	$\widehat{K}_2$	0	0	0	$\widehat{G}_0$	$\widehat{G}_1$	$\widehat{G}_2$

$$E(k) \sim (q^2 \lambda Re_\lambda) \sum_{j=0} Re_\lambda{}^{-j/2}\ \widehat{F}_j(k\lambda Re_\lambda) + (\epsilon\nu^5)^{1/4} \sum_{j=0} Re_\lambda{}^{-j/2}\ \widehat{G}_j(\eta) \tag{4.105}$$

is proposed. The constraints, (4.83) and (4.85), coming from the definitions of turbulent energy and energy dissipation rate, with the choice of $\mu_j(Re_\lambda) = Re_\lambda{}^{-j/2}$ now become

$$\begin{gathered} \int_0^\infty F_0(\xi)d\xi = \tfrac{3}{2}, \\ \int_0^\infty F_1(\xi)d\xi = 0, \\ \int_0^\infty F_{j+2}(\xi)d\xi + \sqrt{15}\int_0^\infty \left(G_j(\zeta) - g_j\zeta^{-5/3}\right)d\zeta = 0, \quad \text{for all } j \geq 0 \end{gathered} \tag{4.106}$$

and

$$\begin{gathered} \int_0^\infty \zeta^2 G_0(\zeta)d\zeta = \tfrac{1}{2} \\ \int_0^\infty \zeta^2 G_j(\zeta)d\zeta = 0 \quad \text{for } j = 1,2,3, \\ 15\int_0^\infty \zeta^2 G_{j+4}(\zeta)d\zeta + \int_0^\infty \xi^2 \left(F_j(\xi) - 15^{2/3} g_j \xi^{-5/3}\right)d\xi = 0 \quad \text{for all } j \geq 0. \end{gathered} \tag{4.107}$$

We now construct an example of the energy spectrum (shown in Fig. 4.16) only using the leading order terms. We choose

$$F_0(\xi) = 15^{2/3} C_K \frac{b\,\xi^2}{1 + b\,\xi^{11/3}} \tag{4.108}$$

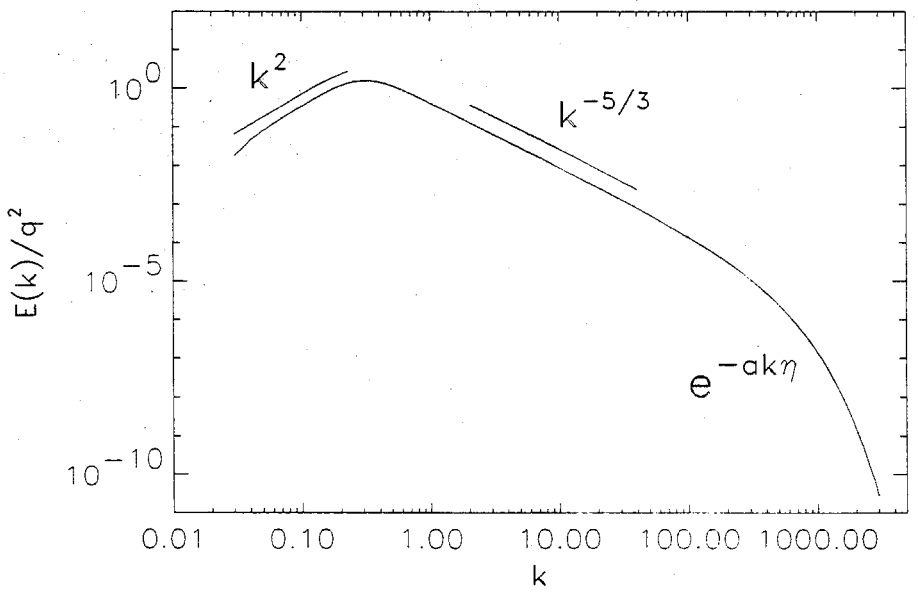

Figure 4.16: An example of the energy spectrum having k^2-behavior near the origin, the $k^{-5/3}$-Kolmogorov's spectrum in intermediate wave numbers, and an exponential tail at large wave numbers. $C_K = 1.5$ is used.

and

$$G_0(\zeta) = C_K \zeta^{-5/3} \exp(-a\zeta), \tag{4.109}$$

where $a = \left(2C_K\Gamma(\frac{4}{3})\right)^{3/4}$ from (4.106) and $b = \left(\frac{2}{11} \cdot 15^{2/3}\, C_K\Gamma(\frac{9}{11})\Gamma(\frac{2}{11})\right)^{-11/2}$ from (4.107). This energy spectrum has a k^2-behavior near the origin of wave numbers, a $k^{-5/3}-$inertial subrange and an exponential tail at very large wave numbers. The energy spectrum when scaled by Kolmogorov scaling and multiplied by the factor $(k\eta)^{5/3}$, sometimes is observed to have a positive "bump" at the intersection of inertial subrange and dissipation range of wave numbers (see experimental data of Saddoughi for example [56]). Our example does not possess such a bump, but it should be easy to construct another example having the bump, if one prefers.

4.6 Far-Dissipation Range of Energy Spectra

Eddies of scales within the far-dissipation range are now considered. These eddies are considered independent of the large-scale characteristics of flows. This independence, as predicted by 1941 Kolmogorov universal equilibrium hypothesis and also supported from the perturbation study presented in the previous section, should be true as long as $Re_\lambda^{3/2} \gg 1$. Dimensional analysis based on the assumption that Kolmogorov dissipation scale η is the only characteristic lengthscale for motions within this range suggests

$$E(k) \sim (\epsilon\nu^5)^{1/4} F(k\eta), \qquad k \gg \Lambda_f^{-1} \tag{4.110}$$

where Λ_f is some integral lengh scale characterizing the large-scale eddies. The precise form of function $F(k\eta)$ is unknown. Many model spectra have been proposed, either purely empirically or derived from the spectral energy equation with some assumed relation between the energy spectrum $E(k)$, the energy transfer spectrum $T(k)$, and the wave number k ([47] [51] [58] [64]). In the present work, we are particularly interested in a slightly generalized form of a spectrum proposed by Smith and Reynolds [64]:

$$E(k) = B(\epsilon\nu^5)^{1/4}\ (k\eta)^{-b} e^{-a(k\eta)^m}, \qquad k \gg \Lambda^{-1}. \tag{4.111}$$

where a, b, and m are constants. Smith and Reynolds [64] actually used (4.111) with $b = -5/3$ to predict the value of skewness S of the velocity derivative for decaying isotropic turbulence.

Experimentally, there exist technical obstacles in measuring the energy spectra beyond the Kolmogorov wave number $k_\eta = 1/\eta$. In our simulations, instead we have flows well resolved much beyond $k_\eta = 1$, although the flows are limited to low-Re_λ. We can then attempt to study the effect of Re_λ on the validity of (4.111) and its relation with the power-law energy decay of isotropic turbulence and its prediction of skewness S.

4.6.1 Together with Power-Law Energy Decay

As noted by Pao [51] as well as by Smith and Reynolds [65], provided Re_λ is large enough so that the contributions to the energy dissipation ϵ from low wave numbers are negligible, we may compute

$$\epsilon = 2\nu \int_0^\infty k^2 E(k) dk \tag{4.112}$$

by assuming (4.111) for all wave numbers. Substituting (4.111) into (4.112), one finds the relation

$$B = \frac{m}{2}\, a^{(b+3)/m}\, \Gamma^{-1}\left(\frac{b+3}{m}\right) \tag{4.113}$$

has to be satisfied. On the other hand, we recall that in isotropic turbulence, the quantity G is computed as follows:

$$G = \frac{2}{35}\frac{\lambda^4}{q^2} \int_0^\infty k^4 E(k) dk, \tag{4.114}$$

which together with (4.111) requires

$$B = \frac{7m}{6\sqrt{15}}\, a^{(b+5)/m}\, \Gamma^{-1}\left(\frac{b+5}{m}\right) \cdot \frac{G}{Re_\lambda}. \tag{4.115}$$

Equation (4.115) should provide a better estimate of B than (4.113) provided G is known due to the factor k^4 in the integrand of (4.114). When Re_λ is not large, the preditions by (4.113) and (4.115) can be very different.

We also recall the dissipation rate equation in the following form

$$\dot{\epsilon} = \frac{\epsilon^2}{K}\left(\frac{7}{30} S Re_\lambda - \frac{7}{15} G\right), \tag{4.116}$$

which gives

$$G = \frac{1}{2} S Re_\lambda + \frac{15}{7}\left(\frac{n+1}{n}\right) \tag{4.117}$$

under the assumption of a power-law energy decay with exponent n. The skewness S is thus predicted by using (4.117) provided G is available as

$$S = \frac{2}{Re_\lambda}\left(G - \frac{15}{7}\left(\frac{n+1}{n}\right)\right). \tag{4.118}$$

Combining with (4.115), (4.118) becomes

$$S = \left\{\frac{12\sqrt{15}}{7m}\, a^{-(b+5)/m}\, \Gamma(\frac{b+5}{m})\right\} B - \frac{30}{7}\left(\frac{n+1}{n}\right) Re_\lambda^{-1}. \tag{4.119}$$

If (4.113) is assumed also, then

$$S = \frac{6\sqrt{15}}{7}\, a^{-2/m}\, \Gamma(\frac{b+5}{m})\Gamma^{-1}(\frac{b+3}{m}) - \frac{30}{7}\left(\frac{n+1}{n}\right) Re_\lambda^{-1}. \tag{4.120}$$

Notice the form of the skewness (4.120) above can be anticipated by the modified similarity hypothesis presented in Sec. 4.4 with the choice of $\beta = 1$ which has the problem of yielding a negative skewness at small Re_λ. This enhances our belief that the modified similarity hypothesis can not be applied at small Re_λ. (Note the analysis in this section is done for large Re_λ.) In the rest of this section, we will use (4.113)-(4.120) to estimate the applicability of the model spectrum to our simulated turbulence.

Note all the above analysis can be applied to stationary turbulence as well as long as the large-scale forcing does not affect the far-dissipation range of energy spectrum. All the terms involving the decay exponent n then disappear. The ratio of B to S for stationary turbulence, or as an asymptotic ratio for decaying turbulence for $Re_\lambda \gg 1$, is thus given by (4.119) as

$$\frac{S}{B} = \frac{12\sqrt{15}}{7m}\, a^{-(b+5)/m}\, \Gamma(\frac{b+5}{m}). \tag{4.121}$$

4.6.2 Numerical Results

We have shown the results of a power-law energy decay and those of the measured quantity G verus Re_λ in Sec. 4.3. Since many investigators [35] [36] have observed an exponential tail for the energy spectrum of the form $E(k,t)(k\eta)^{5/3}/(\epsilon\nu^5)^{1/4}$, we first show the energy spectra in this form in Fig. 4.17ab. The exponential tails are

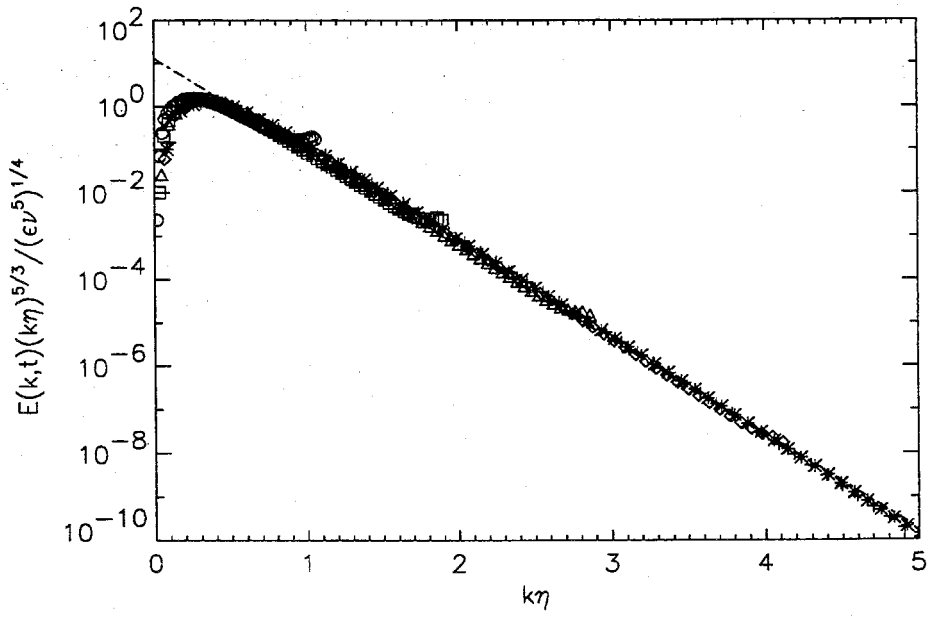

Figure 4.17a: Energy spectra $E(k,t)(k\eta)^{5/3}/(\epsilon\nu^5)^{1/4}$ for run2. —·—·— model spectrum using a=5.0, b=-5/3, m=1 and (4.115).

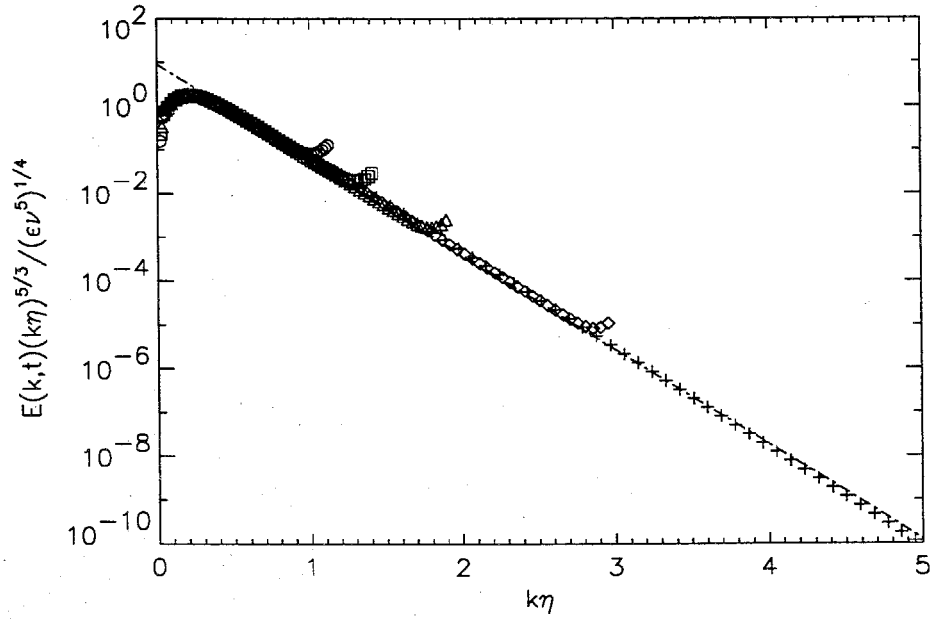

Figure 4.17b: Energy spectra $E(k,t)(k\eta)^{5/3}/(\epsilon\nu^5)^{1/4}$ for run5. —·—·— model spectrum using a=5.0, b=-5/3, m=1 and (4.115).

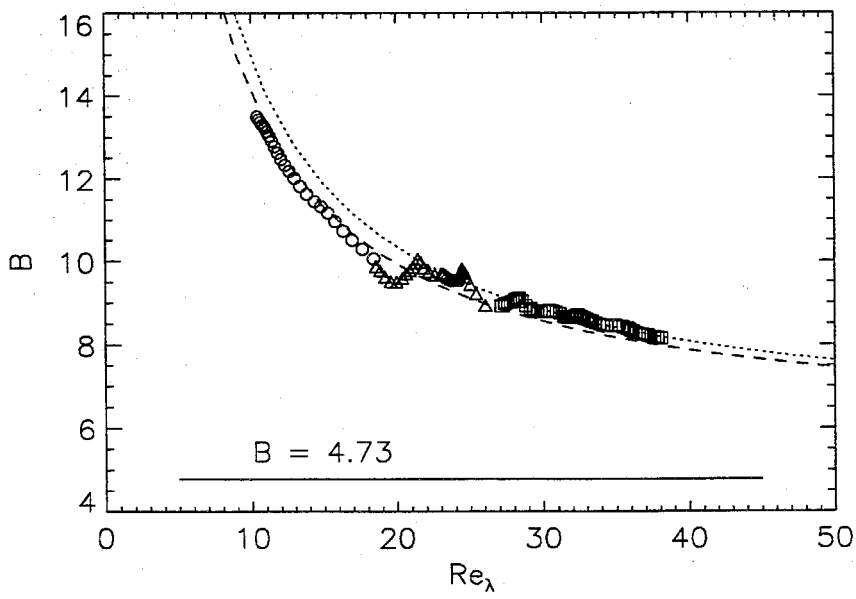

Figure 4.18: B verus Re_λ. Symbols represent the results of (4.115) and the horizontal line represents the constant value of B evaluated by (4.113) with a=5, b=-5/3 and m=1.

observed in our simulations as well, implying m=1 and $b = -5/3$. The exponent a is found nearly constant during the decay. The measured value of $a = 5.0 \pm 0.1$ also agrees with that obtained by earlier investigations [35] [36]. We thus assume $b = -5/3$, $a = 5.0$, and $m = 1$ for the rest of the study.

We next calculate B with the measured G and the assumed values of parameters a, b, and m from both (4.113) and (4.115). The results are shown in Fig. 4.18. The estimate from (4.113) is poor and is no doubt due to the fact that Re_λ are too small for (4.113) to be valid. In Fig. 4.19ab we show the dimensionless dissipation spectrum $D^*(k^*,t) \equiv 2\nu k^2 E(k,t)/(\epsilon\nu)^{3/4}$, where $k^* \equiv k\eta$. As shown, using (4.115) for B gives a reasonable estimate of the spectrum at large wave numbers but not (4.113). Similarly, we also show $\Omega^*(k^*,t) \equiv 2\nu k^4 E(k,t)/(\epsilon^5/\nu^3)^{1/4}$ and $W^*(k^*,t) \equiv 2\nu k^6 E(k,t)/(\epsilon^7/\nu^9)^{1/4}$ in Fig. 4.20ab and Fig. 4.21ab. Equation (4.115) as seen when applied to the present numerical results overestimate $D^*(k^*,t)$ and underestimate

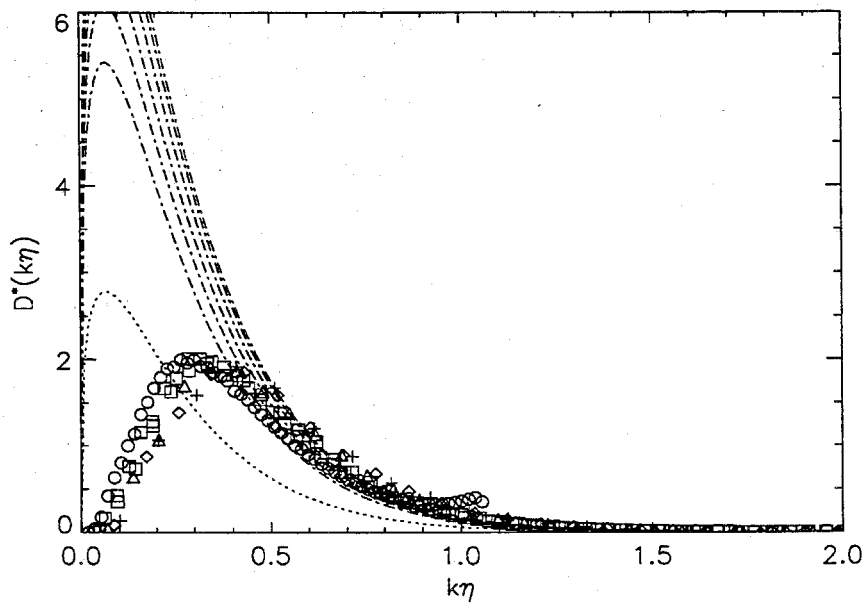

Figure 4.19a: Energy dissipation spectra $D^*(k^*,t)$ for run2. Model spectra using a=5, b=-5/3, and m=1: ····· (4.113) and — · — · — (4.115).

$W^*(k^*,t)$. Although (4.115) is supposed to give a right value of G, its prediction of $\Omega^*(k^*,t)$ does not quite coincide with the simulation data.

It was mentioned above that skewness S calculated by using (4.120) becomes negative at small Reynolds number (see Fig. 4.22). In particular, negative skewness is antipated within the range of Re_λ investigated with the choice of a=5, b=-5/3 and m=1. Therefore, we consider only the estimate (4.118) with simulation data as shown in Fig. 4.23. Solid lines are the predictions from (4.118) by using the measured G from Fig. 4.8 and n listed in Table 4.2. Although the agreement of the spectra is not completely satisfactory, the estimate of skewness S using (4.118) seems reasonably good.

The asymptotic ratio of S to B, (4.121), is shown in Fig. 4.24a (verus a) and Fig. 4.24b (verus m). The value is about 11.59 as m=1 and 0.502 as $m \to \infty$ when a=5.

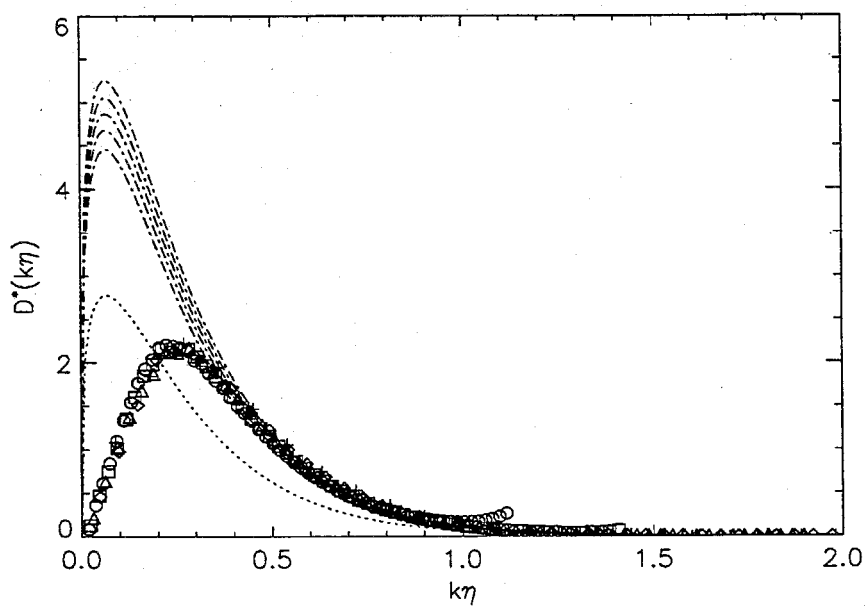

Figure 4.19b: Energy dissipation spectra $D^*(k^*, t)$ for run8. Model spectra using a=5, b=-5/3, and m=1: ····· (4.113) and — · — · — (4.115).

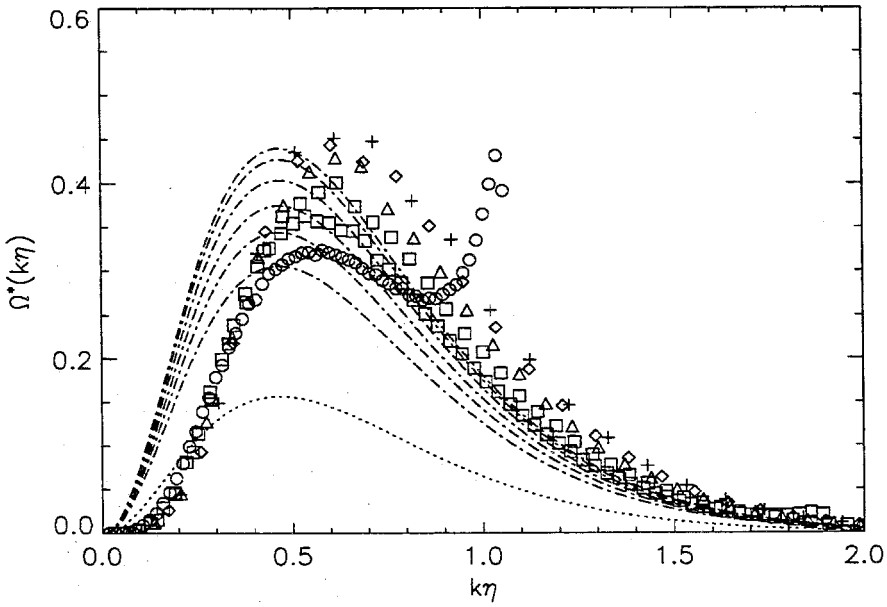

Figure 4.20a: Enstrophy dissipation spectra $\Omega^*(k^*, t)$ for run2. Model spectra using a=5, b=-5/3, and m=1: ····· (4.113) and — · — · — (4.115).

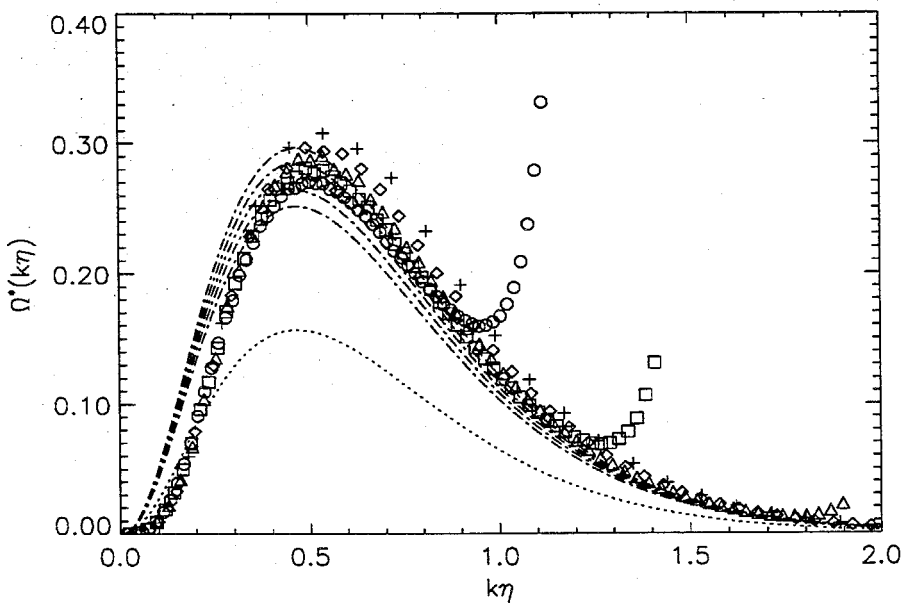

Figure 4.20b: Enstrophy dissipation spectra $\Omega^*(k^*, t)$ for run8. Model spectra using a=5, b=-5/3, and m=1: ····· (4.113) and — · — · — (4.115).

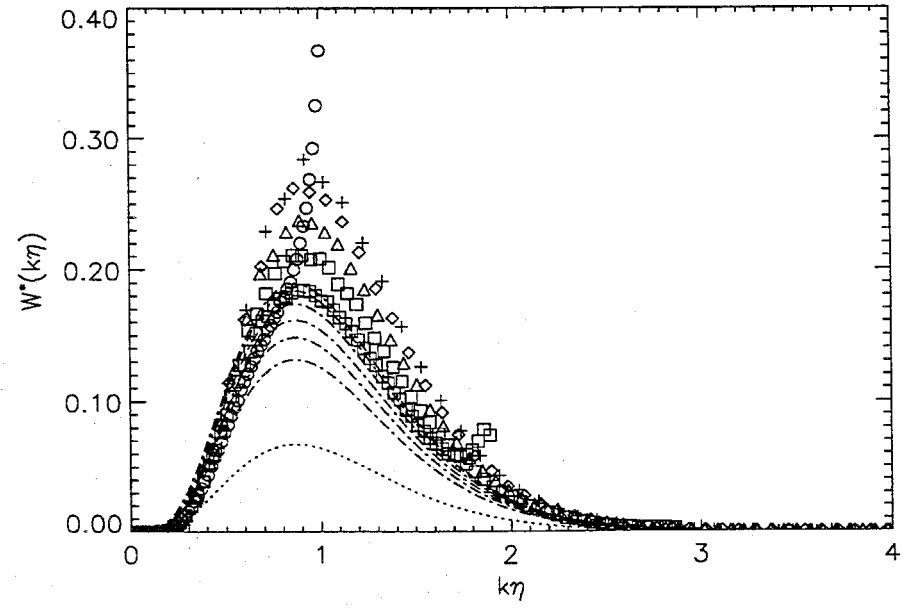

Figure 4.21a: $W^*(k^*)$ for run2. Model spectra using a=5, b=-5/3, and m=1: ····· (4.113) and — · — · — (4.115).

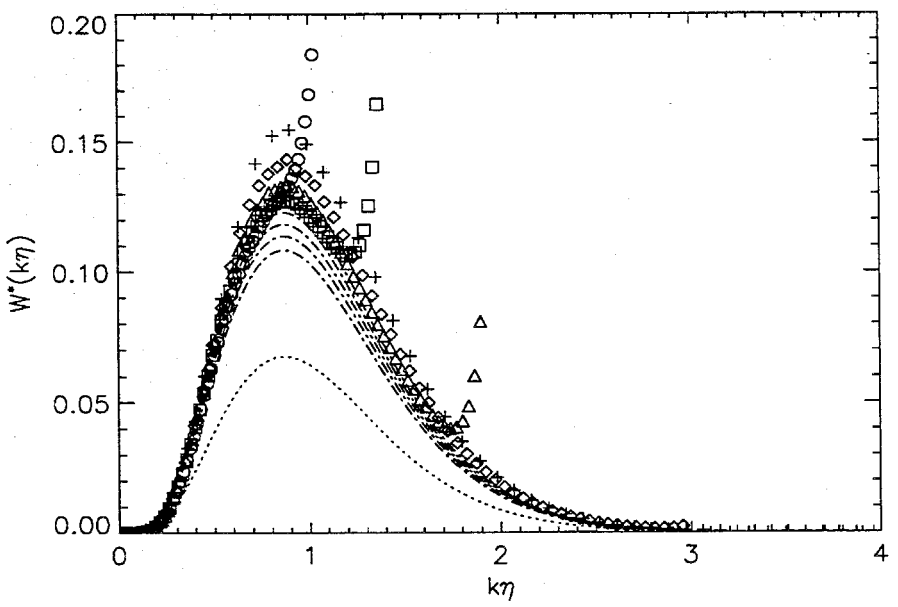

Figure 4.21b: $W^*(k^*)$ for run8. Model spectra using a=5, b=-5/3, and m=1: ····· (4.113) and — · — · — (4.115).

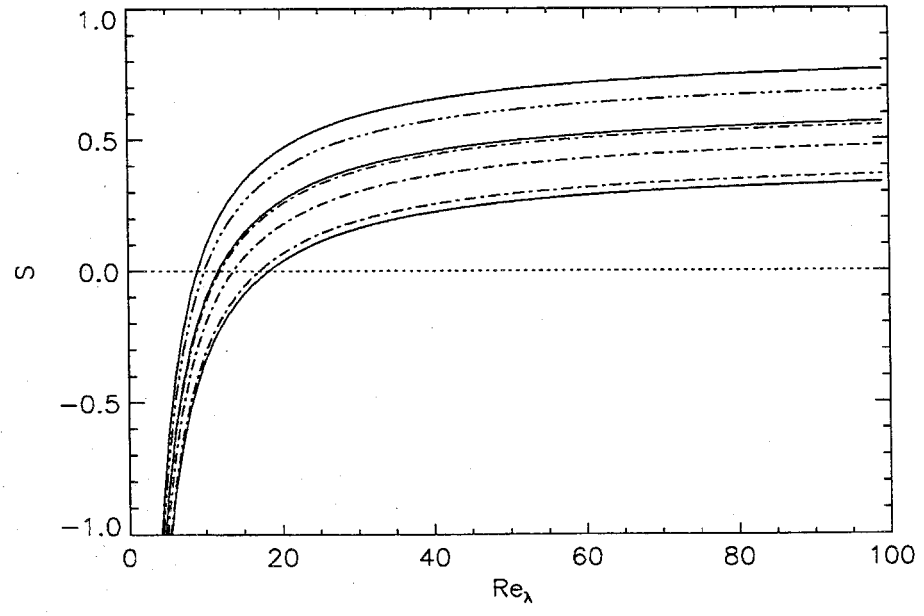

Figure 4.22: $S(a, m)$ from (4.120) with n=1.3 for example. ——— m=1 and — · — · — m=2 with a=3.5, 4, and 5 (S decreases as a increases); ····· m=2 and B=1.5.

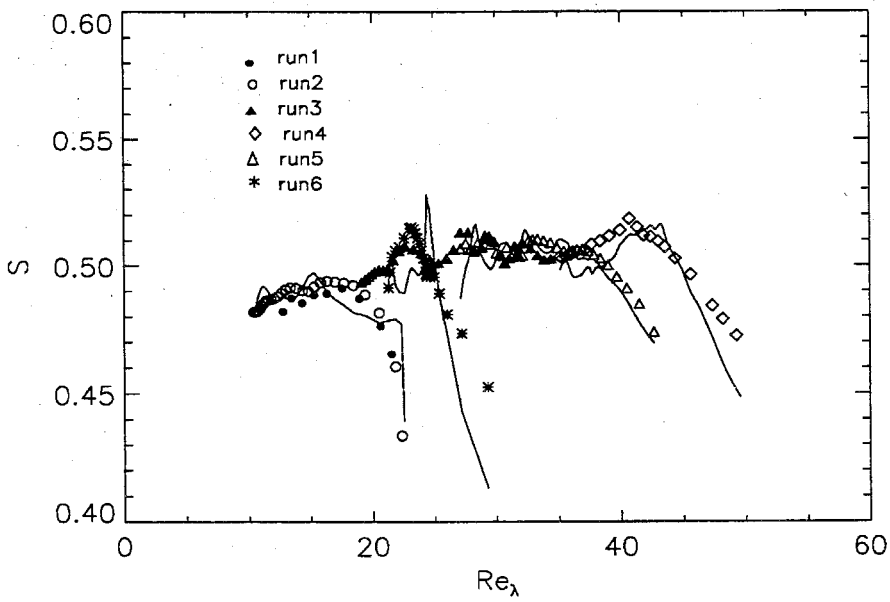

Figure 4.23: S verus Re_λ. Direct computation using simulation data are the symbols. Predictions using (4.118) and measured values of n and G are shown by solid lines.

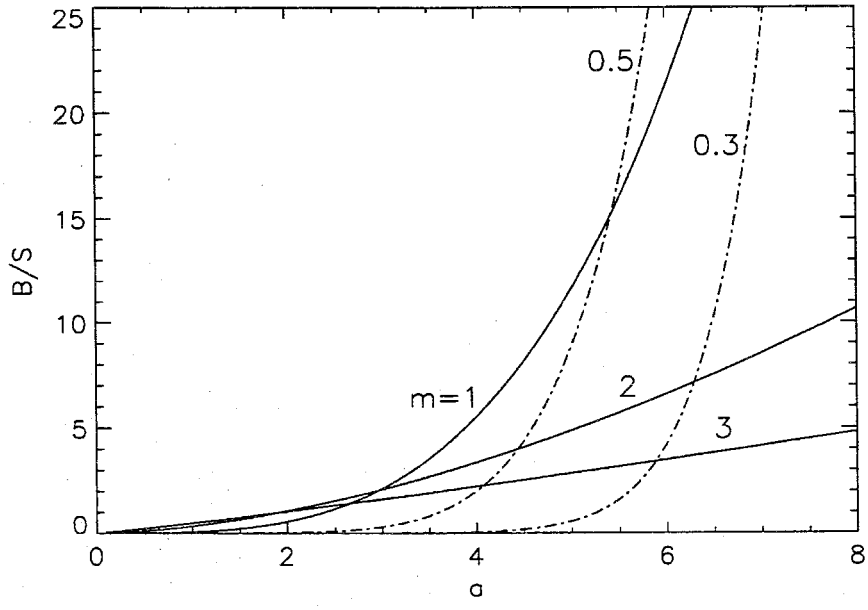

Figure 4.24a: The asymptotic ratio of B to S of decaying turbulence verus m.

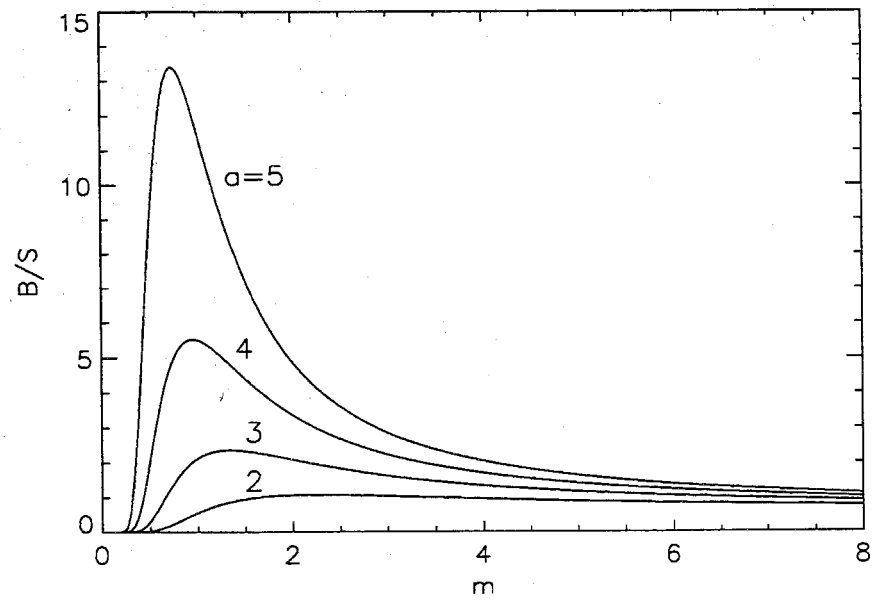

Figure 4.24b: The asymptotic ratio of B to S of decaying turbulence verus a.

4.7 Conclusions

Simulations of decaying homogeneous turbulence at small to intermediate Reynolds numbers have been performed. We find that the turbulent kinetic energy decays eventually as a power-law in time. The decay exponent for the initial conditions summarized in Sec.III.A is found to be about 1.54 for one group of runs and 1.24 for another group. The particular characteristics of the initial conditions that determine the decay exponent are not evident at this time. A new theory of self-similarity for the double and triple velocity correlations of decaying turbulence has been proposed in which the Taylor microscale is the appropriate scaling. The double correlation coefficient is divided into two parts – one has a power-law dependence on the Reynolds numbers and the other does not. The nonlinear terms as measured by the triple velocity correlations vary as $Re_\lambda^{\beta-1}$ during the decay. George's complete self-similarity can be recovered by putting $\beta = 0$. Provided $\beta \neq 0$, two independent equations can

be obtained with three unknown functions. Although the problem is still not closed, the asymptotic behavior of f(r,t) at large separation r is found uniquely related to the decay exponent n. Together with Saffman's proposed asymptotic behavior of f(r,t), the theory predicts a decay exponent of 1.5 in agreement with one of the groups of runs.

A nearly linear relation between Re_λ and G, a quantity related to the dissipation of enstrophy, was observed, in agreement with the observation that the skewness $S \sim Re_\lambda^{\beta-1}$ with $\beta = 1.04$. Provided $\beta > 1$ (so the inertial force increases as Reynolds number increases), the theory may be applicable to the limiting case of zero Reynolds number – to the final period of decay in which the inertial effect is negligible and the double correlation coefficients approach a complete self-similar state. On the other hand, we believe there exists an upper limit for the validity of the proposed similarity. At large Re_λ we anticipate at least two length scales will be required, the Kolmogorov scale, $\eta \sim \lambda Re_\lambda^{-1/2}$, and the empirical lengthscale, $\mathcal{L} \sim \lambda Re_\lambda$. A perturbation method has been used to investigate the uniform expansion of the energy spectrum by assuming it is scaled by $\mathcal{L}$ at small wave numbers and by η at large wave numbers and also assuming Kolmogorov's $k^{-5/3}$-spectrum in the inertial subrange. Dynamical equations for the expansion functions are derived from the spectral energy equation and the order of the functions used in the expanions ($\mu_j(Re_\lambda)$) are found to be ${Re_\lambda}^{-j/2}$. Eddies within the inertial subrange are found of size $\sim \lambda {Re_\lambda}^{1/4}$ and the width of the inertial subrange is $\mathcal{O}({Re_\lambda}^{3/4})$.

Finally, the model energy spectrum (4.111) with $a = 5.0$, $b = -5/3$, and $m = 1$ is compared with our numerical spectra. Skewness is predictable by assuming a power-law energy decay and a model spectrum. Using the measured values of G, a parameter in the dissipation rate equation, and decay exponent n, the prediction agrees reasonably well with the numerical data.

Chapter 5

Lagrangian Studies

In this chapter we study the small-scale properties of turbulence whose importance in the improvement of subgrid models for large-eddy simulations and in the understanding of intermittency phenonmena cannot be overemphasized. In many cases the data was collected from the viewpoint of a Lagrangian tracer, i.e., a point moving with the local velocity of the fluid continuum. Let ξ be the initial position of a fluid particle and $\mathbf{x}_p$ be the position of the particle at time t. A Lagrangian tracer or a fluid particle is thus tracked by solving

$$\frac{d\mathbf{x}_p(t)}{dt} = \mathbf{u}(\mathbf{x}_p, t) \quad \text{with} \quad \mathbf{x}_p(0) = \xi. \tag{5.1}$$

Use of Lagrangian coordinates is natural in the study of turbulent dispersion which is fundamental to heat and mass transport problems. Following a fluid particle, the evolution of an infinitsimal material line element can be easily obtained also by solving

$$\frac{d\underline{\ell}}{dt} = (\underline{\ell} \cdot \nabla)\mathbf{u}(\mathbf{x}_p, t) \ \text{ with } \ell(0) \equiv 1. \tag{5.2}$$

The dynamics of this quantity characterizes the stretching power of turbulence. With the Eulerian velocity field $\mathbf{u}(\mathbf{x}, t)$ at hand, we shall solve (5.1) and (5.2) based on finite-difference methods which interpolate velocity and velocity derivatives at the particle's position. Lagrangian statistics are then collected by taking averages over a large number of fluid particles.

The first part of the present study is focused on the Lagrangian velocity autocorrelation function whose importance was first revealed in Taylor's classic work on the diffusion of fluid particles. According to his work, experimentists can determine the Lagrangian velocity autocorrelation function by measuring particle dispersion. For example, Shlien and Corrsin [63] so measured the autocorrelation function in an approximately isotropic, grid-generated turbulent flow and studied its self-preservation. Sato and Yamamoto [60] [61], by means of an optical tracer-particle tracking method, were able to measure directly the Lagrangian autocorrelation function. The results were then compared with the one-point-two-time Eulerian autocorrelation functions obtained from the two-point-one-time functions under the Taylor "frozen" hypothesis. Both measurement techniques found that the Lagrangian autocorrelation function is larger than the Eulerian for all time lags.

Numerical simulations can be used to determine both Lagrangian and Eulierian temporal velocity autocorrelation functions directly but are limited to small to intermediate Reynolds number. Such determinations made by Riley and Patterson [53] in decaying turbulence as well as by Gotoh et al. [29] in stationary turbulence show that the Lagrangian autocorrelation function is larger at small time lags, but smaller at large time lags as opposed to the above-mentioned experimental observations. We notice the Eulerian autocorrelation function measured according to Taylor's "frozen" hypothesis is different from the numerical one which has zero mean flow.

Theoretical studies include Corrsin's use of a "independence" hypothesis [18] to predict that Lagrangian scales are approximately equal to the Eulerian ones under the assumption that both Lagrangian and Eulerian frequency spectra possess Kolmogorov scaling. This work had been extended by Saffman [57] who derived an integro-differential equation for the Lagrangian autocorrelation function. Tennekes [69] further introduced the "advection" concept which introduces a new cutoff frequency and an advection-inertial subrange in addition to the Kolmogorov inertial subrange. Assuming this new cutoff frequency for the Eulerian frequency spectrum

and Kolmogorov cutoff frequency for the Lagrangian frequency spectrum, he obtained different results from Corrsin's. Our ambition here is to measure directly both Lagrangian and Eulerian, temporal and spatial, velocity autocorrelation functions and then examine their relations compared with theoretical predictions.

The second part of this chapter is devoted to the small-scale properties of turbulence from a Lagrangian viewpoint. Similar studies have been done by Yeung and Pope [72] [73], who developed and tested interpolation schemes for particle tracking and studied the acceleration autocorrelation function. Girimaji and Pope [28] also considered material-element deformation in isotropic turbulence. Their work was concerned exclusively with stationary forced turbulence. As discussed by Yeung and Pope [73], decaying turbulence is more difficult to analyze because the energy is decaying and the eddies are growing. Long-time tracking is not possible. However, with a numerical resolution up to 256^3 available and the high speed calculations on a parallel computer, we are able to collect meaningful Lagrangian data in decaying turbulence. Because no artifical forcing is required in the present simulations, there is no concern about the contamination of integral scales by non-physical forcing. However, the effect of periodicity can be harmful.

This chapter is arranged as follows. A description of the interpolation methods used in the present research is given, and their accuracy is tested in Sec. 5.1. Two-time-one-point and one-time-two-point Lagranian and Eulerian velocity autocorrelations as well as particle dispersion are investigated in Sec. 5.2. Small-scale phenomena are next studied in Sec. 5.3. Effects of small-scale properties such as vorticity magnitude and strain magnitude on the evolution of the vorticity vector and the material line element vector are of particular interest. Finally, we attempt to observe the conditions leading to intense vorticity values by following fluid particles and taking advantage of flow visualization techniques. The results are given in Sec. 5.4. Conclusions are given in Sec. 5.5.

5.1 Interpolation Methods

5.1.1 T13 and T36 Schemes

Yeung and Pope [72] have investigated in detail the accuracy of a variety of interpolation methods for particle tracking. They found that the linear interpolation method is too inaccurate for turbulent flows, but cubic spline interpolation is reasonably good. For a planwise data set, they suggest a method called "T13" based on Taylor's series expansion and 13 grid points. The interpolation errors of T13 are found larger than the cubic spline method, but still within reasonable bounds. However, in this method (T13) velocities and velocity derivatives at both the grid points $\mathbf{x}$ and $\mathbf{x} + \Delta\mathbf{x}/2$ are required. Additional FFTs and memory space are therefore required. In order to make the code more efficient, a scheme slightly different from T13 is developed here. In principle we would like a scheme that requires only velocity fields at grid points $\mathbf{x}$ and remains third-order accurate.

The modified T13 method is described as follows. If $\mathbf{x}_p$ is the particle's postion at time t and it locates within a cube centered at the grid point $\mathbf{x}_9$ as shown in Fig. 5.1, the modified T13 algorithm estimates the particle's velocity as

$$\mathbf{u}(\mathbf{x}_p(t), t) \approx \sum_{i=1}^{13} c_i \mathbf{u}(\mathbf{x}_i, t) \tag{5.3}$$

with

$$\begin{aligned}
c_1 &= (-x - y - z + y^2 + xy + xz + yz - xyz)/8, \\
c_2 &= (-x - y - z + y^2 + xy - xz - yz + xyz)/8, \\
c_3 &= (x - y - z + y^2 - xy + xz - yz - xyz)/8, \\
c_4 &= (x - y - z + y^2 - xy - xz + yz + xyz)/8, \\
c_5 &= (-x + y - z + y^2 - xy + xz - yz + xyz)/8, \\
c_6 &= (-x + y - z + y^2 - xy - xz + yz - xyz)/8, \\
c_7 &= (x + y - z + y^2 + xy + xz + yz + xyz)/8,
\end{aligned}$$

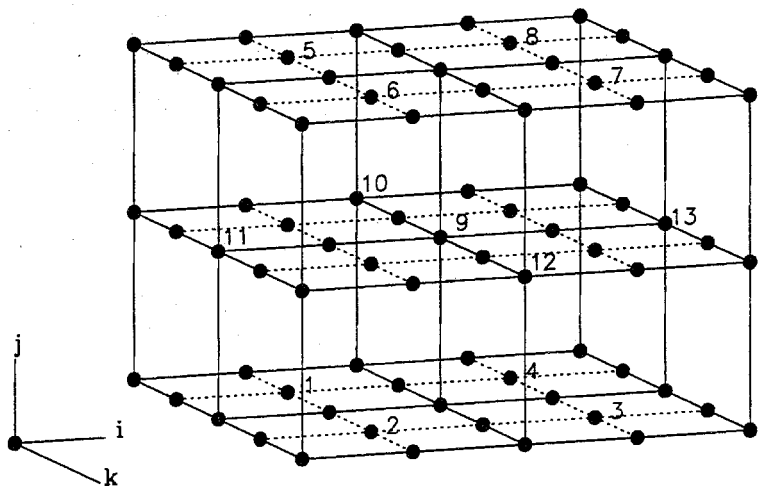

Figure 5.1: Grid points used in the modified T13 scheme. The particle position $\mathbf{x}_p$ is located within the cube shown.

$$
\begin{aligned}
c_8 &= (x + y - z + y^2 + xy - xz - yz - xyz)/8, \\
c_9 &= 1 - \frac{1}{4}x^2 - \frac{1}{2}y^2 - \frac{1}{4}z^2, \\
c_{10} &= (z^2 - y^2)/8, \\
c_{11} &= (x^2 - y^2)/8, \\
c_{12} &= c_{10}, \\
c_{13} &= c_{11},
\end{aligned}
\tag{5.4}
$$

where

$$
\begin{aligned}
x &\equiv (x_p - x_9)/\Delta x, \\
y &\equiv (y_p - y_9)/\Delta y, \\
z &\equiv (z_p - z_9)/\Delta z.
\end{aligned}
$$

It can be shown that with this choice of $\{c_i\}$, the right-hand side of (5.3) gives a third-order accurate particle velocity; that is,

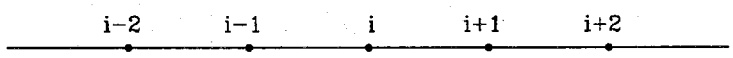

Figure 5.2: Grid points used in (5.6) and (5.7).

$$\sum_{i=1}^{13} c_i \mathbf{u}(\mathbf{x}_i, t) = \mathbf{u}(\mathbf{x}_p, t) + \mathcal{O}(\Delta \mathbf{x}^3). \tag{5.5}$$

In addition, an algorithm, called T36, was developed for interpolating velocity derivatives. The idea of T36 is to reduce the 3-D interpolation problem to a 1-D problem. We consider in a 1-D problem in which $x_i \leq x_p \leq x_{i+1}$, where x_i is the grid point as shown in Fig. 5.2. It can be shown that

$$\begin{aligned} g(x_p) &= \frac{1}{\Delta x}\left(a_{i-1}u(x_{i-1}) + a_i u(x_i) + a_{i+1}u(x_{i+1}) + a_{i+2}u(x_{i+2})\right) \\ &= \frac{\partial u}{\partial x}(x_p) + \mathcal{O}(\Delta x^3) \end{aligned} \tag{5.6}$$

and

$$\begin{aligned} h(x_p) &= b_{i-1}u(x_{i-1}) + b_i u(x_i) + b_{i+1}u(x_{i+1}) \\ &= u(x_p) + \mathcal{O}(\Delta x^3), \end{aligned} \tag{5.7}$$

if

$$\begin{aligned} a_{i-1} &= -\frac{1}{3} + r - \frac{1}{2}r^2, \\ a_i &= -\frac{1}{2} - 2r + \frac{3}{2}r^2, \\ a_{i+1} &= 1 + r - \frac{3}{2}r^2, \\ a_{i+2} &= -\frac{1}{6} + \frac{1}{2}r^2, \end{aligned} \tag{5.8}$$

and

$$b_{i-1} = \frac{1}{2}r^2 - \frac{1}{2}r,$$
$$b_i = 1 - r^2,$$
$$b_{i+1} = \frac{1}{2}r^2 + \frac{1}{2}r, \tag{5.9}$$

and $r = (x_p - x_i)/\Delta x$. In 3D problems, a velocity gradient in a preferred direction is thus so obtained by first forming the third-order accurate velocities in the other two directions using (5.7) and then calculating the gradient in the perferred direction using (5.6). A total of 36 grid points are involved.

5.1.2 Interpoltaion Accuracy

We test the accuracies of the modified T13 and T36 schemes on the gradients of the one-parameter familiy of flows given by

$$u(x, y, z) = \sin(x^n) + \sin(y^n) + \sin(z^n), \tag{5.10}$$

$0 \leq x, y, z \leq 2\pi$ with n = 1, 2 and 3. (T13 is applied to the gradients directly while T36 is applied to the velocity. Therefore, both estimate the gradients of (5.10).) The flows become more complex as n increases. The results of the tests are shown in Fig. 5.3. The errors shown are the averaged absolute difference between the exact solutions and the interpolated results normalized by a factor of $3n(2\pi)^{n-1}$ — the maximum gradient of the flow. Notice that the third-order accuracy is obtained, but larger N is required as the flow becomes more complex as expected, where N is the number of the uniformly distributed grid points in $(0, 2\pi)$. Note T36 scheme behaves strangely when the resolution N is large and the flow is simple. This is probably caused by its using so many grid points and the roundoff errors.

Accuracies of the schemes when tested on the turbulent flows are shown in Fig. 5.4. Turbulent velocity and velocity gradient at $\mathbf{x} + \Delta\mathbf{x}/2$ are interpolated. The difference of the results from those obtained by taking advantage of FFT based on the shifted grid points is treated as the error of the interpolation method. The algorithms are

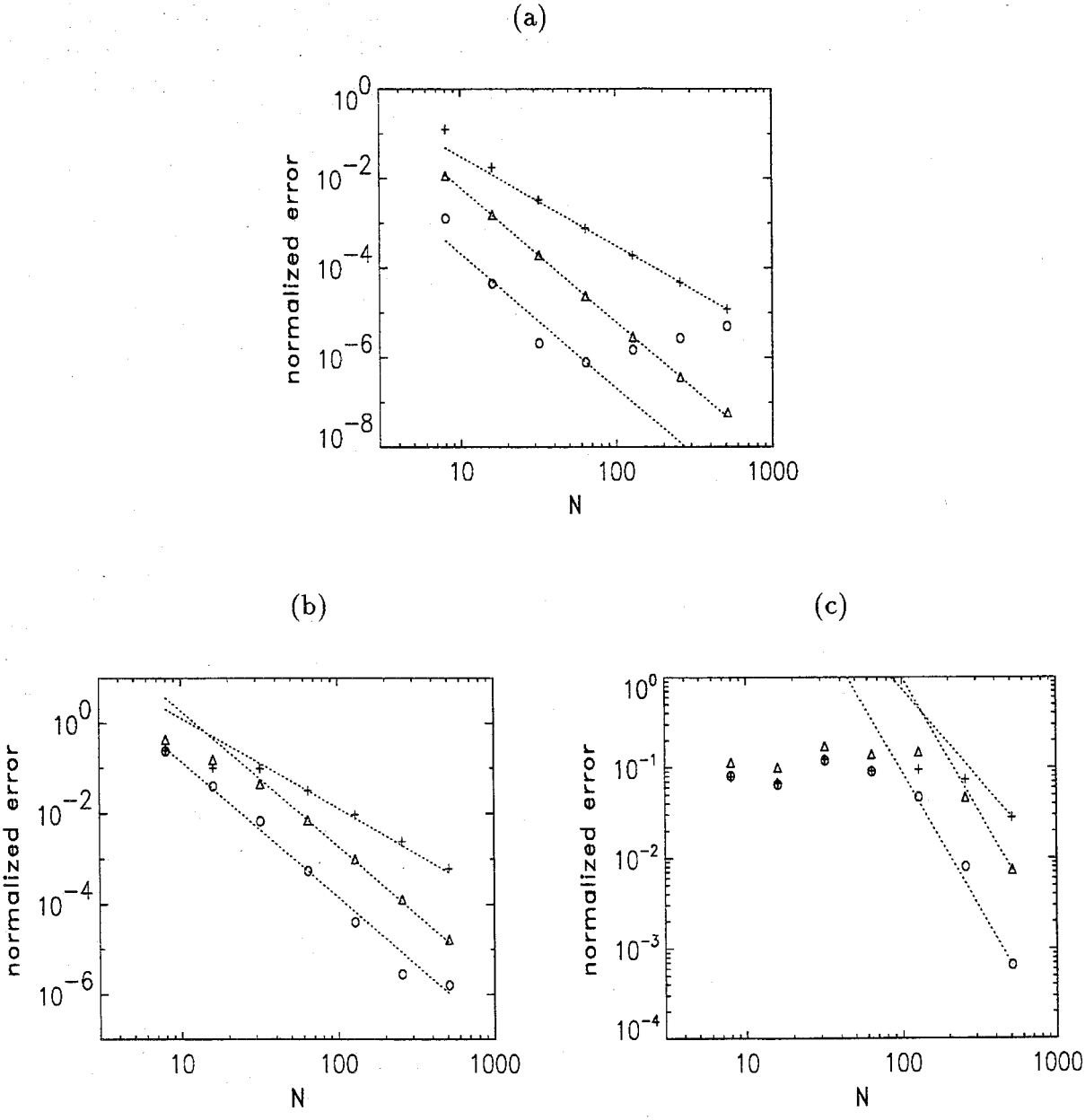

Figure 5.3: Accuracy tests of the modified T13 and T36 schemes on the gradient of the one-parameter (n) family of flows (5.10) with (a) n = 1 (b) n = 2 (c) n = 3. + linear interpolation, Δ T13 , $\circ$ T36

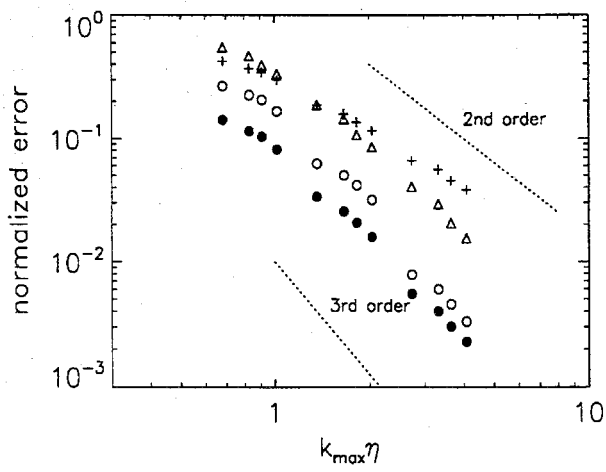

Figure 5.4: Accuracy tests of the modified T13 and T36 schemes on a turbulent flows. + linear interpolation, Δ T13, $\circ$ T36 applied to ∇u; $\bullet$ T13 applied to u.

applied to a single flow at several decaying times. The errors are estimated on one plane of points and normalized by the mean value of the tested field (velocity or velocity derivative). They are plotted as a function of the product of the Kolmogorov's dissipation length η and the maximum available wave number $k_{max} = \frac{\sqrt{2}N}{3}\frac{2\pi}{L}$. In the present simulations, we employ T13 to interpolate particle velocity and T36 to interpolate particle velocity gradients (both methods are applied directly to the velocity field). The above results show that the schemes work well with turbulent flows and suggest that a minimum value of $k_{max}\eta$ of 1.5 is required to have an error under 5%. In the present simulations, we thus release particles at a time at which $k_{max}\eta \approx 2$. The accuracy at later decaying times is expected even better because $k_{max}\eta$ increases with decaying time.

The CPU seconds per time step having the code running on N nodes of the Delta parallel computer with M particles traced are listed in Table 5.1. The increase of CPU times due to the tracing is acceptable.

Table 5.1: CPU seconds per time step for N computer nodes with M particles released.

N \ M	0	4,096	16,384	30,000
128	1.61	2.63	4.50	-
256	7.96	-	11.15	13.17

5.1.3 Simulation Conditions

The Eulerian velocity fields chosen correspond to two of the direct numerical simulations of decaying homogeneous turbulence discussed in chapter 4 (run3 and run5). The Reynolds numbers (Re_λ) of these two cases are about in the same range and $Re_\lambda \approx 42$ when the power-law decay starts ($k_{max}\eta \approx 1$). The box size is 2π on a side for one of the cases (renamed as run1) and 4π for the other (renamed as run2). The latter has twice the Fourier modes in one direction (256) as the former (128) does so that the highest available wavenumbers are the same. Moreover, the decay exponent is found to be about 1.5 for run1 while it is about 1.2 for run2 (see Fig. 5.5 and 5.6). These two cases were chosen primarily to represent the two different decay-exponents. Flow conditions at zero simulated time and at times at which $k_{max}\eta \approx 1$ and $k_{max}\eta \approx 2$ can be found in Table 5.2.

We recall that the initial energy spectrum chosen for run1 is

$$E(\mathrm{k},0) = \begin{cases} Cq^2 \exp(-a)(\mathrm{k}/k_p)^2 & \text{for } 0 \le \mathrm{k} \le k_p \ ; \\ Cq^2(\mathrm{k}/k_p)^{-5/3} \exp\left(-a\ \mathrm{k}/k_p\right) & \text{for } k_p \le \mathrm{k} \end{cases} \tag{5.11}$$

and that for run2 is

$$E(\mathrm{k},0) = \frac{3}{2}\frac{q^2}{k_p}\left(\frac{2k}{k_p}\right)^2 \exp\left(-\frac{2k}{k_p}\right). \tag{5.12}$$

The eddy-turnover time $\mathcal{T}_o$ and the dissipation time scale τ_η are defined as

$$\mathcal{T}_o \equiv \frac{3\pi}{4q}\int_0^\infty \mathrm{k}^{-1}E(\mathrm{k},t)\ d\mathrm{k} \Big/ \int_0^\infty E(\mathrm{k},t)\ d\mathrm{k} \tag{5.13}$$

and

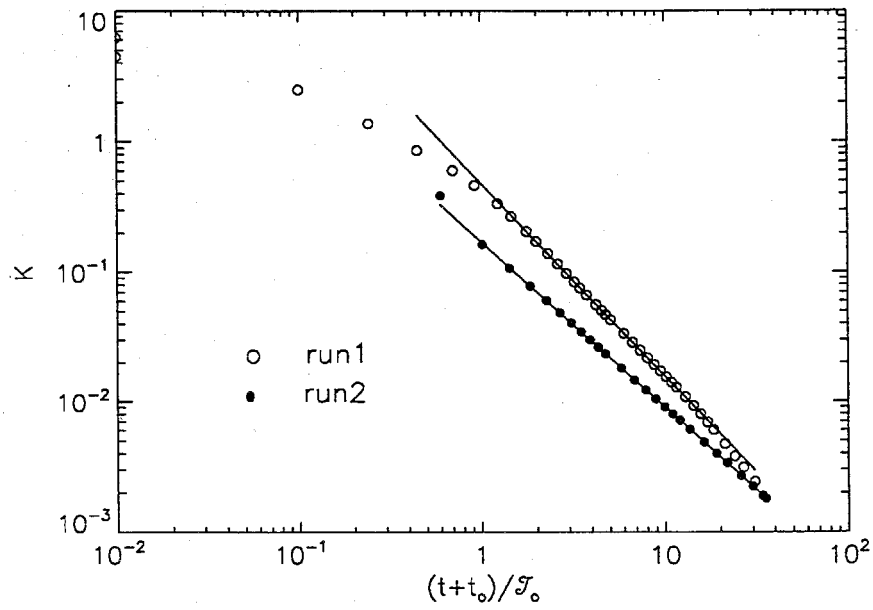

Figure 5.5: Decay of turbulent energy $K = 3q^2/2$. The time is nondimensionalized by the eddy-turn-over time $\mathcal{T}_o$ at a time at which $k_{max}\eta \approx 1$.

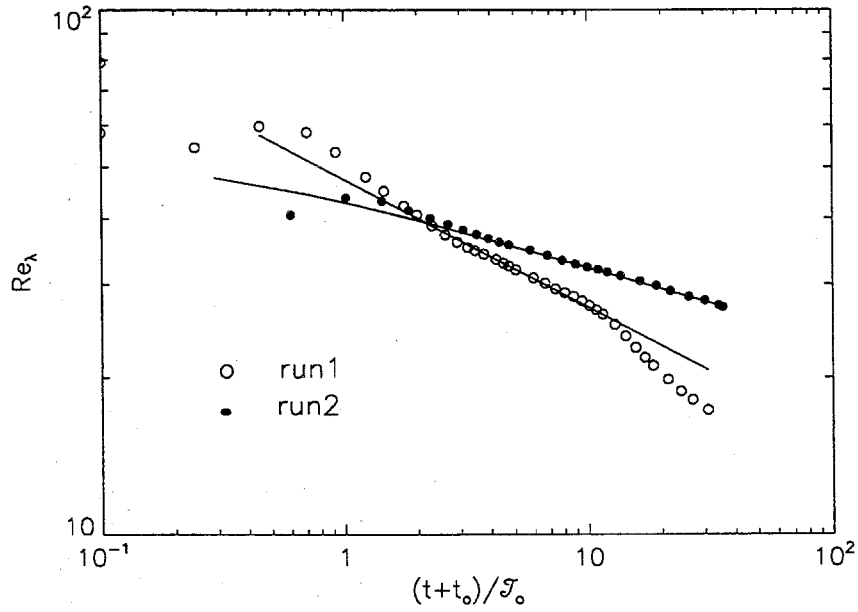

Figure 5.6: Decay of Reynolds number $Re_\lambda = q\lambda/\nu$.

Table 5.2: Flow Conditions at $t = 0$ and at times at which a power-law energy decay starts ($k_{max}\eta \approx 1$) and at which particles were released ($k_{max}\eta \approx 2$ or $t = t_*$).

	k_p	ν	L	N	M	
run1	4	0.002	2π	128	16,384	
run2	6	0.0013	4π	256	30,000	
	$t = 0$		$k_{max}\eta \approx 1$		$k_{max}\eta \approx 2$	
	run1	run2	run1	run2	run1	run2
Re_λ	203.10	165.48	42.29	42.62	32.81	35.74
λ/L	4.3%	1.7%	3.6%	1.7%	5.7%	3.0%
$\mathcal{T}_o$	0.22	0.40	2.09	2.89	5.84	8.26
τ_η	0.022	0.055	0.16	0.22	0.51	0.77

$$\tau_\eta \equiv \eta^2/\nu \tag{5.14}$$

respectively. In the following sections, we will refer a Lagrangian average as an average taken over released particles. There were a total of $128^2 = 16384$ particles released in run1 while 30,000 were released in run2. Particles are initially randomly placed in the periodic physical domain. The sampling error is known proportional to $M^{-1/2}$, where M is the number of particles released. In the present simulations, we estimate that this error is relatively small compared with the interpolating errors and time differencing errors [28].

In the present study, we concentrate on the comparisons of numerical results of simulations with theories assuming isotropic turbulence, even though we observed that simulated decaying turbulence loses isotropy as Re_λ decreases. When applicable, however, we take averages over all three directions.

5.2 Double Velocity Correlations

In studying the transport and dispersion processes in a turbulent flow, G.I. Taylor [67] was first to note the the importance of Lagrangian statistics. In particular, the spread of matter, such as smoke from a smokestack, can be predicted by Lagrangian velocity autocorrelations following a single particle (see [67]) for homogeneous isotropic turbulence

$$\begin{aligned}\frac{d < X^2 >}{d\tau} &= 2\int_0^\tau \overline{u(\xi,\tau)u(\xi,\tau')}d\tau' \\ &= 2\int_0^\tau q(\tau)q(\tau')f_L(\tau',\tau)d\tau' \end{aligned} \tag{5.15}$$

where $< X^2 >$ is the mean square displacement of particles, $q(\tau)$ is turbulent velocity at time τ, and f_L is Lagrangian velocity autocorrelation coefficient defined below. The significance of particle dispersion lies not only in the spread of matter, but also in the significant transport of momentum, heat, and kinetic energy, usually dominating over transport by molecular diffusion.

Considering the anisotropy observed in low-Re_λ turbulence, we average the correlations over the three directions and treat the results as isotropic. We compute the spatial correlation coefficients as follows

$$f(r,\tau) = \frac{1}{3}\overline{u_i(\mathbf{x},\tau)u_i(\mathbf{x}+r\mathbf{e}_i,\tau)}/q^2(\tau), \tag{5.16}$$

where the overbar represents a volume average. The two-time-one-point Eulerian and Lagrangian coefficients are computed as

$$f_E(\tau',\tau) = \frac{1}{3}\overline{u_i(\mathbf{x},\tau)u_i(\mathbf{x},\tau')}/q(\tau)q(\tau') \tag{5.17}$$

and

$$f_L(\tau',\tau) = \frac{1}{3} < u_i(\xi,\tau)u_i(\xi,\tau') > /q(\tau)q(\tau'). \tag{5.18}$$

Note both τ and τ' are measured from the time the particles were released. The notation $< \cdot >$ represents a Lagrangian averaging and ξ is the Lagrangian marker. Moreover, with the Fourier components of velocity fields at hand, we can easily compute f_E as

$$f_E(\tau', \tau) = \frac{1}{3} \sum_{\mathrm{k}} \hat{u}_i(\mathrm{k}, \tau) \hat{u}_i^*(\mathrm{k}, \tau') / q(\tau) q(\tau') \tag{5.19}$$

and

$$\begin{aligned} 3f(r, \tau) = & \sum_{k_1} \left(\sum_{k_2, k_3} \hat{u}_1(\mathrm{k}, \tau) \hat{u}_1^*(\mathrm{k}, \tau) \right) \exp(-ik_1 r) \\ & + \sum_{k_2} \left(\sum_{k_3, k_1} \hat{u}_2(\mathrm{k}, \tau) \hat{u}_2^*(\mathrm{k}, \tau) \right) \exp(-ik_2 r) \\ & + \sum_{k_3} \left(\sum_{k_1, k_2} \hat{u}_3(\mathrm{k}, \tau) \hat{u}_3^*(\mathrm{k}, \tau) \right) \exp(-ik_3 r) \end{aligned} \tag{5.20}$$

where " * " means the complex conjugate.

We now consider time and length scales. The Eulerian and Lagrangian dissipation time scales, τ_E and τ_L, are defined as

$$\tau_E = \left(-\frac{\partial^2 f_E}{\partial^2 \tau'} \right)_{\tau'=\tau}^{-1/2} \tag{5.21}$$

and

$$\tau_L = \left(-\frac{\partial^2 f_L}{\partial^2 \tau'} \right)_{\tau'=\tau}^{-1/2}. \tag{5.22}$$

The integral scales are given by

$$\mathcal{T}_E = \int_0^\infty f_E(\tau', \tau) d\tau', \tag{5.23}$$

and

$$\mathcal{T}_L = \int_0^\infty f_L(\tau', \tau) d\tau'. \tag{5.24}$$

The quantities $\mathcal{L}_E = q\mathcal{T}_E$ and $\mathcal{L}_L = q\mathcal{T}_L$ are then defined as the integral Eulerain and Lagrangian length scales, respectively. The dissipation length scale of $f(r, \tau)$ is well-known as Taylor's microscale λ and its integral scale, denoted by $\mathcal{L}_f$, is given by

$$\mathcal{L}_f = \int_0^\infty f(r, \tau) dr. \tag{5.25}$$

5.2.1 Relations Among Velocity Autocorrelation Functions

5.2.1.1 Dissipation Time and Length Scales

The behaviors of velocity autocorrelation functions at small time lag $(\tau' - \tau)$ or small spatial distance (r) are given in terms of their dissipation time/length scales. Here we introduce two dimensionless parameters as ratios of dissipation scales as follows

$$\alpha \equiv \frac{q\tau_E}{\lambda} \tag{5.26}$$

$$\beta \equiv \frac{q\tau_L}{\lambda}. \tag{5.27}$$

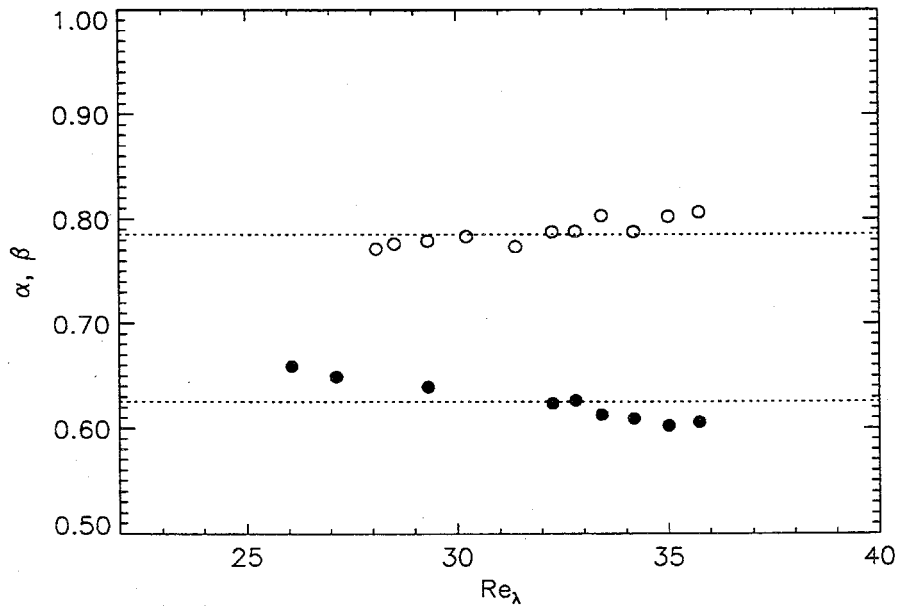

Figure 5.7: (1) • $\alpha \equiv q\tau_E/\lambda$ (2) ∘ $\beta \equiv q\tau_L/\lambda$.

In general we expect α and β to be τ-dependent; our numerical results show the dependence is very weak (see Fig. 5.7). The time scales τ_L and τ_E are calculated by determining the curvatures of f_L and f_E at $\tau' = \tau$ with fourth-order finite differencing

assuming a parabolic behavior near $\tau' = \tau$ for both autocorrelation functions. A slight increase of α and a slight decrease of β with decreasing Re_λ are observed. The average value of α is 0.624 and that of β is 0.785 within the range of Re_λ investigated. We recall that Corrsin [18] applied Kolmogorov scaling in the inertial subrange to the frequency spectra of both the Lagrangian and Eulerian velocity autocorrelation functions and obtained $\alpha,\ \beta \sim {Re_\lambda}^{1/2}$. A prediction by Heisenberg [32] suggests that for low Reynolds number

$$\beta^2 = {Re_\lambda}^2 / \left(a Re_\lambda + b\lambda^4 f^{iv}(0,\tau) \right) \tag{5.28}$$

with constant a and b. Both theories predict an increasing β with increasing Re_λ as observed in our numerical results, although the observed increase is very gradual.

The above prediction of an increasing α with decreasing Re_λ, on the other hand, is in opposition to the present numerical results. Tennekes [69] questioned this result and proposed a modification. Noting that an Eulerian observer sees small eddies convected by large eddies, Tennekes suggests a new cutoff frequency q/η for the Eulerian velocity autocorrelation function, which is larger than the one for the Lagrangian function based on Kolmogorov scaling, namely v_η/η or $(\epsilon/\nu)^{1/2}$. Tennekes further predicts τ_E by assuming Taylor's "frozen" hypothesis, which approximates

$$\frac{\partial u}{\partial t} \approx -u\frac{\partial u}{\partial x} - v\frac{\partial u}{\partial y} - w\frac{\partial u}{\partial z},$$

and by assuming that the energy-containing eddies and the dissipation eddies are statistically independent so that in an isotropic turbulent flow

$$\overline{\left(\frac{\partial u}{\partial t}\right)^2} = 5\overline{u^2}\,\overline{\left(\frac{\partial u}{\partial x}\right)^2}. \tag{5.29}$$

Together with the other isotropic relation $\epsilon = 15\nu\overline{\left(\frac{\partial u}{\partial x}\right)^2}$, he obtains

$$\tau_E^2 \equiv \frac{2\overline{u^2}}{\overline{(\partial u/\partial t)^2}} = \left(\frac{6\nu}{\epsilon}\right) \quad \text{or} \quad \alpha = \sqrt{2/5} \approx 0.632. \tag{5.30}$$

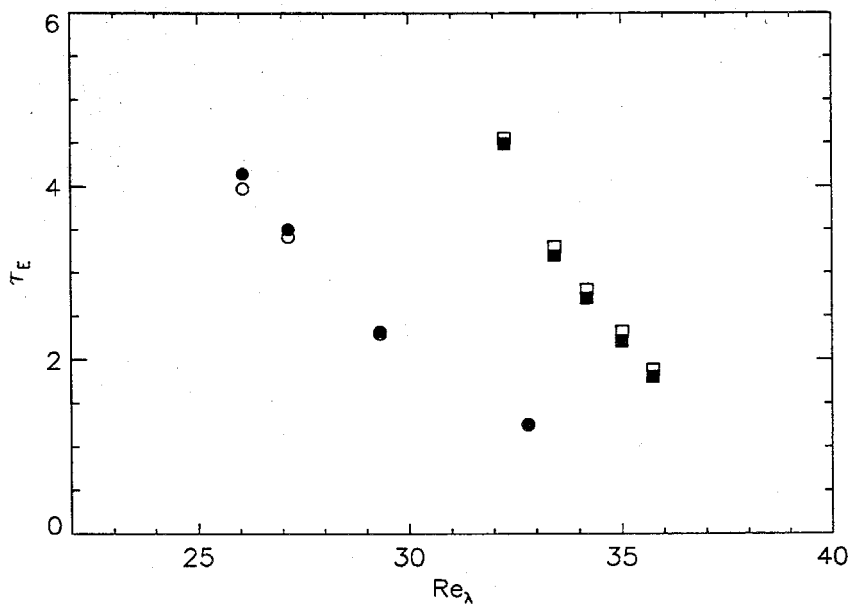

Figure 5.8: Numerical measurements (solid symbols) and Tennekes' prediction (open symbols) of τ_E. o is for run1 and ▫ for run2.

Comparisons between the numerical results and the prediction of (5.30) are given in Fig. 5.8. The agreement is quite good. On the other hand, Yeung and Pope [73] examined Tennekes' assumptions and found no agreement with their numerical results up to at least $Re_\lambda = 93$, the highest Re_λ in their numerical simulations. Their conclusion, however, is questionable because the sample of particles they used (M=4000) was not large and their turbulence was forced. In addition, their examination only included an analysis of one component, $\overline{(\frac{\partial u_1}{\partial t})^2}$, for a single timestep so that isotropy of the data is suspect.

Finally, we notice the result $\alpha < \beta$ actually implies $\tau_E < \tau_L$ or $f_E < f_L$ at small time lags as also observed by previous investigators ([53] [63]). The same result was obtained also by Kaneda and Gotoh who applied the Lagrangian renormalized approximation to a Gaussian velocity distribution [34]. The advection concept of Tennekes suggests that the Lagrangian autocorrelation is more persistent than the Eulerian one (because in the latter case new fluid particles are continuously swept

the observation point), and, therefore, suggests $f_E < f_L$ at small time lags as well.

5.2.1.2 Comparisons

The computed autocorrelation functions are plotted against $(\tau' - \tau)/\mathcal{T}_o(\tau = 0)$ in Fig. 5.9ab and Fig. 5.10ab. These curves are clearly non-symmetric because the turbulence is decaying. Longer tails are observed at positive $(\tau' - \tau)$s than negative ones, implying eddies lose their memory more slowly at later times. The decay of f_E at the larger times appears slow. One might even doubt the existence of its first integral moment, namely $\mathcal{T}_E$. In any case, the results as shown are insufficient to compute $\mathcal{T}_E$ directly.

Finally, we compare the velocity temporal/spatial autocorrelation functions by plotting them together against variables $(\tau' - \tau)/\tau_L$, $(\tau' - \tau)/\tau_E$, and r/λ respectively (see Fig. 5.11ab) [32] [57] [60]. These three autocorrelation functions as seen differ from each other except that f_E (against $(\tau' - \tau)/\tau_E$) is close to $f(r, \tau)$ (against r/λ) for negative $(\tau' - \tau)$s (negative r). Tails of $f_E(\tau', \tau)$ are the longest among the three, implying the convective effect of large eddies to an Eulerian observer as suggested by Tennekes [69].

5.2.2 Similarity of $f_L(\tau', \tau)$

In stationary turbulence. f_E and f_L are self-preserving (depending only on $\tau' - \tau$); in decaying turbulence, it was first argued by Batchelor and Townsend [12] that Lagrangian velocity correlation coefficients may be self-similar as well in a new time variable s, provided a power-law decay of turbulent kinetic energy exists (see [33] [60]). Batchelor and Townsend's argument is described as follows. Suppose that turbulent energy decays according to a power-law, namely

$$K \sim (t + t_o)^{-n} \sim (\tau + \tau_o)^{-n},$$

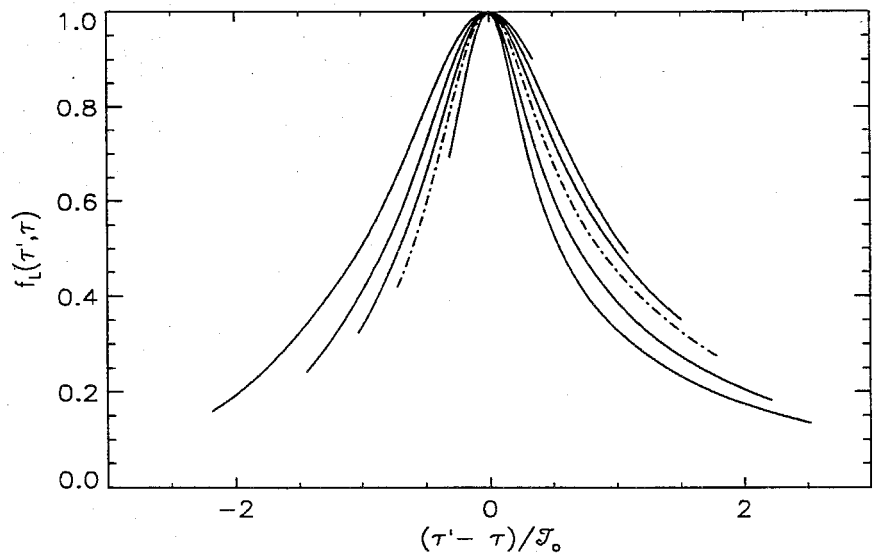

Figure 5.9a: Lagrangian velocity correlation coefficients $f_L(\tau', \tau)$ at several different τ for run1. The dash dotted curve is one of them at one particular time for clarity. Time is nondimensionalized by the eddy-turn-over time $\mathcal{T}_o(\tau = 0) = 5.84$.

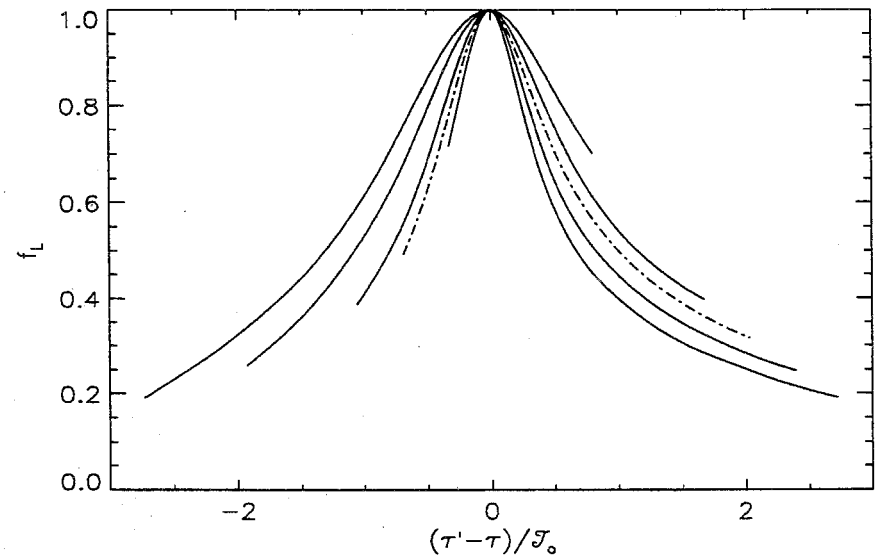

Figure 5.9b: Lagrangian velocity correlation coefficients $f_L(\tau', \tau)$ at several different τ for run2. The dash dotted curve is one of them at one particular time for clarity. Time is nondimensionalized by the eddy-turn-over time $\mathcal{T}_o(\tau = 0) = 8.26$.

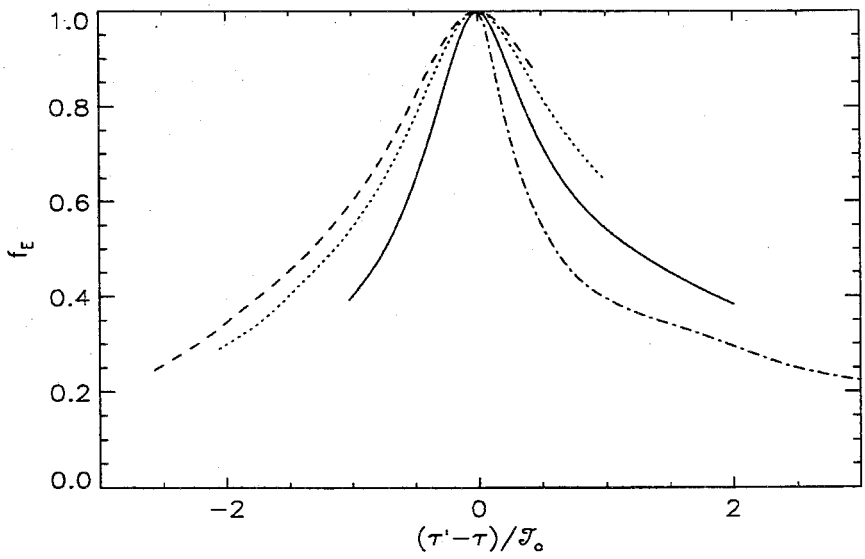

Figure 5.10a: Eulerian velocity correlation coefficients $f_E(\tau', \tau)$ at several different τ for run1.

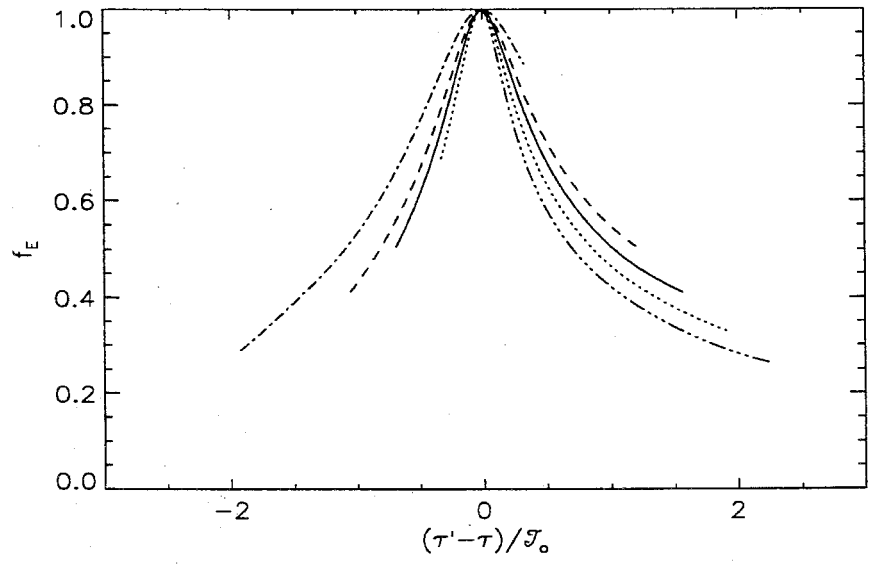

Figure 5.10b: Eulerian velocity correlation coefficients $f_E(\tau', \tau)$ at several different τ for run2.

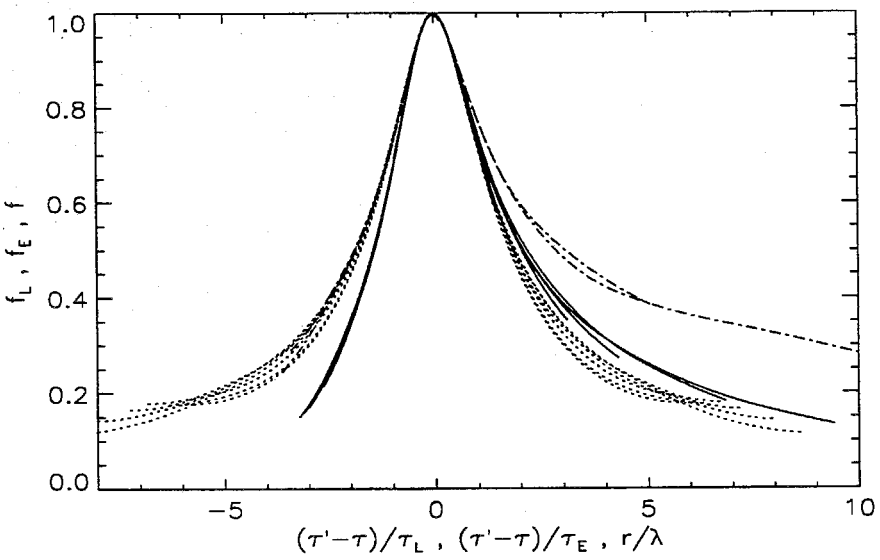

Figure 5.11a: Velocity correlation coefficients (run1): (1) —— $f_L(\tau',\tau)$ (2) $-\cdot-$ $f_E(\tau',\tau)$ (3) $\cdots\cdots$ $f(r,\tau)$ against $(\tau'-\tau)/\tau_L$, $(\tau'-\tau)/\tau_E$ and r/λ respectively.

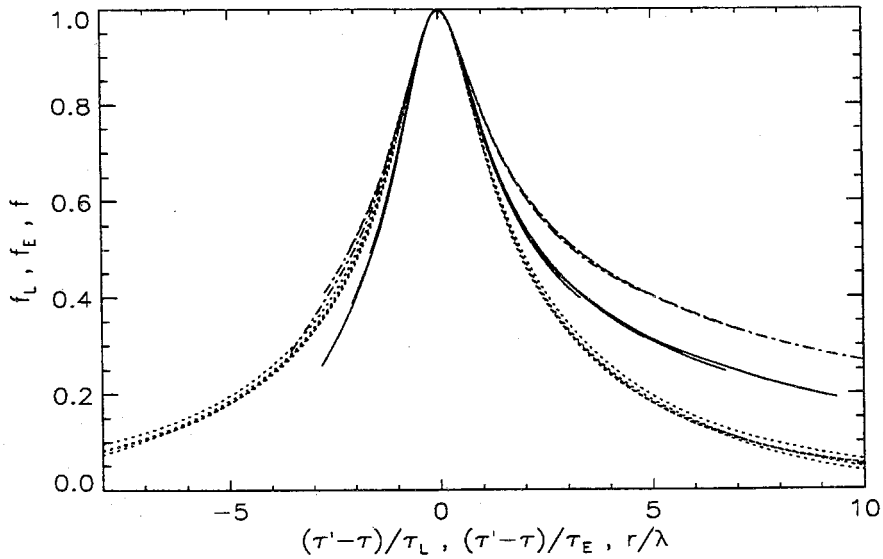

Figure 5.11b: Velocity correlation coefficients (run2): (1) —— $f_L(\tau',\tau)$ (2) $-\cdot-$ $f_E(\tau',\tau)$ (3) $\cdots\cdots$ $f(r/\lambda,\tau)$ against $(\tau'-\tau)/\tau_L$, $(\tau'-\tau)/\tau_E$ and r/λ respectively.

where t_o ($\tau_o = t_o + t_*$) is some reference time origin, there may exist some characteristic time scale, τ_s, such that $u(\tau)\,(1+\tau/\tau_o)^{n/2}$ is a stationary random function of a new time variable s defined by $ds \equiv d\tau/\tau_s(\tau)$. Consequently, the Lagrangian correlation coefficients are self-similar in this new time variable s since

$$\begin{aligned} f_L(\tau',\tau) &\equiv \frac{< u(\xi,\tau)u(\xi,\tau') >}{q(\tau)q(\tau')} \\ &= \frac{< \left(u(\xi,\tau)(1+\tau/\tau_o)^{n/2}\right)\left(u(\xi,\tau')(1+\tau'/\tau_o)^{n/2}\right) >}{\left(q(\tau)(1+\tau/\tau_o)^{n/2}\right)\left(q(\tau')(1+\tau'/\tau_o)^{n/2}\right)} \\ &= \frac{< \tilde{u}(\xi,s)\tilde{u}(\xi,s') >}{\tilde{q}(s)\tilde{q}(s')} \\ &= \bar{f}_L(s',s) \\ &= \tilde{f}_L(s'-s) \equiv \tilde{f}_L(s''), \end{aligned} \tag{5.31}$$

where $\tilde{u}(\tau) \equiv u(\tau)(1+\tau/\tau_o)^{n/2}$ and $\tilde{q}(\tau) \equiv q(\tau)(1+\tau/\tau_o)^{n/2}$.

The determination of $\tau_s(\tau)$ still needs to be made. It should be, as a consequence of the hypothesis, related to the Lagrangian integral time scale $\mathcal{T}_L$ by

$$\begin{aligned} \mathcal{T}_L(\tau) &\equiv \int_\tau^\infty f_L(\tau',\tau)\, d\tau' \\ &= \int_s^\infty f_L(\tau',\tau)\, \tau_s(\tau')\, ds' \\ &= \int_s^\infty \bar{f}_L(s',s)\, \tau_s(s')\, ds' \\ &= \int_0^\infty \tau_s(s+s'')\, \tilde{f}_L(s'')\, ds'', \end{aligned} \tag{5.32}$$

where we write $\tau_s(\tau(s)) = \tau_s(s)$ for simplicity. Batchelor and Townsend [12] suggested that $\tau_s \sim \lambda/q$ while Sato and Yamamoto [60] proposed $\tau_s \sim \mathcal{T}_L$. However, because of different assumptions (Batchelor and Townsend assumed the decay exponent n=1 while Sato and Yamamoto used empirical relations $\mathcal{L}_L/\mathcal{L}_f$=constant and $\mathcal{L}_L/\lambda \sim Re_\lambda$), they both found that $\tau_s(\tau) \sim (\tau+\tau_o)$; therefore, $s = log(1+\tau/\tau_o)$ and $\tau_s(s) = \tau_o e^s$ for $s(\tau=0) \equiv 0$. Although (5.32) does not necessarily give $\tau_s \sim \mathcal{T}_L$, the choice of $\tau_s = (\tau+\tau_o)$ does result in $\tau_s \sim \mathcal{T}_L$. Moreover, $\tau_s(s+s'') = \tau_s(s)\tau_s(s'')/\tau_o$; therefore,

$$\mathcal{T}_L = (\tau+\tau_o)\int_0^\infty e^{s''}\, \tilde{f}_L(s'')\, ds'', \tag{5.33}$$

implying $\mathcal{T}_L$ grows linearly in time. For $\mathcal{T}_L$ to exist, a $\tilde{f}_L(s'')$ must decay faster than $e^{-s''}$.

The choice of $\tau_s \sim \mathcal{T}_L$ seems reasonable, but the empirical relations used by Sato and Yamamoto are not supported by experimental data. Recall the empirical equation describing the energy decay,

$$\frac{dq^2}{dt} \sim \frac{q^3}{\mathcal{L}} \tag{5.34}$$

where $\mathcal{L}$ is the length scale characterizing the decay of energy. A substantial amount of literature has been devoted to the predictions of $\mathcal{L}$, and it is usually believed that $\mathcal{L} \sim \mathcal{L}_f$ for they are both dominated by large-scale eddies. Also, it is usually assumed that $\beta \equiv \mathcal{L}_L/\mathcal{L}_f$ is a constant ([18] [31] [57] [61] [63] [73]) which then implies $\mathcal{L}_L \sim \mathcal{L}_f \sim \mathcal{L}$. Without considering the validity of $\mathcal{L} \sim \mathcal{L}_f$ or the constancy of β, we accept $\mathcal{L} \sim \mathcal{L}_L$. In particular, at large Reynolds number, if one approximates the energy spectrum by

$$E(k) = \begin{cases} 0 & \text{for } k < k_o = \mathcal{L}^{-1} \\ C\epsilon^{2/3}k^{-5/3}, & \text{for } k_o \le k \le k_\eta = 1/\eta \\ 0 & k > k_\eta, \end{cases} \tag{5.35}$$

and approximates the Lagrangain frequency spectrum (frequency ω) by

$$\phi_L(\omega) = \begin{cases} 0 & \text{for } \omega < \omega_o = \mathcal{T}_L^{-1} \\ B\epsilon\omega^{-2}, & \text{for } \omega_o \le \omega \le \omega_\eta = (\epsilon/\nu)^{1/2} \\ 0 & \omega > \omega_\eta, \end{cases} \tag{5.36}$$

then

$$q^2 \sim \int_0^\infty E(k)dk \sim \int_0^\infty \phi_L(\omega)d\omega \tag{5.37}$$

leads to $q\mathcal{T}_L \sim \mathcal{L}$. Consequently,

$$\tau_s \sim \mathcal{T}_L \sim \mathcal{L}/q \sim \lambda Re_\lambda/q \sim (\tau + \tau_o) \tag{5.38}$$

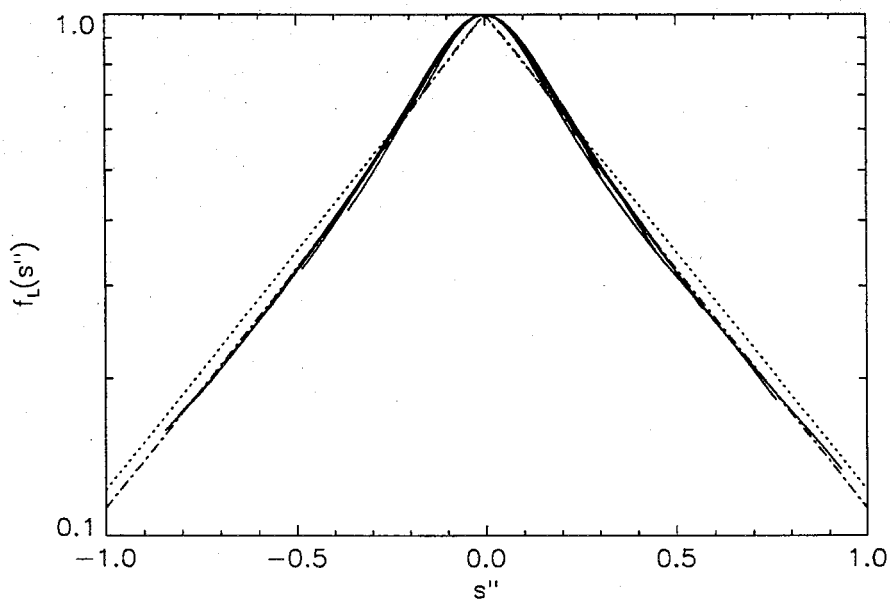

Figure 5.12a: The Lagrangian autocorrelation function $\tilde{f}_L(s'')$ for run1.

and $s = log\,(1 + \tau/\tau_o)$. Note the result is as the same as that of previous investigators but based on the assumptions of $\tau_s \sim \mathcal{T}_L$ and $\mathcal{L}_L \sim \mathcal{L}$.

The function $\tilde{f}_L$ as a function of $s'' = s' - s$ is shown in Fig. 5.12ab. Note this function is even because $f_L(\tau, \tau') = f_L(\tau', \tau)$ implies $\tilde{f}_L(s - s') = \tilde{f}_L(s' - s)$. The existence of a self-similarity is clear. Moreover at large s'', the tail becomes exponential, i.e., $\tilde{f}_L(s'') \sim \exp(-s''/T_s)$, implying an algebraic decay of $f_L(\tau', \tau)$ at large time lags. The measured $T_s < 1$ (see Table 5.3) suggests that the integral in (5.33) converges. If we define $\mathcal{L} = q^3/\epsilon$ and use (5.33) to estimate $\mathcal{L}_L = q\mathcal{T}_L$, the ratio of $\mathcal{L}/\mathcal{L}_L$ is shown in Fig. 5.13. Note since we have used (5.33), a result of the assumptions, Fig. 5.13 only shows how large the ratio $\mathcal{L}/\mathcal{L}_L$ is and its dependence on the initial conditions (about 0.54 for one run and 0.30 for the other), but can not be used to support the assumptions.

With the similarity and (5.33), we can now calculate $\mathcal{T}_L$ (by extending the exponential tail of the self-similar autocorrelation function to infinity) and thus show f_L

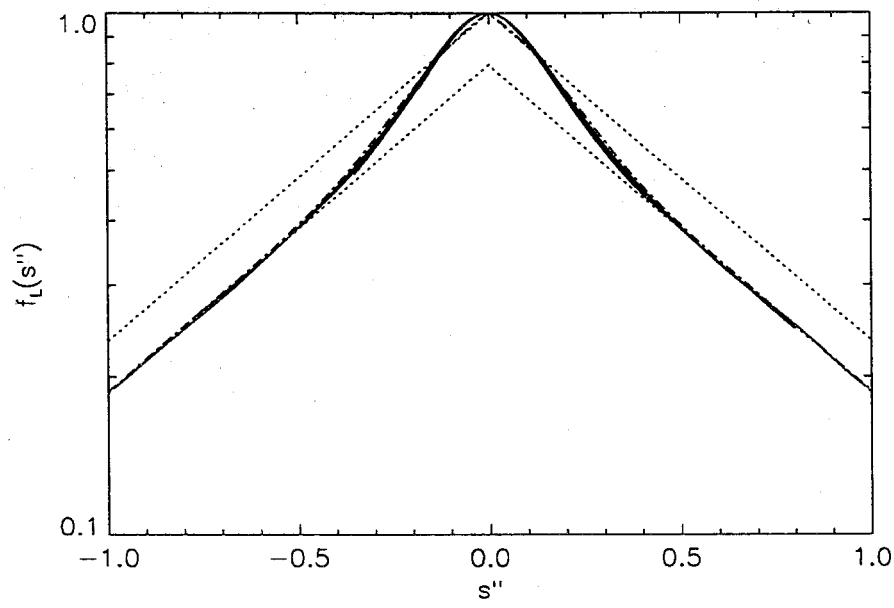

Figure 5.12b: The Lagrangian autocorrelation function $\widetilde{f}_L(s'')$ for run2.

against $(\tau' - \tau)/\mathcal{T}_L(\tau)$. The results are shown in Fig. 5.14 and compared with the data measured by Sato and Yamamoto. Their data agrees with the autocorrelations measured by Yeung and Pope [73] of stationary turbulence, but nontheless not with ours of decaying turbulence, although they declared they had caught the decay effects in their measurements.

Table 5.3: Power-law decay exponents and some important characteristic time scales.

	n	τ_o	T_s	b
run1	1.48	9.61	0.475	12
run2	1.27	13.50	0.688	4

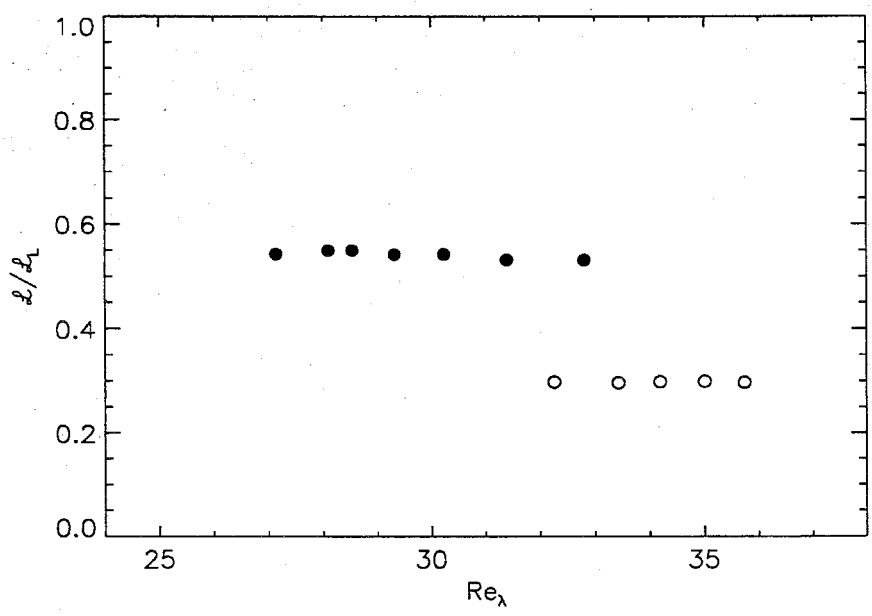

Figure 5.13: The ratio of the integral length scales, $\mathcal{L}/\mathcal{L}_L$: (1) • for run1 (2) ○ for run2.

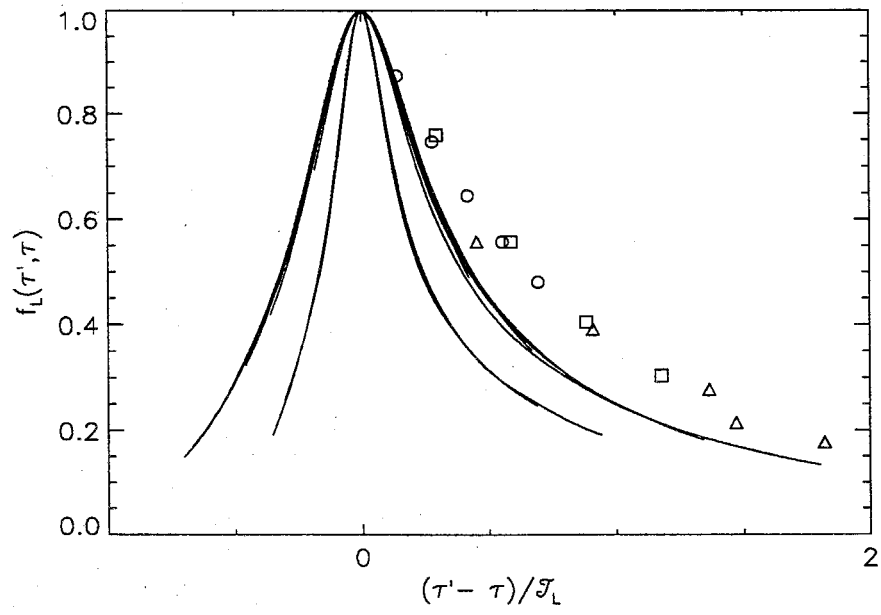

Figure 5.14: f_L verus $(\tau'-\tau)/\mathcal{T}_L$ with $\mathcal{T}_L$ calculated by (5.33). The curves decaying faster are from run2 and the others are from run1. Symbols are from the data of Sato and Yamamoto: △ $Re_\lambda = 66$ ▫ $Re_\lambda = 46$ ○ $Re_\lambda = 25$.

5.2.3 Particle Dispersion

We now compare the diffusion of particles predicted by the classic work of Taylor using our self-similar f_L determined above with "experimental" data obtained by our simulations. Applying the similarity hypothesis to (5.15), one obtains

$$\begin{aligned}\frac{d}{d\tau} < X^2(\tau) > &= 2\tau_o q_o^2\, e^{(1-n)s} \int_0^s \exp\left((1-\frac{n}{2})s''\right) \tilde{f}_L(s'')ds', \\ &= 2\tau_o q_o^2\, e^{(1-n)s} \int_0^s \exp\left(-(1-\frac{n}{2})s''\right) \tilde{f}_L(s'')ds'' \qquad (5.39)\end{aligned}$$

using $q(\tau) = q_o(1+\tau/\tau_o)^{-n/2}$ and $\tilde{f}_L(-s'') = \tilde{f}_L(s'')$, where $q_o \equiv q(\tau = 0)$. For small τ ($s'' \ll 1$), $\tilde{f}_L \approx 1$ and

$$\int_0^s \exp\left(-(1-\frac{n}{2})s''\right) \tilde{f}_L(s'')ds'' \approx s + \mathcal{O}(s^2);$$

therefore,

$$\begin{aligned}\frac{d}{d\tau} < X^2 > &\approx 2\tau_o q_o^2\, s\, e^{(1-n)s} \\ &= 2\tau_o q_o^2\, log(1+\tau/\tau_o)\,(1+\tau/\tau_o)^{1-n} \\ &= 2q_o^2\,\tau + \mathcal{O}(\tau^2). \qquad (5.40)\end{aligned}$$

That is $< X^2 > \approx q_o^2\tau^2$ at small τ. On the other hand, as $\tau \to \infty$ ($s \to \infty$), provided the integral in (5.39) converges, one can show

$$< X^2 > \approx C(n)\, \tau_o^2\, q_o^2\, (1+\tau/\tau_o)^{(2-n)}, \qquad (5.41)$$

where

$$C(n) = \frac{2}{(2-n)} \int_0^\infty \exp\left(-(1-\frac{n}{2})s''\right) \tilde{f}_L(s'')ds''. \qquad (5.42)$$

The long-time growth as seen is different from that of a stationary turbulence. In a stationary turbulence one would expect $< X^2 > \sim \tau$ as $\tau \gg 1$, provided the integral in (5.15) converges. Note the result (5.41) can not be applied to a stationary turbulence by simply assuming n=0 because the new time variable s does not exist at all in a stationary turbulence ($\tau_s \neq \tau_s(\tau)$).

Numerical results and the solutions of (5.39) obtained by assuming

$$\tilde{f}_L(s'') = \exp(-\frac{s''}{T_s}) \tag{5.43}$$

with T_s listed in Table 5.3 and by assuming

$$\tilde{f}_L(s'') = \left(\exp(-s''^2/2s_o^2) + b\exp(-s''/T_s)\right)/(1+b), \tag{5.44}$$

where the parameter b is used to adjust the tail of $\tilde{f}_L(s'')$ to the correct asymptote, are plotted together in Fig. 5.15ab. The use of (5.43) slightly overestimates $< X^2 >$ because it overestimates the exponential tails of $\tilde{f}_L(s'')$. The use of b in (5.44) on the other hand provides an adjustment of the curve to match the measured exponential tails at large values of s''. The improvement of the agreement between theoretical curves and experimental data at large s'' is thus obtained. The asymptotic behavior of $< X^2(\tau) > \sim (1+\tau/\tau_o)^{2-n}$ at large time τ is not observed yet, but expected.

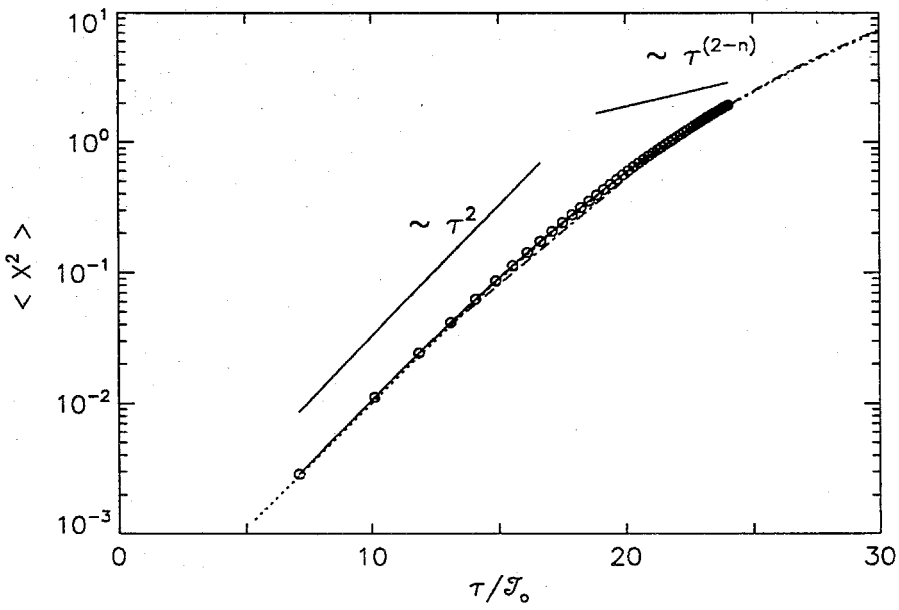

Figure 5.15a: The mean square displacement of particles, $< X^2 >$, for run1. "Experimental" data computed directly from Lagrangian histories are shown by symbols. Predictions based on the similarity hypothesis with (5.43) and (5.44) are shown by the dotted and dash dotted curves, respectively.

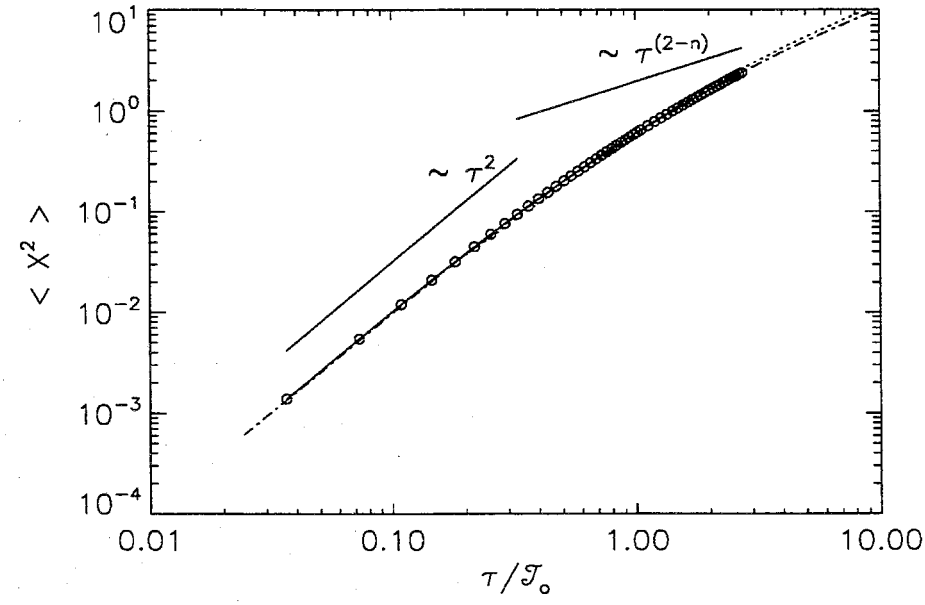

Figure 5.15b: The mean square displacement of particles, $< X^2 >$, for run2.

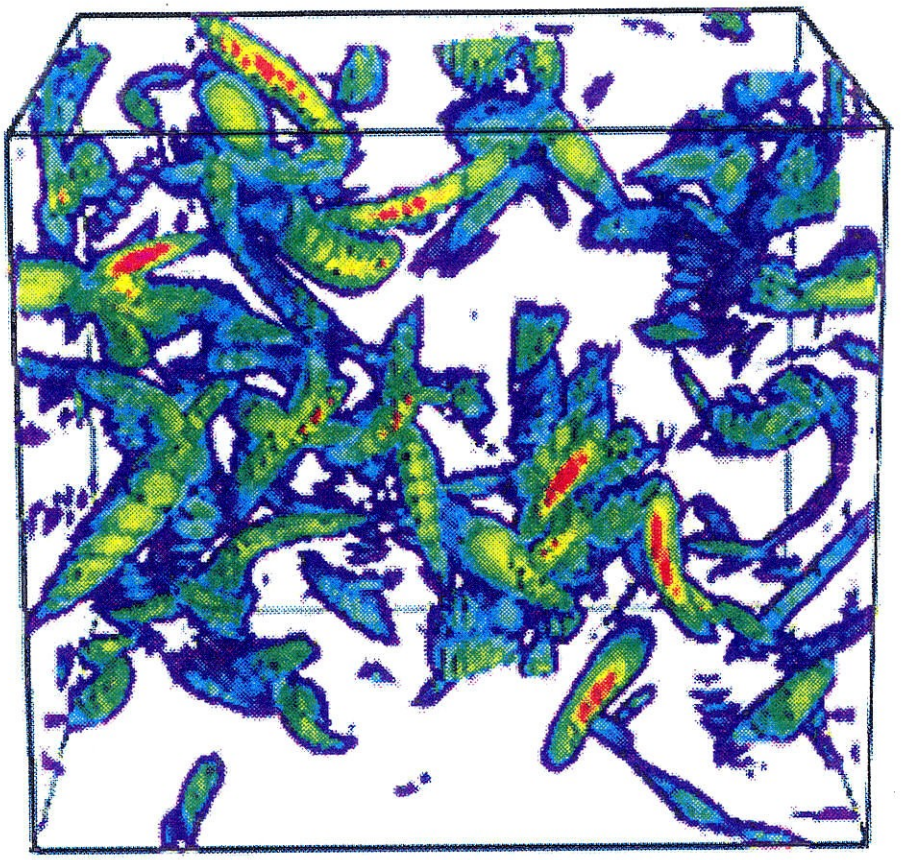

Figure 5.16: Tube-like vorticity structures: constant surfaces with $\|\omega\| > 40\%\|\omega\|_{max}$ are plotted for run1 at $\tau/\mathcal{T}_o^* = 2.57$ ($Re_\lambda = 26$, $\lambda/L = 9\%$).

5.3 Small-Scale Properties

In this section we study the small-scale properties of turbulence primarily from the viewpoint of Lagrangian particle. An example of the small-scale vorticity structures of turbulence are shown in Fig. 5.16 in which only constant surfaces of vorticity magnitude with magnitudes $> 40\%\|\omega\|_{max}$ are plotted. As usual, tube-like or cigar-like structures are observed. Merging of vortices in the presence of viscosity take place constantly. It is these strong vorticity structures that determine other small-

scale statistics of turbulence, although their own mechanism of formation is itself unclear. One of the purposes of the present research is to study the effects and the origin of these small-scale structures.

5.3.1 Growth Rates and the Rate of Strain Tensor

The rate of the strain tensor, the symmetric part of the velocity gradient tensor, is given by $S_{ij} = \frac{1}{2}\left(\frac{\partial u_i}{\partial x_j} + \frac{\partial u_j}{\partial x_i}\right)$. The principal rates of strain will be denoted as α, β, and γ with $\alpha \geq \beta \geq \gamma$. We compute not only the principal rates but also the growth rates of magnitudes of material line elements, ζ, and of the vorticity due to the nonlinear stretching, σ, that is

$$\zeta \equiv \frac{1}{\ell}\frac{d\ell}{dt} = \ell_i S_{ij} \ell_j / \ell^2 \tag{5.45}$$

and

$$\sigma \equiv \omega_i S_{ij} \omega_j / \omega^2. \tag{5.46}$$

All rates are nondimensionalized by the square root of mean enstrophy, $\Omega(\tau) \equiv \sqrt{< \|\omega(\xi,\tau)\|^2 >}$ and the time after released by the dissipation time scale τ_η at $\tau = 0$ ($k_{max}\eta \approx 2$ or $t = t_*$), denoted as τ_η^*. The decay of $\Omega(\tau)$ itself is shown in Fig. 5.17 and the evolution of the principal rates as well as the two growth rates following fluid particles are shown in Fig. 5.18ab. It is found that the dimensionless rates stay approximately constant or approach to a constant value quickly after a transient time period, a period required for particles to forget their initial conditions. The ratios are about 0.39, 0.10, -0.49, 0.11, and 0.14 for $< \alpha > /\Omega$, $< \beta > /\Omega$, $< \gamma > /\Omega$, $< \sigma > /\Omega$, and $< \zeta > /\Omega$ respectively. We recall that Kolmogorov scaling predicts these rates are on the order of square-root-mean enstrophy when Reynold number is large. Our numerical results suggest that it is also true even for flows with Reynolds numbers as low as ours and for decaying flows. These ratios are observed by Girimaji and Pope as well for stationary turbulence [28] except the rate $< \sigma > /\Omega$ which they didn't measure.

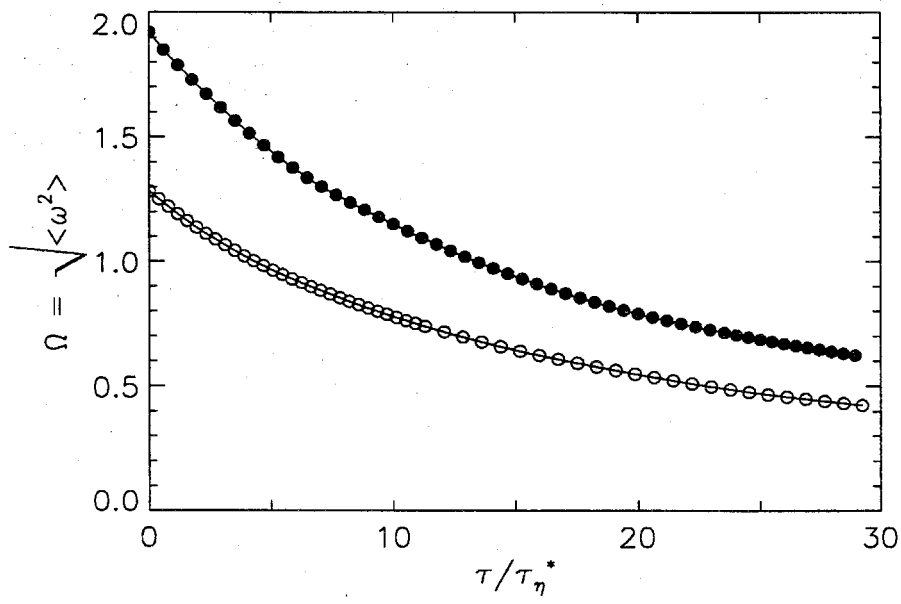

Figure 5.17: The decay of square-root-mean enstrophy $\Omega(t) = \sqrt{< \|\omega\|^2 >}$. Open symbols are for run1 and solid for run2 and $\tau_\eta^* = \tau_\eta(t_*)$.

The ratios of the principal rates, $< \alpha >:< \beta >:< \gamma >$, are about 4:1:-5 as the same as those from Girimaji and Pope's calculations, but different from those of 3:1:-4 observed by Ashurst et al. [3]. Ashurst [2] proposed a physical model of turbulence as a collection of Burger vortices with strength $\Gamma_o/\nu \approx 96\pi$, where Γ_o is the circulation, using the latter set of ratios. Recently Pullin and Saffman [52], starting with the Lundgren-Townsend vortex model, predict many turbulence quantities. In particular, using what they consider is the best set of values for the free parameters, they obtain 4:1:-5 for the principal rates. In estimating these ratios, both models assume (nearly) axisymmetric vorticity structures created by an external straining field (-ar/2, 0, az) in the polar coordinates, where $a > 0$ is the uniform rate of strain, and ignore the axial variation by assuming relatively long structures. The ratios of the principal rates of strain tensors are therefore approximated as

$$< \alpha >:< \beta >:< \gamma >= -\frac{a}{2} + \overline{|e_{r\theta}|} : a : -\frac{a}{2} - \overline{|e_{r\theta}|} \tag{5.47}$$

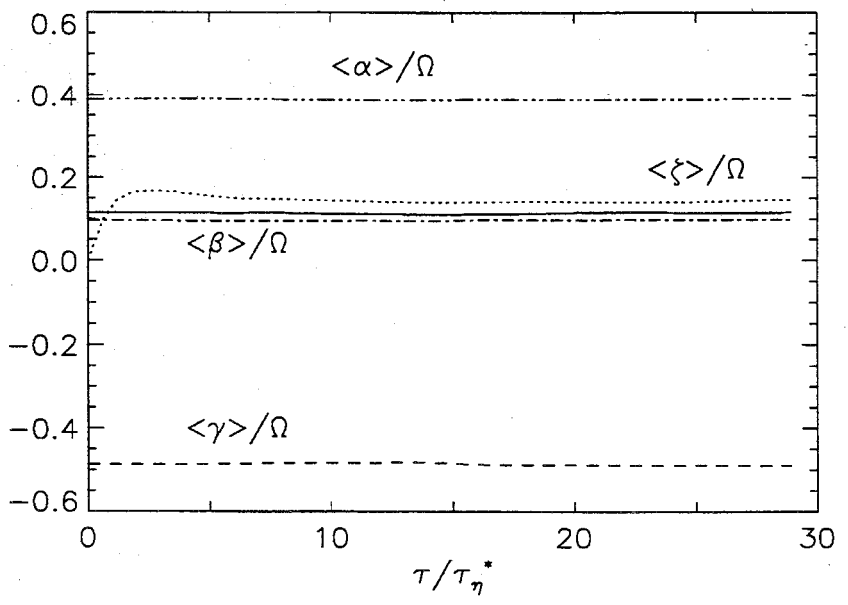

Figure 5.18a: The evolutions of mean growth rates and mean principal rates of strain tensors nondimensionalized by the square root of mean enstrophy for run1. (1) $-\cdot\cdot\cdot-$ α (2) $-\cdot-$ β (3) $---$ γ (4) —— σ (5) $\cdots\cdots$ ζ.

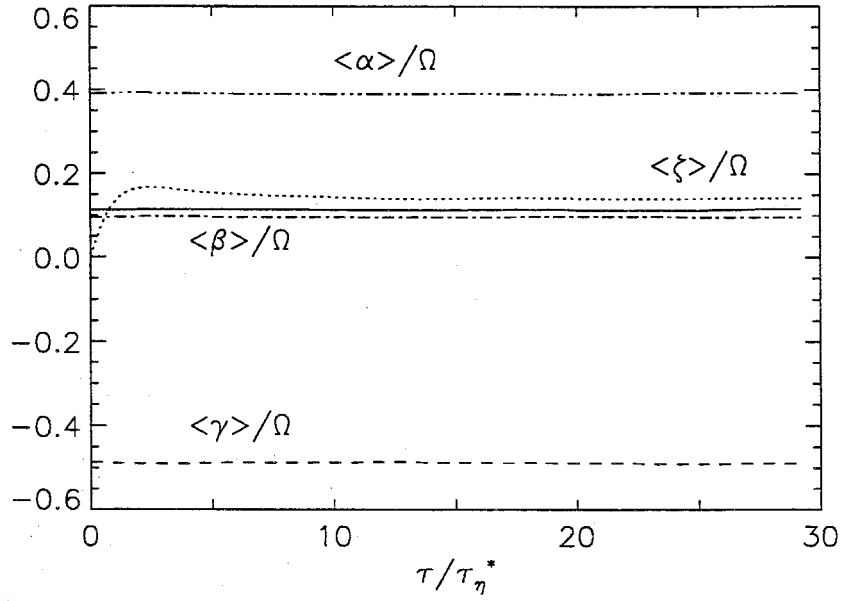

Figure 5.18b: The evolutions of mean growth rates and mean principal rates of strain tensors nondimensionalized by the square root of mean enstrophy for run2. (1) $-\cdot\cdot\cdot-$ α (2) $-\cdot-$ β (3) $---$ γ (4) —— σ (5) $\cdots\cdots$ ζ.

provided $-\frac{a}{2}+\overline{|e_{r\theta}|} > a$, where $e_{r\theta} = \frac{r}{2}\frac{\partial}{\partial r}\left(\frac{u_\theta}{r}\right)$. However, volume averaging and even time averaging over a single vortex history as well do not lead to a convergent $\overline{|e_{r\theta}|}$. Ashurst instead uses the maximum value of $|e_{r\theta}|$ which is about $\frac{0.3a\Gamma_o}{8\pi\nu}$ occurring at $ar^2/4\nu \approx 1.79$ in (5.47). A choice of $\Gamma_o/\nu \approx 96\pi$ (more precisely 93.4π) then gives the ratios 3:1:-4. Pullin and Saffman, on the other hand, suggest approximating $\overline{|e_{r\theta}|}$ by $\sqrt{\overline{e_{r\theta}^2}} = \sqrt{\overline{\omega^2}/4} = \sqrt{\epsilon/4\nu}$. Using their favored values of dimensionless numbers $\Gamma_o/\nu = 100$ and $NR^2/a = 0.6$, they obtain $a\sqrt{\nu/\epsilon} \approx 1/9$ and therefore $< \alpha >:< \beta >:< \gamma >= 4:1:-5$, where N in the model is the rate of creation of vortex length per unit volume per unit time and R is a characteristic radius of the vortex structures. An assumption made by Ashurst based on the numerical results computed by She, Jackson and Orszag [62] is that the Burger vortex has a radius of $\sqrt{4\nu/a}$ and a length of $12\sqrt{4\nu/a}$. (This is similar to assuming a value for N in Pullin and Saffman's model.) By assuming there exists on the average one Burger's vortex within a spherical volume of diameter $12\sqrt{4\nu/a}$, i.e., assuming the volume fraction occupied by these Burger vorticies is $\left(4\pi\nu/a \cdot 12\sqrt{4\nu/a}\right) / \left(\frac{4\pi}{3}(6\sqrt{4\nu/a})^3\right) = 1/24$, Ashurst was then able to calculate $\epsilon = \frac{a^2\Gamma_o}{8\pi}\frac{\Gamma_o/\nu}{96\pi}$. Use of Pullin and Saffman's approximation for $\overline{|e_{r\theta}|}$ with Ashurst's model then predicts the ratios as

$$< \alpha >:< \beta >:< \gamma >= -\frac{1}{2} + \frac{\Gamma_o/\nu}{32\pi\sqrt{3}} : 1 : -\frac{1}{2} - \frac{\Gamma_o/\nu}{32\pi\sqrt{3}}. \tag{5.48}$$

A value of $\Gamma_o/\nu \approx 194\pi$ is then required for 3:1:-4 and 250π for 4:1:-5.

Thus the models suffer from having a number of free parameters and the fact that there is no specific way of approximating $\overline{|e_{r\theta}|}$. The uniform rate a can be estimated as $< \beta >$. The numerical result $< \beta > /\Omega \approx 0.10$ then implies $a\sqrt{\nu/\epsilon} \approx 0.10$ which is close to the value of $1/9$ favored by Pullin and Saffman.

The prediction of $< \zeta > /\Omega$ on the other hand was first given by Batcherlor [7] who believed the material line elements will eventually align with the principal direction corresponding to the maximum principal rate; that is, $< \zeta >=< \alpha >$. Neither our numerical results nor those of Girimaji and Pope [28] support this conjecture.

Girimaji and Pope proposed that vorticity effects and nonpersisting property of the strain tensor are responsible for this disagreement. We will discuss this issue in the next section after more numerical results have been given to shed more light on these effects.

5.3.2 Alignments of Vector Fields

The evolutions of the mean angles between the vorticity vectors and the principal directions of the strain tensors are shown in Fig. 5.19. Those for the material line elements are in Fig. 5.20. The mean angles are defined by

$$\theta_{\alpha,\beta,\gamma} = \cos^{-1} < |\cos \phi_{\alpha,\beta,\gamma}| >, \tag{5.49}$$

where ϕ is the angle between a vorticity vector or a material line element with the principal directions, that is,

$$\cos \phi_{\alpha,\beta,\gamma} = \underline{\ell} \cdot \mathbf{e}_{\alpha,\beta,\gamma}/\ell \tag{5.50}$$

or

$$\cos \phi_{\alpha,\beta,\gamma} = \omega \cdot \mathbf{e}_{\alpha,\beta,\gamma}/|\omega| \tag{5.51}$$

where $\mathbf{e}_{\alpha,\beta,\gamma}$ are the unit vectors in the principal directions of the strain tensor corresponding to the principal rates α, β, and γ. Therefore, $\theta_{\alpha,\beta,\gamma} = 60°$ when a vector field is uniformly randomly directed. This definition of $\theta_{\alpha,\beta,\gamma}$ is slightly different from that in Girimaji and Pope's study [28] in which $< \cos^{-1} |\cos \phi_{\alpha,\beta,\gamma}| >$ is used instead. In this latter case the mean angle is one radian for a random field.

Fig. 5.19 shows, as usually observed, that the vorticity vector is more likely aligned with $\mathbf{e}_\beta$ and its angle with $\mathbf{e}_\alpha$ is close to 60°, the mean of a random vector field. The material line elements show different orientations. After a short transient time, they settle down to a "steady" alignment. Like the vorticity vectors, they are more perpendicular to $\mathbf{e}_\gamma$ but are nearly equally aligned with $\mathbf{e}_\alpha$ and with $\mathbf{e}_\beta$. The "dip" in

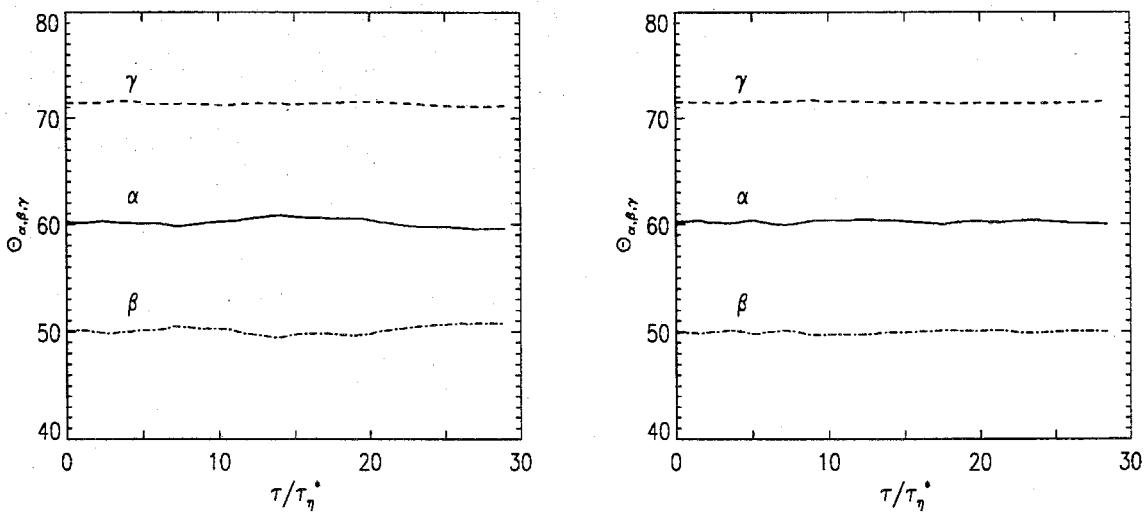

Figure 5.19: The evolutions of the mean angles, $\theta_{\alpha,\beta,\gamma} = \cos^{-1} < |\cos\phi_{\alpha,\beta,\gamma}| >$, between the vorticity vectors and the principal directions of strain tensors. (a) run1 (b) run2.

the evolution of θ_α found by Girimaji and Pope is also observed in our simulations. Girimaji and Pope believe this "dip" is a transition state caused by vorticity effects. They found that by not including the antisymmetric part of the velocity gradient, i.e.,

$$\frac{d\ell_i}{dt} = \ell_j S_{ij} \tag{5.52}$$

that the "dip" disappears. To explore this point further, we examine the equations of evolution of a material line element in new coordinates $\mathbf{e}' = R^T\mathbf{e}$, where R is the transformation matrix which diagonalizes the strain tensor S. All primed quantities in the following are relative to this new base. Considering $\underline{\ell}' = R^T\underline{\ell}$ and

$$\dot{R} = \frac{DR}{Dt} = R\Delta', \tag{5.53}$$

where Δ' is an antisymmetric matrix whose dual vector $-\frac{1}{2}\varepsilon_{ijk}\Delta'_{ij}$ is the instantaneous vector of rotation of the new base, one can write

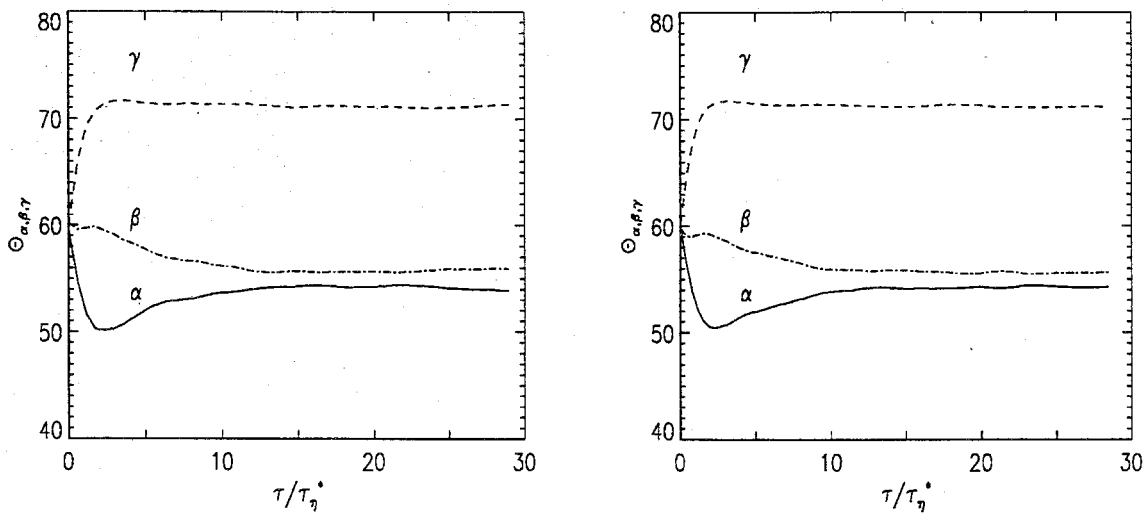

Figure 5.20: The evolutions of the mean angles, $\theta_{\alpha,\beta,\gamma} = \cos^{-1} < |\cos\phi_{\alpha,\beta,\gamma}| >$, between the material line elements and the principal directions of strain tensors. (a) run1 (b) run2.

$$\dot{\underline{\ell}}' = -\Delta'\underline{\ell}' + S'\underline{\ell}' + A'\underline{\ell}', \tag{5.54}$$

where A is the antisymmetric part of the velocity gradient tensor; or by denoting the diagonal elements of S' by S_1', S_2', and S_3', one has

$$\begin{aligned}
\dot{\ell}'_1 &= S_1'\,\ell_1' - \left(\frac{1}{2}\omega_3' + \Delta_{12}'\right)\,\ell_2' + \left(\frac{1}{2}\omega_2' + \Delta_{31}'\right)\,\ell_3', \\
\dot{\ell}'_2 &= S_2'\,\ell_2' + \left(\frac{1}{2}\omega_3' + \Delta_{12}'\right)\,\ell_1' - \left(\frac{1}{2}\omega_1' + \Delta_{23}'\right)\,\ell_3', \\
\dot{\ell}'_3 &= S_3'\,\ell_3' - \left(\frac{1}{2}\omega_2' + \Delta_{31}'\right)\,\ell_1' + \left(\frac{1}{2}\omega_1' + \Delta_{23}'\right)\,\ell_2'.
\end{aligned} \tag{5.55}$$

From the incompressible Navier-Stokes equations, one can show that

$$\Delta_{ij}' = \begin{cases} \dfrac{\frac{1}{4}\omega_i'\omega_j' + \Pi_{ij}' - \nu\Phi_{ij}'}{S_i' - S_j'}, & \text{if } i \neq j; \\ 0, & \text{otherwise,} \end{cases} \tag{5.56}$$

where $\Pi_{ij} \equiv \dfrac{\partial^2 P}{\partial x_i \partial x_j}$ accounts for the anisotropic effects of the pressure gradients and $\Phi = \nabla^2 S$ comes from the dissipation terms. Since Δ' is antisymmetric as well, the

effects of the rotation of the principal directions of the strain tensor on the evolution of a material line element is nothing more than modifying the antisymmetric part of velocity gradient tensor.

If both Δ' and A' are zero matrices, the growth rates of the components of material line elements are just the principal rates of the strain tensor and therefore Batchelor's predictions follow, unless two principal rates become equal at some time so that the principal direction corresponding to the most positive principal rate is thus switched with another one. On the other hand, as discussed above, simulations of equation (5.52) ignore A' but keep Δ' and show no "dip." Ignoring Δ' and keeping A' instead, we find the characteristic polynomial for (5.55) is

$$\lambda^3 + \lambda(S_1'S_2' + S_2'S_3' + S_3'S_1' + \frac{1}{4}\omega^2) - (S_1'S_2'S_3' + \frac{1}{4}\sigma\omega^2) = 0, \tag{5.57}$$

where $\omega^2 = \omega_1'^2 + \omega_2'^2 + \omega_3'^2$ and $\sigma\omega^2 = \omega_1'^2 S_1' + \omega_2'^2 S_2' + \omega_3'^2 S_3'$ as before. If we further assume that σ equals to some principal rate, say S_2' (numerical results suggest it would most likely be the intermediate principal rate), the growth rates are then S_2' and $-S_2'/2 \pm \sqrt{(S_1' - S_3')^2 - \omega^2}/2$. Therefore, two of the growth rates can be both positive and about the same if $(S_1' - S_3')^2/\omega^2 > 1$. All features of Fig. 5.20 may be possible with this "model" (a transient state and a competition among the growths of the three components of a material line element).

We can see now from (5.55) that the alignment of a material line element is actually determined by the balance between S' and $A' - \Delta'$. The latter is in turn determined by ω_i, S_{ij}, and $\nabla^2 S_{ij}$. An investigation of the growth rates and alignments conditioned on the vorticity magnitudes, ω^2, and the strain magnitudes, $tr\ S^2$, might provide more useful information for us as discussed in the following.

5.3.2.1 Rotation Effects

The distributions of the growth rates ζ and σ conditioned on the magnitudes of vorticity are shown in Fig. 5.21 for run2 at three times — in the transient state as well

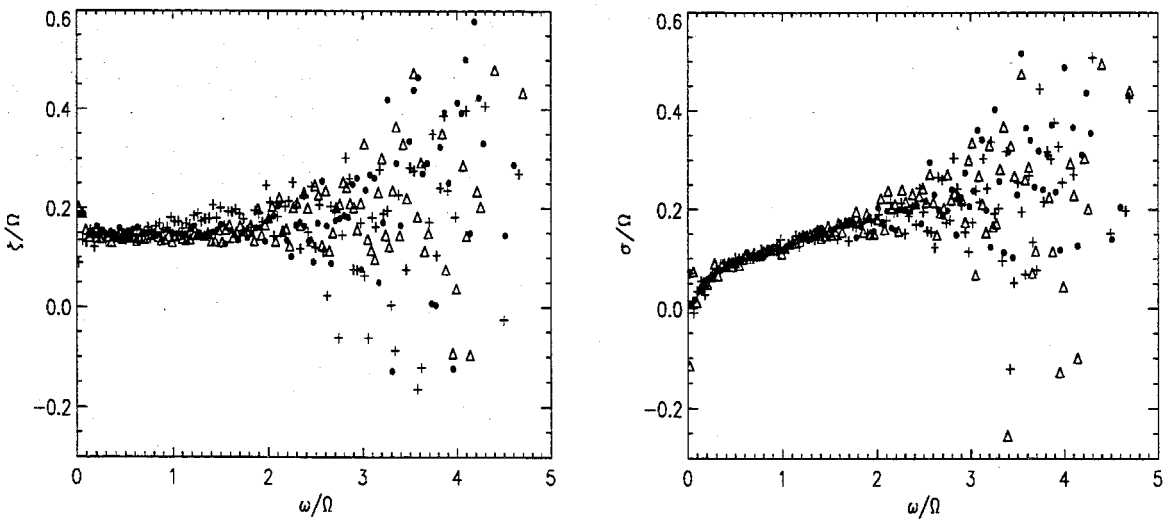

Figure 5.21: The mean growth rates (a) ζ and (b) σ conditioned on the magnitudes of vorticity ω. $\tau/\tau_\eta(t_*) = +\ 1.56\ \bullet\ 5.84\ \triangle\ 17.53$.

as in the "steady" state. Discarding the data at very small and very large vorticity magnitudes which fluctuate significantly due to the small number of samples there, σ is seen to increase as ω increases but, surprisingly, ζ is nearly uncorrelated with ω. Although the definitions of both rates do not depend on the vorticity magnitude explicitly, a correlation between strain magnitude and vorticity magnitude is expected and therefore correlations between vorticity magnitude and growth rates are also expected.

The mean angles between these vectors conditioned on ω are shown in Fig. 5.23 and Fig. 5.24. At early time, the effect of vorticity is not yet dominant (the angles show no dependence on ω). The material line elements are simply stretched in $\mathbf{e}_\alpha$ direction and compressed in $\mathbf{e}_\gamma$ direction at the time they are released, which causes the rapid increase of ζ at small times. As time increases, the vorticity effect starts to appear (see Fig. 5.24b). At small ω, material line elements have a bias toward $\mathbf{e}_\alpha$ as expected. As ω increases (the vorticity effect increases), a competition between

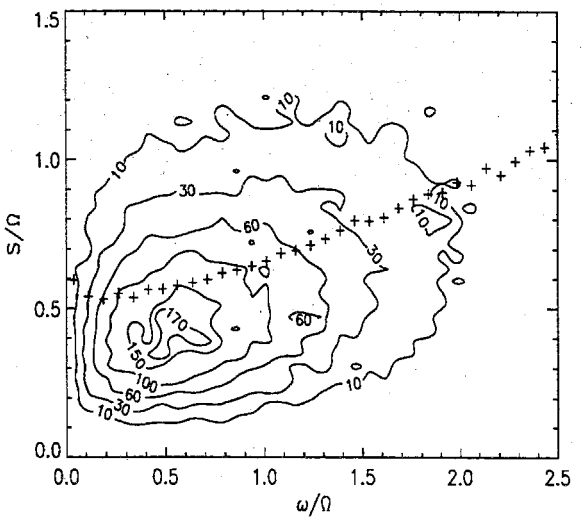

Figure 5.22: Joint probability distribution of ω/Ω and S/Ω at $\tau/\tau_\eta(t_*) = 17.53$. The contours are labelled by the numbers of particles collected. Plus signs (+) are the conditional mean values of S/Ω on ω/Ω.

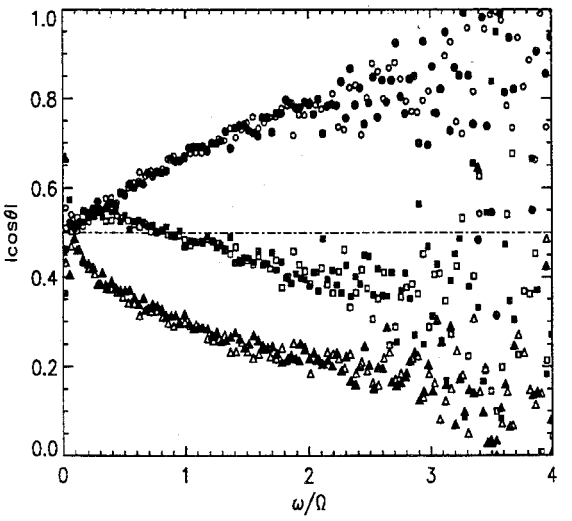

Figure 5.23: The mean angles between vorticity vectors and principal directions of strain tensors conditioned on the magnitudes of vorticity ω.
$\square$: $\cos\theta_\alpha$, $\circ$: $\cos\theta_\beta$, $\triangle$: $\cos\theta_\gamma$
$\tau/\tau_\eta(t_*) = 5.84$ (open) and 17.53 (solid symbols).

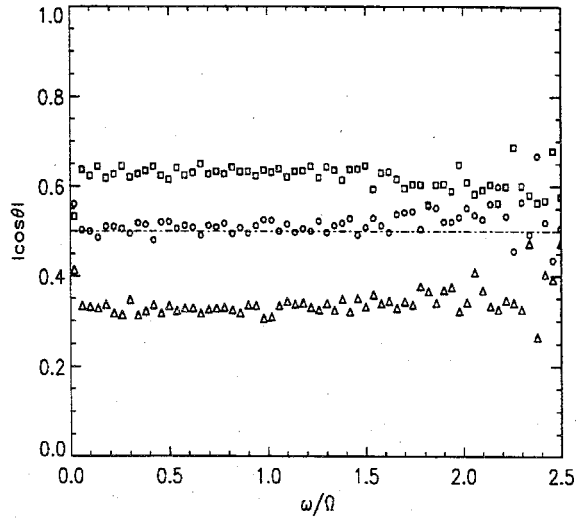

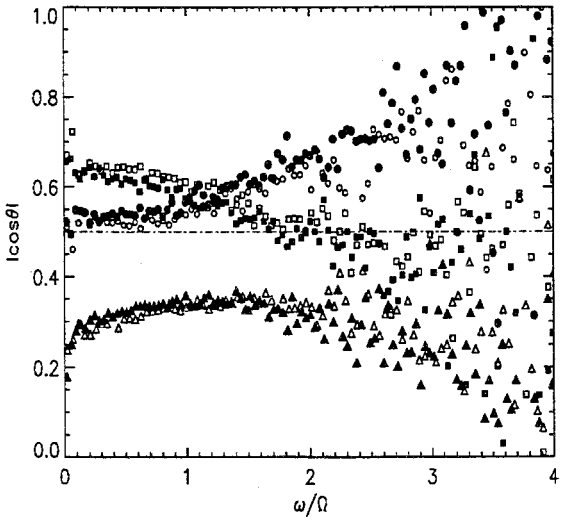

Figure 5.24: The mean angles between material line elements and principal directions of strain tensors conditioned on the magnitudes of vorticity ω. $\square$: $\cos\theta_\alpha$, $\circ$: $\cos\theta_\beta$, $\triangle$: $\cos\theta_\gamma$ (L) $\tau/\tau_\eta(t_*) = 1.56$ (R) $\tau/\tau_\eta(t_*) = 5.84$ (open) and 17.53 (solid symbols).

θ_α and θ_β takes place and eventually material line elements tend to align with $\mathbf{e}_\beta$ instead. The switch occurs at an $\omega/\Omega = 1 \sim 1.5$. The material line element seems to adjust its alignment in such a way so that ζ is nearly independent of ω, even though the vorticity magnitude is correlated with straining magnitude.

The dependence of the alignment of the vorticity vector on its own magnitude is shown in Fig. 5.21b and Fig. 5.23 and agree with previous findings. Basically a strong bias toward $\mathbf{e}_\beta$ is observed, especially when the vorticity is large. This observation has been used in many existing models such as Ashurst's as well as Pullin and Saffman's discussed above.

5.3.2.2 Effects of Straining Magnitudes

The mean growth rates conditioned on the straining magnitude $S = \sqrt{S_{ij}S_{ij}}$ are shown in Fig. 5.25. A nearly linear dependence of ζ is observed. By examining the definitions, we see that this strong correlation is not so surprising. One may write $\underline{\ell} = \ell(\cos\theta, \sin\theta\cos\psi, \sin\theta\sin\psi)$ in the coordinates $(\mathbf{e}_\alpha, \mathbf{e}_\beta, \mathbf{e}_\gamma)$ and consider

$$\zeta = \ell_i S_{ij} \ell_j / \ell^2 = \alpha \int_0^{2\pi} d\psi \int_0^{\pi} \sin\theta d\theta \sin^2\theta(\cos^2\psi - \sin^2\psi) P(\theta, \psi; S)$$
$$- \gamma \int_0^{2\pi} d\psi \int_0^{\pi} \sin\theta d\theta (\sin^2\theta \sin^2\psi - \cos^2\theta) P(\theta, \psi; S),$$

where $P(\theta, \psi; S)$ is the probability distribution function, conditioned on the straining magnitude S, of the direction of a material line element relative to the principal directions of the strain tensor, for example $\zeta = 0$ if $P(\theta, \psi; S) = 1$. A linear dependence of ζ on S $(= \sqrt{\alpha^2 + \beta^2 + \gamma^2})$ implies that $P(\theta, \psi; S)$ has only a weak dependence on S.

The probability density function (p.d.f.) of the normalized straining magnitude $\widehat{S} = (S - < S >)/\sigma_S$ is shown in Fig. 5.26, where σ_S is the variance. The p.d.f. is close to a lognormal distribution as many other turbulent small-scale quantities. Conditional mean angles for vorticity are shown in Fig. 5.27 and those for material line elements are in Fig. 5.28. The dependence of the mean angle of vorticity on

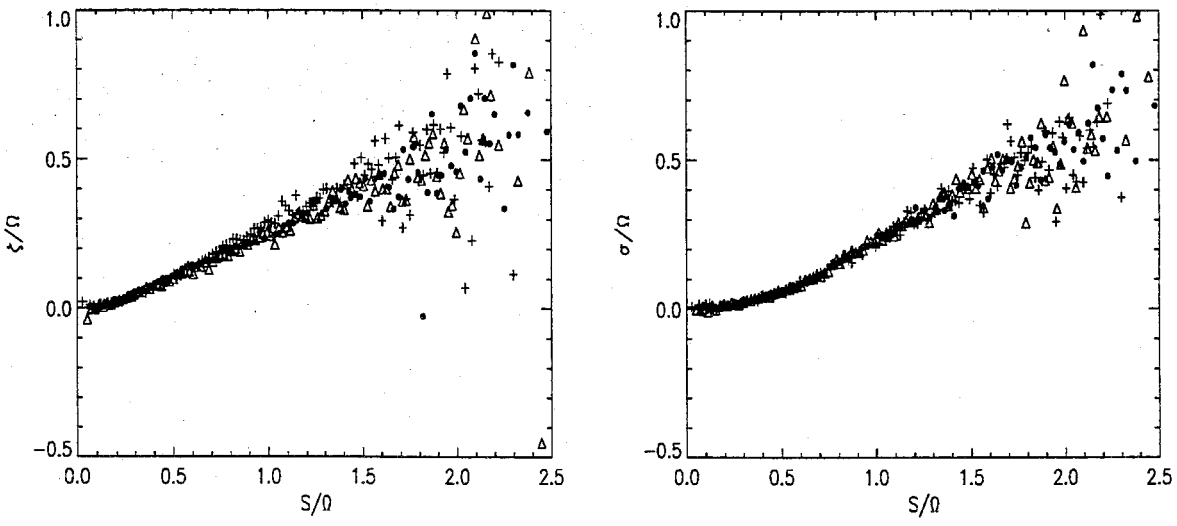

(a) (b)

Figure 5.25: The growth rates (a) ζ and (b) σ conditioned on the straining magnitude $S \equiv \sqrt{S_{ij}S_{ij}}$. $\tau/\tau_\eta(t_*) = +\ 1.56\ \bullet\ 5.84\ \ \triangle\ 17.53$.

S is close to its dependence on ω and very similar to that found by She [62] who investigated the distribution of $< \cos^2\phi >$. The dependence of $\underline{\ell}$ on S, on the other hand, changes somewhat, especially in the angle θ_γ. At small S, it seems that the material line elements are directed randomly, producing a small growth rate ζ. The curves for $\cos\theta_\alpha$ and $\cos\theta_\beta$ also intersect at an S in the range (0.5,1). This switch of $\mathbf{e}_\alpha$ and $\mathbf{e}_\beta$ must reduce the slope of the curves in Fig. 5.25a to some extent but not so significantly as the vorticity effect does. Recall a slope ≈ 0 in Fig. 5.21a was observed.

Some conclusions are made. First the alignment of material line elements is adjusted by the vorticity or the rotation of the strain tensor (Δ') in such a way that ζ is independent of $\|\omega\|$. The strong dependence on the straining magnitude S of growth rates comes directly from their definitions. The intersection of the distributions for $\cos\phi_\alpha$ and $\cos\phi_\beta$ in Fig. 5.24 and 5.28 suggests that the competition between θ_α and θ_β in Fig. 5.20 may also be explained by a switch of the principal directions $\mathbf{e}_\alpha$ and

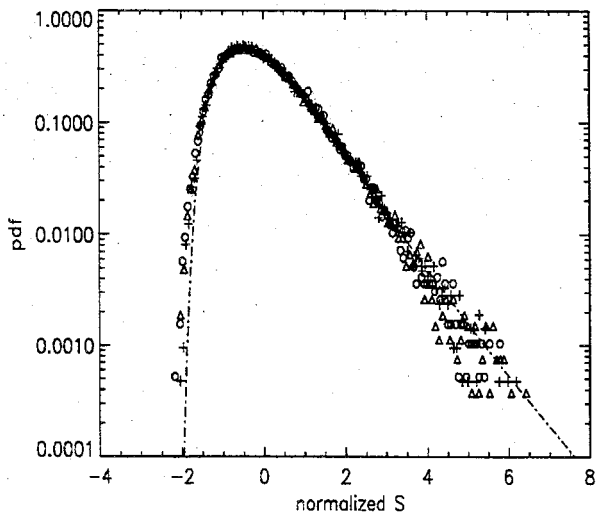

Figure 5.26: P.d.f. of $\widehat{S} = (S - < S >)/\sigma_S$. The dash dotted curve is a log-normal distribution with mean $< S >$ and variance σ_S. $\tau/\tau_\eta(t_*) = +$ 1.56 ∘ 5.84 △ 17.53.

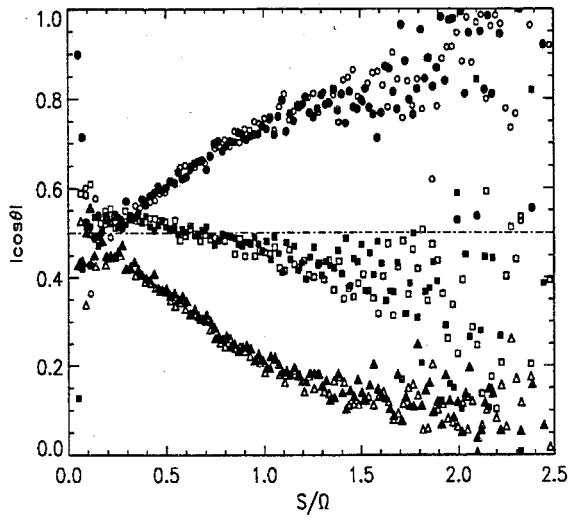

Figure 5.27: The mean angles between vorticity vectors and principal directions of strain tensors conditioned on the straining magnitude $S \equiv \sqrt{S_{ij}S_{ij}}$. □ : $\cos\theta_\alpha$, ∘ : $\cos\theta_\beta$, △ : $\cos\theta_\gamma$ $\tau/\tau_\eta(t_*) = 5.84$ (open) and 17.53 (solid symbols).

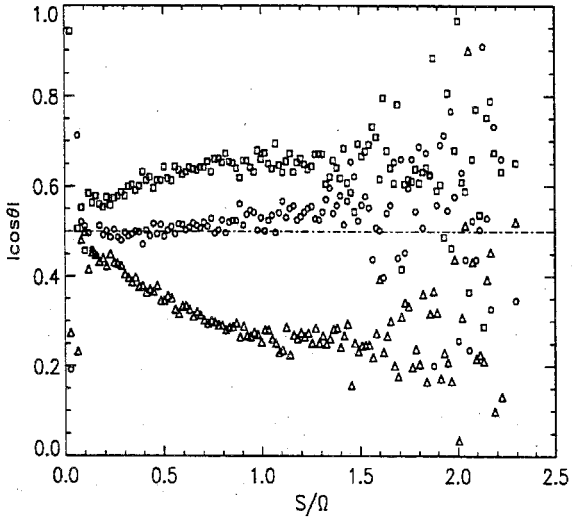

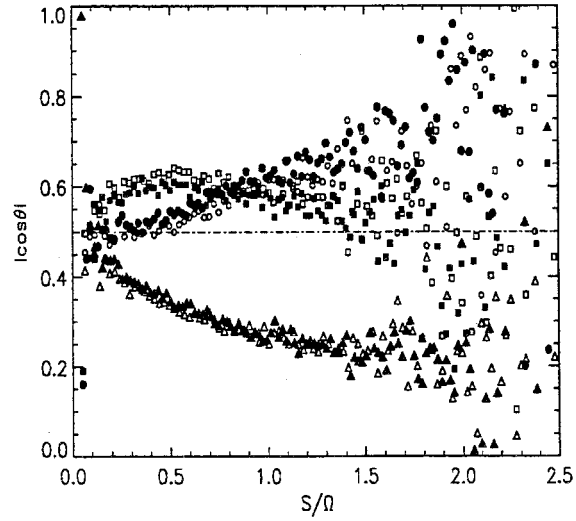

Figure 5.28: The mean angles between material line elements and principal directions of strain tensors conditioned on the straining magnitude $S \equiv \sqrt{S_{ij}S_{ij}}$. □ : $\cos\theta_\alpha$, ∘ : $\cos\theta_\beta$, △ : $\cos\theta_\gamma$ (L) $\tau/\tau_\eta(t_*) = 1.56$ (R) $\tau/\tau_\eta(t_*) = 5.84$ (open) and 17.53 (solid symbols).

$\mathbf{e}_\beta$. The reason is not so obvious but will become clear when we show an example in which the evolution of a material line element under the action of a Burger vortex is studied.

5.3.3 Burger's Vortex Model

We explore the evolution of the alignment of a material line element under the action of Burger's vortex model. In cylindrical coordinates, the material line element is governed by

$$\begin{aligned}
\frac{d\ell_r}{dt} &= \frac{\ell_\theta u_\theta}{r} + (\underline{\ell}\cdot\nabla)u_r, \\
\frac{d\ell_\theta}{dt} &= -\frac{\ell_r u_\theta}{r} + (\underline{\ell}\cdot\nabla)u_\theta, \\
\frac{d\ell_z}{dt} &= (\underline{\ell}\cdot\nabla)u_z,
\end{aligned} \tag{5.58}$$

where

$$(\underline{\ell}\cdot\nabla) = \ell_r\frac{\partial}{\partial r} + \frac{\ell_\theta}{r}\frac{\partial}{\partial\theta} + \ell_z\frac{\partial}{\partial z}. \tag{5.59}$$

We consider $(u_r, u_\theta, u_z) = (-ar/2, u_\theta(r), az)$, where a is the uniform rate of straining and $u_\theta(r)$ is given by

$$u_\theta(r) = \frac{\Gamma_o}{2\pi r}\left(1 - exp(-ar^2/4\nu)\right). \tag{5.60}$$

Denoting the initial z-component of the material line element as ℓ_{zo}, we define the following dimensionless variables:

$$\begin{aligned}
&\widehat{t} = at, \quad \widehat{r} = r/\ell_{zo}, \quad \widehat{u}_\theta = u_\theta/a\ell_{zo}, \quad \text{and} \\
&(\widehat{\ell}_r, \widehat{\ell}_\theta, \widehat{\ell}_z) = (\ell_r/\ell_{zo},\ \ell_\theta/\ell_{zo}, \ell_z/\ell_{zo}).
\end{aligned}$$

Equation (5.58) then becomes

$$\begin{aligned}
\frac{d\widehat{\ell}_r}{d\widehat{t}} &= \frac{\widehat{\ell}_\theta\widehat{u}_\theta}{\widehat{r}} - \frac{\widehat{\ell}_r}{2}, \\
\frac{d\widehat{\ell}_\theta}{d\widehat{t}} &= -\frac{\widehat{\ell}_r\widehat{u}_\theta}{\widehat{r}} + \widehat{\ell}_r\frac{\partial\widehat{u}_\theta}{\partial\widehat{r}}, \\
\frac{d\widehat{\ell}_z}{d\widehat{t}} &= \widehat{\ell}_z,
\end{aligned} \tag{5.61}$$

and the dimensionless azimuthal velocity is

$$\hat{u}_\theta(\hat{r}) = \frac{\hat{\Gamma}}{2\hat{r}}\left(1 - exp(-\hat{r}^2/\hat{R}^2)\right), \tag{5.62}$$

where $\hat{\Gamma} \equiv \frac{\Gamma_o}{\pi a \ell_{zo}^2}$ and $\hat{R}^2 \equiv \frac{4\nu}{a\ell_{zo}^2}$ are two of the three dimensionless parameters in problem. The other dimensionless parameter, $\hat{r}_o$, is the ratio of the initial r-component of the material particle, r_o, to ℓ_{zo}.

The particle pathline, $\mathbf{x} = (r(t), \theta(t), z(t))$, is determined by

$$\frac{d\mathbf{x}}{dt} = \mathbf{u} = (u_r, u_\theta, u_z). \tag{5.63}$$

In this flow $\hat{r}(\hat{t}) = \hat{r}_o \exp(-\hat{t}/2)$. The system of equation (5.61) is thus nonautomonous. To reduce the number of free parameters, we will assume (5.48) with $\Gamma/\nu = 144\sqrt{3}\pi$ ($\approx 250\pi$). Consequently $\hat{\Gamma} = 36\sqrt{3}\hat{R}^2$. The competition between uniform straining (a) and straining due to the vortex ($e_{r\theta}$) is then characterized by $\hat{R}$ and the initial condition is controlled by the parameter $\hat{r}_o = r_o/\ell_{zo}$.

Equation (5.61) was first solved with a random initial orientation of $\underline{\ell}$ with fixed $\hat{R}$ and $\hat{r}_o$ (by fourth order Runge-Kutta method). The results did not differ qualitatively. Therefore, to study the effect of $\hat{R}$ and $\hat{r}_o$, we then choose initial angles, ϕ_α, ϕ_β, ϕ_γ defined in the previous sections, to be $cos^{-1}\frac{1}{\sqrt{3}} \approx 54.7°$. With $\hat{R}$ fixed (=1) and $\hat{r}_o$ varied, the evolutions of these angles are shown in Fig. 5.29 and those with $\hat{r}_o$ fixed (=1) and $\hat{R}$ varied are in Fig. 5.30.

The growth of ℓ_z is simply exponential ($\sim \exp(\hat{t}\,)$), but ℓ_r and ℓ_θ are stretched by $e_{r\theta}$ and compressed by $\partial u_r/\partial r$. The evolutions of ℓ_r and ℓ_θ are similar due to the interaction through the terms $\ell_\theta u_\theta/r$ and $-\ell_r u_\theta/r$, respectively. In this flow the principal directions of the strain tensor are $\mathbf{e}_z$, $(\mathbf{e}_r + \mathbf{e}_\theta)/\sqrt{2}$, and $(\mathbf{e}_r - \mathbf{e}_\theta)/\sqrt{2}$ with corresponding principal rates a, $-a/2 + e_{r\theta}$, and $-a/2 - e_{r\theta}$, where $e_{r\theta}$ is

$$\frac{e_{r\theta}}{a} = -\frac{\hat{\Gamma}}{2\hat{r}^2}\left(1 - \exp(-\hat{r}^2/\hat{R}^2)\right) + \frac{\hat{\Gamma}}{2\hat{R}^2}\exp(-\hat{r}^2/\hat{R}^2). \tag{5.64}$$

Therefore, $\mathbf{e}_z = \mathbf{e}_\beta$ if $-a/2 + |e_{r\theta}| > a$; otherwise, it is $\mathbf{e}_\alpha$. In the flow created by a single Burger vortex and the uniform straining field, both cases exist. In addition, $\mathbf{e}_\alpha$

and $\mathbf{e}_\gamma$ switch whenever $e_{r\theta}$ changes signs. For simplicity, In Fig. 5.29 and 5.30 we plot angles defined as $\cos^{-1}\ell_z/\ell$, $\cos^{-1}(\ell_r+\ell_\theta)/\sqrt{2}\ell$, and $\cos^{-1}(\ell_r-\ell_\theta)/\sqrt{2}\ell$ which are continuous.

The successive stretching and compression of ℓ_r and ℓ_θ are reflected in the oscillation appearing in Fig. 5.29 and Fig. 5.30. This results in negligible net growth of ℓ_r and ℓ_θ compared to the exponential growth of ℓ_z. A larger $\widehat{r}_o$, i.e., the particle is initially farther from the center of the vortex, yields a delay of the fast oscillations as observed in Fig. 5.29. Moreover, the amplitudes of oscillations are larger when a fluid particle is farther away, so that the material line element components in the (r,θ) plane are significantly stretched and compressed also. On the other hand, a decrease in $\widehat{R}$ implies a decrease in $e_{r\theta}$ ($\widehat{R}\sim\widehat{\Gamma}\sim\Gamma/a$). The uniform straining becomes dominant and thus the oscillations caused by rotation are reduced.

We conclude that the above observations are not, obviously, the same as those observed for particles in turbulent flow (Fig. 5.20) in which $\theta_\alpha\approx\theta_\beta$ and θ_γ is closer to 90°. But such particles are subject to the same effect of rotation on alignment as that revealed by Fig. 5.24. First of all, we believe the amplifications of some components of $\underline{\ell}$ are much reduced in the process of successive stretching and compression due to the rotation effect. Moreover, if we consider an averaging which takes into account the switch of the principal directions, for example $\mathbf{e}_z$ sometimes is $\mathbf{e}_\alpha$ and sometimes is $\mathbf{e}_\beta$ in the Burger's vortex model, the averaged angles $<\phi_\alpha>$ and $<\phi_\beta>$ in the model over the history of a particle for a finite period of time, could be made very close. Thus the observed competition between θ_α and θ_β in Fig. 5.20 could also be a result of the averaging process and the switch of principal directions, in addition to being a result of the vorticity effect (A') and the rotation effect of the strain tensor (Δ') as discussed in Sec. 5.3.2.

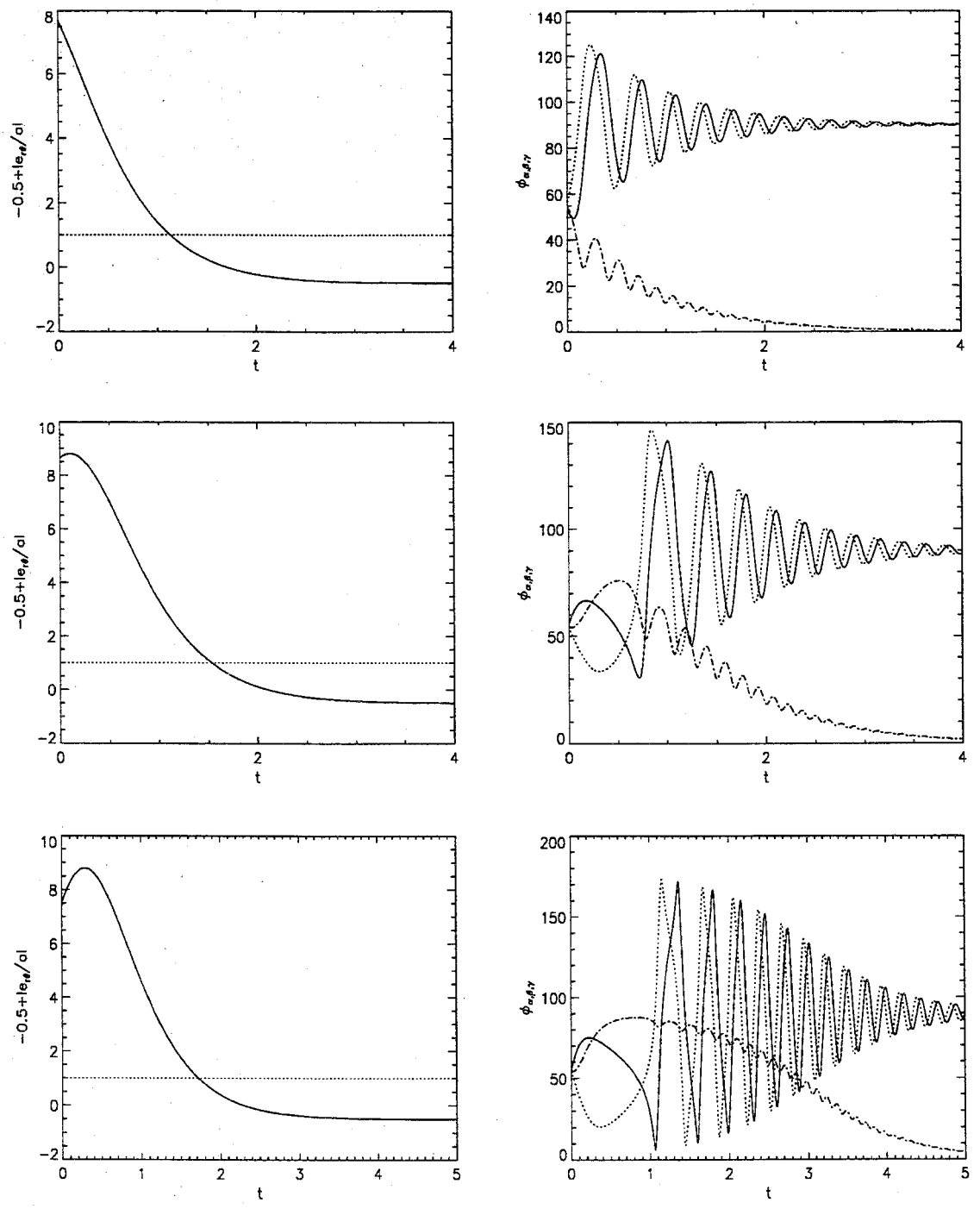

Figure 5.29: The evolutions of angles $\phi_{\alpha,\beta,\gamma}$ under the action of Ashurst's Burger vortex model. $\widehat{R} = 4\nu/a\ell_{zo}^2 = 1$ and $\widehat{r}_o = r_o/\ell_{zo} = 1$, 1.5, and 1.8. $-\cdot-$ $\phi_z = \phi_\beta$ whenever $-0.5 + |e_{r\theta}/a| > 1$; ϕ_α otherwise. —— and ..... are $\cos^{-1}(\ell_r \pm \ell_\theta)/\sqrt{2}\ell$.

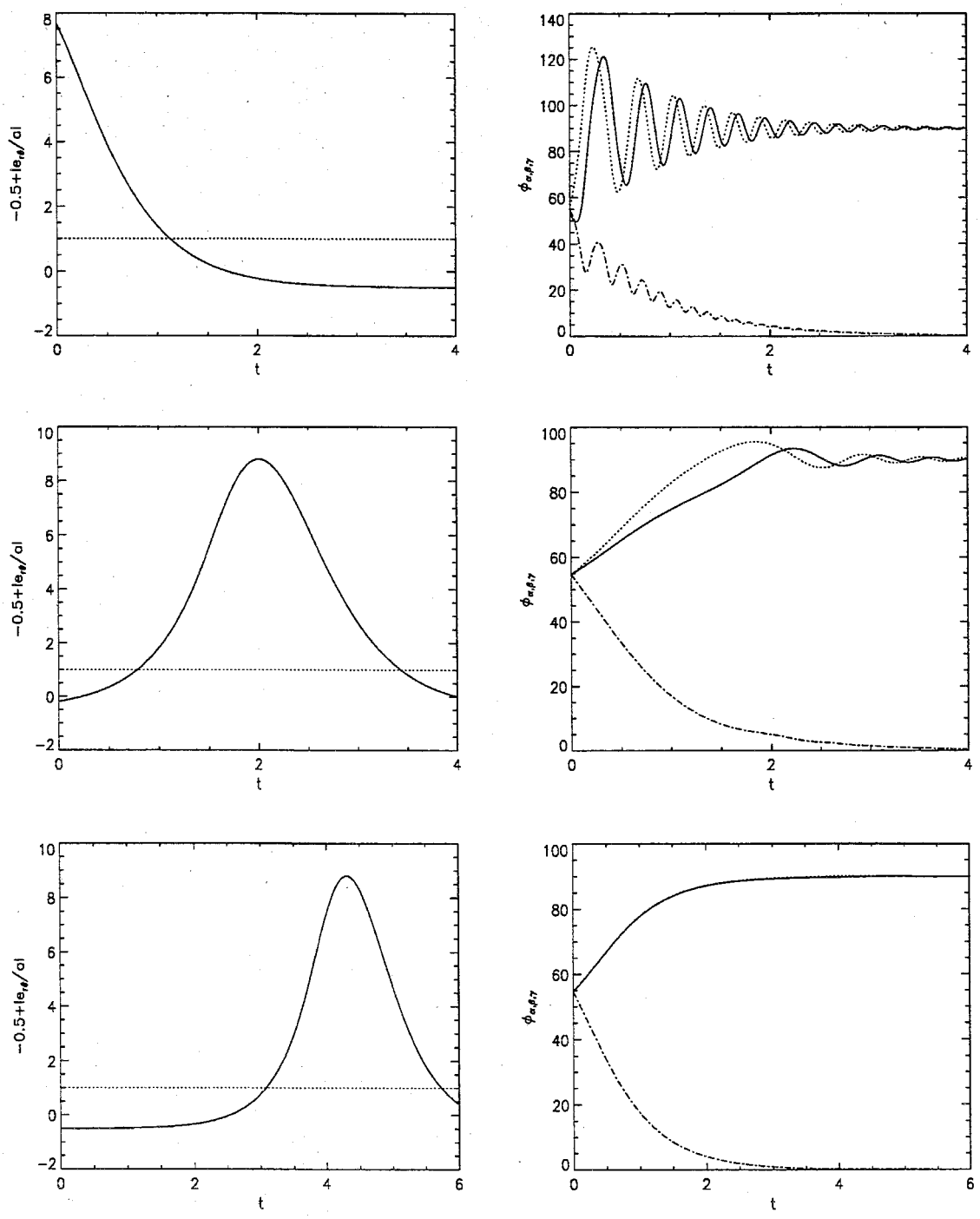

Figure 5.30: The evolutions of angles $\phi_{\alpha,\beta,\gamma}$ under the action of Ashurst's Burger vortex model. $\widehat{r}_o = r_o/\ell_{zo} = 1$ and $\widehat{R} = 4\nu/a\ell_{zo}^2 = 1$, 0.1, and 0.01. $-\cdot-$ $\phi_z = \phi_\beta$ whenever $-0.5 + |e_{r\theta}/a| > 1$; ϕ_α otherwise. —— and ..... are $\cos^{-1}(\ell_r \pm \ell_\theta)/\sqrt{2}\ell$.

5.4 Origin of Vorticity Structures

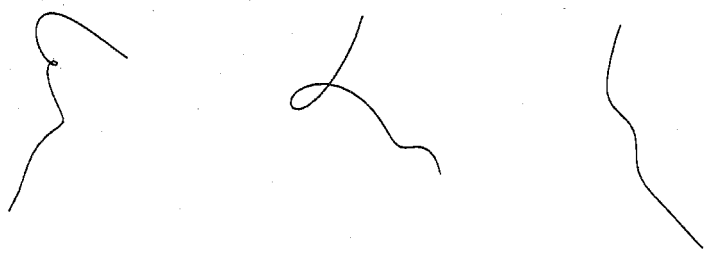

Figure 5.31: Pathlines of the selected particles (L) #1 (M) #2 (R) #3.

We attempt to observe the origin of the small-scale vorticity structures in turbulence by following 16,384 material particles. Particles are selected for further investigation if their vorticity satisfies $\omega^2/ < \omega^2 > \ > 18$ at any τ. A total of 16 particles are so selected. We then examine the histories of these 16 particles and choose three of them for a detailed study of the surrounding vorticity structures. The pathlines of the three particles are shown in Fig. 5.31. The evolution of particular quantities associated with these particles are shown in Fig. 5.32abc. The histories of the other 13 particles are either similar to these or less interesting. The results presented here surely can not be taken as a serious quantitative study, but we believe this can help in understanding the physics of turbulence.

As seen, particle #1 has a peak in its evolution of $\omega^2/ < \omega^2 >$ and particle #2 has two. The time scale for an excursion is seen to be about one initial eddy-turnover time ($\mathcal{T}_o(t_*)$). Particle #3, on the other hand, is continuously stretched and has a montonically increasing $\omega^2/ < \omega^2 >$. Notice that the cosine of the angle between the vorticity vector and $\mathbf{e}_\beta$ is very close to one during the peak times, consistent with the previous observations as shown in Fig. 5.23. The material line elements on the other hand show no bias toward $\mathbf{e}_\alpha$ even during the peak times. In particular, the oscillations appearing in the evolution of $\cos\phi_\alpha$ of particle #2 support our beliefs concerning the rotation effects on the alignment of material line elements as discussed

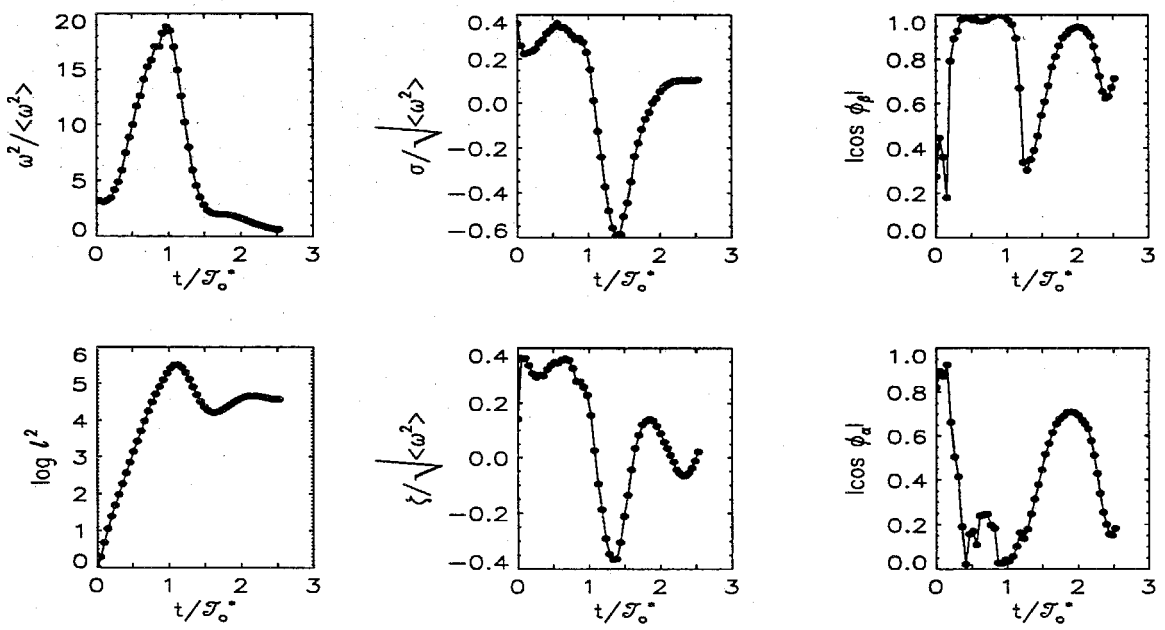

Figure 5.32a: History of particle #1. $\mathcal{T}_o^* = \mathcal{T}_o(t_*)$.

in the previous sections.

From Fig. 5.33 to Fig. 5.35 vorticity structures, defined as vorticity regions with $\|\omega\| > 50\%\|\omega\|_{max}$, are plotted at a series of times. The magnitudes are represented by colors, decreasing from red to yellow to green to blue, scaled at each particular time. Shown together is the particle pathline (open circles) with their initial positions indicated by solid square symbol, and their positions at each particular time, at which vorticity structures are superposed, by solid circles. The reader may need these symbols to orient themselves in these 3D plots. The boxes shown are subsets of the 128^3 data set which enclose the particle pathline. The box for particle #1 consists of $31 \times 16 \times 26$ grid points; $50 \times 31 \times 31$ grid points are required for particle #2 and $51 \times 26 \times 16$ for particle #3.

In the neighborhood of the initial position of particle #1, there exist many vorticity structures which quickly merge together and catch up to the particle. The peak observed in the particle's history starts to fall off as the structure decays to some

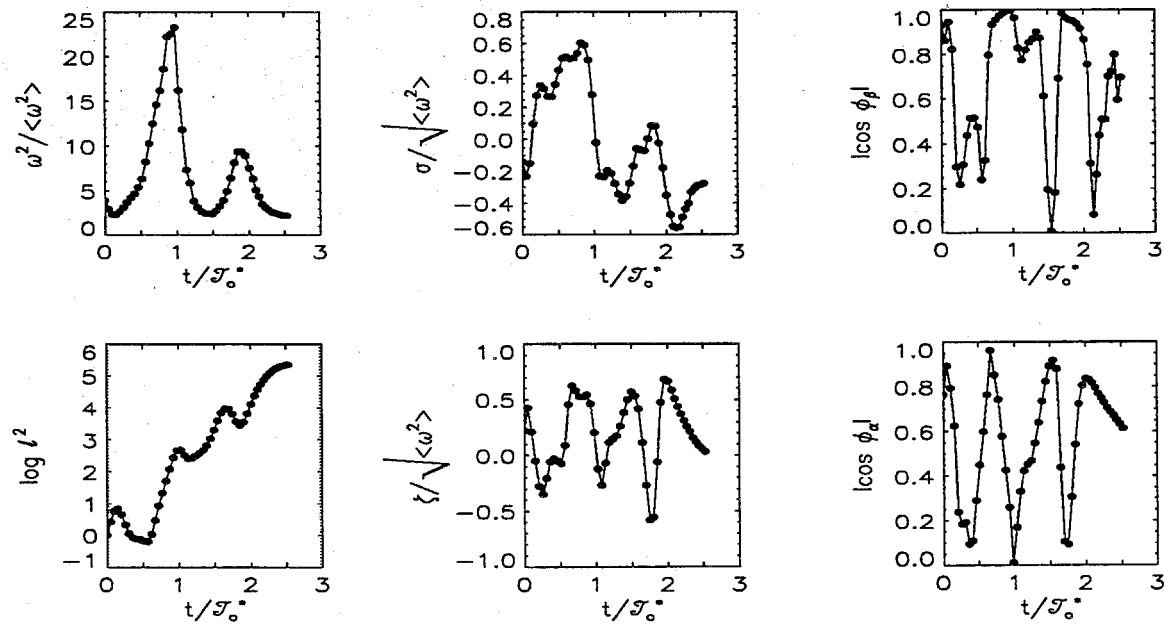

Figure 5.32b: History of particle #2. $\mathcal{T}_o^* = \mathcal{T}_o(t_*)$.

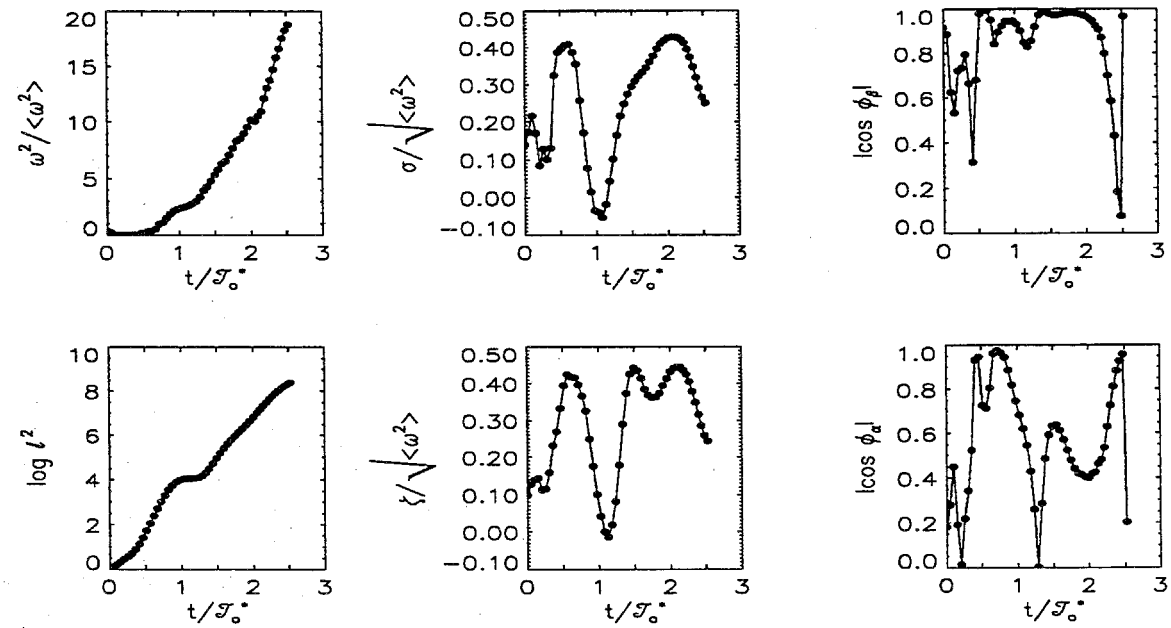

Figure 5.32c: History of particle #3. $\mathcal{T}_o^* = \mathcal{T}_o(t_*)$.

extent and the particle no longer moves together with the structure. In the case of particle #2, a small vorticity blob is first formed ($\tau/\mathcal{T}_o^*$=0.513) and seems to attract the particle when the first peak begins. The particle stays within the structure as the structure gradually changes its shape and merges with other structures. A sheet-like structure is created when two tube-like structures merge with each other ($\tau/\mathcal{T}_o^*$ = 0.822 and 1.027). This sheet structure is then diffused and becomes again tube-like ($\tau/\mathcal{T}_o^*$=1.438). Apparently the interaction in the neighborhood of particle #2 is so strong that the second peak is created. The 3D plots for the final two times suggest that more peaks can be expected if the tracing is continued because the interactions among vortex structures are still strong. Similar phenomena are observed following particle #3. In particular, a sheet structure is observed ($\tau/\mathcal{T}_o^*$ = 0.822 and 1.027), which gradually becomes a tube ($\tau/\mathcal{T}_o^*$=2.397). Particle #3 remains close to the sheet as its vorticity begins to be amplified. It stays inside the structure till the end of the simulation. The lifetime of these vorticity structures is fairly long ($\mathcal{O}(\mathcal{T}_o)$). Vortex lines from some of the structures are shown in Fig. 5.36. The lines appear relatively straight when $\|\omega\|$ is large and more spiral when $\|\omega\|$ is smaller.

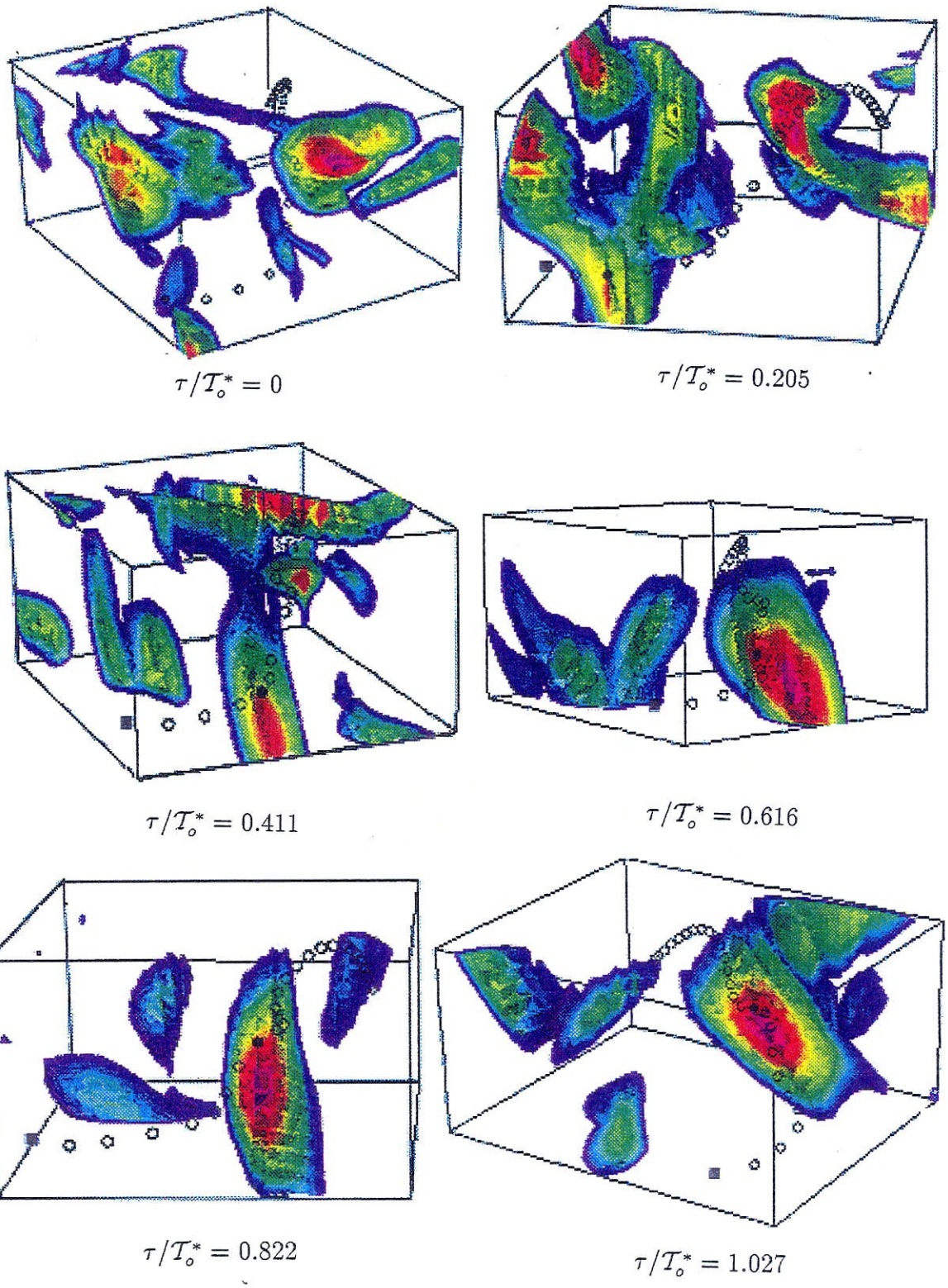

Figure 5.33: (1) Vorticity structures in the neighborhoods of particle #1 which location at the particular time is indicated by the solid circle and which initial position is presented as the solid square; $\mathcal{T}_o^* = \mathcal{T}_o(t_*) = 5.84$.

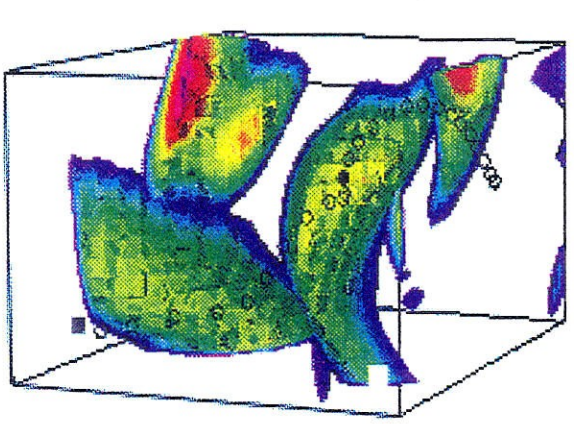

$\tau/\mathcal{T}_o^* = 1.232$

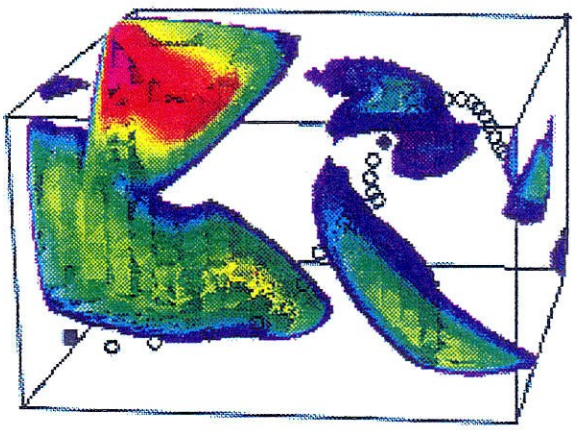

$\tau/\mathcal{T}_o^* = 1.438$

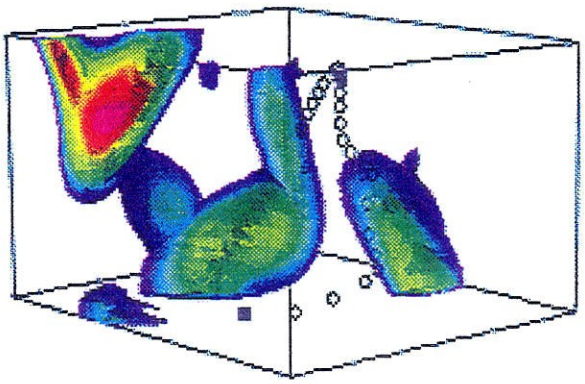

$\tau/\mathcal{T}_o^* = 1.643$

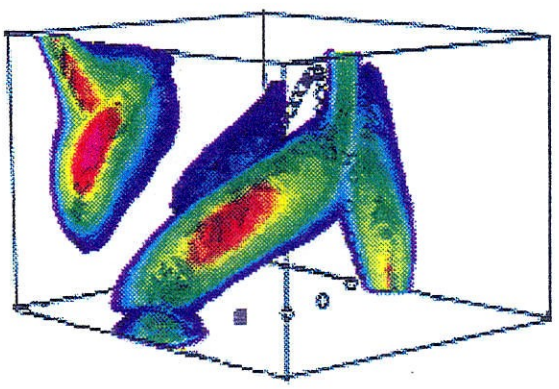

$\tau/\mathcal{T}_o^* = 2.055$

Figure 5.33: (2) Vorticity structures in the neighborhoods of particle #1 which location at the particular time is indicated by the solid circle and which initial position is presented as the solid square; $\mathcal{T}_o^* = \mathcal{T}_o(l_*) = 5.84$.

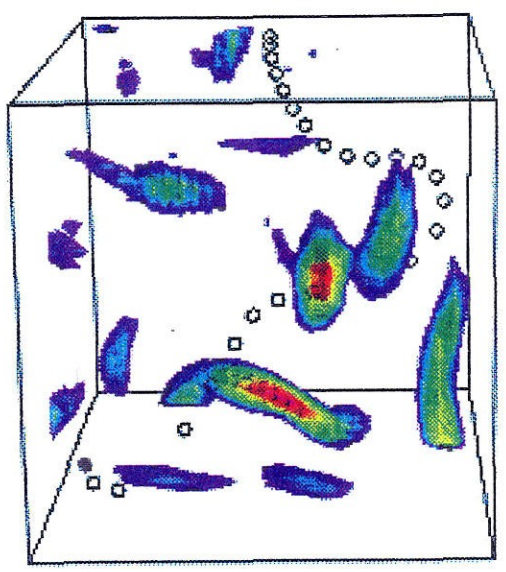

$\tau/\mathcal{T}_o^* = 0$

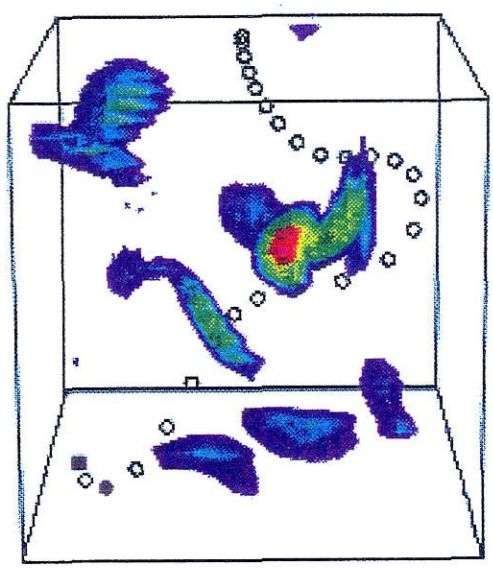

$\tau/\mathcal{T}_o^* = 0.205$

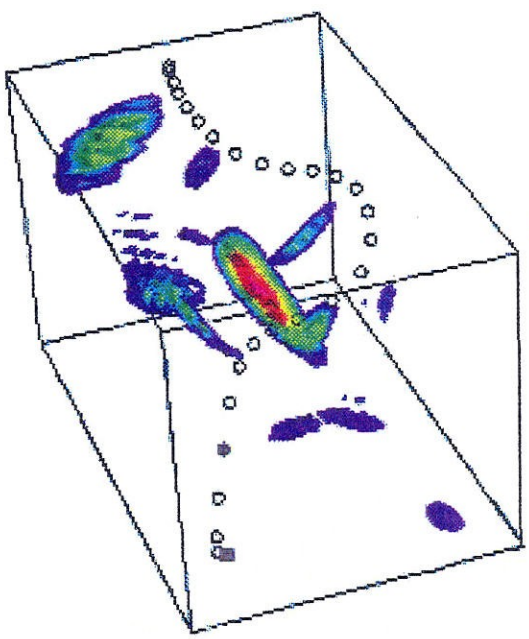

$\tau/\mathcal{T}_o^* = 0.411$

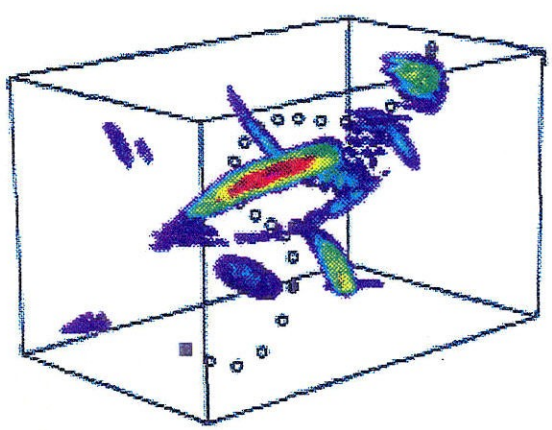

$\tau/\mathcal{T}_o^* = 0.513$

Figure 5.34: (1) Vorticity structures in the neighborhoods of particle #2 which location at the particular time is indicated by the solid circle and which initial position is presented as the solid square; $\mathcal{T}_o^* = \mathcal{T}_o(t_*) = 5.84$.

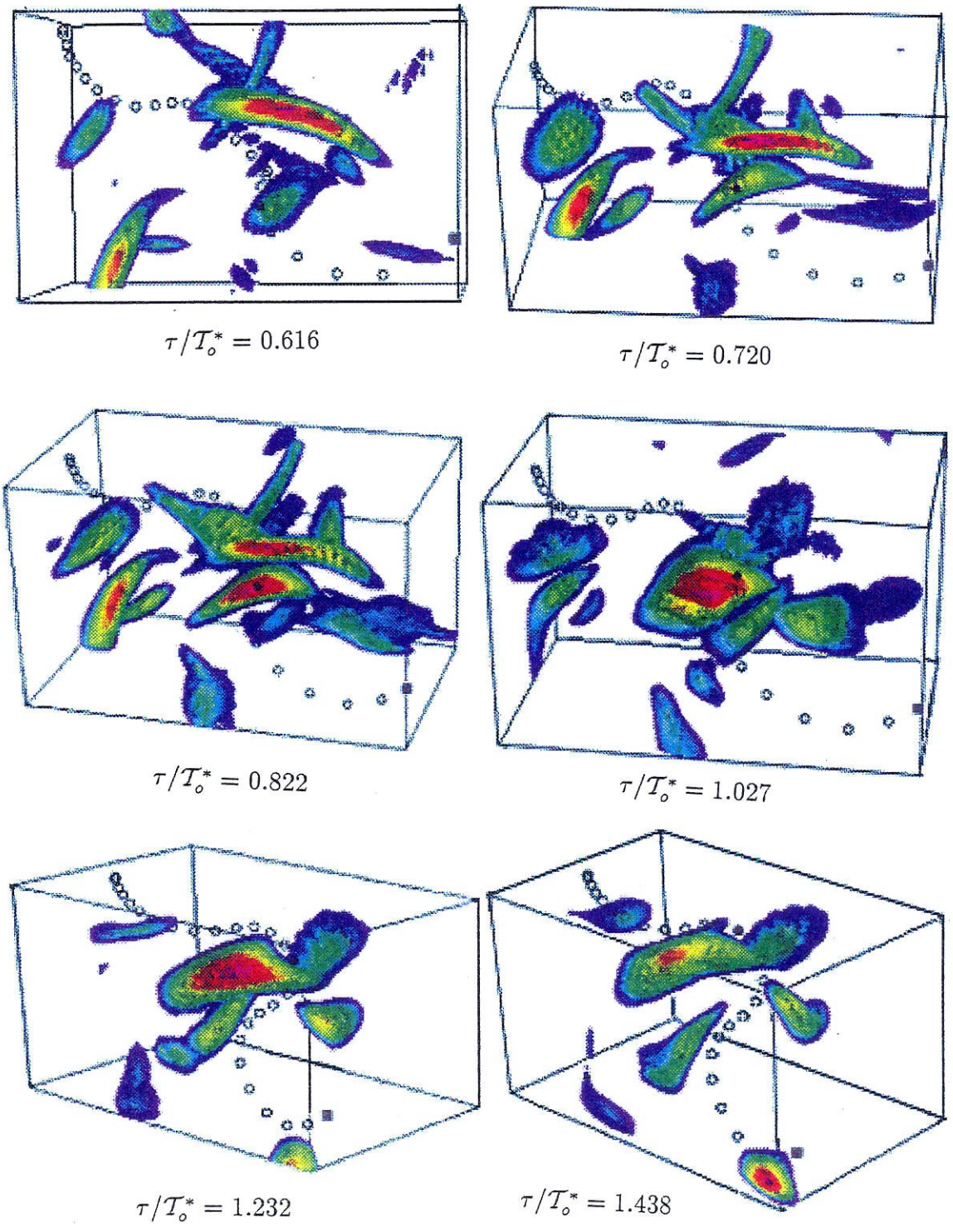

Figure 5.34: (2) Vorticity structures in the neighborhoods of particle #2 which location at the particular time is indicated by the solid circle and which initial position is presented as the solid square; $\mathcal{T}_o^* = \mathcal{T}_o(t_*) = 5.84$.

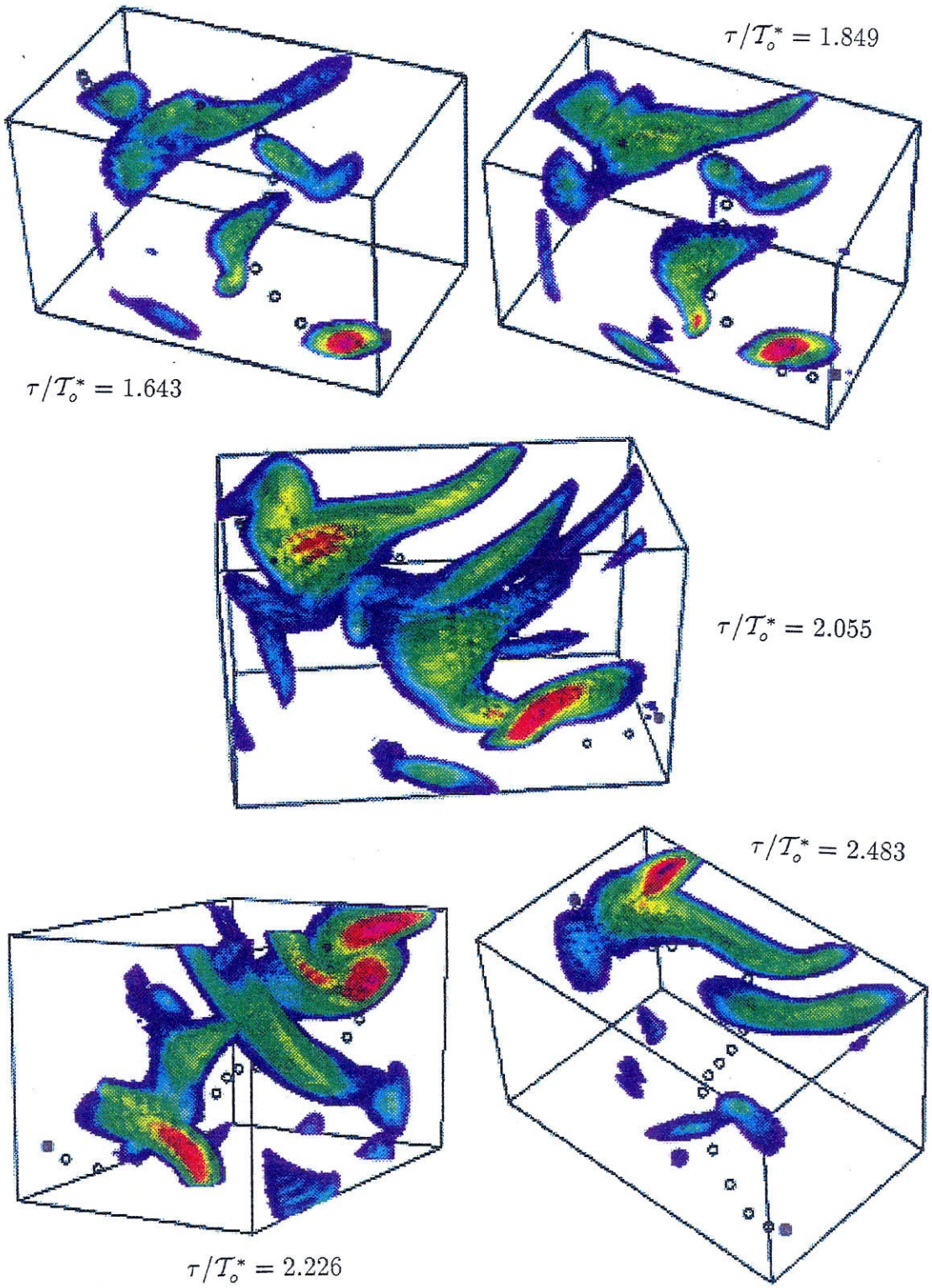

Figure 5.34: (3) Vorticity structures in the neighborhoods of particle #2 which location at the particular time is indicated by the solid circle and which initial position is presented as the solid square; $\mathcal{T}_o^* = \mathcal{T}_o(t_*) = 5.84$.

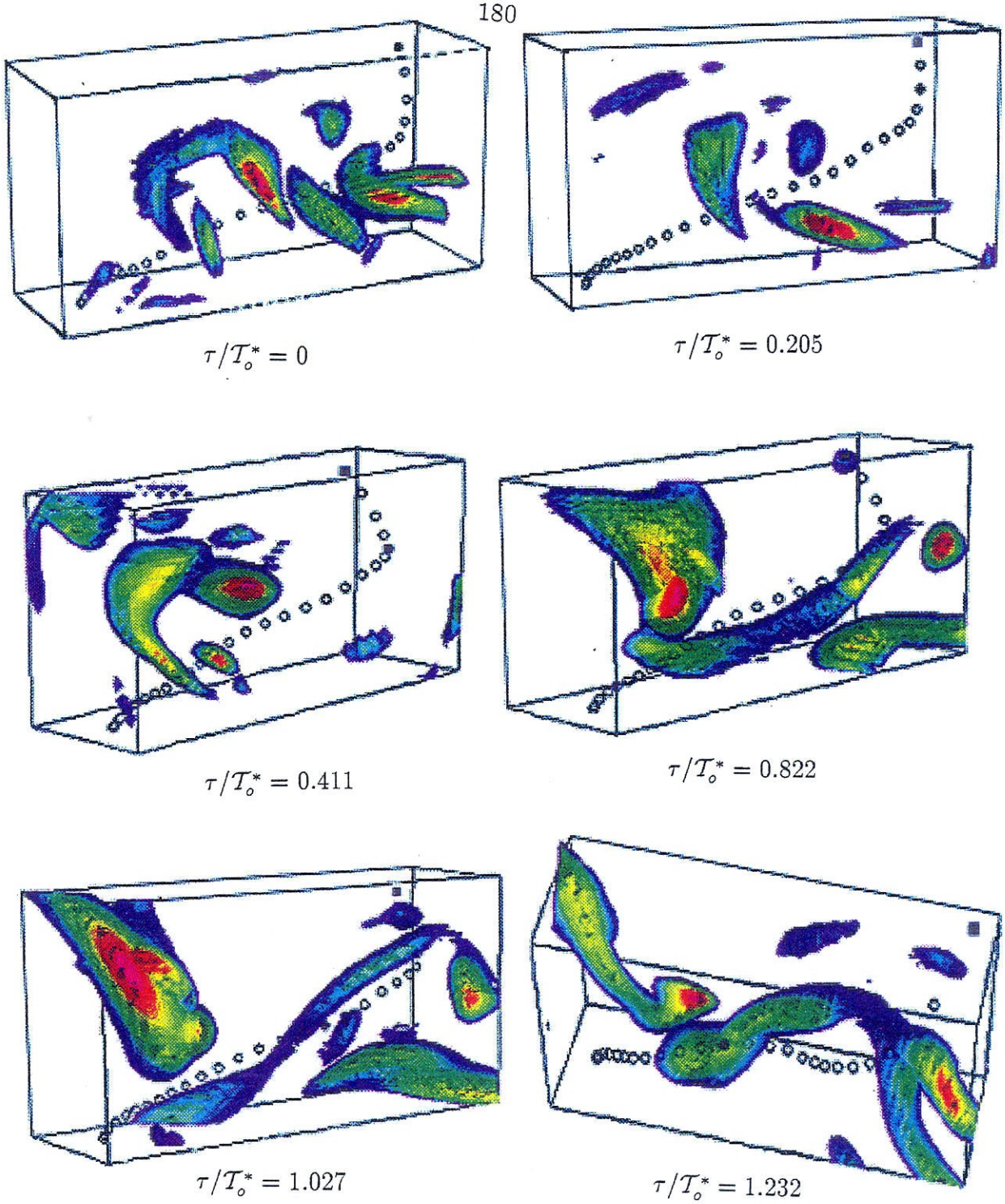

Figure 5.35: (1) Vorticity structures in the neighborhoods of particle #3 which location at the particular time is indicated by the solid circle and which initial position is presented as the solid square; $\mathcal{T}_o^* = \mathcal{T}_o(t_*) = 5.84$.

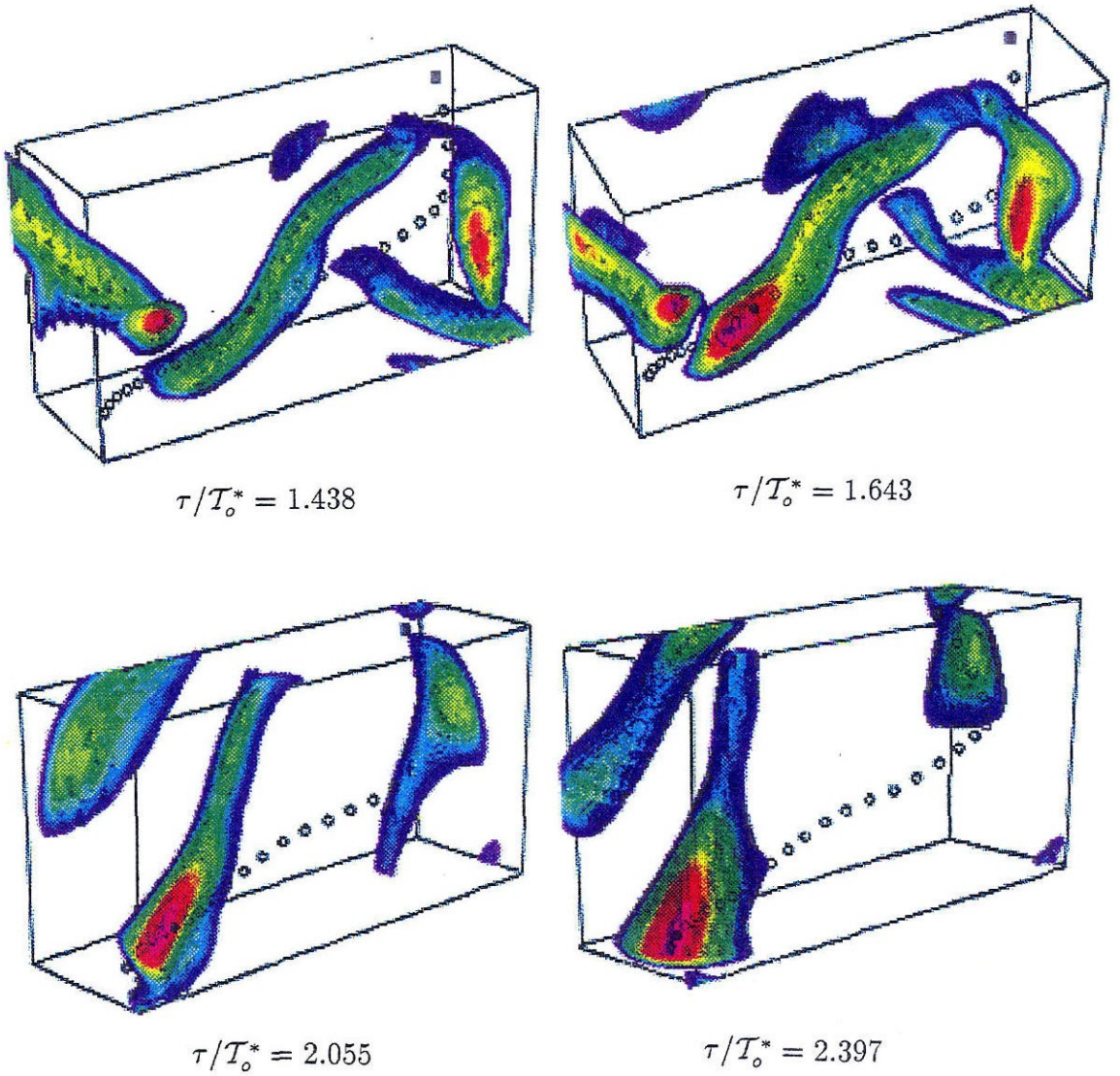

Figure 5.35: (2) Vorticity structures in the neighborhoods of particle #3 which location at the particular time is indicated by the solid cirycle and which initial position is presented as the solid square; $\mathcal{T}_o^* = \mathcal{T}_o(t_*) = 5.84$.

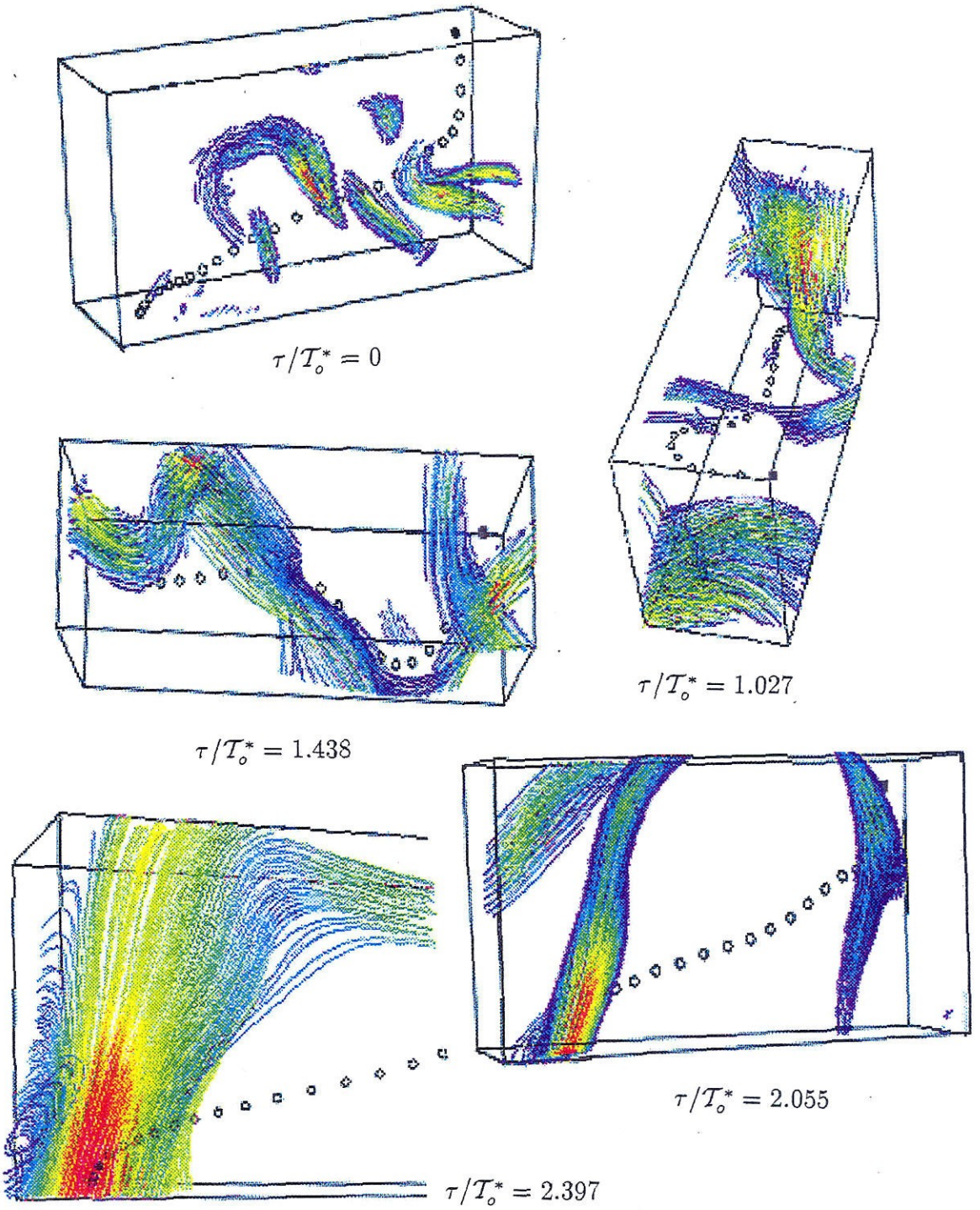

Figure 5.36: The vortex lines of the vorticity structures in the neighborhoods of particle #3 which location at the particular time is indicated by the solid circle and which initial position is presented as the solid square; $\mathcal{T}_o^* = \mathcal{T}_o(t_*) = 5.84$.

5.5 Conclusions

The origin of intense vorticity structures is observed by tracking material particles. The conjecture according to what was observed is the following. Little vorticity blobs are created first. Under the stretching of the nonlinear forces, they gradually become tube-like. When tube-like structures merge together, sheet-like structure is observed temperarily. The sheet-like structures gradually become tube-like again because of the diffusion and/or the instability of the sheet-like structures at later times.

The combination of these vorticity structures causes successive stretching and compression of the material line element vectors. The component which suffers more continuous stretching thus dominates. This component is either ℓ_α or ℓ_β determined by the relative magnitude of the local straining rate ($e_{r\theta}$ in the Burger vortex model) to the background straining rate (a in the model). The balance of the symmetric part with the antisymmetric part of the velocity gradients and the rotation as well as the switch in time and/or in space of the principal directions of the strain tensors cause $\ell_\alpha \approx \ell_\beta \gg \ell_\gamma$ and a mean growth rate $\beta < \zeta < \alpha$.

The mean growth rates of magnitudes of material line elements and vorticity vectors by the nonlinear force are found to be proportional to the square-root of mean enstrophy during the decay of turbulence. So are the mean principal rates of strain tensors. The proportional coefficients are 0.39,0.10, and -0.49 for the principal rates and 0.11 and 0.14 for the growth rates.

Velocity autocorrelation functions, Lagrangian and Eulerian, spatial and temporal, are computed. The measured Eulerian dissipation times agree with Tennekes' prediction under Taylor's "frozen" hypothesis and his independence hypothesis. It was also proved numerically that the Lagrangian autocorrelation functions are self-similar in a new time variable. The similarity is then used to predict particles' diffusion in decaying turbulent flows.

Chapter 6

Conclusions and Future Work

6.1 Conclusions

In the present research, we have investigated the fundamental physics of homogeneous isotropic turbulence numerically and theoretically. The conclusions of each aspect are summarized as follows.

1. Use of the ABC Flows as a Dynamo

In order to search for a possible vortex pattern for a turbulent flow, Townsend [70] explored the solution of the vorticity equations in which the velocity is assumed to be a known large-scale motion while the vorticity solution represents the small-scale motion evolving under the action of the known large-scale motion. Vortex patterns such as tubes and sheets were found in this way. In this thesis, we assume the large-scale motion to be the so-called ABC flow and solve the same problem numerically. The correlation between the geometry of the vorticity solutions and the features of the ABC flow was investigated.

It was observed in all cases that the decay of vorticity by dissipation is overcome by the stretching (dynamo actions). The geometry of intense vorticity regions (struc-

tures) is dominated by the external straining in a way as described as follows. When the ABC flows are integrable, amplifications of vorticity are focused within a small neighborhood of the heteroclinic orbits. Tube-like vorticity structures are observed, although those heteroclinic orbits form planes. When the ABC flows have stagnation points, tube-like structures are observed around the local unstable manifolds of the α-type stagnation points (which have one positive and two negative eigenvalues). The result is not so surprising because the local flow pattern ($\mathbf{u}$) near an α-type stagnation point of the ABC flow is similar to one of the flow patterns used by Townsend which gives him the tube-like vorticity solution. When there are no stagnation points involved, amplifications are found to be confined within the chaotic regions of the ABC flows. We have also found that vorticity vectors of very large mangitudes are nearly aligned with the principal direction corresponding to the most positive principal rate of the local strain tensor of the ABC flow.

The above results suggest the small-scale structures are completely dominated by the external large-scale motion. In numerical simulations of incompressible isotropic homogeneous turbulence, it has been observed that, on the average, two of the principal rates of the strain tensors are positive. Townsend's work suggests sheet-like structures. According to the observations in the present research, a tube-like structure with a flattened cross section is also possible. Nonetheless, in both studies, the induced fluid motion by the small-scale motion, i.e., the effects of the small-scale motion on the imposed large-scale motion, is ignored. The nonlinear interactions between motions of different scales in a turbulent flow are, therefore, not modelled properly.

2. Power-Law Energy Decay of Isotropic Homogeneous Turbulence

Over the years, a power-law energy decay of a turbulent flow has been observed from experimental as well as numerical data. Theoretically, decay exponents of 1, 6/5, 3/2, 10/7, and others have been proposed. In this thesis, we performed high-resolution numerical simulations on the Intel Delta parallel computer of incompressible isotropic homogeneous turbulence and found two decay exponents, 1.2 and 1.5. We examined classic theories, which predict a power-law energy decay, by measuring and comparing dynamic quantities such as skewness $S = -\lambda^3 k'''(r=0)$ and $G = \lambda^4 f^{IV}(r=0)$, where λ is Taylor's microscale, and $f(r,t)$ and $k(r,t)$ are the double and triple velocity autocorrelation functions, and we found no theory in agreement. New theories are thus required.

A power-law energy decay can be obtained by assuming a self-similar solution to the Kármán-Howarth equation for isotropic homogeneous turbulence. A self-similar solution proposed by Von Kármán and Howarth of the form $f(r,t) = \tilde{f}(r/\lambda)$ and $k(r,t) = \tilde{k}(r/\lambda)$ requires a decay exponent n=1, which was not observed. A self-similar solution of the form $f(r,t) = \tilde{f}(r/\lambda)$ and $k(r,t) = Re_\lambda^{-1}\tilde{k}(r/\lambda)$ is compatible with an arbitrary decay exponent n, but suggests a stronger nonlinear interaction with decreasing Reynolds number. As a modification, we propose a new self-similar solution of the form $f(r,t) = f_1(r/\lambda) + Re_\lambda^{\alpha+1} f_2(r/\lambda)$ and $k(r,t) = Re_\lambda^{\alpha} k_2(r/\lambda)$. This self-similar solution is shown to be consistent with a power-law energy decay with an arbitary decay exponent and can be physically reasonable with $\alpha > 0$, i.e., it predicts a stronger nonlinear interaction with increasing Reynolds number. In addition, the predicted behavior of S and G agrees with the numerical results.

A transitional state, during the initial period of decay and before the flow enters into the proposed similarity state, was observed in our numerical simulations. For such a transitional state, we conjecture that a self-similar solution of the form $f(r,t) = f_1(r/\lambda) + Re_\lambda^{\alpha+1} f_2(r/\lambda)$ and $k(r,t) = Re_\lambda^{-1} k_1(r/\lambda) + Re_\lambda^{\alpha} k_2(r/\lambda)$ may apply.

The combination of the two proposed self-similar solutions and the numerical result that $\alpha \approx 0$, therefore, suggests that during the decay, the skewness increases with decreasing Reynolds number, reaches a maximum value, and then stays approximately constant as Reynolds number decreases further.

The Reynolds number Re_λ in our numerical simulations ranges from 10 to 50, which is probably not large enough to separate characteristic lengthscales of the energy containing range and the dissipation range, and, therefore, the proposed self-similarity, involving only one lengthscale, works reasonably well. For turbulence with very large Reynolds number, we expect that there exist more than one characteristic lengthscale.

A candidate for the characteristic lengthscale of large eddies is the lengthscale $\mathcal{L} \sim \lambda Re_\lambda$ appearing in the empirical equation of energy decay of turbulence, i.e., $dq^2/dt \sim q^3/\mathcal{L}$, while Kolmogorov dissipation lengthscale η is chosen to be the characteristic lengthscale of small eddies. Using $k\lambda Re_\lambda$ and $k\eta$ as the self-similar variables, we propose an energy spectrum of the form $E(k) \sim q^2 \lambda Re_\lambda \sum_{j=0} Re_\lambda^{-j/2} F_j(k\lambda Re_\lambda)$ at small wave numbers and of the form $E(k) \sim (\epsilon\nu^5)^{1/4} \sum_{j=0} Re_\lambda^{-j/2} G_j(k\eta)$ at large wave numbers, where F_j and G_j, j=0,1,2,$\cdots$, are self-similar functions of variables $k\lambda Re_\lambda$ and $k\eta$ respectively. This particular energy spectrum was shown to be consistent with a power-law energy decay and with the spectral Kármán-Howarth equation.

Finally we show that the above similarity of the energy spectrum at large wave numbers and the observation of an exponential tail of the energy spectrum of the form $(k\eta)^{5/3} E(k\eta, t)/(\epsilon\nu^5)^{1/4}$ in the far-dissipation range can be used to predict the skewness of the longitudinal velocity derivative for turbulence with a power-law energy decay.

3. Lagrangian Studies

In order to collect Lagrangian statistics which are very helpful in understanding turbulent transport, we developed third-order finite difference interpolation schemes to track fluid particles and simulate the motion of material line elements. In addition, we compute the Lagrangian double velocity autocorrelation function (f_L), the two-time-one-point (f_E), and two-point-one-time (f) Eulerian autocorrelation functions. The numerical results show that f_E is smaller than f_L at small time lags, suggesting that f_L is more persistent, in agreement with the advection hypothesis proposed by Tennekes. The function f_E, however, has a longer tail than f_L at both positive and negative large time lags. It implies that more energy is contained within eddies of small frequencies for an Eulerian observer than for a Lagrangian observer.

With the observation of a power-law energy decay, i.e., $q^2 \sim q_o^2(1+\tau/\tau_o)^{-n}$, we reconsider the classical hypothesis of Batchelor and Townsend that $u(\tau)(1+\tau/\tau_o)^{n/2}$ is a stationary random function of some new time variable s, where $u(\tau)$ is particle's velocity and $ds = d\tau/\tau_s$. With the assumption that $\tau_s \sim \mathcal{T}_L$, where $\mathcal{T}_L$ is the Lagrangian integral time scale, and the assumption that $q\mathcal{T}_L \propto \lambda Re_\lambda$, we find $\tau_s = \tau+\tau_o$, and therefore, we obtain a self-similar Lagrangian velocity autocorrelation function of variable $s = log(1+\tau/\tau_o)$, as observed from our numerical results. This similarity enables us to predict particle dispersion in decaying turbulence by evoking Taylor classical work of 1921. The long-time growth of the mean square displacement of fluid particles is $\propto \tau^{2-n}$. Note the growth is $\propto \tau$ in a stationary turbulence. The agreement of the theoretical prediction with the numerical data was observed.

In addition to the Lagrangian velocity autocorrelation function, Lagrangian statistics of certain small-scale quantities of decaying turbulence were collected. We remark the results as follows. The mean principal rates of the strain tensor were found to be proportional to the square root of mean enstrophy. The proportional coefficients are about 0.4, 0.1, and -0.5, remaining constant during the decay. The ratios of the mean

principal rates are 4:1:-5 which are as the same as those measured by Girimaji and Pope from a simulation of stationary turbulence but different from those measured by Ashurst who measured 3:1:-4. These ratios, (4:1:-5), could be used as a check or as an input to phenomenological models of turbulence such as Ashurst's Burger vortex model and Pullin and Saffman's Lundgren-Townsend vortex model.

The mean growth rate of the magnitude of a material line element and that of the magnitude of vorticity due to the nonlinear forces are found proportional to the square root of mean enstrophy as well. The proportional coefficient is 0.10 for vorticity and 0.14 for material line elements and both also remain nearly constant during the decay.

The mean absolute values of the cosines of the angles between a material line element and the principal directions of the strain tensor corresponding to the most stretching and the intermediate principal rates are found about the same. This fact and the observed difference in the line element growth rate and the maximum principal rate imply the importance of vorticity effects and rotation effects of the strain tensor on the evolution of a material line element. The switch of principal directions could be a factor also. The evolution of a material line element under the action of a Burger vortex is also studied. The results show that a process of successive stretching and compression is caused by the above effects, resulting in a net small amplification of the components in the plane normal to the vortex. The component aligned with the axis of the vortex, which is the principal direction either corresponding to the largest principal rate or to the intermediate one, depending on the relative magnitude of the local straining to the external straining, therefore becomes dominant.

Numerical results show that there is no correlation between the growth rate of the magnitudes of material line elements with the vorticity magnitudes. The growth rate, on the other hand, increases approximately linearly with straining magnitudes. Further investigation is needed to explain these phenomena.

Finally by taking advantage of the flow visualization tools and following material particles, we were able to observe the origin of high-magnitude vorticity structures in

turbulence. Vortex sheets are observed temporarily when tube-like structures merge together, but they gradually become tube-like at later times because of the diffusion and/or the instability of the sheet-like structures.

6.2 Future Work

A few observations follow regarding future investigations of the physics of homogeneous isotropic turbulence.

1. Decaying turbulence

a. It was observed in chapter4 that the periodicity of the flow contaminates seriously the velocity autocorrelations and therefore the numerical results can not be used to verify the proposed similarity form, in particular at large separations. Simulations of decaying homogeneous turbulence with Reynolds numbers high enough so that the integral lengthscales are relatively small compared to the box size and so that the eddies remain isotropic should be performed in the future when they become possible.

b. The similarity forms found herein for the double and triple velocity autocorrelation functions are applicable to flows with small and/or intermediate Reynolds number; while Kármán-Howarth's similarity may be expected for flows with very large Reynolds numbers. Also, we have discussed the possibility that George's similarity may be a transient state during the initial period of decay. Future research could be directed towards classifying all the possible self-similar solutions of the Kármán-Howarth equation, in identifying the range of validity of these solutions, and studying how turbulence passes from one state to another.

2. Lagrangian studies

a. The history of a single particle shows that the material line element is stretched and compressed successively, resulting in a net positive growth. The characteristic time period and the characteristic growth rate during the stretching periods and/or compression periods must characterize in some way the lifetime of nearby vorticity structures and the dispersion of particles by turbulence. A study along these lines should be carried out in the future.

b. The Lagrangian statistics of the small-scale properties of turbulence are valuable in helping subgrid modellers select free parameters in their models. It was found the ratios of principal rates of the strain tensor are 4:1:-5 and many other important rates are proportional to the square root of mean enstrophy in decaying as well as stationary turbulence. However the mean growth rate of the magnitude to a material line element is even found to be uncorrelated with the magnitude of the vorticity. This information and more should be used in the development of subgrid models.

c. We know the rotation of the strain tensor acts on the material line element like a vorticity vector, but how does the strain tensor rotate as we follow a material particle? An investigation of the Lagrangian history of the strain tensor may help answer these questions.

d. Finally, the particle's tracing scheme can be easily extended to simulate the evolutions of material surfaces and material volumes so that applications to turbulent combustion problems can be made.

References

[1] V.I. Arnold. *C.R. Acad. Sci. Paris*, 261, 1965.

[2] Wm.T. Ashurst. Is turbulence a collection of burgons? *Phys. Fluids*, 1992.

[3] Wm.T. Ashurst, A.R. Kerstein, R.M. Kerr, and C.H. Gibson. Alignment of vorticity and scalar gradient with strain rate in simulated navier-stokes turbulence. *Phys. Fluids*, 30, 1987.

[4] G.J. Barenblatt. *Similarity, Self-Similarity, and Intermediate Asympototics.* Plenum, New York, 1979.

[5] G.J. Barenblatt and A.A. Gavrilov. On the theory of self-similar degeneracy of homogeneous isotropic turbulence. *Sov. Phys. JETP*, 38, 1974.

[6] G.K. Batchelor. Energy decay and self-preserving correlation functions in isotropic turbulence. *Quarterly of Applied Mathematics*, 6, 1948.

[7] G.K. Batchelor. *The Theory of Homogeneous Turbulence.* Cambridge, 1953.

[8] G.K. Batchelor and I. Proudman. The large-scale structure of homogeneous turbulence. *Proc. Soc. London Ser. A*, 248, 1956.

[9] G.K. Batchelor and A.A. Townsend. Decay of isotropic turbulence in the initial period. *Proc. Roy. Soc. London*, 193A, 1948.

[10] G.K. Batchelor and A.A. Townsend. Decay of turbulence in the final period. *Proc. Roy. Soc. London*, 194A, 1948.

[11] G.K. Batchelor and A.A. Townsend. Decay of vorticity in isotropic turbulence. *Proc. Roy. Soc. A*, 190, 1948.

[12] G.K. Batchelor and A.A. Townsend. Turbulent diffusion. *Surveys in Mechanics*, 1956.

[13] B.J. Bayly. Infinitely conducting dynamics and other horrible eigenproblems.

[14] R. Benzi, G. Paradin, G. Parisi, and A. Vulpiani. *J. Phys. A*, 17, 1984.

[15] F.H. Champagne. The fine-scale structure of the turbulent velocity field. *J. Fluid Mech.*, 86, 1978.

[16] S. Childress. New solutions of the kinematic dynamo problem. *J. Math. Phys*, 11, 1970.

[17] S. Corrsin. Turbulent dissipation fluctuations. *Phys. Fluids*, 5, 1962.

[18] S. Corrsin. Estimates of the relations between eulerian and lagrangian scales in large reynolds number turbulence. *J. Atm. Sciences*, 20, 1963.

[19] S.W.H. Cowley. *Radio Sci.*, 8, 1973.

[20] P.E. Dimotakis. Some issues on turbulent mixing and turbulence. *GALCIT Report*, FM93-1a, 1993.

[21] T. Dombre, U. Frisch, J.M. Greene, M. Henon, A. Mehr, and A.M. Soward. Chaotic streamlines in the abc flows. *J. Fluid Mechanics*, 167, 1986.

[22] N. Dunford and J.T. Schwartz. *Linear Operators I.* 1958.

[23] V. Eswaran and S.B. Pope. An examination of forcing in direct numerical simulations of turbulence. *Computers and Fluids*, 16, 1988.

[24] J.M. Finn and E. Ott. Chaotic flows and fast magnetic dynamos. *Phys. Fluids*, 31, 1988.

[25] U. Frisch, P.L. Sulem, and M. Nelkin. *J. Fluid Mechanics*, 87, 1978.

[26] D. Galloway and U. Frisch. Dynamo action in a family of flows with chaotic streamlines. *Geophys. Astrophys. Fluid Dynamics*, 36, 1986.

[27] W.K. George. The decay of homogeneous isotropic turbulence. *Phys. Fluids A*, 4, 1992.

[28] S.S. Girimaji and S.B. Pope. Material-element deformation in isotropic turbulence. *J. Fluid Mechanics*, 220, 1990.

[29] T. Gotoh, R.S. Rogallo, J.R. Herring, and R.H. Kraichnan. Lagrangian velocity correlations in homogeneous isotropic turbulence. *Turbulence Research Center, Stanford*, 1992.

[30] D. Gottlieb and S.A. Orszag. *Numerical Analysis of Spectral Methods: Theory and Applications.* 1981.

[31] S.R. Hanna. Lagrangian and eulerian time-scale relations in the daytime boundary layer. *J. Appl. Met.*, 20, 1981.

[32] W. Heisenberg. Zur statischen theorie der turbulenz. *Z. Physik*, 124, 1948.

[33] J.O. Hinze. *Turbulence.* McGRAW-HILL, 1975.

[34] Y. Kaneda and T. Gotoh. Lagrangian velocity autocorrelation in isotropic turbulence. *Phys. Fluids A*, 3, 1991.

[35] R.M. Kerr. Velocity, scalar and transfer spectra in numerical turbulence. *J. Fluid Mechanics*, 211, 1990.

[36] S. Kida and Y. Murakami. Kolmogorov similarity in freely decaying turbulence. *Phys. Fluids*, 30, 1987.

[37] A.N. Kolmogorov. Dissipation of energy in locally isotropic turbulence. *C.R. Acad. Sci. U.R.S.S.*, 32, 1941.

[38] A.N. Kolmogorov. The local structure of turbulence in incompressible viscous fluid for very large reynolds numbers. *C.R. Acad. Sci. U.R.S.S.*, 30, 1941.

[39] A.N. Kolmogorov. On degeneration of isotropic turbulence in an incompressible viscous liquid. *C.R. Acad. Sci. U.R.S.S.*, 31, 1941.

[40] A.N. Kolmogorov. *J. Fluid Mechanics*, 13, 1962.

[41] L.G. Loitsianskii. Some basic laws of isotropic turbulent flow. *Natl. Advisory Comm. Aeronaut. Tech. Mem.*, No. 1079, 1945.

[42] T.S. Lundgren. Strained spiral vortex model for turbulent fine structure. *Phys. Fluid*, 25, 1982.

[43] B. Mandelbrot. *J. Fluid Mechanics*, 1976.

[44] N.N. Mansour and A.A. Wray. Decay of isotropic turbulence at low reynolds number. *NASA Ames Research Center*, 1993.

[45] C. Meneveau and K.R. Sreenivasan. *Phys. Rev. Lett.*, 59, 1987.

[46] H.K. Moffatt and M.R.E. Proctor. Topological constraints associated with fast dynamo action. *J. Fluid Mechanics*, 154, 1985.

[47] A.M. Oboukhov. On the distribution of energy in the spectrum of turbulent flow. *Compt. rend.acad.sci URSS*, 32, 1941.

[48] A.M. Oboukhov. *J. Fluid Mechanics*, 13, 1962.

[49] S.A. Orszag. Numerical simulation of incompressible flows within simple boundaries. i. galerkin (spectral) respresentations. *Studies in Applied Mathematics*, L, 1971.

[50] S.A. Orszag. Comparison of pseudospectral and spectral approximation. *Studies in Applied Mathematics*, LI, 1972.

[51] Y.H. Pao. *Phys. Fluids*, 8, 1965.

[52] D.I. Pullin and P.G. Saffman. On the lundgren-townsend model of turbulent fine scales. *Physical Fluid A*, 5, 1993.

[53] J.J. Riley and G.S. Patterson. Diffusion experiments with numerical integrated isotropic turbulence. *Phys. Fluids*, 17, 1974.

[54] G.O. Roberts. Spatially periodic dynamics. *Philos. Trans. R. Soc. London*, 266, 1970.

[55] R.S. Rogallo. Numerical experiments of homogeneous turbulence. *NASA Technical Memorandum*, 81315, 1981.

[56] S.G. Saddoughi and S.V. Veeravalli. Local isotropy in turbulent boundary layers at high reynolds numbers. *CTR Manuscript 142, Stanford*, 1993.

[57] P.G. Saffman. An approximate calculation of the lagrangian auto-correlation coefficient for stationary homogeneous turbulence. *Appl. Sci. Res. A*, 11, 1962.

[58] P.G. Saffman. On the fine-scale structure of vector fields convected by a turbulent fluid. *J. Fluid Mechanics*, 16, 1963.

[59] P.G. Saffman. The large-scale structure of homogeneous turbulence. *J. Fluid Mechanics*, 27, 1967.

[60] Y. Sato and K. Yamamoto. Empirical equations for the structure of isotropic turbulence. *J. Chem. Engng. Japan*, 16, 1983.

[61] Y. Sato and K. Yamamoto. Lagrangian measurement of fluid-particle motion in an isotropic turbulent field. *J. Fluid Mechanics*, 175, 1987.

[62] Z. She, E. Jackson, and S.A. Orszag. Structure and dynamics of homogeneous turbulence: Models and simulations. *Proc. R. Soc. Lond. A*, 434, 1991.

[63] D.J. Shlien and S. Corrsin. A measurement of lagrangian velocity autocorrelation in approximately isotropic turbulence. *J. Fluid Mechanics*, 62, 1974.

[64] L.M. Smith and W.C. Reynolds. The dissipation-range spectrum and the velocity-derivative skewness in turbulent flows. *Phys. Fluids A*, 3, 1991.

[65] M.R. Smith, R.J. Donnelly, N. Goldenfeld, and W.F. Vinen. Decay of vorticity in homogeneous turbulence. 1993.

[66] C.G. Speziale and P.S. Bernard. The energy decay in self-preserrving isotropic turbulence revisited. *J. Fluid Mechanics*, 241, 1992.

[67] G.I. Taylor. Diffusion by continuous movements. *Proc. London Math. Soc. Ser. 2*, 20, 1922.

[68] H. Tennekes. Simple model for the small-scale structure of turbulence. *Phys. Fluids*, 11, 1968.

[69] H. Tennekes. Eulerian and lagrangian time microscales in isotropic turbulence. *J. Fluid Mechanics*, 67, 1975.

[70] A.A. Townsend. On the fine-scale structure of turbulence. *Proc. Roy. Soc. (London)*, A208, 1951.

[71] Th. von Karman and L. Howarth. On the statistical theory of isotropic turbulence. *Proc. Roy. Soc. London*, 164A, 1938.

[72] P.K. Yeung and S.B. Pope. An algorithm for tracking fluid particles in numerical simulations of homogeneous turbulence. *J. Computational Physics*, 79, 1988.

[73] P.K. Yeung and S.B. Pope. Lagrangian statistics from direct numerical simulations of isotropic turbulence. *J. Fluid Mechanics*, 207, 1989.

[74] Ya.B. Zeldovich, A.A. Ruzmaikin, and D.D. Sokoloff. Gordon and Breach, 1983.